Title	Precursor-Dependent Local Structure of Rh/Al2O3 Catalysts Analyzed by Scanning Tunneling Microscopy and X-ray Absorption Fine Structure
Author(s)	Chen, Zhiwen
Citation	大阪大学, 2012, 博士論文
Version Type	VoR
URL	https://hdl.handle.net/11094/24914
rights	
Note	

Precursor-Dependent Local Structure of Rh/Al_2O_3 Catalysts Analyzed by Scanning Tunneling Microscopy and X-ray Absorption Fine Structure

A dissertation submitted to

THE GRADUATE SCHOOL OF ENGINEERING SCIENCE

OSAKA UNIVERSITY

in partial fulfillment of the requirements for the degree of

DOCTOR OF PHILOSOPHY IN SCIENCE

BY

Zhiwen Chen

MARCH 2012

Abstract

Supported metal catalysts comprising small metal particles dispersed on the high-surface-area support material (e.g. Al_2O_3, SiO_2, MCM-41) have a wide range of industrial and environmental applications. It is well known that activity, selectivity and stability of supported catalysts are influenced by the precursor used for the preparation of the catalysts. For example, Rh/SiO_2 catalysts prepared from different precursors of $Rh(OOCCH_3)_3$, $RhCl_3$, and $Rh(NO_3)_3$ showed quite different activity and selectivity for CO_2 hydrogenation reaction. In spite of previous intensive studies, however, we do not get our hands on the microscopic mechanisms of the precursor dependent formation of the catalytically active sites. In this thesis, I studied on the precursor dependent structure of Rh/Al_2O_3 catalysts by using two kinds of approach: one is the surface science approach using high-spatial resolution microscopy of scanning tunneling microscopy (STM) for flat catalyst model surfaces, and the other is conventional spectroscopic approach using X-ray absorption fine structure (XAFS) for local structural analyses of high surface-area catalysts. I have proved that these analyses gave consistent and complementary results and would be a powerful methodology to study the precursor dependencies. The contents of this thesis are as follows.

A brief review of the heterogeneous catalysts and previous surface science approaches to catalyses with some methodologies are described in Chapter 1. Experimental techniques and some theoretical background are described in Chapter 2.

In Chapter 3, precursor dependent structure of Rh/Al_2O_3 catalysts were analyzed by high-resolution STM measurements. I found that homogeneous Rh dimer species could be randomly dispersed on Al_2O_3 thin film/NiAl(110) by using $[Rh^{II}(OAc)_2]_2$ precursor. Moreover, the Rh dimer species are quiet stable up to 800 K. However,

when common precursor $RhCl_3$ is used for the precursor instead, larger Rh particles were formed. This phenomenon is very important because the homogeneity and high stability of active species are of high demand issues for catalysts.

In Chapter 4, the precursor dependence of Rh/Al_2O_3 catalysts that I found by STM measurements (Chapter 3) were examined by XAFS spectroscopy. I confirmed that the same phenomena occurred on the high surface area Al_2O_3 support when the appropriate pre-treatment of Al_2O_3 and similar preparation procedure were adopted. Metallic Rh cluster with size of 1-3 nm were generated from $RhCl_3$, while rhodium-oxide-like compounds formed in the case of $[Rh^{II}(OAc)_2]_2$ and $Rh^{III(}OAc)_3$ precursors. Furthermore, XAFS results suggested that Rh-O bond preferentially formed along with the decomposition of acetate ligand and it stabilized the Rh core on the Al_2O_3 surface. By using FEFF calculation and real space model method, we have successfully determined the local structures of these rhodium-oxide-like compounds: one or two Rh atoms from the Rh precursors are selectively fixed on three or four-fold sites on the γ-Al_2O_3 surface. These results give a good agreement with previous STM study.

Conclusions of this thesis and outlook of future studies are described in Chapter 5.

Contents

Chapter 3 STM Studies on the Formation of Precursor -Dependent Rh Clusters on Al_2O_3/NiAl(110) Surface..................93

Chapter 4 XAFS Analyses on Precursor-Dependent Local Structures of Supported Rh Cluster Catalysts 139

Chapter 1 General Introduction

Catalysts are indispensable materials in many areas of our modern life and catalytic reactions also happen incessantly in our bodies. Catalyst refers to the material by which the rate of a chemical reaction can be accelerated and it is not substantially consumed in the process.[1] The earliest catalysis was discovered by Döbereiner in the 18th century. He found that the spongy platinum could bring about the combination of hydrogen and oxygen at room temperature and then invented a lighter by taking advantage of this phenomenon.[2] Nowadays, numerous kinds of catalysts have been created to satisfy different demands from not only industrial production but also environmental revolution, new energy generation and so on. The catalysts can be roughly divided into three groups: heterogeneous catalysts, homogeneous catalysts and biological catalysts.[3]

This research is mainly related to the heterogeneous catalysts. Thus, the objective in this chapter is to introduce the heterogeneous catalysts briefly and then explain our motivation and strategies.

1.1 Brief Introduction to Heterogeneous Catalysts

Heterogeneous catalysts are distinguished from homogeneous catalysts by the different phases present during reaction. Homogeneous catalysts are present in the same phase, usually liquid, while heterogeneous catalysts are present in a different phase, usually solid. For example, in the H_2O photodecomposition, the catalyst TiO_2 is solid, while reactant H_2O is liquid and product H_2 and O_2 are gas.[4] The main advantage of using a heterogeneous catalyst is that being a solid material, it is easy to be separated from the gas and/or liquid reactants and products of the overall catalytic reaction. Additionally, heterogeneous catalysts are typically more tolerant of extreme operating conditions than homogeneous ones.

Heterogeneous catalysts are always playing an extremely important role in the progress of our life. And now it has been estimated that 90% of all chemical process use heterogeneous catalysts.[5] From the late 18th century, the heterogeneous catalysts were mostly applied to the large-scale synthesis of simple but important chemicals. Winkler (1875) and Knietsch (1888) applied platinum and V_2O_5 into synthesis of sulfuric acid and successfully improved production from 50 tons/year to one million tons/year in the UK.[6] Another important application was in the development of ammonia process. Haber, Bosch and Mittash (1906) used Fe-based catalysts to synthesize the NH_3 from N_2 and H_2 under elevated temperature and pressure condition.[6] After these successes, many complex catalytic processes evolved in the chemical industry, such as: synthesis of methanol from CO and H_2 (ZnO/Cr_2O_3, 1923), Fischer-Tropsch reaction: production of hydrocarbon (Fe, Co, Ni, 1925), dehydrogenation of alkene to diene (bismuth molybdates, phosphates, and tungstates, 1950) for production of synthetic rubber and the polymerization of alkene (Ti compounds, 1954) to produce plastics.[6, 7] In the middle of the 19th century, the large-scale industrial application of heterogeneous catalysts emerged into the petroleum. Two kinds of heterogeneous catalysts: zeolites as cracking catalysts and supported metal clusters (e.x. Cu-based catalysts) as reforming catalysts were widely used in the petroleum industry. Until 1970, the heterogeneous catalyst mainly played an active part in the chemical industry. History of the catalysis of industrial process is summarized in Table 1.1

Over the last several decades, environmental pollution and energy consumption problems began to cause great attention. The environmental revolution and new energy generation have been globally accepted as the most important issues from the end of 20th century until now. The heterogeneous catalysts still play a critical role in attacking these problems. Earlier in

1975, Pt/Al_2O_3 called three-way catalyst was introduced into the automobile to reduce CO, hydrocarbon and NO_X emission as shown in the Figure.1.1.1.[8, 9] And then NO_X Storage Reduction (NSR) catalysts[10-12] and Selective Catalytic Reduction (SCR) catalysts[13,14] were developed to reduce NO_X emissions in the lean-burn condition, in which higher fuel efficiency and thus lower CO_2 emission could be achieved. On the other hand, with respect to the new energy generation, a lot of new catalytic processes were developed. A promising environmentally friendly technology is the production of electrical power with fuel cells.[15] However, fuel cells require hydrogen as a fuel, which is extremely difficult to store and transport.[16, 17] Thus, the generation of hydrogen *in situ* by reforming of alcohols and hydrocarbons became a hopeful solution.[18,19] Especially, methanol is currently the main fuel in industry because of its low carbon-content and low reforming temperature. Copper-based catalysts (Cu/ZrO_2, Cu/ZnO) are the most commonly used for methanol reforming process to achieve the high activity and selectivity. The reforming reaction is described as follow:

$$CH_3OH + H_2O \rightleftarrows CO_2 + 3H_2 \qquad \Delta H = 49.7 \text{ kJ mol}^{-1} \tag{1.1}$$

$$CH_3OH \rightleftarrows CO + 2H_2 \qquad \Delta H = 90.2 \text{ kJ mol}^{-1} \tag{1.2}$$

$$CO + H_2O \rightleftarrows CO_2 + H_2 \qquad \Delta H = -41.2 \text{ kJ mol}^{-1} \tag{1.3}$$

Beside the main reaction, two side reactions commonly occur. In Eq (1.2) methanol decomposition, side-product CO will poisons the electrode of fuel cell, thus selective oxidation technology is applied to remove CO from H_2 gas. Supported Au catalyst is a promising catalyst, by which CO can be selectively oxidized at low temperature.[20, 21] And Eq (1.3) is water-gas-shift reaction which is a well-know step for upgrading CO to H_2 in the production of synthesis gas. In this system, ceria supported metal catalysts such as Au/CeO_2, Pt/CeO_2 can remove the side-product CO from Eq (1.2) to purify the hydrogen gas.[22-25]

Table 1.1 History of the catalysis of industrial processes[6]

Catalytic reaction	Catalyst	Discoverer or company/year
Sulfuric acid (lead-chamber process)	NO_x	Désormes, Clement, 1806
Chlorine production by HCl oxidation	$CuSO_4$	Deacon, 1867
Sulfuric acid (contact process)	Pt, V_2O_5	Winkler, 1875; Knietsch, 1888 (BASF)
Nitric acid by NH_3 oxidation	Pt/Rh nets	Ostwald, 1906
Fat hardening	Ni	Normann, 1907
Ammonia synthesis from N_2, H_2	Fe	Mittasch, Haber, Bosch, 1908; Production, 1913 (BASF)
Hydrogenation of coal to hydrocarbons	Fe, Mo, Sn	Bergius, 1913; Pier, 1927
Oxidation of benzene, naphthalene to MSA or PSA	V_2O_5	Weiss, Downs, 1920
Methanol synthesis from CO/H_2	ZnO/Cr_2O_3	Mittasch, 1923
Hydrocarbons from CO/H_2 (motor fuels)	Fe, Co, Ni	Fischer, Tropsch, 1925
Oxidation of ethylene to ethylene oxide	Ag	Lefort, 1930
Alkylation of olefins with isobutane to gasoline	$AlCl_3$	Ipatieff, Pines, 1932
Cracking of hydrocarbons	Al_2O_3/SiO_2	Houdry, 1937
Hydroformylation of ethylene to propanal	Co	Roelen, 1938 (Ruhrchemie)
Cracking in a fluidized bed	aluminosilicates	Lewis, Gilliland, 1939 (Standard Oil)
Ethylene polymerization, low-pressure	Ti compounds	Ziegler, Natta, 1954
Oxidation of ethylene to acetaldehyde	Pd/Cu chlorides	Hafner, Smidt (Wacker)
Ammoxidation of propene to acrylonitrile	Bi/Mo	Idol, 1959 (SOHIO process)
Olefin metathesis	Re, W, Mo	Banks, Bailey, 1964
Hydrogenation, isomerization, hydroformylation	Rh-, Ru complexes	Wilkinson, 1964
Asymmetric hydrogenation	Rh/chiral phosphine	Knowles, 1974; L-Dopa (Monsanto)
Three-way catalyst	Pt, Rh/monolith	General Motors, Ford, 1974
Methanol conversion to hydrocarbons	Zeolites	Mobil Chemical Co., 1975
α-olefines from ethylene	Ni/chelate phosphine	Shell (SHOP process) 1977

Table 1.1 (continued) History of the catalysis of industrial processes[6]

Catalytic reaction	Catalyst	Discoverer or company/year
Sharpless oxidation, epoxidation	Ti/ROOH/tartrate	May & Baker, Upjohn, ARCO, 1981
Selective oxidations with H_2O_2	titanium zeolite (TS-1)	Enichem, 1983
Hydroformylation	Rh/phosphine/ aqueous	Rhône-Poulenc/Ruhrchemie, 1984
Polymerization of olefines	zirconocene/MAO	Sinn, Kaminsky, 1985
Selective catalytic reduction SCR (power plants)	V, W, Ti oxides/ monolith	~1986
Acetic acid	$Ir/I^-/Ru$	„Cativa“-process, BP Chemicals, 1996

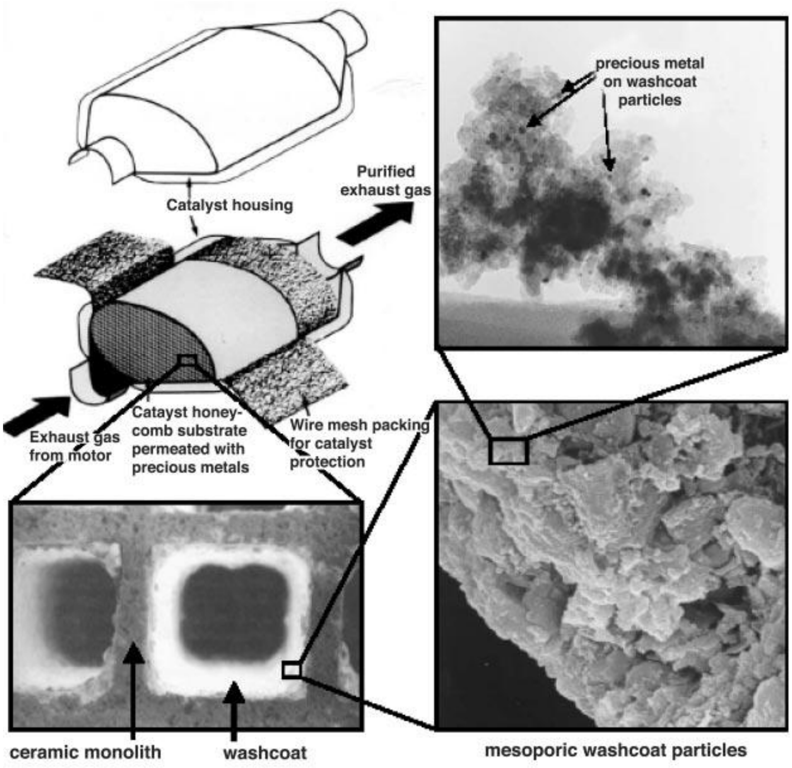

Fig.1.1.1 Illustration of the placement of nanoparticles in automotive catalytic converter [26]

There are also a large amount of new heterogeneous catalysts applications in lots of areas, such as photocatalysts[27], chiral synthesis[28] and so on. Just from the examples above it is undoubtable that heterogeneous catalyst technology is always a key factor in progress of our daily life.

To satisfy the demands from our modern life, not only new heterogeneous catalyst technologies are invented, but also intrinsic properties of heterogeneous catalyst need be well understood. More specially, in the 21st century, emphasis of catalyst development shifts to the ***selectivity and stability*** due to both of the environmental considerations and limitation of resource. It is required to obtain more and more detailed physicochemical insights into catalyst system, such as: the determinant factor that control activity, selectivity and stability of catalysts, element steps of catalytic reaction. It is well-known almost catalytic reaction occurs on the heterogeneous surface. However, most heterogeneous catalysts consist of nanometer-sized particles called active sites dispersed on a high-surface-area amorphous support as shown Figure 1.1.1. The properties of active sites are significantly affected by the size of particle,[29, 30] distribution,[31, 32] local structure[33] and interaction with the support surface[34-36] (see some examples in Figure 1.1.2[37] and 1.1.3[38]). Heterogeneousness of both the particles and support surface leads to the heterogeneous properties of each active site. The average knowledge on the performance of active sites obtained in the traditional catalyst research is sometimes unable to provide correct information about catalysis. That is also the reason why heterogeneous catalyst developments are always based on “trial and error” method. Thus, it is required a local range or molecule level characterization technology to monitor the catalyst surface. In this regard, the surface science studies carried out on the model surfaces (e.g. metal single crystals or thin oxide films, metal nanoclusters) under vacuum conditions or reaction gas atmosphere can meet this demand.[39-42]

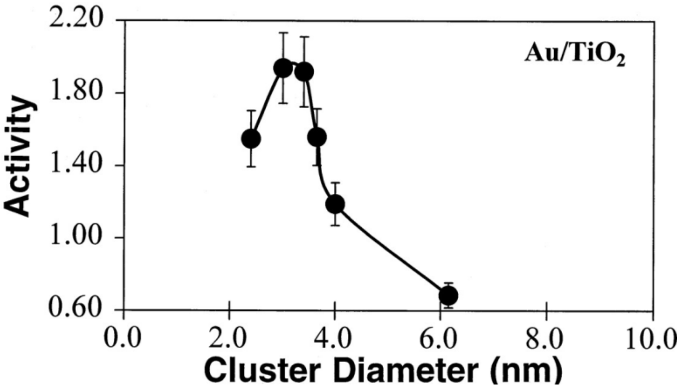

Figure 1.1.2 Illustration of relation between the Au particle size and turnover of frequency of CO oxidation on Au/TiO$_2$ at 350 K. The highest activity appeared at the Au particle size of 2.0 nm ~ 4.0 nm.[37]

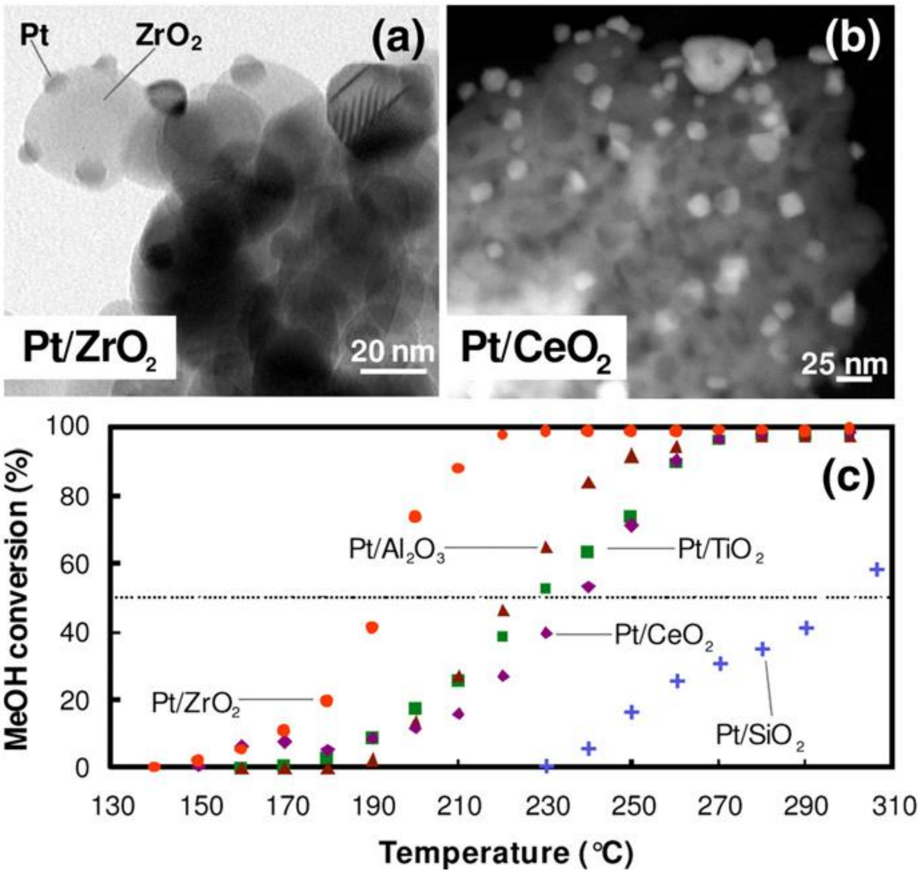

Figure 1.1.3 **(a)** TEM image of Pt NPs supported on nanocrystalline ZrO$_2$. **(b)** High angle annular dark field image obtained by scanning transmission electron microscopy (STEM) of Pt NPs deposited on CeO$_2$. (c) Relative conversion during the direct MeOH decomposition over Pt NPs supported on Pt/ZrO$_2$ (full circles), Pt/Al$_2$O$_3$ (full triangles),Pt/TiO$_2$ (full squares), Pt/CeO$_2$ (full diamonds), and Pt/SiO$_2$ (crosses).[38]

1.2 Surface Science Approach

Since the complexity of heterogeneous catalysts obstructs deep insights into the fundamental issues in heterogeneous catalysis, a new strategy that extracts the essential parts of catalysts and then simplifying to the model surface which can be studied by surface science techniques has been developed (as schematically shown in Figure 1.2.1).[42]

Early in the middle of 20th century, Otto Beeck first used evaporated metal films to study the chemisorptions and catalytic properties of metals.[43] However, the genuine surface science studies began in the 1960s when the techniques for preparation of clean single crystal surface and ultrahigh vacuum (UHV) technologies became available to the research.[44, 45] G. Somorjai and co-workers developed an instrument which permitted isolation of the single crystal from the UHV after the surface preparation and characterized by electron diffraction and electron spectroscopy techniques. The isolated crystal could be exposed to reactant gases at high pressure.[46] By using this technique, Somorjai measured the rates of synthesis of NH_3 from H_2 and N_2 on the Fe(111), Fe(100), Fe(110), Fe(211), Fe(210) and found the Fe(111) showed highest activity (Figure 1.2.2).[46,47] This result first provided direct evidence for the long-held view that (111) surface of α-Fe is the most active surface for NH_3 synthesis.[48] And since that, the concepts of structure -sensitive or -insensitive were introduced into the catalysis research.[49] Another remarkable achievement was the studies on the CO oxidation behavior on Pt.[50-52] This reaction followed the Langmuir-Hinshelwood mechanism, however, it was self-poisoned in the case of high coverage of CO and turnover rate exhibited oscillation patterns. G. Ertl used PEEM (photoelectron emission microscopy) to image these oscillations in time and space of CO oxidation on Pt(110) (Figure 1.2.3). He explained these rate oscillations originated from adsorbate induced reconstruction of the metal surface. That is to say, chemisorptions can lead to not only the restructuring of adsorbates but also reconstruction of single crystal surface.

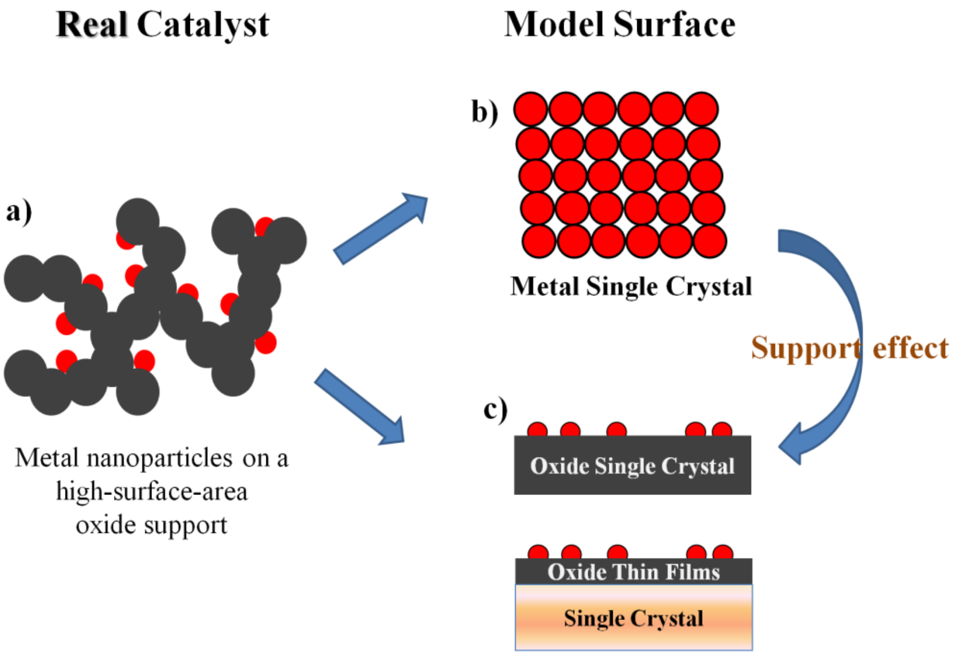

Figur 1.2.1 Illustration of the concept of model surface **a)** real catalyst: metal particles (red balls) dispersed on a high-surface-area oxide support; **b)** A metal single crystal model; c) Metal particles on thin oxide films or oxide single crystal.

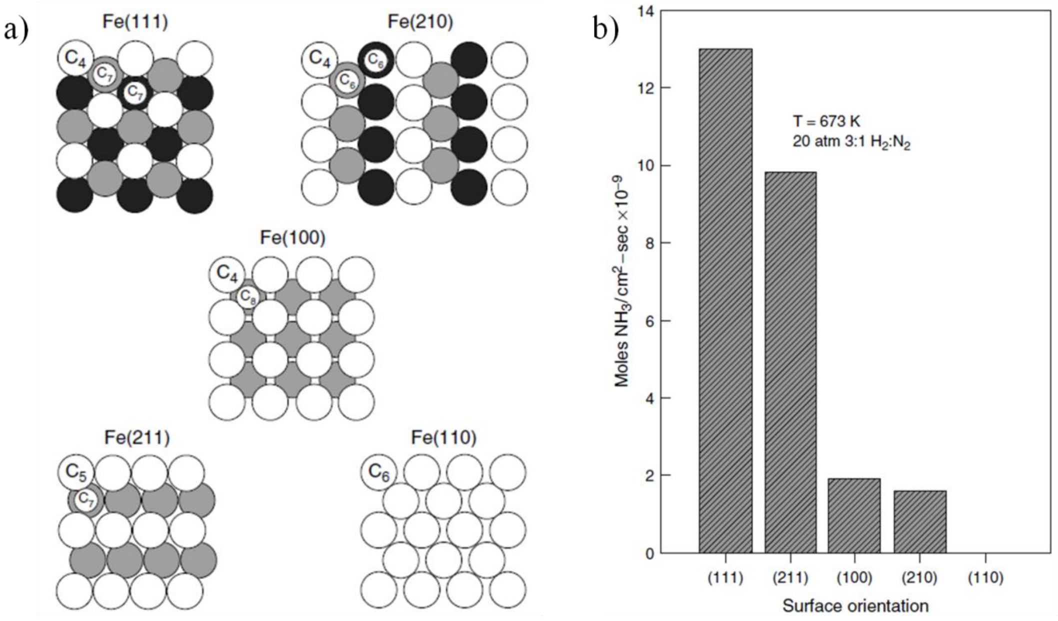

Figur 1.2.2 **a)** Schematic representation of the idealized surface structures of the (111), (210), (100), (211) and (110) orientations of iron single crystals. The coordination of each surface is also indicated by C_X. **b)** Rate of NH_3 synthesis over five Fe large, single crystal surfaces with different orientations.[46]

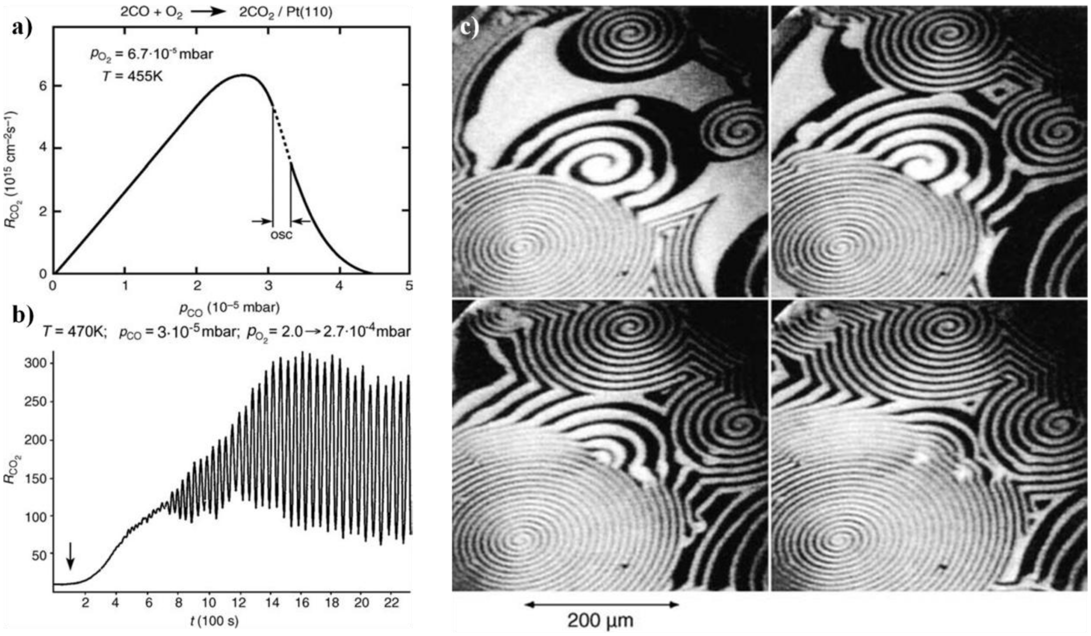

Figure 1.2.3 CO oxidation on Pt(110) surface. **a)** Steady-state rate of CO_2 formation in the catalytic oxidation of CO as a function of P_{CO} at fixed P_{O2} and T. **b)** Onset of kinetic oscillations in the rate of CO oxidation at a Pt(110) surface. **c)** A sequence of PEEM images from a Pt(110) surface during spiral wave formation in CO oxidation taken at intervals of 30 s. T = 448 K, $P_{O2} = 4 \times 10^{-4}$ mbar, $P_{CO} = 4.3 \times 10^{-5}$ mbar [52]

Until the early 1990s, large amounts of surface structures have been studies mainly by Low energy electron diffraction (LEED), Auger electron spectroscopy (AES) and X-ray photoelectron spectroscopy (XPS). A revolutionary development of surface science studies occurred around 1990s when one technique, namely scanning tunneling microscopy (STM) was invented by G. Binning and co-workers.[53] This powerful tool was capable of resolving the atomic-scale structure of planar surface to provide morphology information about surface atoms of single crystal and adsorbates under various conditions: vacuum, atmosphere or liquid phase. In this regard, by using STM, a true atomic and molecular level observation on the morphological change of the surface during the chemical reactions can be achieved. Moreover, scanning tunneling spectroscopy (STS) and inelastic tunneling spectroscopy (IETS) can provide useful information about electronic state of local surface structure and vibration features of

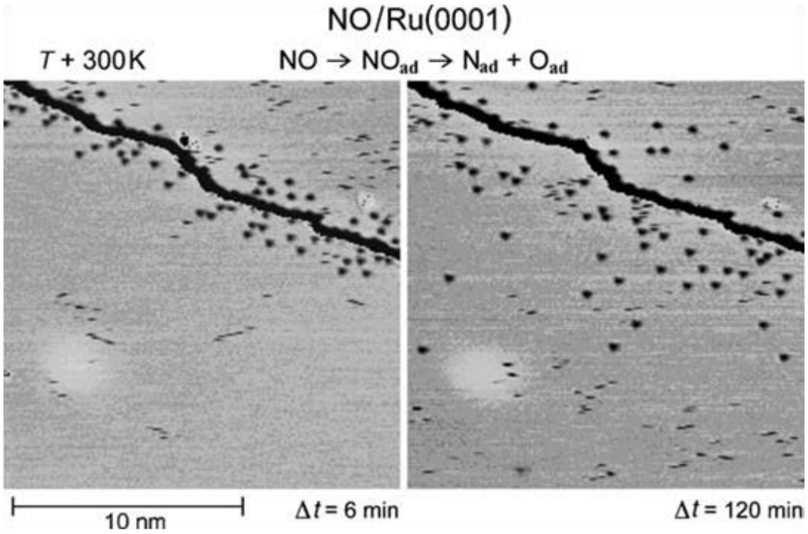

Figure 1.2.4 STM images from NO interacting with a Ru(0001) surface exhibiting a monoatomic step. After association, N atoms slowly leave from the step. [54]

adsorbates. Thus, combination of the STM observation and STS, IETS measurements enable us to address the correlation between the structure/ position and properties of surface atoms (or adsorbates). Additionally, nowadays, the improvement of the image acquisition rate renders STM to be able to provide not only high spatial but also high temporal resolution, by which dynamic surface process can be followed and analyzed in situ. *in situ* STM measurements can be used to determine the active sites for chemisorptions. Zambelli et.al. found that NO molecules easily dissociated at the step edges of Ru(0001) at room temperature, and N atoms slowly diffuse away from step edges while O atoms migrate too fast to be observable by STM.[54] This result gave instinctive evidence that catalytic reaction usually occurred at some special sites of catalyst surface. Mitsui et al. studied the process of hydrogen dissociation on Pd(111) surface and pointed out that three or more empty Pd sites were necessary for the dissociation of H_2 molecules which broke the traditional view that two neighboring empty sites were necessary for the dissociation of a diatomic molecule.[55, 56] *in situ* STM techniques are more widely applied to trace reaction intermediates (e.x. hydrogen oxidation[57]), measure the reaction kinetics (e.x. CO oxidation[58]), etc. to give us fundamental insight into mechanism of heterogeneous catalysis.

Although the early studies on single crystal surfaces made lots of brilliant achievements on the fundamental understanding of the nature of heterogeneous catalysis, some problems remain, in connecting the information from metal single crystal surface under UHV to the real catalyst. These problems have been called as the material gap and pressure gap. The material gap refers to the gap between the nature of metal single crystals and real catalysts. Real catalysts usually comprise of small metal particles of several nm ~ several tens nm and dispersing on a high-surface-area oxide support. Not only the size effect but also support effect can modify the structures and properties of supported metal particles. For example, it was well-known that bulk gold was inactive, however, Haruta et al.[59] found that Au particles with nanometer sizes exhibited even higher activity than Pt. Figure 1.1.2 shows the correlation between the size of Au particles on TiO_2 and turnover frequency of CO oxidation estimated by Goodman et al. Evidently, Au particles ranging from 2 nm ~ 4 nm showed highest activity.[29] n regard to support effect, early in the 1970s, Tauster et al. discovered that the Pt and Ir which were supported on the TiO_2 and reduced at high temperatures showed a suppressed CO and H_2 chemisorption and enhancement of methanation reactivity.[60-62] And they termed this effect as "Strong metal support interaction (SMSI)" which is now widely used to explained the unusual properties of supported metal particles. The pressure gap refers to the difference of reaction condition whereas the surface science studies are performed under UHV (~10^{-10} Torr), the real catalysis reactions take place under atmosphere or higher pressure. Thermodynamically, if the pressure of reactant gas is raised from UHV 10^{-8} Torr to atmosphere, the chemical potential of reactants is increased by an amount of ~ 30 kJ/mol at room temperature. That is to say, difference of pressure may strongly change the chemisorptions and interactions of reactants on the catalyst surface.

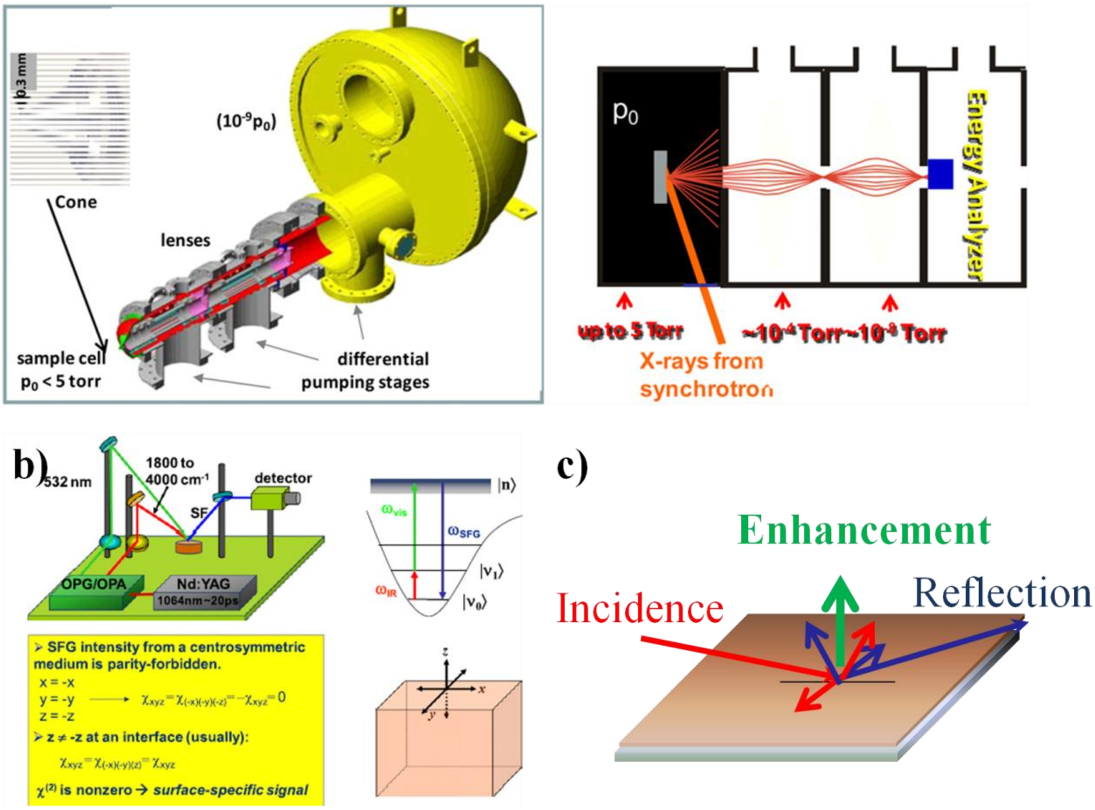

Figure 1.2.5 High-pressure techniques. [63] **a)** High-pressure XPS containing differential pumping stages.**b)** Sum-Frequency-Generation (SFG). **c)** Infrared reflection-absorption spectroscopy (IRAS)

In the past two decades, numerous efforts have been devoted to solve these problems. Somorjai & Salmeron group and Goodman group have mainly contributed to bridge the pressure gap by inventions of high pressure instruments and techniques. These works can be divided into 3 parts as shown Figure 1.2.5:

1) The first one is development of combining the differential pumping stages with conventional UHV surface science techniques based on electrons, ions, or molecular beams all of which do not possess long enough mean free path to reach the detector under high pressure, such as Low-energy ion scattering (LEIS), Transmission electron microscopy (TEM), X-ray photoelectron spectroscopy (XPS).[63-66]

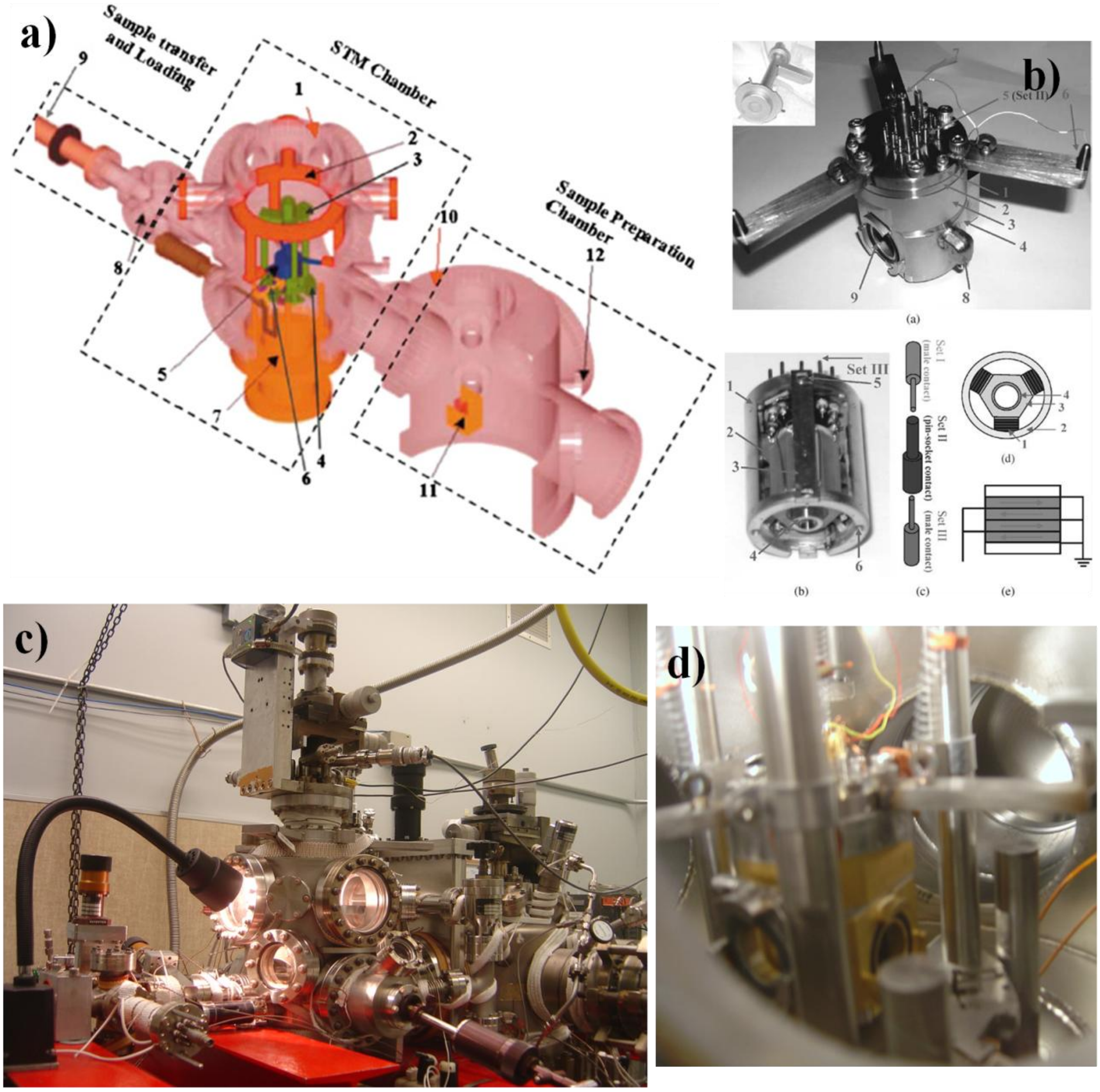

Figure 1.2.6 **a)** Scheme of High-pressure STM.[63] **b)** Photo of UHV-compatible high pressure reaction cell from ref. 74. **c), d)** Photos of High-pressure STM instrument made by Somorjai group. (taken by author during visit of Somorjai and Samleron's lab.

2) The second is the application of optical probes, such as Sum-Frequency-Generation (SFG), Polarization modulation-infrared reflection-absorption spectroscopy (PM-IRRAS).[67-69]

3) The third one is scanning probe microscopy techniques. Somorjai and Tao design a UHV-compatible high pressure reaction cell, where the sample prepared under vacuum can be

examined by STM under high pressure.[70-73] (Figure 1.2.6)

On the other hand, the progress in bridging the material gap brought another revolutionary development of surface science. A new type of material called "supported model surface" comprising of nanometer particles deposited onto a planar oxide or a well-ordered oxide film was introduced into surface science studies (Figure 1.2.1c). Two techniques played important roles in this development.

1) Preparation of oxide thin films: Due to the insulation of most bulk oxide (expect of TiO_2, ZnO, etc.) electron and ion spectroscopic measurements, such as LEED, STM cannot be carried out. The ultra-thin films grown on metallic substrates are an excellent choice to circumvent the conducting problems.[75-80] The thickness of a few angstroms ~ nm can exhibit similar physical properties characteristic to the bulk material, simultaneously enable the application of electron and ion-based techniques on the surface.[81] There are three kinds of preparation of oxide thin films: the traditional one is direct oxidation of the native metal.[81] However, this method always results in amorphous or polycrystalline films (e.g. Al_2O_3 on Al[82],SiO_2 on Si[83]) or appearance of high defect density,[84] because of large lattice mismatch between metal and corresponding oxide in the most cases, except of Cr_2O_3 on Cr(110).[85, 86] Second method proposed by Goodman et al is to evaporate the metal onto a host, mostly a appropriate metal single crystal in an appropriate oxygen atmosphere.[87, 88] CeO_2(111)/Ru(0001) is a good example: stoichiometric film can be prepared and the thickness is controllable.[89] The third one is the oxidation of a suitable alloy sample containing the metal which should be oxidized. A well-known example is Al_2O_3 on NiAl single crystals. The crystal phase of Al_2O_3 can be varied by using different NiAl surface.[90-93] Al_2O_3/NiAl(110) will be discussed in detailed in Chapeter 3. Some common combinations of oxide and metal substrate and preparation methods have been listed in Table 1.2. The important points[80] for preparation of well-ordered

films are:

a) The atomic arrangement in the metal surface should match the symmetry of oxide unit cell along the desired growth direction.

b) Difference between metal and oxide lattice constants should not exceed 5% to enable pseudomorphic growth.

c) Support must have a good thermal and mechanical stability to enable high-temperature treatment of the as-grown film.[94]

The other important technology is to deposit the metal of interest onto the oxide surface: 1) Physical vapor deposition (PVD) of metal atoms in UHV, 2) Deposition of mass-selected metal clusters in UHV, 3) Nanolithography, 4) Deposition of metal precursors solution onto support surface (direct drop method or spin-coating method) in atmosphere, 5) Chemical deposition of metal precursors (CVD).

<u>1) Physical vapor deposition (PVD)</u>: PVD is the most convenient and used frequently in the preparation of supported model catalyst.[79] The process can be divided into several steps: (1) solid metal material (a wire or a block) is converted into vapor by physical methods such as heat treatment; (2) the vapor atoms are transported across a region of low pressure (~ 10^{-4} Torr) from its source to the substrate; (3) the atoms move across the surface depending on its kinetic energy and surface diffusion barrier. The surface defects such as steps, kinks, vacancies or other ad-atoms will trap these energetic atoms to form nuclei for subsequent growth processes. In the most case, due to the diffusion is random, the nucleation and growth process should be heterogeneous except the substrate surface has been well designed. The disadvantage of this method: a) particle size is heterogeneous. b) precursor effect which is

extremely important in catalyst cannot be studied.

Table 1.2 Ordered thin oxide films grown on metal substrates [90]

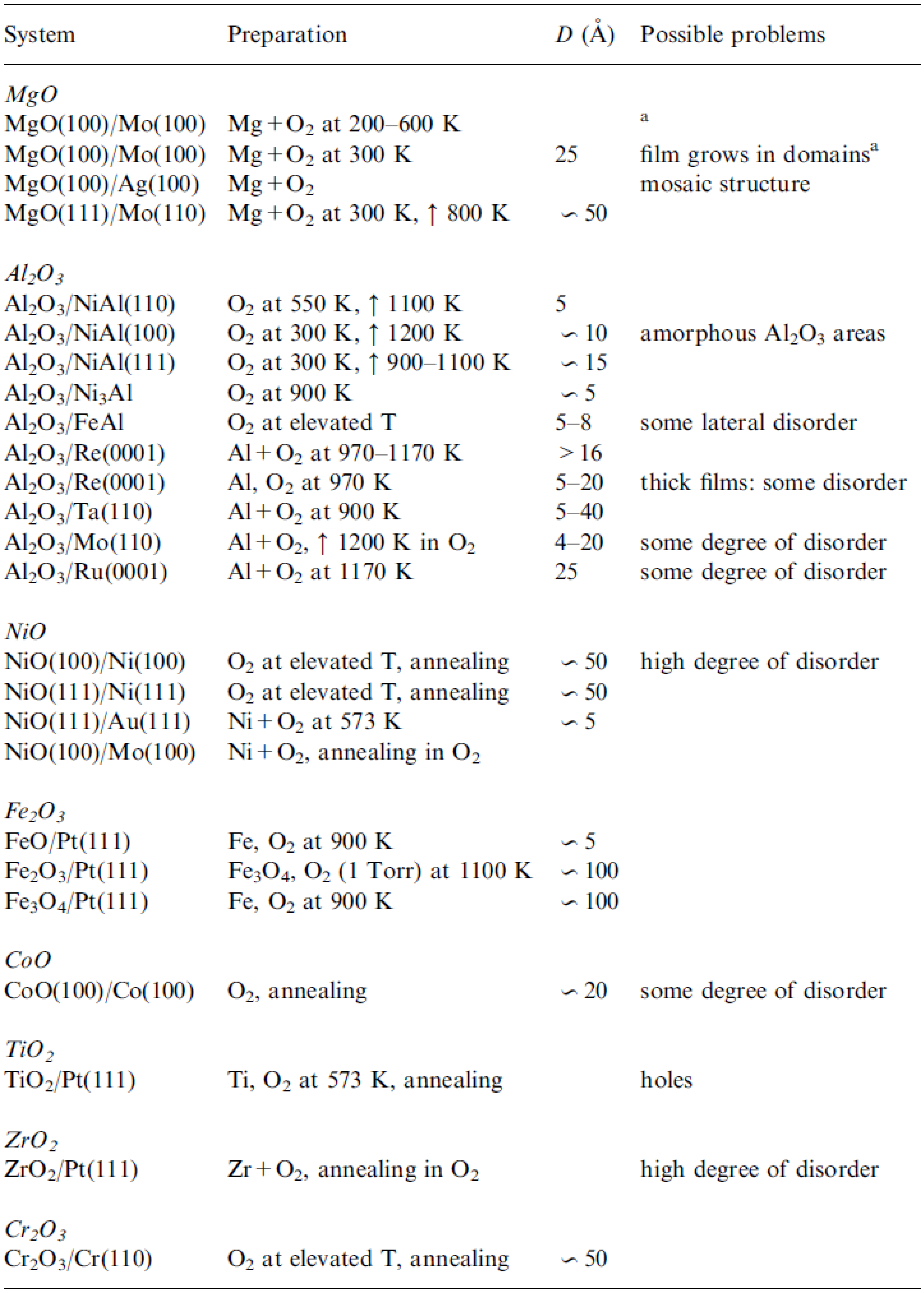

System	Preparation	D (Å)	Possible problems
MgO			
MgO(100)/Mo(100)	Mg + O_2 at 200–600 K		[a]
MgO(100)/Mo(100)	Mg + O_2 at 300 K	25	film grows in domains[a]
MgO(100)/Ag(100)	Mg + O_2		mosaic structure
MgO(111)/Mo(110)	Mg + O_2 at 300 K, ↑ 800 K	~ 50	
Al_2O_3			
Al_2O_3/NiAl(110)	O_2 at 550 K, ↑ 1100 K	5	
Al_2O_3/NiAl(100)	O_2 at 300 K, ↑ 1200 K	~ 10	amorphous Al_2O_3 areas
Al_2O_3/NiAl(111)	O_2 at 300 K, ↑ 900–1100 K	~ 15	
Al_2O_3/Ni_3Al	O_2 at 900 K	~ 5	
Al_2O_3/FeAl	O_2 at elevated T	5–8	some lateral disorder
Al_2O_3/Re(0001)	Al + O_2 at 970–1170 K	> 16	
Al_2O_3/Re(0001)	Al, O_2 at 970 K	5–20	thick films: some disorder
Al_2O_3/Ta(110)	Al + O_2 at 900 K	5–40	
Al_2O_3/Mo(110)	Al + O_2, ↑ 1200 K in O_2	4–20	some degree of disorder
Al_2O_3/Ru(0001)	Al + O_2 at 1170 K	25	some degree of disorder
NiO			
NiO(100)/Ni(100)	O_2 at elevated T, annealing	~ 50	high degree of disorder
NiO(111)/Ni(111)	O_2 at elevated T, annealing	~ 50	
NiO(111)/Au(111)	Ni + O_2 at 573 K	~ 5	
NiO(100)/Mo(100)	Ni + O_2, annealing in O_2		
Fe_2O_3			
FeO/Pt(111)	Fe, O_2 at 900 K	~ 5	
Fe_2O_3/Pt(111)	Fe_3O_4, O_2 (1 Torr) at 1100 K	~ 100	
Fe_3O_4/Pt(111)	Fe, O_2 at 900 K	~ 100	
CoO			
CoO(100)/Co(100)	O_2, annealing	~ 20	some degree of disorder
TiO_2			
TiO_2/Pt(111)	Ti, O_2 at 573 K, annealing		holes
ZrO_2			
ZrO_2/Pt(111)	Zr + O_2, annealing in O_2		high degree of disorder
Cr_2O_3			
Cr_2O_3/Cr(110)	O_2 at elevated T, annealing	~ 50	

2) Mass-selected deposition: Mass-selected deposition instruments were mainly developed by Binns, it is very similar to PVD, but mass selection part has been added. As shown in Figure 1.2.7, mass selection is performed with a Wien velocity filter, where crossed electric E and magnetic B fields dispersions with respect to their different velocities. The Wien filter allows velocities of $v = E/B$ to pass through undeflected. Thus mass selection can be performed with an ion beam of a well defined kinetic energy. Deposition of size selected clusters can produce supported model surface with uniform size in order to study the size effect. But, the shape of cluster seems hard to be controlled.[94]

3) Nanolithography: In regard to controlling both size and shape of metal clusters, nanolithography should be the best choice. The principle of this method is illustrated in Figure. 1.2.8.[95] The fatal disadvantage of this method is bigness of clusters ranging from 10-100 nm.[63]

4) Drop method and Spin-coating method: Just deposit the solution onto the surface and then remove solvent by physical means. The difference of the spin-coating method is that deposition is performed on a rotating sample. Both of them are most similar to the preparation of real catalysts- wet impregnation. However, neither of them can be carried out in UHV condition, where the most model oxide surface can keep their well-ordered structures.

5) Chemical vapor deposition (CVD): The oxide surface is exposed to the volatile precursor and then decomposition of precursor is carried out mainly by heat treatment. Since this method can be performed in UHV condition, it is widely used to study the properties of precursors by surface science approaches. However, chemical vapor deposition method is just applicable to the precursor which can be converted to vapor state before decomposition. It is not suitable for low vapor-pressure precursors (ex. inorganic precursors as chlorides, nitrides etc.), or some precursors with low decomposition temperatures.

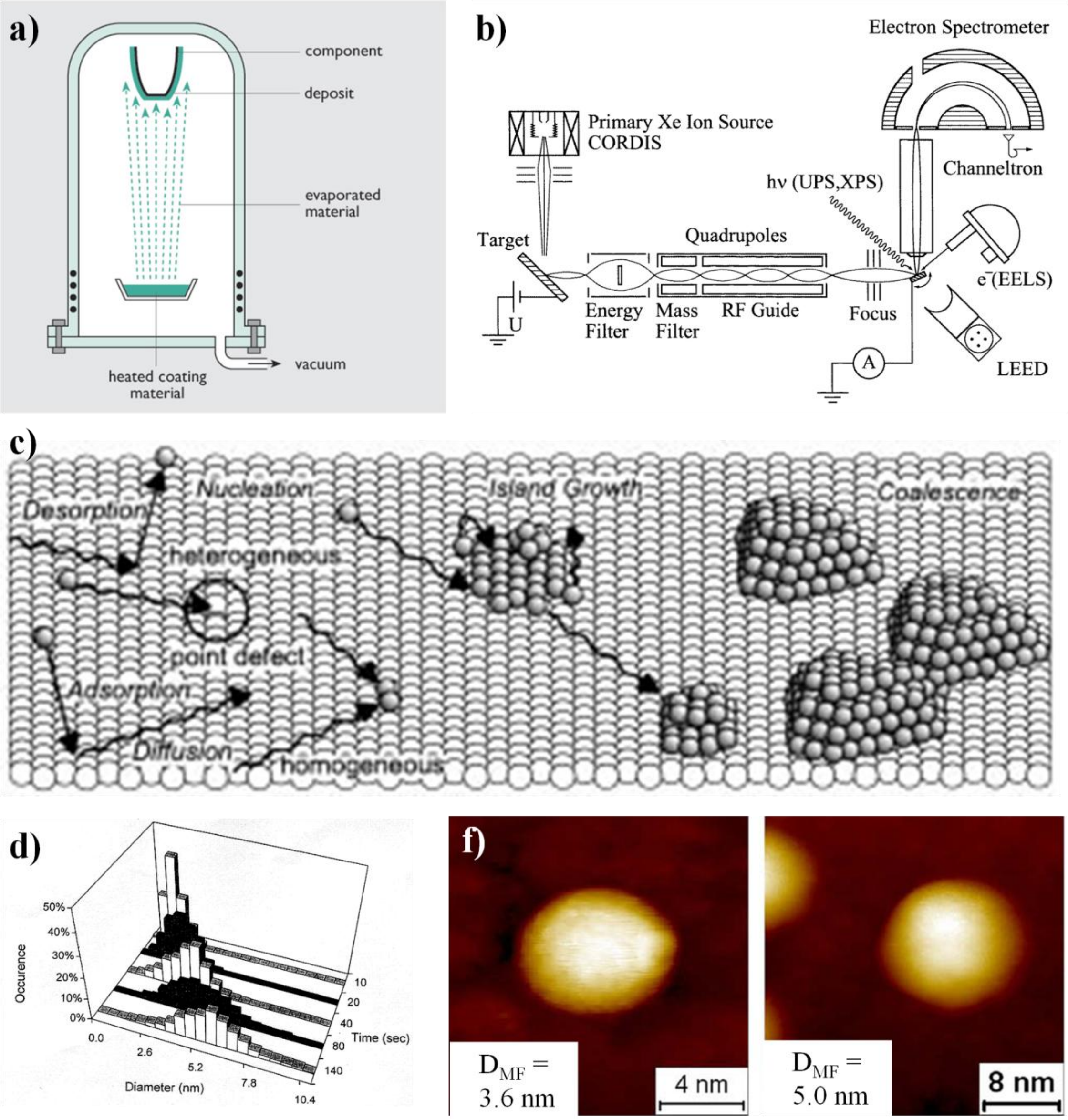

Figure 1.2.7 **a)** Illustration of PVD instrument: Bell-jar. **b)** Illustration of mass-selected PVD instrument. **c)** Visualization of the elementary steps taking place during the deposition of metal atoms **d)** An example of PVD: Deposition of Pd onto MgO: the diameter vs deposition time. **f)** STM images of individual mass-selected Ru nanoparticles. (right) DMF = 3:6 nm, (left) DMF = 5 nm. [94]

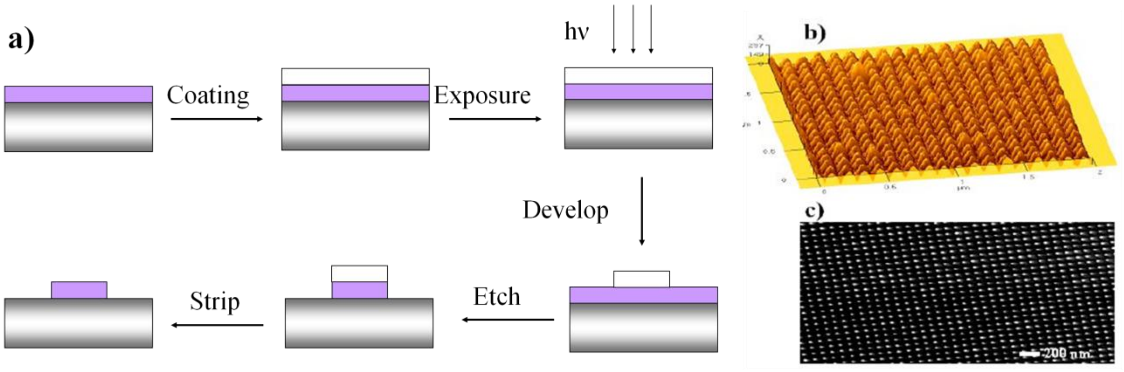

Figure 1.2.8 a) Scheme of the Nanolithography process, and a instance of preparation of Pt nanoparticles **b)** AFM image of Pt nanoparticle array showing Pt particle height of 15 nm c) SEM image of Pt nanoparticle array showing particle diameters of 28 nm and particle spacing of 100 nm [95]

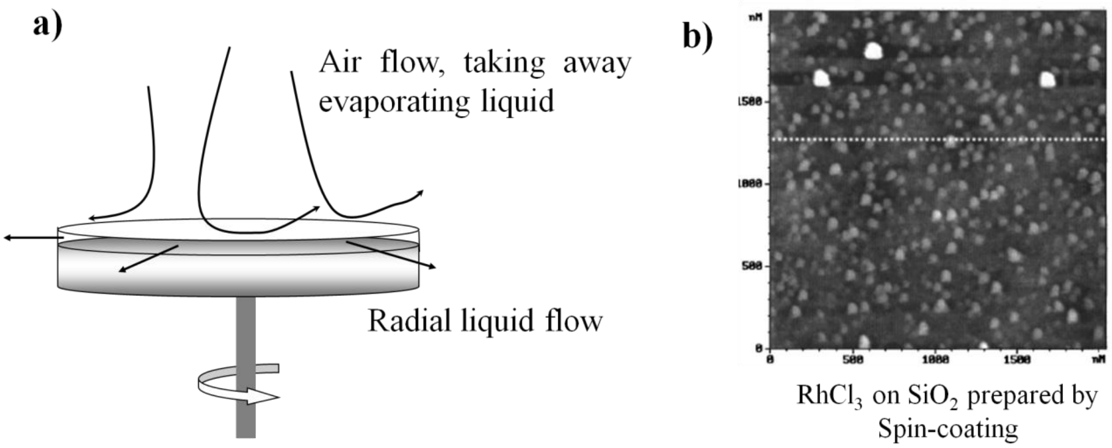

Figure 1.2.9 a) Scheme of the Spin-coating method, and a instance b) AFM image of $RhCl_3$ on SiO_2 prepared by this method.

The advantages and disadvantages of each method have been summarized in Table 1.3. Evidently, none of them can be applicable to all precursors. However in the last row of Table 1.3, the method termed “Pulse valve deposition” which is first introduced into the surface science studies in this work can be applicable to every precursor in principle. By using this method, we have successfully prepared the $RhCl_3$ and $[Rh^{II}(OAc)_2]_2$ on Al_2O_3/NiAl(110) in UHV condition. It will be discussed in detailed in Chapter 2 and Chapter 3. The purpose of presenting this table is not to emphasize which method is the best, but to make clear that the difference of every method. It is wise to choose the appropriate preparation method according to the purpose of research.

Table 1.3 Summary of the advantages and disadvantages of each preparation method. The last row in the green column is the preparation method used in this work and will be discussed in detailed in Chapter 2 and Chapter 3.

Method	Advantage	Disadvantage
Mass selected physical vapor deposition	Convenient Applicable to various metal Size-controlled	Lack of precursor information Unable to control the shape
Nanolithography	Shape and Size can be controlled.	Large size: 10 nm ~ 100 nm
Drop method & Spin-coating method	Similar to wet-impregnation	Not applicable in UHV condition Unable to control the shape and size
Chemical vapor deposition	Precursor effect can be studied.	Not applicable to low vapor-pressure precursors Unable to control the shape and size
Pulse Valve method	Applicable to various precursor	Unable to control the shape and size

1.3 New Research Strategy of Surface Science Studies

The surface science originated from simple concept as how to reduce the complexity of heterogeneous catalysts, can single crystals surface be used as models for industrial catalyst, because almost catalysis reaction occurs on the surface of catalysts. After a series developments and revolutions of methodologies and techniques, surface science becomes more and more important in the progress of heterogeneous catalysts. The fundamental insights into the catalyst surface can not only help to elucidate the catalytic phenomena, but also accelerate the invention of high-performance catalysts. In other words, nowadays, surface science study is not just a tool to shed light on some element surface processes, the new concepts generated in the process of surface science studies sometimes can bring about evolution of catalysis. In this regard, a research strategy proposed here is to first extract the unanswered questions in real catalysts, select an *appropriate model* with few gaps as possible to tackle the problems, scrutinize the factors that may influence these systems, and at last, the most important step is to check and apply the results or new concepts from surface science studies on an *appropriate real catalyst*.

1.4 Outline of this work

As mentioned above, the catalyst research in 21st century is focusing on the “selectivity” and “stability”. Both of them are determined by the properties of active metal species such as size, distribution, local structure, interaction with the support surface in the field of heterogeneous catalyst. Generally, these parameters are significantly dependent upon the preparation methods, the nature of supports and the variety of metal precursors. Thus, fundamental understanding on the relationship between these preparation conditions and formation process of the active metal species provide the probability to optimize the performance of supported catalysts with respect to target reaction.

Numerous efforts[9, 21-26] have been made to obtain the detailed insight into this fundamental relationship. Gates and co-workers have shown the size-dependent catalytic activity of supported metal clusters prepared from organometallic precursors.[34] Qiang and Wagner have reviewed experimental and theoretical results of the interactions between metals and oxide (TiO_2, $SrTiO_3$, Al_2O_3, MgO, SiO_2, etc.) and demonstrated the possible routes to desirably control the formation of metal/oxide interface so as to tune the catalytic performance.[95] Szanyi and co-workers have used magic-angle spinning (MAS) nuclear magnetic resonance (NMR) spectroscopy and high-angle annular dark-field scanning transmission electron microscopy (HA-ADF STEM) to study the formation of catalytically active phase of Pt/γ-Al_2O_3 and find out that Pt atoms can be anchored on unsaturated pentacoordinate Al^{3+} centers atomically at low loading (≦1 wt%).[97] Nilius have reported the properties and adsorption behavior of various oxide thin films studied by scanning tunneling microscopy and conductance spectroscopy.[80]

In spite of so many wonderful studies, understanding on the relationship between the preparation conditions and formation process of the active metal species is still in progress. To answer the questions including “Where and how do the precursors convert to final products?”, “What are the final products, how about the distribution?”, “How about the influence of ligands in precursors?” etc., it is required to get a molecule-level insight into the adsorption behavior of active composition before and after decomposition on the support surface, decomposition mechanism. Certainly, surface science approach, especially scanning tunneling microscopy with atomic-resolution can meet these demands. However, one difficulty remained is how to deposit the precursor onto the well-ordered surface in vacuum, especially for some inorganic precursors with low vapor-pressure.

Recently, a new deposition technique: pulse deposition method (PDM) has been developed by Kawai et al.[98] They injected a small amount of solution containing DNA molecules onto Cu(111) surface in vacuum through a pulse valve and successfully image DNA by STM. The concept of this method is very simple, solvents (such as H_2O, C_2H_5OH, CH_2Cl_2, $C_6H_5CH_3$…) just act as carriers to take the target compounds onto the substrate surface, the solvent molecules will vanish by vacuum expansion or after heat treatment. Because of the injection of solution, this method can be applicable to various compounds.

In this study, we take advantage of this deposition method to study the precursor-dependence on a well-order oxide surface: Al_2O_3/NiAl(110) in order to get some fundamental information about this unsolved problem. We focus on Rh/Al_2O_3 catalyst which is widely used in petroleum industry and as a part of three-way catalyst. And we chose $[Rh^{II}(OAc)_2]_2$ and $RhCl_3$ as precursors since significant precursor dependence of reactivity and selectivity on CO hydrogenation reaction has been reported.

We estimated the properties and adsorption behavior of these two precursors on Al_2O_3/NiAl(110) before and after decomposition by using STM measurements and found remarkable difference in local structure between these two precursor. It seems that the acetate ligands perhaps increased the interaction between the Rh and support surface. Then, we applied this concept to preparation of real catalyst. By using XAFS measurements, we confirmed that same phenomenon also happened on the powder Rh/Al_2O_3 prepared from by $[Rh^{II}(OAc)_2]_2$ wet-impregnation. Furthermore, XAFS results suggested that Rh-O bond preferentially formed along with the decomposition of acetate ligand and it stabilized the Rh core on the Al_2O_3 surface.

References

1 B. Cornil; W.A. Herrmann; R. Schlogl; C.-H. Wang; Ed.; “*Catalysis from A to Z: A Concise Encyclopedia”*; Wiley-VCH: Weinheim, 2000.

2 A. J. B. Robertson *Platinum Metals Rev.* 1975, **19**, 64.

3 Practical Dictionary of Catalysts, Kogyo Chosakai Publishing, Tokyo, 2004.

4 A. Fujishima and K. Honda *Nature*, 1972, **238**, 37

5 R. A. Van Santen; P. W. N. M. v. Leeuwen; J. A. Mooulijn; B. A. Averill; *Catalysis: An Integrated Approach*; Elsevier Science B.V., Amsterdam, 1999 (574 pp)

6 J. Hagen, “Industrial Catalysis: a practical approach”: WILEY-VCH Verlag, GmbH & Co. KGaA, 2006

7 J. H. Sinfelt *Surf. Sci.* 2002, **500**, 923

8 G. Ertl and J. Koch; “*in Proceedings of the 7th International Congress on Catalysis”*, Miami Beach (FL) 1972, ed. J. W. Hightower, North Holland Publ. Co., Amserdam, 1973 pp. 969-979.

9 T. Engel and G. Ertl, *Adv. Catal.* 1979, **28**, 1.

10 N. Takahashi, H. Shinjoh, T. Iijima, T. Suzuki, K. Yamazaki, K. Yokota, H. Suzuki, N. Miyoshi, S.Matsumoto, T. Tanizawa, T. Tanaka, S. Tateishi, K. Kasahara. *Catal. Today*, 1996, **27**, 63.

11 N. Miyoshi, S. Matsumoto. *Stud. Surf. Sci. Catal*., 1999, **121**, 245.

12 S. Matsumoto, *CATTECH*, 2000, **4**, 102.

13 L.J. Muzio, *Int. J. Environ. Pollut.* 2002, **17**, 4.

14 W. S. Epling, *Catal. Rev. Sci. Technol.*, 2004, **46**, 163.

15 D. Ramirez, L. F. Beites, J. C. Ballesteros, *Int. J. Hydrogen Energy* , 2008, **33**, 4433.

16 G. A. Olah, A. Goeppert, G. K. S. Prakash, "*Beyond Oil and Gas: The Methanol Economy"*, 2nd Ed., Wiley- VCH Verlag GmbH & Co. KGaA, Weinheim, 2008.

17 C. Liu, Y. Chen, C. Z. Wu, S. T. Xu, H. M. Cheng. *Carbon*, 2010, **48**, 452.

18 A. S. Damle, *J. Power Sources*, 2008, **180**, 516.

19 S. Sa, H. Silva, L. Brandao, J. M. Sousa, A. Mendes. *Appl. Catal. B*, 2010, **99**, 43.

20 M. Haruta, *Catal. Today* , 1997, **36**, 153.

21 K. Qian, W. Huang, J. Fang, S. Lv, B. He, Z. Jiang, S. Wei *J. Catal.*, 2008, **255**, 269.

22 B. A. Peppley, J. C. Amphlett, L. M. Kearns, R. F. Mann *Appl. Catal. A*, 1999, **179**, 21.

23 B. A. Peppley, J. C. Amphlett, L. M. Kearns, R. F. Mann, *Appl. Catal. A*, 1999, **179**, 31.

24 R. J. Gorte, *AIChE Journal*, 2010, **56**, 1126.

25 D. Mendes, *Asia-Pac. J. Chem. Eng*., 2010, **5**, 111.

26 A. T. Bell, *Science*, 2003, **299**, 1688.

27 M. N. Chong, B. Jin, C. W. K. Chow, C. Saint, *Water Res.*, 2010, **44**, 2997.

28 K. D. M. Harris and S. J. M. Thomas, *ChemCatChem.*, 2009, **1**, 223.

29 M. Valden, X. Lai, D. W. Goodman, *Science* 1998, **281,** 1647.

30 W. E. Kaden, W. A. Kunel, M. D. Kane, F. S. Roberts, S. L. Anderson, *J. Am. Chem. Soc.* 2010, **132**, 13097.

31 K. Yuzaki, T. Yarimizu, K. Aoyagi, S. Ito, K. Kunimori, *Catal. Today* 1998, **45**, 129.

32 H. Sakagami, S. Ogata, N. Takahashi, T. Matsuda, *Phys. Chem. Chem. Phys.* 2001, **3**, 1930-1934.

33 S. Mostafa, F. Behafarid, J. R. Croy, L. K. Ono, L. Li, J. C. Yang, A. I. Frenkel, B. R. Cuenya, *J. Am. Chem. Soc.* 2010; **132**; 15714.

34 B. C. Gates, *Chem. Rev*. 1995, **95**, 511

35 K. K. Bando, K. Asakura, H. Arakawa, K. Isobe, Y. Iwasawa, *J. Phys. Chem.* 1996, **100**, 13636.

36 M. Tada, R. Bal, Y. Iwasawa, . *Catal. Today* 2006, **117**, 141.

37 M. Valden, X. Lai, D. W. Goodman,. Science 1998, **281**, 1647.

38 B. R. Cuenya, *Thin Solid Films*, 2010, **518**, 3127.

39 Kurt W. Kolasinski, "*Surface Science: Foundations of Catalysis and Nanoscience Second Edition*" John Wiley & Sons, Ltd, 2008

40 H. –J. Freund, *Chem. Eur. J.* 2010, **16**, 9384.

41 H. –J. Freund, Top. Catal. 2008, **48**, 137.

42 G. Ertl, G.; Knözinger, H.; Schüth, F.; Weitkamp, "*Handbook of Heterogeneous Catalysis*": Wiley-VCH Verlagsgesellschaft mbH: Weinheim, 2nd edn., 2007. pp 1259 ~

43 O. Beeck, *Rev. Mod. Phys.*, 1945, **17**, 61.

44 L. H. Germer, *Adv. Catal.*, 1962, **13**, 191.

45 H. E. Farnsworth, *Adv. Catal.*, 1964, **15**, 31.

46 G. A. Somorjai, "*The surface science of heterogeneous catalysis*", Proceedings of the Robert A. Welch Foundation Conferences on Chemical Research, Houston, Texas, November 9-11, 1981, Heterogeneous Catalysis, Vol. XXV, pp. 265 ~.

47 D. R. Strongin, J. Carrazza, S. R. Bare, G. A. Somorjai, *J. Catal.*, 1987, **103,** 213.

48 C. Bokhoven, C. van Heerden, R. Westrik, P. Zwietering, *Research on ammonia synthesis since 1940*, in: P. H. Emmett (Ed.), Catalysis, vol. III, Reinhold, New York, 1955, pp. 265~.

49 M. Boudart, G. Djega-Mariadassou, “*Kinetics of Heterogeneous Catalytic Reactions”*, Princeton University Press, Princeton, NJ, 1984, pp. 155~

50 G. Ertl, P. R. Norton, J. Rüstig, *Phys. Rev. Lett.*; 1982, **49**, 177.

51 G. Ertl, *Faraday Discuss.*, 2002, **121**, 1.

52 R. Imbihl and G. Ertl, *Chem. Rev.*, 1995, **95**, 697.

53 G. Binning, H. Rohrer, Ch. Gerber, E. Weibel, *Phys. Rev. Lett*., 1982, **49**, 57.

54 T. Zambelli, J.Trost, J. Wintterlin, G. Ertl, *Phys. Rev. Lett.*, 1996, **76**, 795.

55 T. Mitsui, et.al., *Nature*, **422**, (2003), 705.

56 M. Salmeron, *Top. Catal.*, 2005, **36**, 55.

57 C. Sachs, M. Hildebrand, S, Völkening, J. Wintterin, G. Ertl, *Science*, 2001, **293**, 1635.

58 J. Wintterlin, S, Völkening, T. V. W. Janssens, T. Zambelli, G. Ertl, *Science*, 1997, **278**, 1931.

59 M. Haruta, T. Kobayashi, H. sano, N. Yamada, *Chem. Lett.*, 1987, **16**, 405.

60 S. J. Tauster, *Accounts of Chemical Research*, 1987, **20**, 389.

61 S. J. Tauster, S. C. Fung, R. T. K. Baker, J. A. Horsley, *Science*, 1981, **211**, 1121.

62 S. J. Tauster, S. C. Fung, R. L. Garten, *J. Am. Chem. Soc*. 1987, **100**, 170.

63 D. F. Ogletree, H. Bluhm, G. Lebedev, C. S. Fadley, Z. Hussain, M. Salmeron, *Rev. Sci. Insrumt.*, 2002, **73**, 3872.

64 W. P. A. Jansen, A. W. Denier v. d. Gon, G. M. Wiijers, Y. G. M. Rikers, H. H. Brongersma, P. W. v. d. Hoogen, J. A. M. de Laat, T. M. Mass, E. C. A. Dekkers, P. Brinkgreve, *Rev. Sci. Instrum.*, 2002, **73**, 354.

65 T. W. Hansen, J. B. Wagner, P. L. Hansen, S Dahl, H. Topsøe, C. J. H. Jacobsen., *Science*, 2001, **294**, 1508.

66 M. Salmeron and R. Schlögl, *Surf. Sci. Rep.*, 2008, **63**, 169.

67 X. C. Su, P. S. Cremer, Y. R. Shen, G. A. Somorjai, *Phy. Rev. Lett.*, 1996, **77**, 3858.

68 T. Dellwig, G. Rupprechter, H. Unterhalt, H. –J Freund, *Phy. Rev. Lett.,* 2000, **85**, 776.

69 E. Ozensoy, C. Hess, D. W. Goodman, *J. Am. Chem. Soc.*, 2002, **124**, 8524.

70 B. J. Mcintyre, M. Salmeron, G. A. Somorjai, *J. Vac. Sci. Tech. A*, 1993, **11**, 1964.

71 B. J. Mcintyre, M. Salmeron, G. A. Somorjai, *Rev. Sci. Instrum*., 1993, **64**, 687.

72 G. A. Somorjai, *Angew. Chem. Int. Ed.*, 2008, **47**, 9212.

73 G. A. Somorjai, *PNAS, September 29, 2010*

74 Michael Bowker and Philip R. Davies Ed. " *Scanning Tunneling Microscopy in Surface Science, Nanoscience and Catalysis*" WILEY-VCH Verlag GmbH, 2010.

75 C. R. Henry, *Surf. Sci. Rep.,* 1998, **31**, 235.

76 S. A. Chambers, *Surf. Sci. Rep.,* 2000, **39**, 105.

77 C. T. Campbell, *Surf. Sci. Rep.,* 1997, **27**, 1.

78 D. W. Goodman, *J. Phys. Chem.,* 1996, **100**, 13090.

79 M. Baumer and H.-J. Freund, *Prog. Surf. Sci.*, 1999, **61**, 127.

80 N. Nillius, *Surf. Sci. Rep.,* 2009, **64**, 595.

81 H.-J Freund, *Phys. Status Solidi (b)* 1995, **192**, 407.

82 J. G. Chen, J. E. Crowell, J. T. Yates Jr. *Surf. Sci.,* 1987, **185**, 373.

83 F. Rochet, S. Rigo, M. Froment, C. d'Anterroches, C. Maillot, H. Roulet, G. Dufour, *Adv. Phys.* 1986, **35**, 237.

84 M. Bäumer, D. Cappus, H. Kuhlenbeck, H. –J. Freund, G. Wihelmi, A. Brodde, H. Neddermeye, *Surf. Sci.,* 1991, **253**, 116.

85 H. Kuhlenbeck, C. Xu, B. Dillmann, M. Habel, B. Adam, D. Ehrlich, S. Wohlrab, H. –J. Freund, U. A. Ditzinger, H. Neddermeyer, M. Neuber, M. Neumann, *Ber. Bunsenges. Phys. Chem.*, 1992, **96**, 15.

86 F. Rohr, M. Bäumer, H. –J. Freund, J. A. Mejias, V. Staemmler, S. Müller, L. Hammer, K. Heinz, *Surf. Sci.*, 1997, **389**, 391.

87 D. W. Goodman, *Surf. Rev. Lett.*, 1995, **2**, 9.

88 D. W. Goodman, *J. Vac. Sci. Technol. A*, 1996, **14**, 1526.

89 D. R. Mullins, P. V. Radulovic, S. H. Overbury, *Surf. Sci.*, 1999, **429**, 186.

90 R. M. Jaeger, H. Kuhlenbeck, H. –J. Freund, M. Wuttig, W. Hoffmann, R. Franchy, H. Ibach, *Surf. Sci.*, 1991, **259**, 235.

91 H. Niehus, *Nucl. Instrum. Methods Phys. Res., Sect. B*, 1988, **33**, 876.

92 R.-H. Blum, D. Ahlbehrendt, H. Niehus, *Surf. Sci.* 1998, **396**, 176.

93 C. Becker, J. Kandler, H. Raaf, R. Linke, T. Pelster, M.. Drager, M. Tanemura, K. Wandelt, *J. Vac. Sci. Technol. A*, 1998, **16**, 1000.

94 R. M. Nielsen, S. Murphy, C. Strebel, M. Johansson, J. H. Nielsen, I. Chorkendorff, *Surface Science*, 2009, **603**, 3420.

95 S. Benedetti, P. Torelli, S. Valeri, H. M. Benia, N. Nilius, G. Renaud, *Phys. Rev. B*, 2008, **78**, 195411.

96 Q. Fu and T. Wagner, *Surf. Sci. Rep.* 2007, **62**, 431.

97 J. H. Kwak, J. Hu, D. Mei, C.-W. Yi, D. H. K, C. H. F. Peden, L. F. Allard, J. Szanyi, *Science*, 2009, **325**, 1670.

98 T. Kanno, H. Tanaka, T. Nakamura, H. Tabata, T. Kawai, *Jpn. J. Appl. Phys.* 1999, 38, L606

Chapter 2
Experimental setup and Techniques

2.1 Ultra High Vacuum (UHV) Instrument[1, 2]

All of the scanning tunneling microscopy (STM) measurements were performed in an ultra high vacuum (UHV) instrument (Oxford Instru.), which consisted of a main chamber (base pressure < 2×10^{-8} Pa) and a fast entry load-lock chamber (base pressure < 2×10^{-6} Pa) as shown in Figure 2.1.1. The main chamber is evacuated by an ion pump (IP) and a titanium sublimation pump (TSP) mounted at the bottom as vibration-free pumps while operating the STM. The fast entry chamber is evacuated by a combination of a turbo molecular pump (TMP) and a rotary pump (RP). The gate valve A isolates the main chamber from the fast entry chamber.

The main chamber is equipped with a low-energy electron diffraction (LEED) optics used for LEED and Auger electron spectroscopy (AES) measurements, an ion sputtering gun, a quadrupole mass spectrometer, and variable-temperature (VT) STM head. The VT-STM head is designed to operate over a range of temperature from room temperature to 1000 K. It features very high levels of thermal and mechanical stability and incorporates an eddy-current damped spring suspension mechanism.[3] The heater and controlling thermocouple contained within the sample hold will be described in detail below. Thermal drift is reduced by its symmetrical design and by referencing both the sample surface and tip holder to the same “reference” plane. As shown in Figure 2.1.2, STM head is mounted on a copper stage. Generally, copper stage is fixed onto bottom magnet parts by suspension clamps. During the STM measurements, the

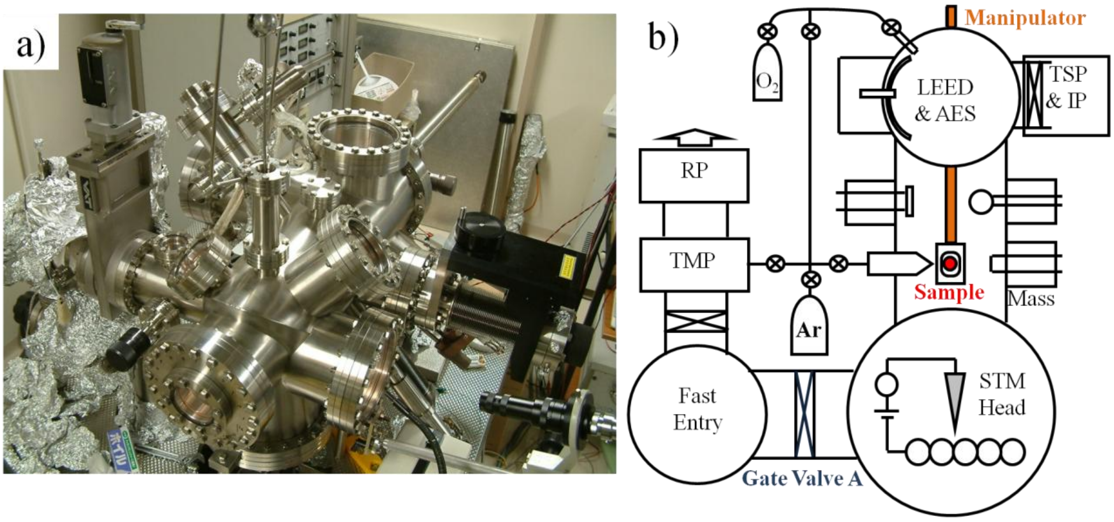

Figure 2.1.1 a) Photo of the Oxford UHV-VT-STM instrument. **b)** Schematic of instrument.

suspension clamps are released by using the rotary drive to separate the stage from the bottom parts in order to isolate head from environmental noise. Also the entire instrument is mounted onto four air damped springs for further reduction of environmental noise.

A sample is mounted in a molybdenum holder and can be heated up to 1500 K by radiation from a home-made tungsten filament placed at the back side of the sample and the temperature is measured with a K-type thermocouple mounted on the side face of sample. Figure 2.1.3 shows the holder in detail. Two of four corner screws are shorter and are used to hold the heater assembly. This part comprises of a base plate, a home-made tungsten filament (length: 3 mm; diameter: 0.1 mm with 13 rolls) spot welded on two heater side plates, which are isolated from the base plate and a sample clamp by four ceramic insulators. The sample clamp is used to adjust the separation between the filament and the sample or the sample shield. In order to get a good thermal radiation efficiency, the separation should be less than 1 mm, but no direct conduction between the filament and sample.

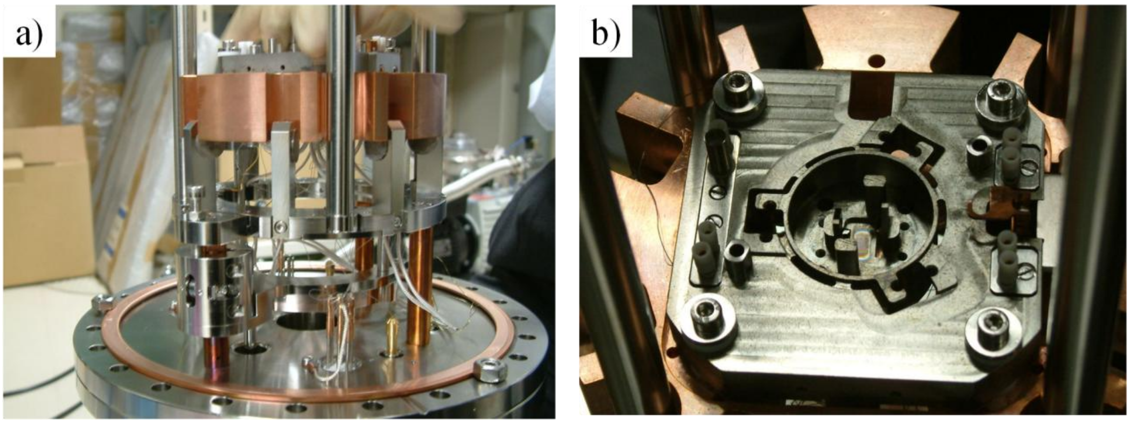

Figure 2.1.2 Photos of the STM head stage: **a)** side view **b)** top view

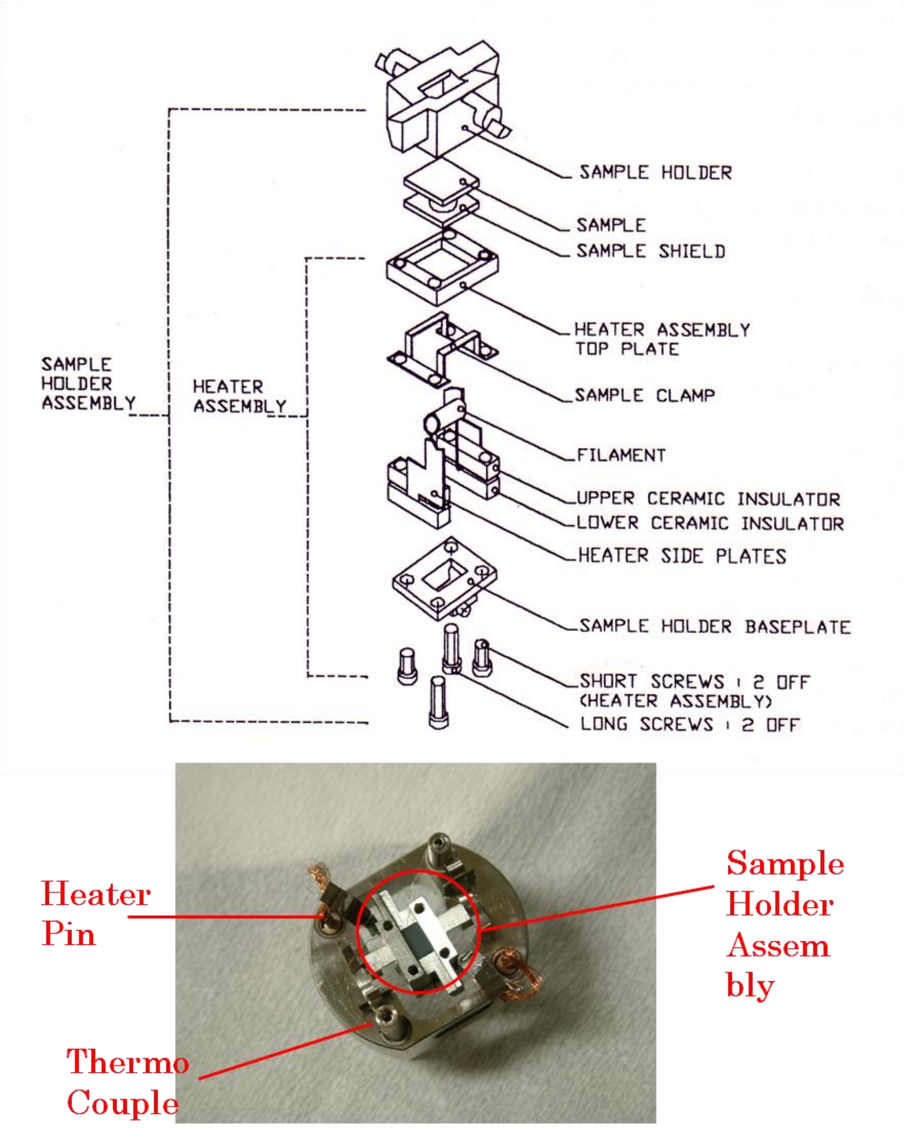

Figure 2.1.3 a) Schematic and **b)** photo of the sample holder

2.2 Scanning Tunneling Microscopy (STM)

Scanning Tunneling Microscopy (STM) was invented in 1982 by Binnig and Rohrer at IBM Zurich [4-6]. As mentioned in Chapter 1, the invention of this technique brought a great evolution to surface science.[7] Nowadays, STM has developed into one of the most important tools to expand our knowledge about the nano-size world, meanwhile the range of phenomena studied by this technology is remarkably broad.[8] These include surface topography, electronic and vibrational properties (by STS and IETS), contact charging, molecular manipulation and so on. Because of this revolutionary invention, they were awarded the Nobel Prize in physics.[9] In this section, the principle of STM will be introduced briefly. The basic operation of the STM is illustrated in Figure 2.2.1

2.2.1 Tunneling Current

Here, we consider a situation where an STM tip and a metal surface are brought close to each other but are not directly connected. As shown in Figure 2.2.2 (a), the Fermi energies of tip and the sample are E_t and E_s, respectively. The wavefunction and energy of electron in this range can be described by a one-dimensional Schrödinger equation

$$\psi = exp(\pm \kappa z), \quad \kappa^2 = 2m_e(V_B - E)/\hbar^2 \qquad (2.2.1)$$

where, m_e, $\hbar$, E, V_B are the electron mass, Planck constant, electron energy and potential energy, then $V_B - E$ is just the work function. Generally, V_B is dependent on the distance between the tip and surface. But, we regard V_B as vacuum level. Then the transmission probability, or the tunneling current I decays exponentially with barrier width d as

$$I \propto exp(-2\kappa d) \qquad (2.2.2)$$

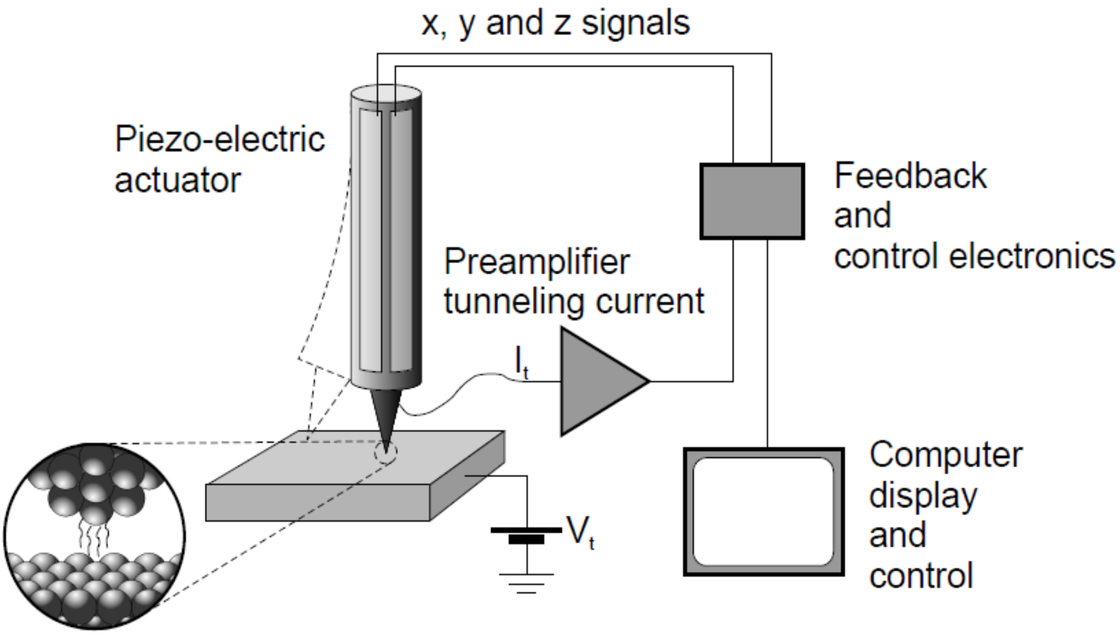

Figure 2.2.1 Illustration of the Scanning Tunneling Microscope. When a bias voltage V_s is applied to the sample, a tunneling current I_t will flow strongly depending on the distance between the tip and the sample. In order to keep the tunneling current constant, a feedback circuit continually adjusts the height of the tip as it is scanned over the surface. In this way a topographic map of the surface is obtained.[7]

If we apply a positive bias voltage to the sample as shown in Figure 2.2.2(c), a tunneling current will flows from the tip to the sample. Since the work function of metal surface is about 2 ~6 eV, κ is about 0.1 nm^{-1}. Thus, the tunneling current I will be proportional to exp($-2\kappa d$). That is to say, if the distance decreases just 0.1 nm, the tunneling current will decrease about one magnitude. This is the reason why tunneling current is good probe to detect the surface morphology.

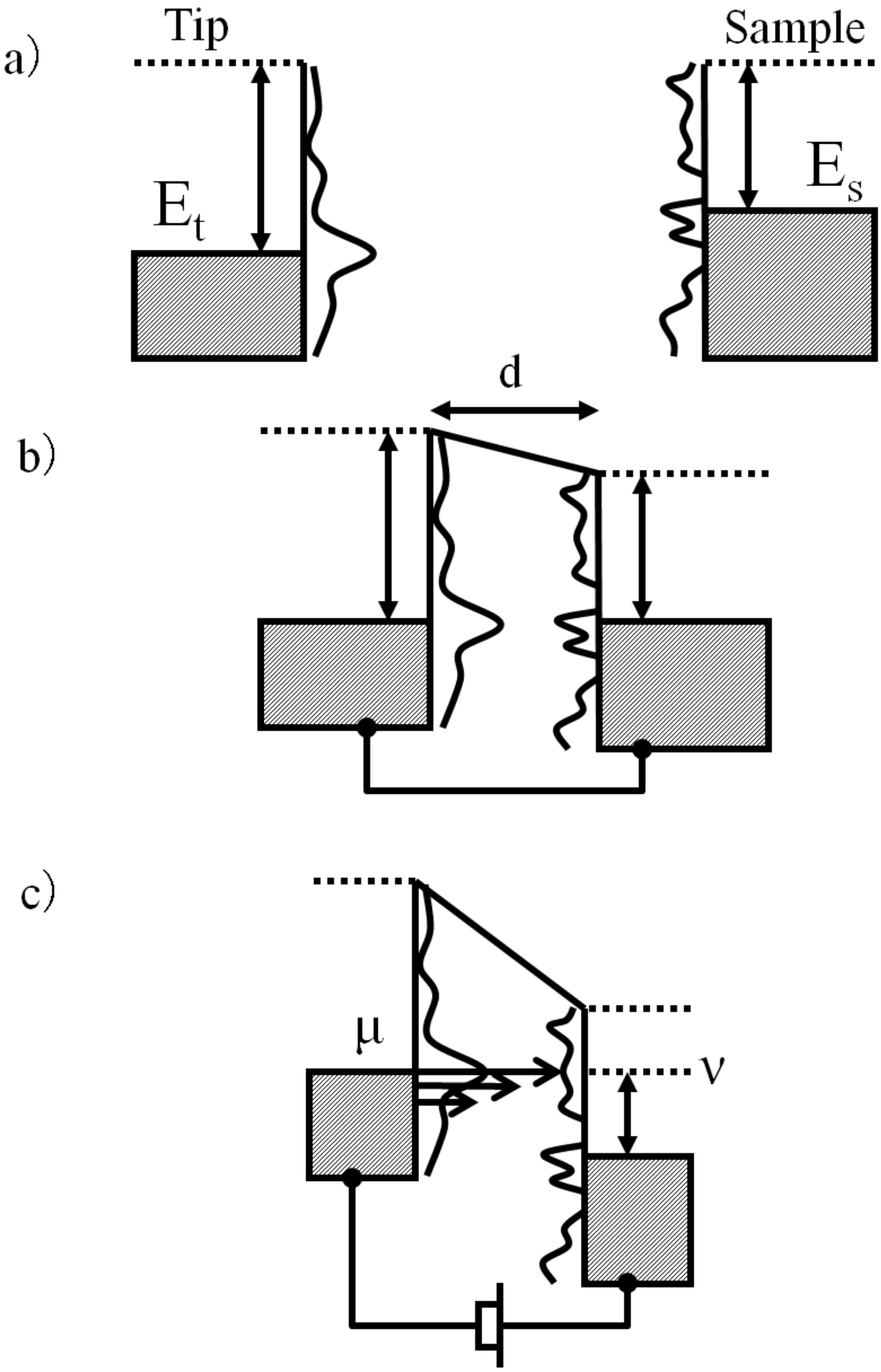

Figure 2.2.2 Illustrations of the Fermi and the vacuum level positions for two metals separated by a distance *d*. **a)** Isolated metals. **b)** After electrical contact, in the absence of an applied bias. **c)** Applying bias voltage shifts the relative position of the Fermi levels and makes electrons tunnel into unoccupied states of the sample in an energy window eV.

2.2.2 Scanning Tunneling Microscopy [6]

A special case of tunneling has been discussed in previous section, then a real situation in which STM tip is scanning a two-dimensional surface will be discussed in this section. The tunneling probability from state μ to state v between the tip and sample surface (tip → sample surface) can be described by Fermi`s Golden Rule:

$$\omega = \frac{2\pi}{h}\left|M_{\mu v}\right|^2 \delta(E_\mu - E_v) \tag{2.2.3}$$

where, $M_{\mu v}$ is tunneling matrix element between state μ and state v of the respective electrodes. According to Bardeen perturbation theory, $M_{\mu v}$ is

$$M_{\mu v} = \frac{h^2}{2m}\int dS \cdot (\psi_u^* \nabla \psi_v - \psi_v^* \nabla \psi_u) \tag{2.2.4}$$

On the other hand, the tunneling current can be described by Fermi distribution function $f(E)$:

$$I = e\sum_{\mu v} \omega \left\{ f(E_\mu)\left[1 - f(E_v)\right] - \left[1 - f(E_\mu)\right] f(E_v) \right\} \tag{2.2.5}$$

$$f(E_\mu) = \left\{ 1 + \exp\left[{(E_\mu - E_F)}/{kT} \right] \right\}^{-1} \tag{2.2.6}$$

where k is Boltzmann's constant, T is the absolute temperature. The Fermi distribution $f(E)$ gives the distribution of electron around the Fermi energy in the tip, while the 1-$f(E)$ corresponds to the hole distribution on the sample surface. Similar to section 2.2.1, if we apply a positive bias between the tip and sample, the tunneling current can be described as:

$$I = \frac{2\pi e}{h}\sum_{\mu v} \left\{ f(E_\mu - eV) - f(E_v) \right\} \left|M_{\mu v}\right|^2 \delta(E_\mu - eV - E_v) \tag{2.2.7}$$

Tersoff and Hamann [10] simplified Eq. (2.2.7) as below by some assumption such as only considering the s-function, low temperature and very small bias.

$$I = \frac{2\pi}{h} e^2 V \sum_{\mu\nu} \left| M_{\mu\nu} \right|^2 \delta(E_\nu - E_F)\delta(E_\mu - E_F) \tag{2.2.8}$$

At last we suppose that the wavefunction is localized around the tip, thus the transition matrix element $M_{\mu\nu}$ is just dependent on the magnitude of surface state density $|\psi_\nu^2|$. That is to say:

$$I \propto V\rho_s(r_0, E_F) = V\,|\psi_\nu^2|\,\delta(E_\nu - E_F) \tag{2.2.9}$$

tunneling current is strongly dependent on the distance between the tip and sample surface.

Actually, STM image is arising from the convolution of tip and sample electronic structure. Unfortunately the bumps in an image are not labeled with atomic symbols. For instance, an oxygen atom does not always look the same. It may appear as a protrusion at one voltage and as a depression at another. On one substrate it may be imaged at one voltage whereas a different voltage is required on a different substrate. The lack of chemical specificity in STM images represents one difficulty with the technique.

2.3 X-ray spectroscopies

X-rays refer to electromagnetic waves with wavelength ranging from 0.01 nm ~ 10 nm. *X-ray radiation* can be generated by various processes, mainly resulting from the interaction of high energy particles or photons with matter: 1) *Synchrotron radiation* results from the acceleration of charged particles in circular orbits by strong electric and magnetic fields. 2) *Bremsstrahlung* refers to radiation emitted as a result of the retardation of high-energy particles by matter. *Bremsstrahlung* and *synchrotron radiation* are used in X-ray spectroscopy as sources of continuous X-ray radiation. 3) *Characteristic X-rays* are emitted during electronic transitions to the inner shell states in atoms of modest atomic number. These X-rays have characteristic energies related to the atomic number, and each element therefore has a characteristic X-ray spectrum.

Since, X-rays possess the same energy range to binding energy of core electrons, incident X-ray may excite the core electrons to high energy level simultaneously leaving holes in the inner shell. As the properties of excited electrons or holes are dependent on the element, analyses on the excited electrons or holes can provide some information about the target element.

Several X-ray spectroscopic methods are listed in Figure 2.3.1 [11, 12]

1) X-ray photoelectron spectroscopy (XPS): XPS based on the photoelectric effect, in which an atom absorbs a photon with energy of hν and then a core electron (binding energy E_b) ejected with kinetic energy E_k:

$$E_k = h\nu - E_b - \varphi \quad \text{(}\varphi\text{ is the work function)} \qquad (2.3.1)$$

XPS is used to measure the elemental composition, empirical formula and electronic state of the elements that exist within a material. XPS spectra are obtained by irradiating a material with

X-rays while simultaneously measuring the kinetic energy and number of electrons that escape from the top 1 to 10 nm of the material being analyzed. XPS is a surface chemical analysis technique that can be used to analyze the surface chemistry of a material not only on planar surfaces but also powder samples. An example of Rh/Al_2O_3 prepared by impregnating with a solution of $RhC1_3$ in water is shown in Figure 2.3.2 [13]

2) X-ray absorption spectroscopy (XAS): In XAS, a core electron is excited into unoccupied atomic/molecular orbitals above the Fermi level. XAS is divided into two regimes: X-ray absorption near-edge structure (XANES) or near edge X-ray absorption fine structure (NEXAFS) for bound states and low energy resonances in the continuum, and extended X-ray absorption fine structure (EXAFS) when the outgoing electron is well above the ionization continuum. XANES provides information about chemical state of analyzed atoms, while EXAFS offers the structure information. A detailed introduction about X-ray absorption fine structure (XAFS) will be given in the next section.

3) X-ray emission spectroscopy (XES): It provides a means of probing the partial occupied density of electronic states of a material. XES is element-specific and site-specific, making it a powerful tool for determining detailed electronic properties of materials.

4) Resonant inelastic X-ray scattering (RIXS): Inelastic X-ray Scattering is a fast developing experimental technique in which one scatters high energy X-ray photons inelastically off matter. It is a photon-in/photon-out spectroscopy where one measures both the energy and momentum change of the scattered photon. The energy and momentum lost by the photon are transferred to intrinsic excitations of the material under study and thus RIXS

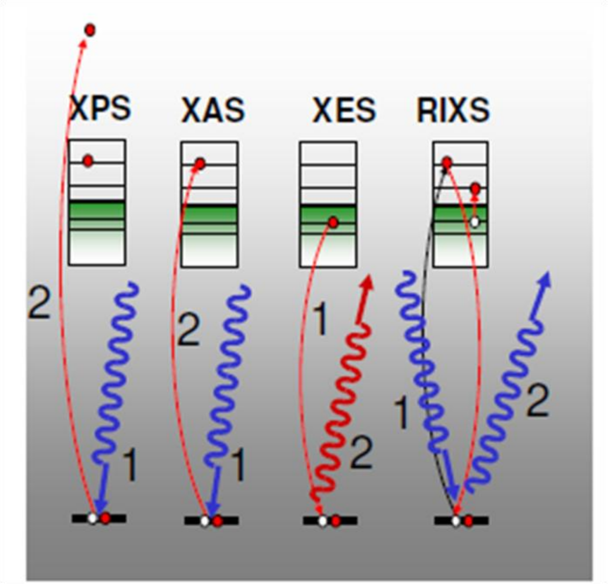

Figure 2.3.1 Schematic illustration of X-ray spectroscopic process: X-ray photoelectron spectroscopy (XPS), X-ray absorption spectroscopy (XAS), X-ray emission spectroscopy (XES), resonant inelastic X-ray scattering (RIXS)

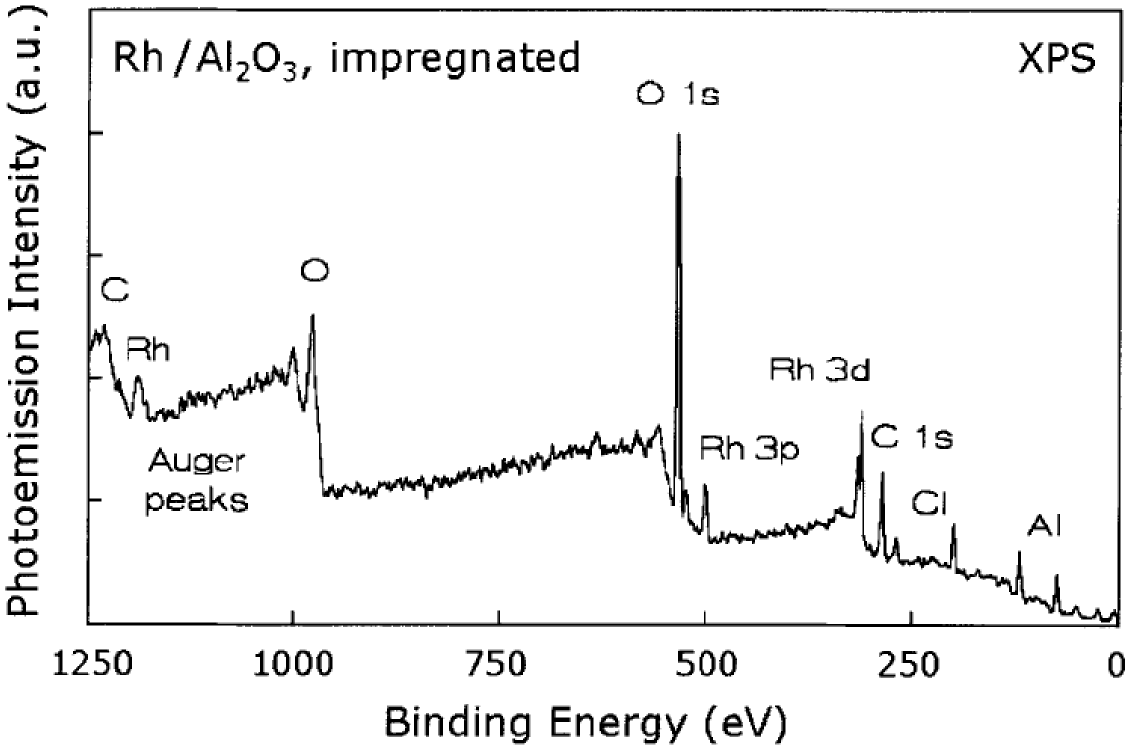

Figure 2.3.2 XPS spectrum of a Rh/Al_2O_3 model catalyst prepared by impregnating a thin film of $A1_2O_3$ on aluminum with a solution of $RhC1_3$ in water (courtesy of L.C.A. van den Oetelaar, Eindhoven [13]).

provides information about those excitations. The RIXS process can also be described as a resonant X-ray Raman or resonant X-ray emission (RXE) process.

2.3.1 X-ray Absorption Fine Structure (XAFS)

As shown in Figure 2.3.3, if someone throws a stone into a pool, a series water waves in the shape of concentric circles will be produced (a). However, if there are some floaters such as woods on the pool, the water waves will show a complex interference pattern (b). This complex pattern is dependent on the position and number of floaters and properties of stones. Reversely, by analyzing the complex pattern, one can get the information about the properties of stones and around condition. XAFS is quite similar to this phenomenon.

X-ray absorption refers to a core electron excitation into unoccupied atomic/molecular orbitals above the Fermi level. Although this phenomenon has been known since about 70 years ago [14-19], until last two decades, no valuable application had been found. The major reasons were the lack of efficient X-ray sources and a suitable theoretical description. With the invention of synchrotron and improvement of the XAFS theory [20]-28], the situation has completely changed.

In the absorption experiment, the absorption of monochromatic synchrotron radiation is measured as a function of energy. This process is described by the absorption law:

$$\mu(E) = ln(I_i / I_f) \tag{2.3.2}$$

where I_i is the X-ray radiation intensity of incident beam and I_f is a radiation intensity of transmitted beam, $\mu(E)$ is an absorption coefficient. The energy dependence of the absorption $\mu(E)$ is illustrated in Figure 2.3.4. In the energy dependence of $\mu(E)$ three main features can be observed. First, the $\mu(E)$ decreases with the energy increases. This is mainly due to static repulsion from the photoelectric defect. Second, in the $\mu(E)$, the

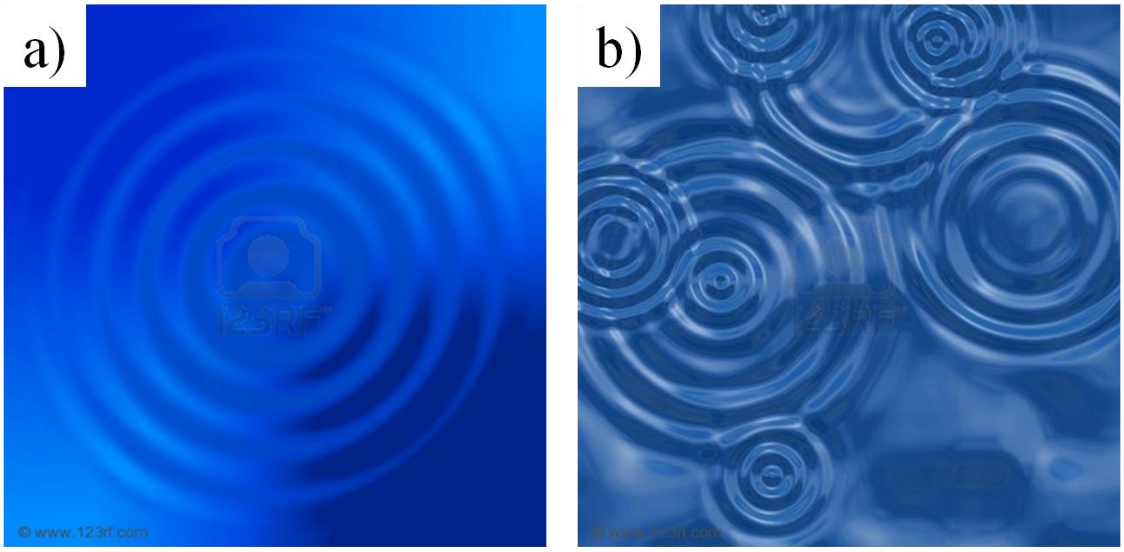

Figure 2.3.3 Illustration of water wave **a)** concentric circle. **b)** Complex interference pattern

absorption edge (K edge, L_{I}, L_{II}, L_{III} edge…) appear at predetermined energies dependent on the element. The last, the oscillations of $\mu(E)$ shown in Figure 2.3.5(b) can be observed at the energy range higher than absorption edge, with the amplitude of few percent of edge step. It must be mentioned that if the absorbing atom is isolated in space like in Figure 2.3.5(c), the photoelectron propagates as an unperturbed wave without oscillation (Figure 2.3.5(d)), however in most cases there are other atoms around the absorber in real material. This interference phenomenon, for a given energy of the photoelectron, depends on the distance between emitting and scattering atoms, and their atomic numbers.

Near the edge, there may appear absorption peaks due to excitation of core electrons to some bound states. Therefore, this pre-edge region contains information about the energetic of virtual orbitals, configuration and symmetry. As shown in Figure 2.3.6, the region at ~ 40 eV after edge is the X-ray absorption near edge structure (XANES). Its shape is dependent on many-body interactions, multiple scatterings, distortion of the excited state wave function by the coulomb field, band structure, etc. The edge position contains information about the oxidation

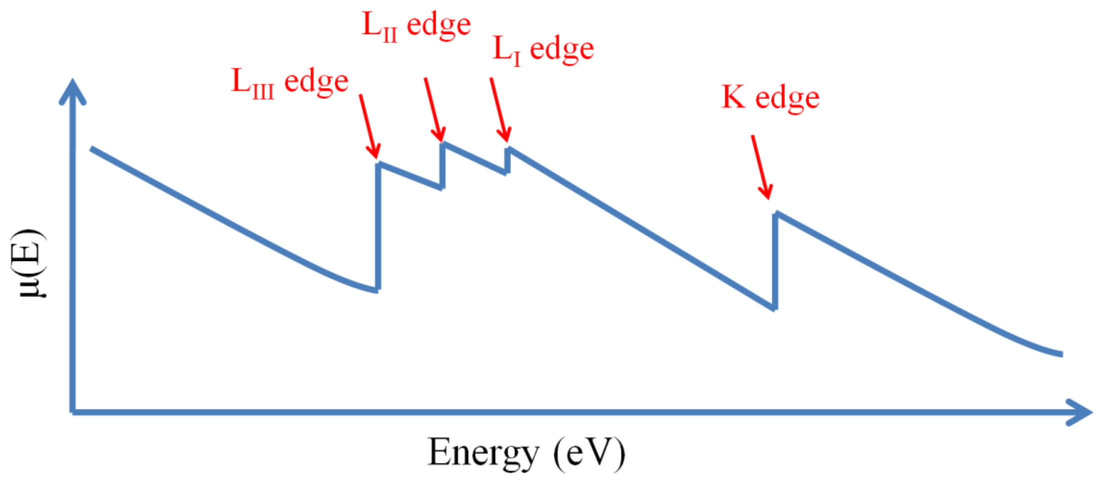

Figure 2.3.4 Energy dependence of the absorption coefficient. The absorption edges are marked

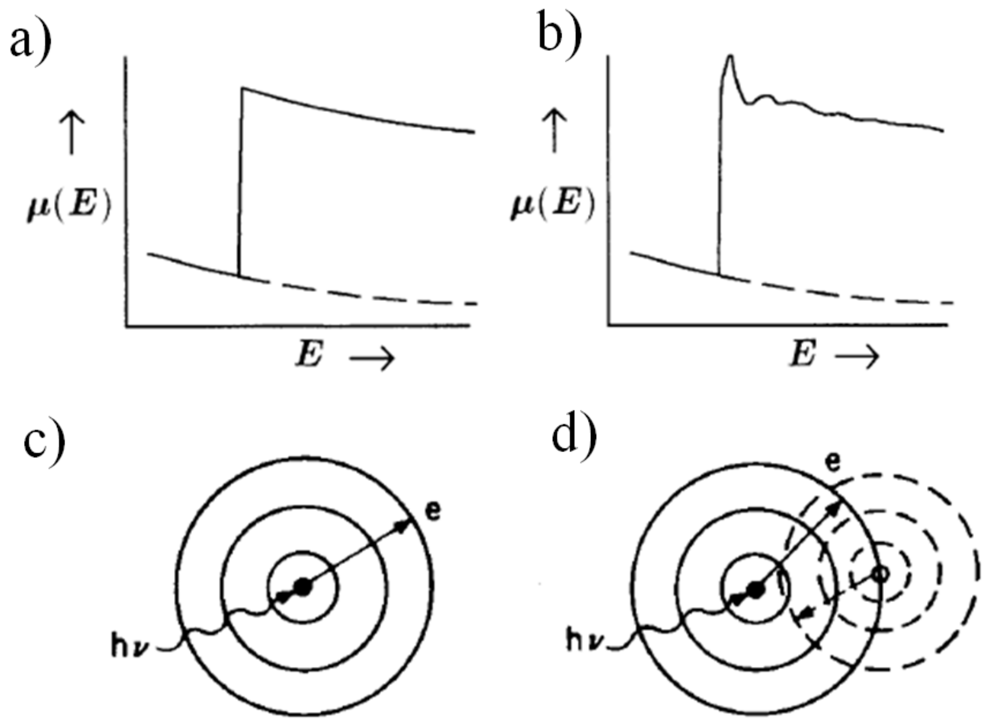

state of

Figure 2.3.5 The absorption coefficient μ(E) as a function of photon energy *E* (a) for a single atom and (b) for an atom surrounded by backscattering atoms. (c) and (d) indicate the processes of X-ray absorption spectroscopy

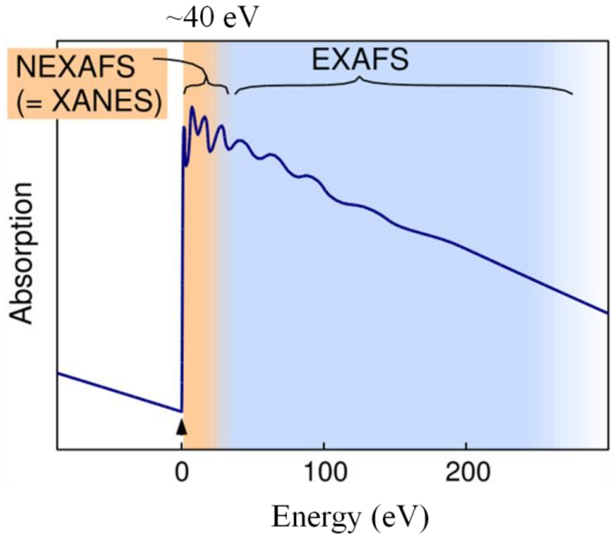

Figure 2.3.6 Example of a near edge (XANEs) region and far edge (EXAFS) region for an absorbing atom. In general, XANES ranging from 30 eV before edge to about 40 eV after the edge and EXAFS starts from 40 eV after the edge.

state of the absorbing atom. Extend X-ray absorption fine structure (EXAFS) spectroscopy refers to the oscillatory structure from 40 eV to several hundred eV after the edge. The EXAFS region provides information on the local environment of the X-ray absorbing atom such as coordination number, the interatomic distance between the absorbing atom and the backscattering atoms and Debye-Waller factor which accounts for the disorder due to the static displacements and thermal distortion. Thus, the measurement of the energy dependence of the X-ray absorption coefficient can be used to determine the local environment around the absorbing atoms. Since the position of the K and L edges are dependent on the element under investigation, the suitable choice of incident X-ray energies makes it possible to excite a particular element and hence to probe its environment. The elements suitable for EXAFS study are determined by the spectral region of the X-ray source.

2.3.2 Theory of EXAFS [25, 26, 29-31]

The ejected electron has kinetic energy E_k:

$$E_k = E - E_0 \tag{2.3.3}$$

where E is the energy of the X-ray photon and E_0 is the threshold energy. In order to determine the relationship between the quantities characterizing the neighborhood environment around the absorbing atom, it needs to extract the oscillation curve from the X-ray spectroscopy. The X-ray absorption coefficient $\mu(E)$ is necessary to be corrected and normalized by the background absorption $\mu_0(E)$. The oscillation curve $\chi(E)$ is described as:

$$\chi(E) = \frac{\mu(E)-\mu_0(E)}{\mu_0(E)} \tag{2.3.4}$$

The next step is to convert the $\chi(E)$ to $\chi(k)$, where k is the magnitude of the electron wave number which is estimated according to Eq.(2.3.3) from the energy E of incident X-ray and the position of the absorption edge E_0

$$k = \sqrt{2me(E - E_0)/\hbar^2} \qquad \hbar = h/2\pi \tag{2.3.5}$$

Here, m_e is the mass of the electron and h is the Planck's constant. In order to extract structural information from experimental spectra, a simple analytical expression that relates the EXAFS signal to the structural parameters is required. To obtain a simplified EXAFS formula, some approximations have to be assumed. First of all, the dipole approximation, which describes the interactions among core electrons and X-ray photons. This approximation allows to express the absorption cross-section as:

$$P_{if} = (\vec{\varepsilon},\ \vec{r})^2 = \frac{2\pi^2 e^2}{m_e^2 \omega} \left|M_{if}\right|^2 \rho\left(E_j\right) \tag{2.3.6}$$

where, $\vec{\varepsilon}$, $\vec{r}$ are an electric field vector and an atom position vector, respectively. The subscript i and f are initial and finial states of the electron, respectively. $\rho\left(E_j\right)$ is the state density available to the electron, ω is the incident photon frequency and $|M_{if}|$ is a dipole matrix element related to the transition of electron from the initial state to the finial state. The most difficult issue during the analysis is to obtain a good expression of the final state wave function. This can be done by choosing a proper approximation for the potential function that describes the system. In most case, this problem can be overcome by using the "muffin-tin" approximation. Under these conditions, final wave function Ψ_f depends on the absorbed photon energy and can be written as a linear combination of two terms: the wave function for the outgoing photoelectron from the excited atom Ψ_{out}, and a perturbing term Ψ_{SC} represents the backscattered wave.

$$\chi(k) = \frac{<\Psi_{out}+\Psi_{sc}|(\vec{\varepsilon},\vec{r})^2 e|\Psi_i>}{<\Psi_{out}|(\vec{\varepsilon},\vec{r})^2 e|\Psi_i>} - 1 \tag{2.3.7}$$

Here, considering a simple model: the photoelectron from an isolated atom is represented as a spherical outgoing wave of wave number $\vec{k}$. The amplitude of outgoing wave is proportional to

$$\Psi_{out} \sim \frac{exp\left(-i\vec{k}\vec{r}+i\delta_c(\vec{k})\right)}{|\vec{r}|} \tag{2.3.8}$$

where, $\delta_c(\vec{k})$ is the phase shift of central atom (absorbing atom). Suppose the nearest-neighbor atoms are at position $\vec{R}$. Thus the outgoing wave at $\vec{R}$ can be described as

$$\Psi_{out}\left(\vec{R}\right) \sim \frac{exp\left(-i\vec{k}\vec{R}+i\delta_c(\vec{k})\right)}{|\vec{R}|}\ exp\ (-\frac{|\vec{R}|}{\lambda(\vec{k})}) \tag{2.3.9}$$

$\lambda(\vec{k})$ is the electronic mean-free path in sample. Hence, the backscattering wave function is

$$\Psi_{sc} \sim \frac{exp\left(-i\vec{k}\vec{R}+i\delta_c(\vec{k})\right)}{|\vec{R}|} exp\left(-\frac{|\vec{R}|}{\lambda(\vec{k})}\right)\ f(\vec{k}) \tag{2.3.10}$$

$f(\vec{k})$ is complex backscattering probability. Finally, the superposition of outgoing wave function and backscattered wave function can be described as

$$\Psi_{out} + \Psi_{sc} \sim \frac{exp\left(-i\vec{k}\vec{R}+i\delta_c(\vec{k})\right)}{|\vec{R}|} exp\left(-\frac{|\vec{R}|}{\lambda(\vec{k})}\right)\ f(\vec{k}) \frac{\exp\left(-i\vec{k}(\vec{R}-\vec{r})+i\delta_c(\vec{k})+i\delta_a(\vec{k})\right)}{|\vec{k}||\vec{R}|} \tag{2.3.11}$$

a)

$$\Psi_{out} \sim \frac{exp(-ikr + i\delta_c(k))}{r}$$

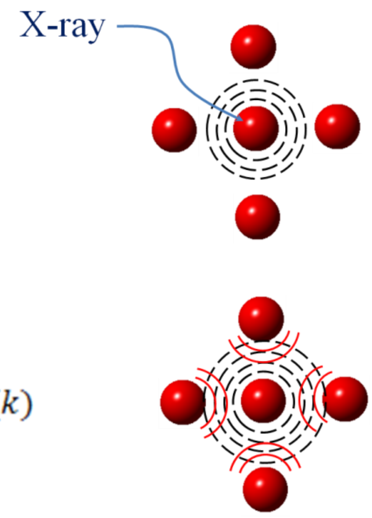

$$\Psi_{sc} \sim \frac{exp(-ikR + i\delta_c(k))}{R} exp\left(-\frac{R}{\lambda(k)}\right) f(k)$$

Single Scattering

$$\frac{exp(-ikR + i\delta_c(k))}{R} exp\left(-\frac{R}{\lambda(k)}\right) f(k) \frac{exp(-ik(R-r) + i\delta_c(k) + i\delta_a(k))}{kR}$$

b)

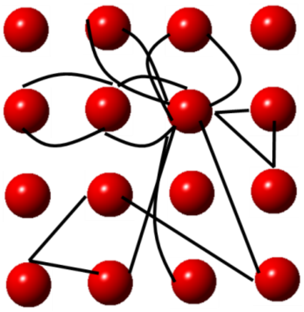

Figure 2.3.7 An illustration of the photoelectron scattering model. **a)** Single scattering in detail; the black broken circles are outgoing wave and the red ones are back scattering wave. **b)** Path of a photoelectron during propagation in the crystal. It can be reflected once, twice or more times before it returns to the central atom. This process is called multiple scattering.[29, 31]

where $i\delta_a(\vec{k})$ is backscattering atom phase shift.. This formula is just for one-atom single scattering. Reflected photoelectron can propagate back to the central atom and of course it can also propagate to other atoms which are close. After several times scattering, it returns back to the central atom. This situation is called multiple scattering. All possible traces of the photoelectron are call paths. An illustration of the photoelectron scattering model is shown in Figure 2.3.7.

With respect to the compounds with multiple atoms N_i in a shell i, starting from this formula and with several mathematical transformation, we can obtain the $\chi(k)$ as

$$\chi(\vec{k}) \approx S_0^2 \sum_i N_i(\vec{\varepsilon},\vec{r})^2 \left|f(\vec{k})\right| exp\left(-\frac{2r}{\lambda(\vec{k})}\right) exp(-2k^2\sigma^2) \frac{sin\left(2\vec{k}\vec{r} + 2\delta_c(\vec{k}) + \delta_a(\vec{k})\right)}{kr^2}$$

$$(r = |\vec{r}|, k = |\vec{k}|) \qquad (2.3.12)$$

σ is the Debye-Waller factor. It is clear that each EXAFS (i) wave is determined by the amplitude $N_i \times |f(\pi,k)| \times S_0^2$, and modified by the reduction factors exp $(-2k^2\sigma^2)$, $(\sin(2kr + 2\delta_c(k) + \delta_a(k)))$ and $e^{-2r/\lambda(k)}$, $1/r^2$.

2.4 XAFS Experimental Setup[32]

All of the XAFS measurements were performed at NW-10A station of Photon Factory advanced ring (KEK-PF-AR) for pulse X-rays in the Institute of Material Structure Science High Energy Accelerator Research Organization.[33, 34] The schematic layout of a beamline is shown in Figure 2.4.1. The X-ray source is a bending magnet NW11 in the 6.5 GeV Advanced Ring. The beam port is attached to the neighboring bending magnet NW10, thus named as NW10. The critical energy of the bending magnet is 26.3 keV, which is suited for the hard x-ray experiments. The main components of NW-10 station are: the monochromator used to select the X-ray energy, a Pt-coated bent cylindrical focusing mirror used to get high flux (e.g. 1×10^{10} photons/s at 20 keV and 7×10^{9} photons/s at 30 keV though a 1 mm square slit), and an experimental hutch. Each of these components will be introduced briefly in the following sections.

2.4.1 Monochromator[35, 36]

The double crystal monochromator adopted in NW-10A is comprised of two parallel silicon crystals as shown in Figure 2.4.2. The first crystal is set at an angle θ with respect to the X-ray beam to select the desired energy, and the second one is set to the parallel to the first one so as to reflect the beam to the experimental hutch.

The X-ray energy selected by the monochromater is determined by the Bragg condition. The Bragg condition is expressed as

$$2Dsin\theta = m\lambda \tag{2.4.1}$$

thus, the energy corresponding to the wave length λ is determined by θ and an integer, m. When, m = 1, the $\lambda_1 = 2Dsin\theta$ is desired energy. However, according to the Bragg condition,

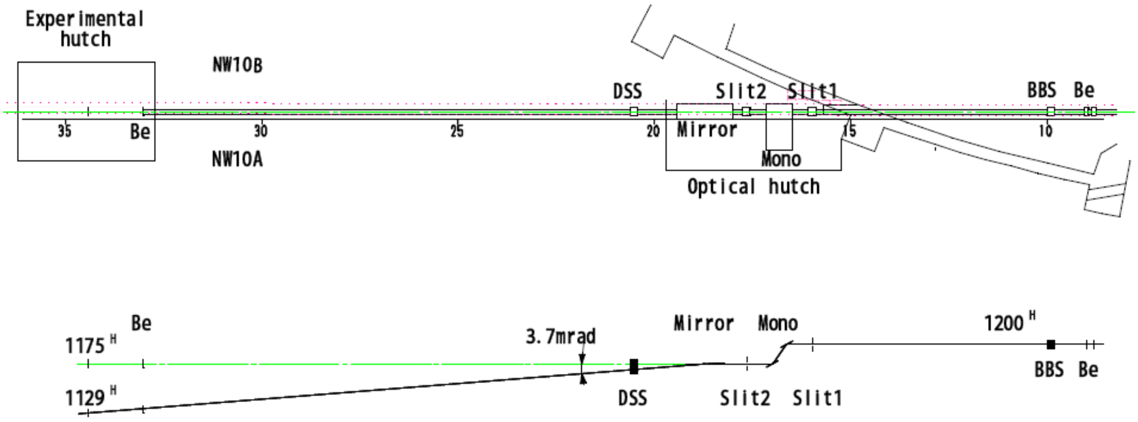

Figure 2.4.1 Schematic layout of the NW10A beamline. White X-rays are monochromatized with a Si(311) double crystal monochromator. The monochromatic beam is focused at 32.8 m by a bent cylindrical mirror placed at 20.5 m. [33]

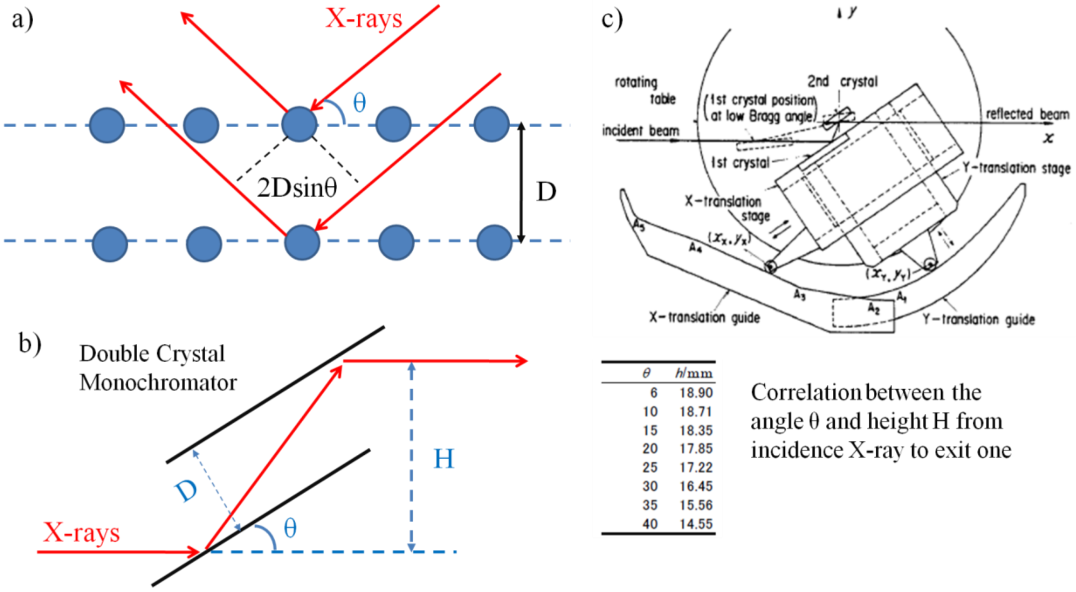

θ	h/mm
6	18.90
10	18.71
15	18.35
20	17.85
25	17.22
30	16.45
35	15.56
40	14.55

Correlation between the angle θ and height H from incidence X-ray to exit one

Figure 2.4.2 **a)** The Bragg condition. $2Dsin\theta = m\lambda$ where *m* is an integer. This means that the energy is determined by m and λ. X-ray with higher energy will be selected together with the desired one. **b)** Arrangement of two parallel silicon crystals. First one is used to select the energy and the second is rotated and translated to keep a fixed exit beam position and directions. **c)** A mechanism to keep the exit beam height constant and correlation between the angle θ and height H. [36]

X-ray with higher energy (λ_m called m-th harmonic) must be removed along with the desired energy. Available energy range by several silicon monochromator crystals are listed in Table 2.4.1. The energy range is dependent on the plane type and size of the crystal which determines the θ range. In NW10A station, Si(311) crystal is used to selected energy. So the available energy is from 7 keV to 43 keV. The Second harmonics is not allowed in this condition due to the systematic absences. And the higher harmonics (>3th) are negligible, thus, only the 3rd harmonics would distort the XAFS signal. The elimination of the harmonics will be discussed in the mirror section.

Table 2.4.1 Available energy range with several silicon monochromator crystals (Angle: 5 to 35 °)

h	k	l	2d (Å)	Energy range (keV)	Second harmonics
1	1	1	6.2708	4 to 23	Not allowed
2	2	0	3.8400	6 to 37	Allowed
3	1	1	3.2744	7 to 43	Not allowed
4	0	0	2.7154	8 to 52	Allowed

The exit beam energy is determined by rotation angle θ of Si(311) crystal, however, the change of angle will alter the position of exit-beam. In order to keep exit-beam height constant in a wide energy range. A fixed-exit double-crystal monochromator is adopted in NW10A station. As shown in Figure 2.4.2(c), the first crystal mounted on X- and Y- translation stages which cross each other orthogonally. The translational motions of the X- and Y- stages are controlled by mechanical cams when both of two crystals are rotated about a single rotation axis. The motion of the Y- stage is perpendicular to the diffracting plane to keep the exit beam height always constant. And the motion of X- translation stage is parallel to the diffracting plane of the crystal; the first crystal is moved to a position at which it can be hit by the incident beam. The correlation between the rotation angle θ and X-direction displacement can be described as:

$$X = H / tan(2\theta) \tag{2.4.2}$$

2.4.2 Mirror[37]

A focusing mirror is placed at 20.5 m from the source and focuses the beam at 32.8 m. Platinum is chosen as the coating material in order to realize higher irradiation angle and higher reflectivity at 40 keV. Comparing to the sagittal focusing of the monochromator, the advantage and disadvantage are listed as follows:

Advantage:

1) Easy to reduce the beam size,

2) The beam size and shape are regardless of the energy,

3) Elimination of the higher harmonics.

Disadvantage:

1) Hard to increase the intensity, since the acceptance in horizontal direction depends on the shape of mirror;

2) Expensive,

3) The mirror has to be placed far from source,

4) Difficult to use for high energy beam.

In NW10A station, the beam irradiation angle was chosen as 1.85 mrad to increase the flux above 40 keV as shown in Figure 2.4.3(a) (The calculation value is 1.9 mrad for 44 keV, however, flux above 40 keV decreased at this condition). In order to realize the focusing condition, the sagittal radius is chosen as 29.2 nm and the tangential one as 8092 m. The material (silicon) and the thickness (70 mm) are chosen to minimize the deformation of the mirror by the gravity. The focus size is evaluated to 0.5 mm (H) × 1.1 mm (V). Photon flux is evaluated by using an ionization chamber and is compared with the non-focused beam. The gain of flux is significant above 20 keV: 20 times at 20 keV, 70 times at 25.5 keV and 200 times at 30 keV.

The elimination of X-rays with high harmonic energy is achieved by different reflectivity between normal beam (λ_1) and 3rd harmonics (λ_3) on the coating Pt surface or silicon. Figure 2.4.3(b) shows intensity ratio between 3rd harmonic and normal beam. The ratio is low enough after install a parallel, double mirror system.

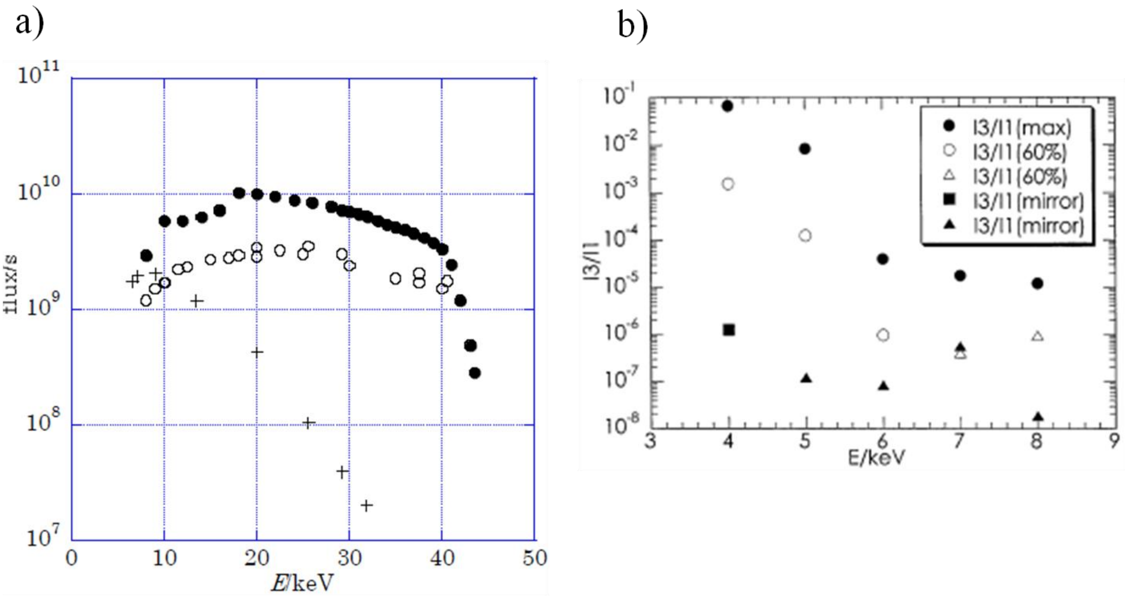

Figure 2.4.3 **a)** The flux obtained at NW10A. Closed and open circles indicate the flux with and without focusing, respectively. **b)** The ration of 3rd harmonics and normal beam at various energies. Closed symbols (●, ■, ▲) indicate the ration taken with fully tuned double crystal monochromator (DXM) whereas open ones (○, △) indicate that with detuned DXM so as to provide 60% of its maximum. ■ and ▲ are the cases which contain an elimination mirrors. Triangles indicate the estimated highest ratio. Obviously, the present of mirror helps to reduce the influence of 3rd harmonics at low energy region. [33]

2.4.3 Experimental Hutch[38]

The size of the experimental hutch is 4.0 m (optical axis) ×3.2 m (width)× 2.8 m (height) as shown in Figure 2.4.4. The main standing facilities in hutch contain

1) Setup for XAFS experiment: This setup is assembled on an optical bench, which is mounted on a motor driven table (2000 mm (L)×1200 mm (W)). The beam height is ca. 348 mm from the top of the table and 188 mm from the top of the optical bench.

2) Ionization chamber and gas supply systems for XAFS measurements in transmission mode: 4 chambers (gas length: 5 cm×1, 17 cm×1, 31 cm×2) can be used. 6 kinds of gases (N_2 (100%), N_2 + Ar (15%), N_2 +Ar (25%), N_2 +Ar (50%), Ar (100%)) and Kr are prepared as default.

3) 19-element Ge solid state detector (ORTEC Co.) for fluorescent XAFS measurements

4) Cryocooler for sample cooling and the temperature controller (SI MODEL 9700) which can control the temperature of sample between room temperature and 10 K.

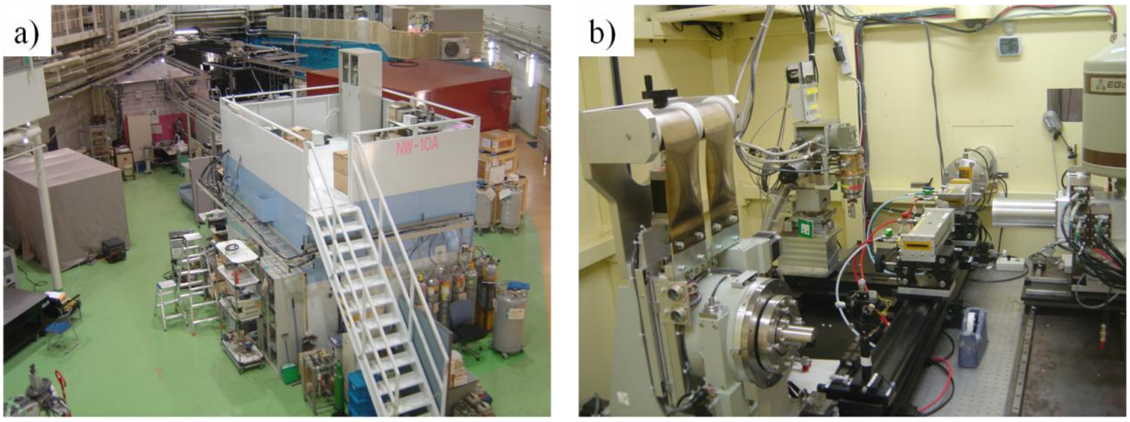

Figure 2.4.4 The photos of **a)** NW10A station and **b)** experimental hutch

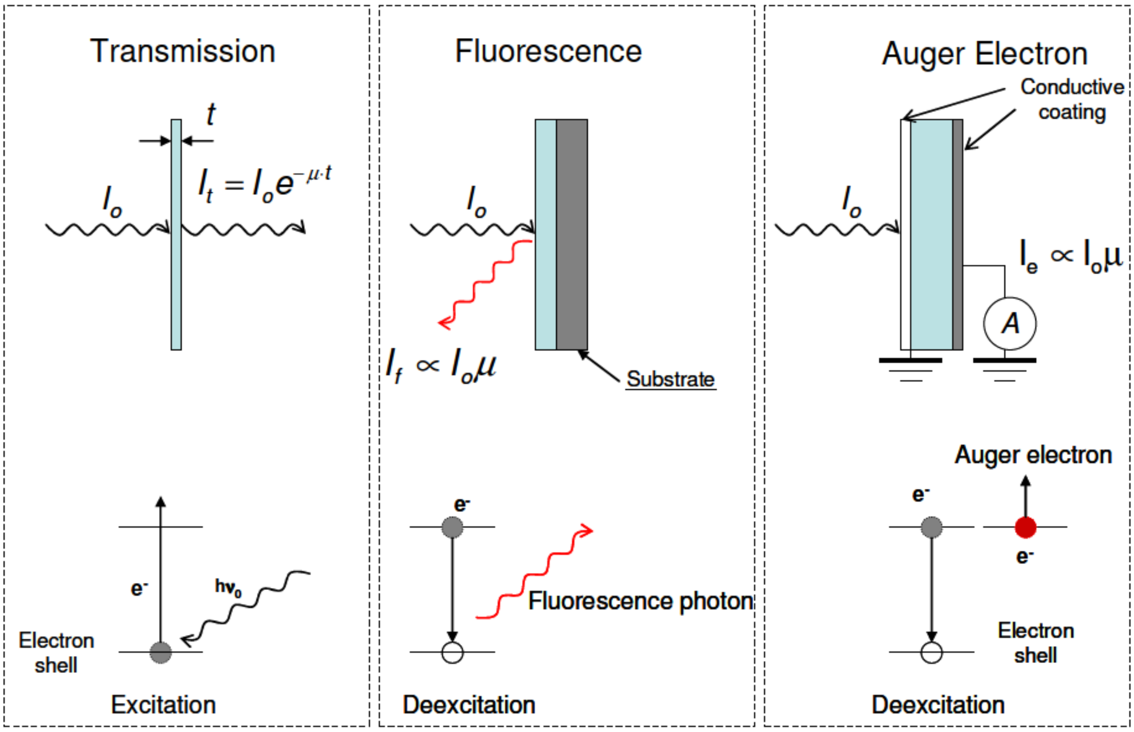

Figure 2.4.5 Principle and mechanism of three EXAFS detection techniques in transmission mode, fluorescence mode and total-electron yield.(from left to right) [39]

Before detailed discussion on these facilities, a brief introduction of XAFS data collection will be given at first. There are generally three data collection methods available, i.e., transmission, fluorescence and total-electron-yield (TEY). The basic principles and mechanisms of these methods are illustrated in Figure 2.4.5. [39] The transmission method is to directly measure the incident beam (I_0) and transmitted beam (I), and calculate the $\mu(E)$ by Lambert-Beer's law, this method typically provides the best signal to noise. Fluorescence and total-electron yield are alternative collections which measure $\mu(E)$ indirectly. Both of them are basing on the relaxation process of core hole resulted from photoelectron emission. The measurements of fluorescence or Auger electrons can provide information about $\mu(E)$. [40]

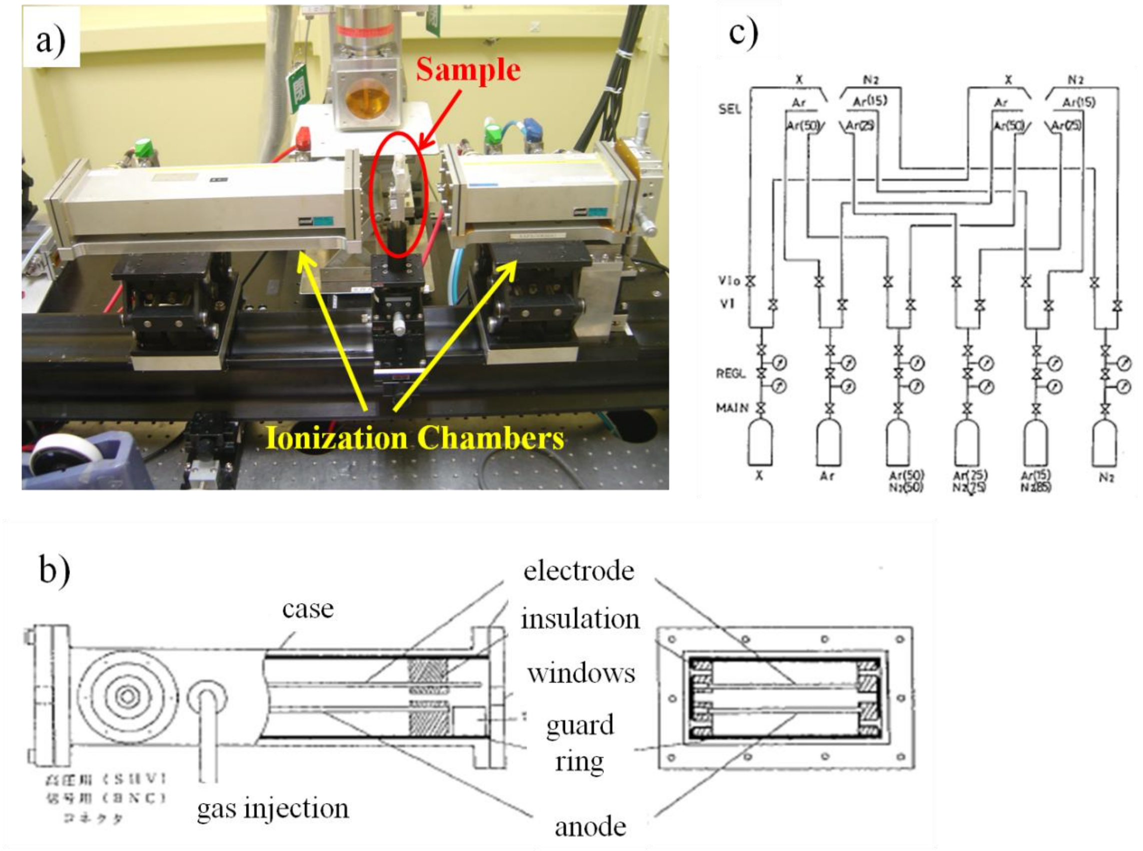

Figure 2.4.6 **a)** Photo of XAFS measurement in transmission mode. Two rectangle boxes marked by yellow arrows are ionization chambers. **b)** Structural illustration of ionization chamber. **c)** The arrangement of gas lines.

< Transmission Method >

The most widely used method is transmission detection. By measuring the incident beam (I_0) and transmitted beam (I). The absorption $\mu(E)$ can be given by Lambert-Beer's law as follows:

$$\frac{I}{I_0} = exp(-\mu(E)x),\ thus\ \mu(E)x = ln(\frac{I_0}{I}) \tag{2.4.3}$$

Gas ionization chambers are usually used to measure beam flux o the incident synchrotron beam and the transmitted beam. The ionization chamber comprises of two parallel electrodes and a region filled with a gas in between. Inside the chamber, an electric field about 100 V/cm is applied between two electrodes and the electrons are collected at the anode. Once the beam travels through the chamber, a fraction of gas will be ionized. The electrons and ions are then pulled to anode by the electric field. When these charged particles hit the anode, they will produce a current, which is very weak. The current is sent directly to a preamplifier to be changed to a voltage that we measure. The voltage is directly proportional to the amount of ionization. The relationship between the output voltage and beam intensity can be described as:

$$Voltage = Amplifier\ Gain \times \frac{e \times X\ ray\ Energy}{Effective\ Ionization\ Energy} \times X\ ray\ intensity \tag{2.4.4}$$

where effective ionization energy is dependent on the active length of the ionization chamber, the properties of the chamber gas, and the X-ray absorption cross section at the appropriate photon energy. Generally, the effective ionization energy is about 130 ~ 150 eV (including the absorption coefficient). Then, as an example, in the case of a beam with energy of 8 keV and intensity of 10^{10} photons/s, the signal current is calculated to the 8.5×10^{-8} A. Thus, the amplifier gain must be set at the range for 10^7 ~ 10^9 V/A to give a detectable voltage signal.

In order to get good signal, it is necessary to pay attention on the preparation of sample. Here, considering a solid sample with thickness of X. Incident beam intensity is I_{inc}, and the transmitted beam intensity I_t detected by the second ionization chamber is given by

$$I_t = I_{inc}\ exp(-(\mu_A + \mu_B)X) \tag{2.4.5}$$

where μ_A is absorption of target element and μ_B is the absorption of surrounding. The incident beam intensity I_{inc} is estimated by ionization chamber with length of X_i and gas absorption of μ_g. If the intensity of initial beam from source is I_{inc}, thus signal I_d from ionization chamber is

$$I_d = I_0(1 - exp(-\mu_g X_i)) \tag{2.4.6}$$

Then, the signal of XAFS S depended on $\frac{I_d}{I_t}$ can be described as

$$S = \frac{\partial\left(\frac{I_d}{I_t}\right)}{\partial\mu_A}\Delta\mu_A = \Delta\mu_A X\frac{I_d}{I_t} = \Delta\mu_A X\frac{1-exp(-\mu_g X_i)}{exp(-\mu_g X_i)\,exp(-(\mu_A+\mu_B)X)} \qquad (2.4.7)$$

where μ_A is the intensity of XAFS oscillation. The noise can be calculated simply as

$$\mathrm{N} = \frac{I_d}{I_t}\left[\left(\frac{\Delta I_d}{I_d}\right)^2 + \left(\frac{\Delta I_t}{I_t}\right)^2\right]^{\frac{1}{2}} = \frac{I_d}{I_t}\left[\frac{1}{I_d}+\frac{1}{I_t}\right]^{\frac{1}{2}} \qquad (2.4.8)$$

The S/N ratio is equal to

$$S/N = \Delta\mu_A X\left[\frac{1}{I_d}+\frac{1}{I_t}\right]^{-\frac{1}{2}} = \Delta\mu_A X\sqrt{I_d}\left[\frac{1}{1+\frac{I_d}{I_t}}\right]^{\frac{1}{2}} \qquad (2.4.9)$$

the I_d is dependent on the ionization chamber. Therefore, the appropriate thickness X is an important key to get the best S/N ratio.

Preparation of XAFS sample for transmission measurement:

For simplicity, only powder sample will be discussed here. In order to get good S/N, it is necessary to reduce the background absorption and enhance the target absorption. The best thickness can be calculated strictly by Eq. (2.4.9). Empirically, good S/N ratio can also be achieved, while the thickness meets following two conditions:

a) total elements absorption:

$$\mu_S(E)\mathrm{X} = \left(\mu_A(E)+\mu_B(E)\right)\mathrm{X} \le 3-4 \qquad (2.4.10)$$

b) target absorber absorption:

$$\mu_A(E)\mathrm{X} \ge 0.2 \qquad (2.4.11)$$

And, in other words, the transmission detection loses its advantage on the dilute sample (e.g. $\mu_A(E)\mathrm{X} \le 0.2$), a detailed discussion will be given at following section.

< Fluorescence mode >

Transmission detection is not preferable to the dilute sample, since it is difficult to isolate the XAFS signal from the background. [41, 42] In these cases, X-ray fluorescence and emission of Auger electrons [43] which directly measure the absorption probability will provide better S/N than the transmission mode. These two phenomena are competing processes for relaxation of an inner shell hole. In light elements Auger emission is more probable, while for heavy elements fluorescence becomes more commonly. For the same element, fluorescence is more likely for K-shell than L-shell. In this study, all of measurements on dilute samples were performed in fluorescence mode.

For simplicity, considering the geometrical arrangement where the incident beam and fluorescence make equal angels with the sample normal. [42] The incident beam has energy E, the fluorescence has energy E_f, and the detector subtends a solid angle Ω. Then, the fluorescence counting rate is given by

$$I_f = I_d \frac{\epsilon\left(\frac{\Omega}{4\pi}\right)\mu_A(E)}{\mu_S(E)+\mu_S(E_f)} \left\{1 - \exp\left(- X(\mu_S(E) + \mu_S(E_f))\right)\right\} \qquad (2.4.12)$$

$$\mu_S(E) = \mu_A(E) + \mu_B(E) \qquad (2.4.13)$$

where, ϵ is the fluorescence yield. Two important cases are discussed here. One is a thin but concentrate sample for which $(\mu_S(E) + \mu_S(E_f))\mathrm{X} \ll 1$, and the other is a dilute but thick sample for which $(\mu_S(E) + \mu_S(E_f))\mathrm{X} \gg 1$. In these two case, (2.4.10) can be transformed to

$$I_f = I_d\, \epsilon \left(\frac{\Omega}{4\pi}\right) \mu_A(E) X \qquad \text{(thin, concentrated)} \qquad (2.4.1)$$

$$I_f = I_d \frac{\epsilon\left(\frac{\Omega}{4\pi}\right)\mu_A(E)}{\mu_S(E)+\mu_S(E_f)} \qquad \text{(thick, dilute)} \qquad (2.4.15)$$

Similar to the < Transmission Method > section, the signal to noise ratio can be given by

$$S/N = \frac{\partial\left(\frac{I_f}{I_d}\right)}{\partial \mu_A} \Delta\mu_A / \left(\frac{I_d}{I_f}\left[\frac{1}{I_d} + \frac{1}{I_f}\right]^{\frac{1}{2}}\right) \qquad (2.4.16)$$

Therefore,

$$\mathrm{S/N} = \begin{cases} \left[I_d \epsilon \left(\frac{\Omega}{4\pi}\right) \mu_A(E)\right]^{1/2} \frac{\Delta\mu_A}{\mu_A(E)} \left(\frac{1}{1+\frac{I_d}{I_f}}\right)^{1/2} \text{(thin, concentrated)} & (2.4.17) \\ \left[I_d \frac{\epsilon\left(\frac{\Omega}{4\pi}\right)\mu_A(E)}{\mu_S(E)+\mu_S(E_f)}\right]^{1/2} \frac{\Delta\mu_A}{\mu_A(E)} \left(\frac{1}{1+\frac{I_d}{I_f}}\right)^{1/2} \text{(thick, dilute)} & (2.4.18) \end{cases}$$

Comparing the S/N ratio of different detection methods: transmission (2.4.9) and fluorescence (2.4.17), (2.4.18), if $\frac{I_d}{I_f} \ll 1$, the difference of S/N ratio between two detection methods are roughly determined by two terms: $\epsilon\left(\frac{\Omega}{4\pi}\right)$ and $\frac{\mu_{A(E)}}{\mu_S(E)}$. Generally speaking, if the total efficiency of the fluorescence $\epsilon\left(\frac{\Omega}{4\pi}\right)$ is greater than $\frac{\mu_{A(E)}}{\mu_S(E)}$, the transmission technique is not preferred. More specifically, for a given efficiency one can determine the absorber concentration at which the fluorescence become more favorable. For atom number Z = 20 to Z = 100, ϵ are in the range from 0.1 to 1. For a modest value of $\left(\frac{\Omega}{4\pi}\right)$ is ~ 10^{-2}, the fluorescence S/N ratio is greater than that of transmission when $\frac{\mu_{A(E)}}{\mu_S(E)} < 10^{-3}$.[40]

For dilute sample, fluorescence detection can give better S/N than transmission as shown above, however, it does not mean fluorescence detection is a superset with respect to transmission. Conversely, fluorescence detection is just substitute method, when good S/N ratio cannot be obtained in transmission mode. Some problems of fluorescence detection are listed below:

1) Only available to thin & concentrated sample or thick & dilute sample.

2) Hindrance of X-ray scattering and X-ray fluorescence of surrounding atoms.

3) Difficulty of background removal.

< Solid State Detector (SSD) > [44]

A 19-element high purity germanium semiconductor diode detector with good energy resolution and large solid angle is used for fluorescence mode XAFS in this study (Figure 2.4.7). Semiconductor detectors are always fabricated in the structure of p-n diode. It is well known that p-n junction can exhibit high conductivity when a voltage is applied in the forward direction, but it is insulated when voltage in the reverse direction.

In practical operation, the SSD is usually completely depleted under reverse voltage in order to extend the depletion region through the semiconductor wafer. This is for the purpose to get an electric field everywhere in the absorber so that all of the radiation-generating electron-hole pairs can be separated and collected at the two poles of the diode. Moreover, it is recommended that sufficient over-voltage (higher than complete-depletion) would be applied so that the electric field is high enough to impart saturated drift velocities to the charge carries, minimizing the collection time and the detrimental effects due to carrier recombination and trapping.

However, under reverse voltage, a small leakage current resulting from thermal generation of electron-hole pairs within the depletion region is observed. The probability is given by:

$$P(T) = CT^{3/2}(-\frac{E_g}{2kT}) \tag{2.4.19}$$

where E_g is the bandgap of the semiconductor. Since the bandgap of Ge is very small (about 0.7 eV), large thermally-induced leakage current will occur during the operation of Ge-SSD at room-temperature. Thus, generally, Ge-SSD is cooled to low temperature (77K, liquid nitrogen) to reduce the leakage current.

The main advantage of SSD is the smallness of the ionization energy, the values of which at low temperature (e.g. 77 K) are 3.76 eV for silicon and 2.96 eV for germanium [45], compared with about 130 ~ 150 eV required to generate an ion pair in ionization chamber as mentioned above. Therefore, for a given energy of the photon deposited in the detector, the number of charge carriers is several tens larger than the ionization chamber.

Generally speaking, for SSD, a high energy resolution and a high counting-rate capability cannot be realized at the same time. [46, 47] The performance of SSD is usually dependent on the preamplifier (Figure 2.4.7(b)). As shown in Figure 2.4.8, over the last two decades, reset-type preamplifiers have been developed to meet the high counting rate requirement without seriously sacrificing the energy resolution. However, the counting-loss cannot be ignored. In the signal counting-processing circuit, there is delay-period during the signal-processing of spectroscopy amplifier. This delay-period is called dead time. The dead time can result in serious non-linear distortions for XAFS data collection. Nomura reported dead time correction of multi-element SSD and provided a file to correct the dead-time loss of fluorescent XAFS measured in PF or PF-AR station. In this study, all of fluorescent XAFS signals were collected by SSD systems with shaping time of 0.5 microsecond.

< Cryocooler >

Cryocooler shown in Figure 2.4.9 is refrigerating machine, which is able to achieve and to maintain cryogenic temperatures. In NW10A station, cryocooler is usually combined with temperature controller to cool the sample to the low temperature ranging from 10 K to room temperature. A home-made sample holder set is shown in Figure 2.4.10.

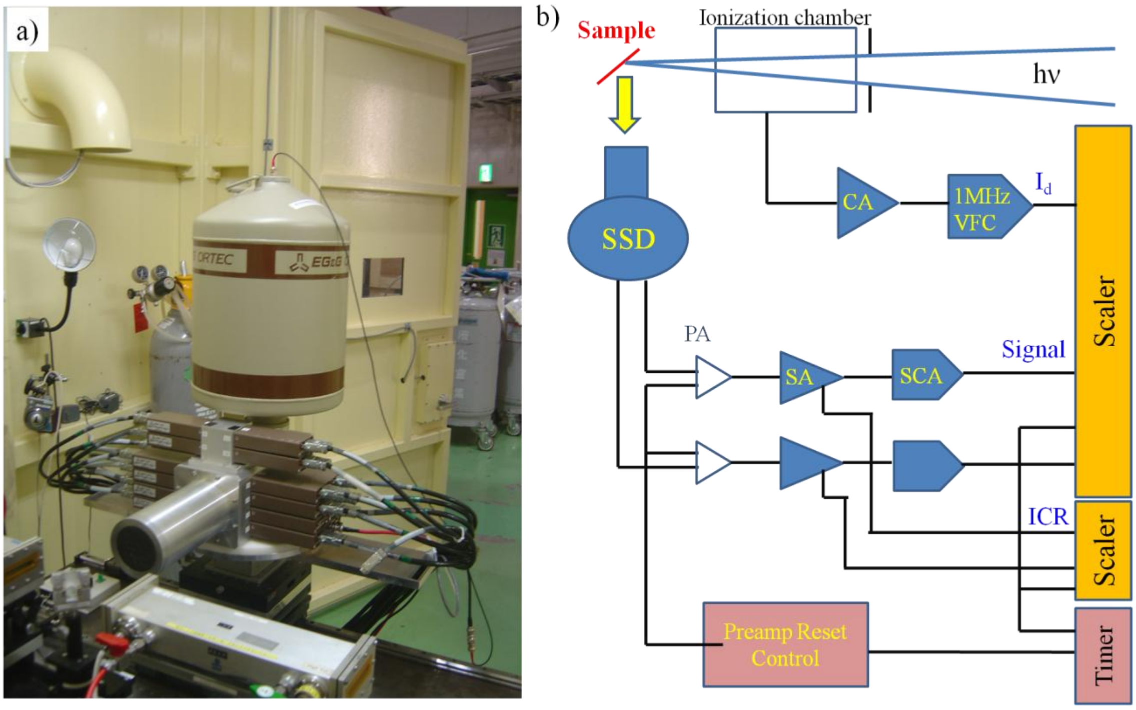

Figure 2.4.7 **a)** Photo of 19-element SSD. **b)** Counting systems of fluorescent XAFS.

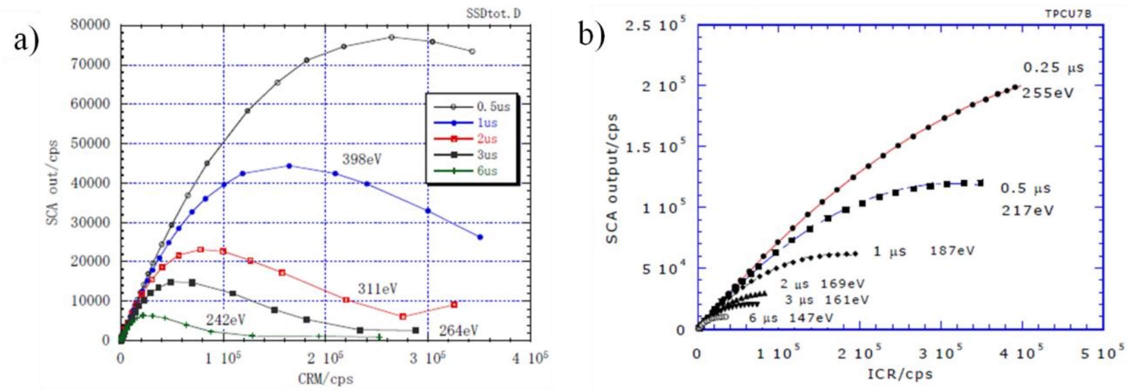

Figure 2.4.8 Relative throughput curves as functions of the shaping time and counting rate. The vertical axis is the signal rate passing through an SCA. **a)** Ge-SSD in 1980s, the preamplifier was transistor reset. CRM is Count Rate Monitor. When the shaping time is set to 6 µs**,** the energy resolution is about 242 eV, however the counting is only several thousand cps. **b)** Recent Ge-SSD: the pentafet preamplifier is used. The system can count up to 370 k cps for each channel when the shaping time is adjusted to 0.25 µs. [44]

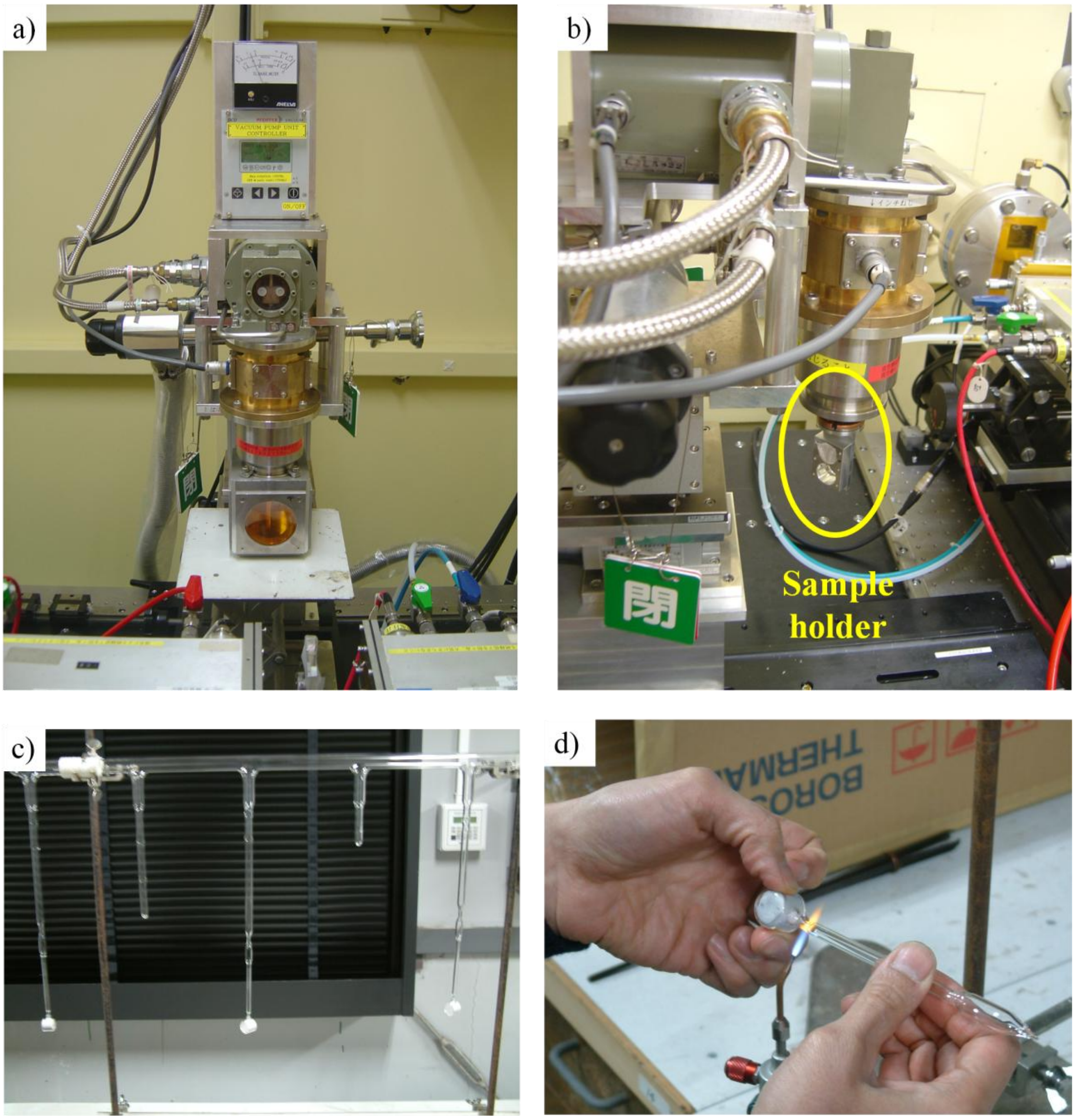

Figure 2.4.9 Photos of cryocooler **a)** Front view. The pumping system comprises of rotary pump and turbo-molecular pump. **b)** Sample holder with two glass cells was mounted on the cryocooler. The glass cells were sealed after being pumped as shown in **c)-d)**. **c)** Vacuum line for pumping sample cells. **d)** Seal operation of sample cell. (Operator: Mr. Sakaguchi, a staff in Renovation Center of Instruments for Science Education and Technology, Osaka University)

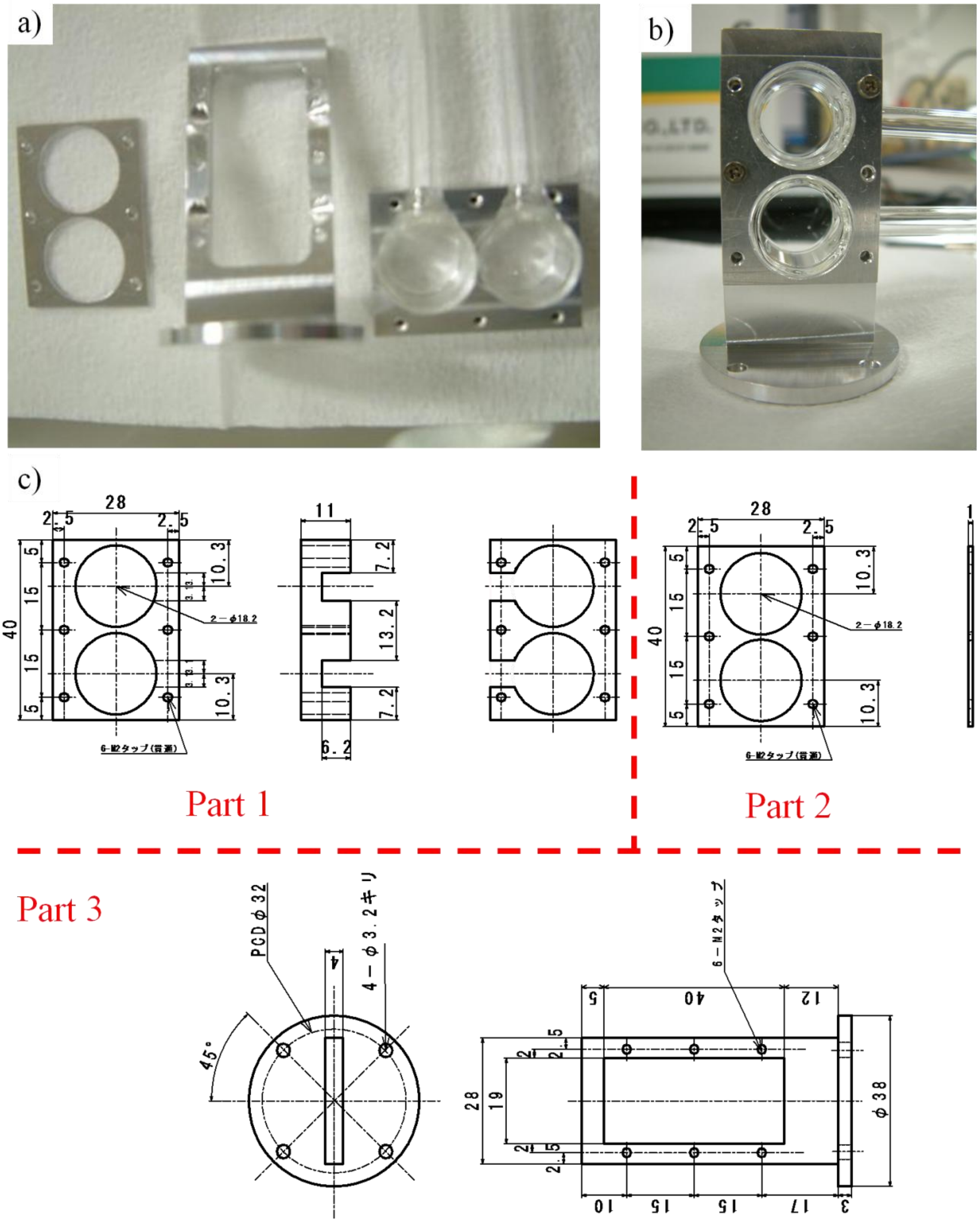

Figure 2.4.10 Photos of sample holder for low temperature measurements. **a)** Parts of sample holder. **b)** Assembly view. **c)** Blueprints of individual parts.

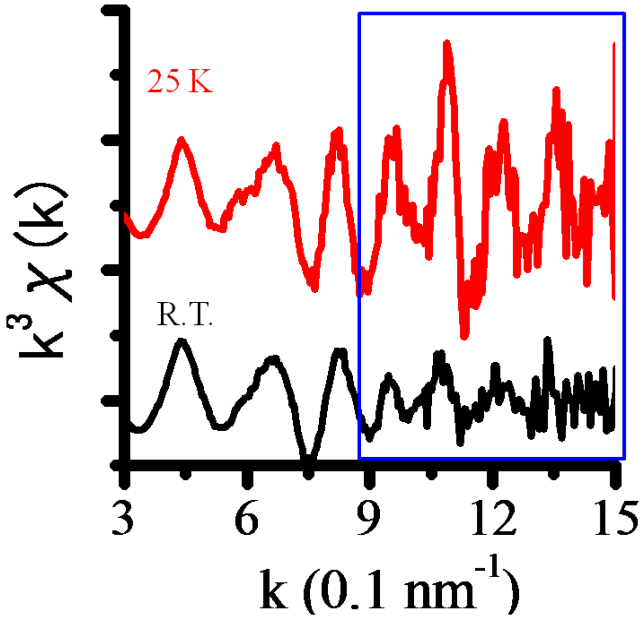

Figure 2.4.11 Comparison of k^3-weight EXAFS oscillation obtained at room temperature (black curve) and 25 K (red curve). The R.T. data is damped from the k ~ 9 Å^{-1} (marked by blue rectangle) and becomes noisy, while the 25 K data keeps its density in this range due to the decrease of Debye-Waller factor at low temperature.

Why we need low temperature? Beside scientific demands, low temperature can reduce the vibration between two adjacent atoms or lattice vibration so that the Debye-Waller factor decreases. Debye-Waller factor is used to describe the lattice disorder, which is arising from thermal motion of the atoms in the lattice or inherent lattice distortion. In the EXAFS oscillation equation (2.3.12), Debye-Waller factor σ^2 influences the intensity of EXAFS oscillation by term "$\exp(-2k^2\sigma^2)$", which means that intensity is strongly affected by Debye-Waller factor particularly in the large k range. Therefore, reducing the Debye-Waller factor can improve the quality of XAFS signal and is helpful to extract accurate structural information from EXAFS oscillation, especially for heavy scattering atoms.

A good example is shown in Figure 2.4.11, the XAFS measurements have been performed on Rh/γ-Al_2O_3 prepared from $Rh_2(OAc)_4$ precursors at room temperature (R.T.) and 25 K, respectively. Comparing the k^3-weighted χ(k) curves, the R.T. data is damped from the k ~ 9 (0.1 nm^{-1}) and becomes noisy, while the 25 K data keeps its density in this range.

2.5 EXAFS data analyses

The information about the local structure of absorbing atom such as element, number of surrounding atoms, their distances, and their MSRD (mean-square relative displacement from the absorbing atom) is included in the post edge oscillation region. Nowadays, it is routine to extract EXAFS oscillation curve from X-ray absorption spectra by using some softwares such as IFEFFIT, WinXAS, REX2000, etc. However, to obtain the reliable and accurate structural information from the oscillation is still difficult. Two important parameters: the backscattering amplitude $|f(\pi,k)|$ and phase shift functions ($2\delta_c(k)+\delta_a(k)$) are needed (see Eq. (2.3.8)). Although these parameters can be experimentally obtained from EXAFS spectra of standard sample, with respect to unknown materials, it may be still awkward.

Early in 1970s, the pioneering work was performed by Sayers, Stern and Lytle (1971).[20] They reported a simply point-scattering theory of XAFS, which gave excellent agreement with experimental structure, and successfully extracted structure information from experimental EXAFS data by using Fourier transform (FT). It is the beginning of the XAFS theory.

In the late 1970s, Teo and Lee (1979) published a tabulation of theoretically determined amplitude and phase shift functions by using a plane wave approximation for the scattering of the outgoing photoelectrons by the neighboring atom.[48] However, this approximation is unsatisfactory at low photoelectron momentum especially for heavy elements.

As an improvement, McKale (1988) performed the curved wave formalism to calculate these parameters and created a table containing nearly all the elements in the periodic table.[24] Even now, these McKale parameters are used for rough curve-fitting.

Nowadays, the most widely used calculation method is FEFF which is developed by Rehr in University of Washington.[49,50,51] FEFF uses an *ab intio* self-consistent real space multiple scattering (RSMS) approach for clusters of atoms (Z < 99). Calculations are based on an all-electron, real space relativistic Green's function. The method combines both full multiple scattering and a high-order path expansion.[52]

In this study, all of the EXAFS analyses were carried out by REX2000 (Rigaku CO.)[53] containing a FEFF 8.40 code. The EXAFS analysis steps and some examples of Rh foil reference sample will be introduced at following section.

2.5.1 Extraction of the EXAFS oscillation

Step1 Pre-edge subtraction

As shown in Figure 4.3.1, the pre-edge part is fitted with a linear function. Four functions can be chosen:

Victoreen 1: $(C\lambda^3-D\lambda^4+ Const.)$

Victoreen 2: $(C\lambda^3-D\lambda^4)$

Constant: Using value of Pre-Edge start

Least-Square: Using up to 6th degree polynomial equation.

Generally, Victoreen 1 can provide a good fitting curve.

The parameters P_S (Pre-edge start) and P_E (Pre-edge end) can be adjusted by a user.

Step 2 Edge step E_0

In REX2000 program, the edge energy E_0 is defined as a maximum of derivative $(d\mu/dE)$. E_0 will be used to determined wave number k for Fourier transform.

$$k = \sqrt{2m(E-E_0)/\hbar^2} \tag{2.5.1}$$

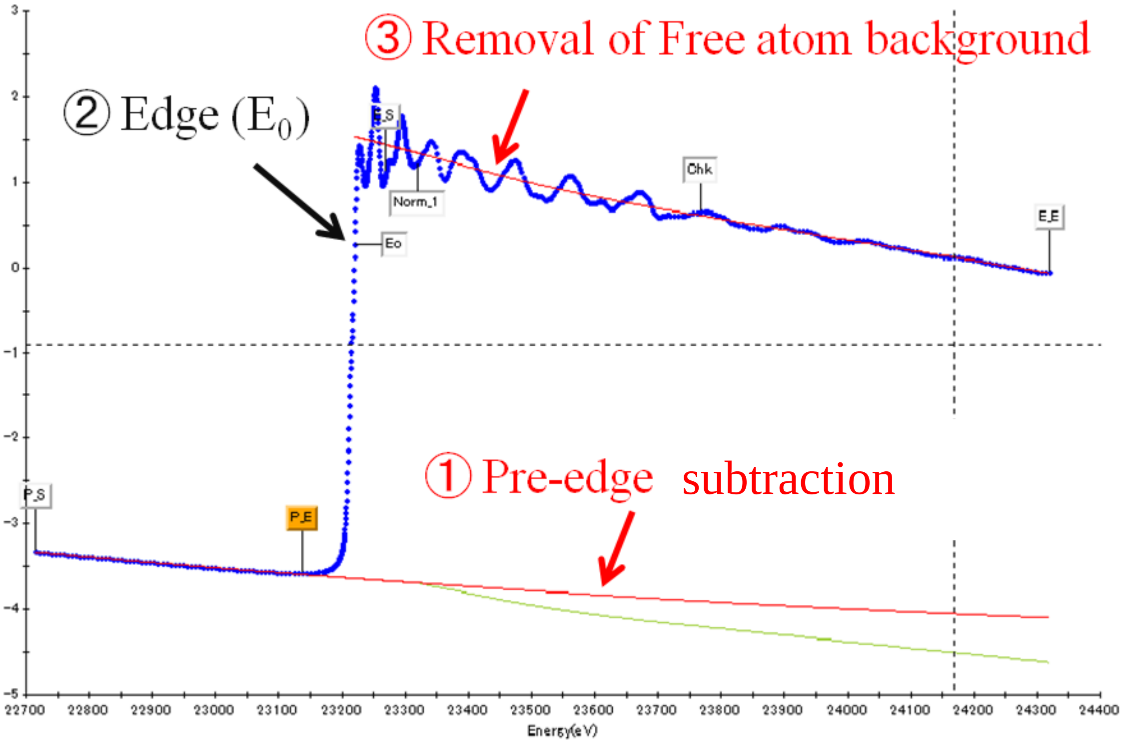

Figure 2.5.1 Extraction of EXAFS oscillation of a Rh foil reference. Three steps are shown here. ① Pre-edge subtraction, ② Edge (E_0) determination, ③ Removal of free atom background μ_0

Step 3 Removal of free atom background (μ_0)

In order to extract the EXAFS oscillation curve, the spectra μ_0 of isolated atom must be removed from X-ray adsorption spectra. The REX2000 program contains several procedures to find optimal free atom absorption $\mu_0(E)$. In this study, we used spline smoothing method, which minimizes of $FT(\chi(k))$ in the range from 0 to *rbkg* (an input parameter for this spline procedure). Others parameters such as: Fourier transform window, *k* range, *k*-weight, etc. are also adjustable, but do not affect the μ_0 a lot.

A good background removing is shown in Figure 2.5.1, the shape of which does not follow the EXAFS oscillation curve. In the REX2000, the EXAFS oscillation $\chi(k)$ is calculated according to the Eq. (2.5.2)

$$\chi(k) = \frac{\mu(E)-\mu_0(E)}{\Delta\mu_{obs}} \times \left|\frac{\mu(E_{edge})}{\mu(E)}\right| \tag{2.5.2}$$

The EXAFS oscillation $\chi(k)$ of Rh foil reference is shown in Figure 2.5.2(a). According to the Eq. (2.3.12) in Chapter 2, the $\chi(k)$ is in inverse proportion to k in the EXAFS equation and $|f(k)|$ is roughly dependent on the $1/k^2$, thus, the amplitude of $\chi(k)$ decays remarkably at high k region. Usually the function is weighted by a factor of k^n (n =1, 2, 3) to compensates for the $1/k^3$ dependence and to obtain more suitable function for the Fourier transformation. Note that the higher n is, the more emphasis on the contributions from heavier scatters since the scattering amplitude is in proportion to the atomic number Z. I n general, the factor k^3 is used for heavier elements. Figure 2.5.2(b) shows a $k^3\chi(k)$ of Rh foil reference for comparison.

2.5.2 Fourier transform

As mentioned above, the introduction of Fourier transform by Sayer and coworkers raised the curtain on the theory of XAFS. It is well known in mathematics that Fourier transform of a periodic oscillation function, either *sine* or *cosine* gives the delta function of the oscillation, and FT of a composite function of *sine* and *cosine* generates the delta functions of the corresponding frequencies.

In the EXAFS oscillation $\chi(k)$ equation, frequency k and distance r together determine the phase $2kr$, thus the Fourier transform of the oscillation function of either k or r will generate the other one as frequency. Furthermore, if the oscillation contains multiple frequencies, they can be separated into multiple peaks of delta functions. FT of EXAFS oscillation $\chi(k)$ is performed as

$$\Phi(r) = (2\pi)^{-1/2} \int_{k_{min}}^{k_{max}} W(k) \cdot k^n \cdot \chi(k) \cdot exp(-2ikr)\, dk \tag{2.5.3}$$

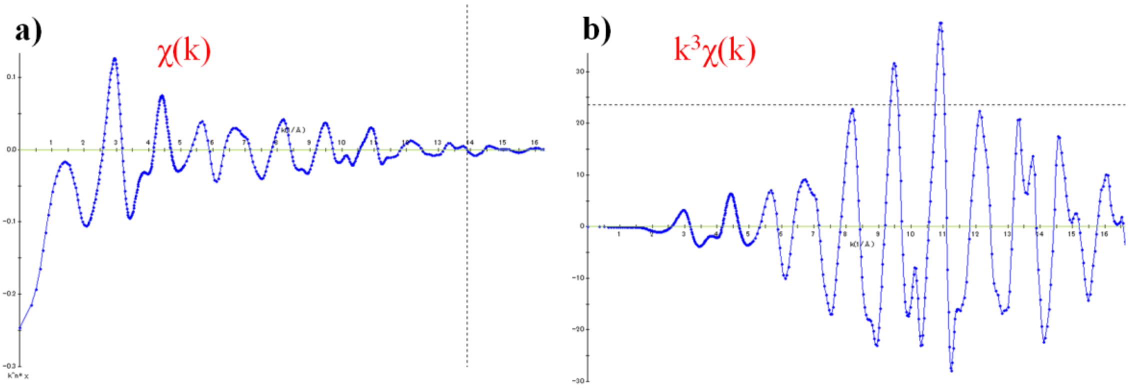

Figre 2.5.2 EXAFS oscillation of a Rh foil reference. **a)** $\chi(k)$ and **b)** k^3-weighted $\chi(k)$

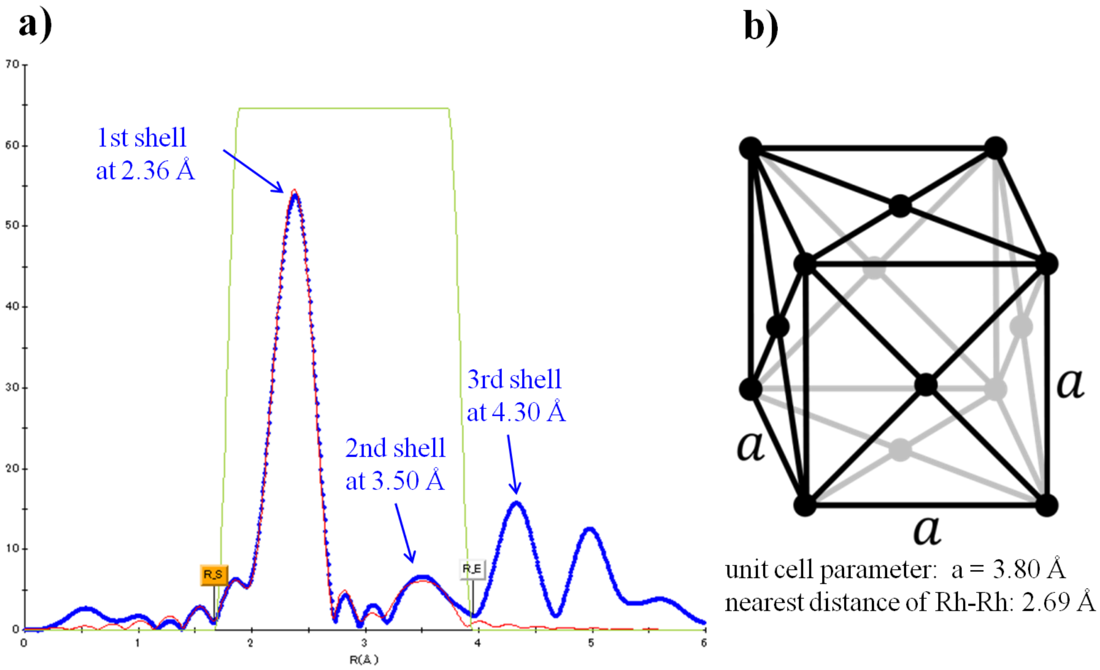

Figre 2.5.3 **a)** $|FT\ of\ k^3\chi(k)|$:Fourier transform of k^3-weighted EXAFS oscillation of the Rh foil reference without correction of phase shift (blue dotted line) and fitting curves for the first and second shell based on the phase shift and backscatter amplitude for experimental data. **b)** The unit cell of Rh single crystal. The cell parameter a is 3.80 Å, thus the nearest neighbor distance is 2.69 Å.[53] Fourier fitting range marked by green line is 1.16 ~ 3.95 Å. [54]

Due to the finiteness of k range in the XAFS measurements, the window function *W(k)* is used to zero-value outside of the chosen k range. The window function adopted in REX2000 is HANNING function:

$$W(k) = \begin{cases} \frac{1}{2}\left[1 - cos\left(\pi\left(\frac{k-k_{min}}{d}\right)\right)\right] & k_{min} < k < k_{min} + d \\ 1 & k_{min} + d < k < k_{max} - d \\ \frac{1}{2}\left[1 - cos\left(\pi\left(\frac{k_{max}-k}{d}\right)\right)\right] & k_{max} - d < k < k_{max} \end{cases} \tag{2.5.4}$$

Figure 2.5.3(a) shows the $|\Phi(r)|$ of Rh foil reference in the k range from 3 ~ 17 Å^{-1}. Generally, the range below 3 Å^{-1} is mainly attributed to the XANES region and the upper limit should be chosen as large as possible, which is dependent on quality of EXAFS oscillation. The larger k range is, the better separation of individual peak.

The position of peak corresponds to the average shell distance ant the peak height is related to the atoms and their coordination number in the shell, the disorder parameter Debye-Waller factor σ^2 and the window range chosen. Something must be noted here, *firstly,* there is difference between peak position in $|\Phi(r)|$ and the actual shell distance, the difference is usually about 0.2 ~ 0.5 Å. For an example, the first 3 peaks (at 2.38 Å, 3.50 Å, 4.35 Å) in $\Phi(r)$ arise from the nearest-neighbor shell (CN = 12, 2.69 Å), second shell (CN = 6, 3.80 Å) and third shell (CN = 12, 4.65 Å) in the rhodium FCC crystal structure shown in the Figure 2.5.3(b).[54] These deviations are due to the phase shift of photoelectrons as $\delta_c(k)$, $\delta_a(k)$ shown in the Eq. (2.3.12). Thus $|\Phi(r)|$ is not a true radial distribution function, it is usually called as phase-uncorrected radial distribution function by XAFS experts. *Secondly,* in $\Phi(r)$, the peaks at very short distance such as below 1 Å are usually neglected because they are originated from insufficient background subtraction. On the other hand, the peaks appeared at long distance like beyond 6 or 8 Å generally come from much higher frequency oscillation than real EXAFS features such as data noise and glitches in the original data. Thus, the most reliable and available part in the $\Phi(r)$ is in the r range from 2 to 6 Å. *Finally*, the $|\Phi(r)|$ can give an intuitive view about the local structure of absorbing atoms, however, actually, $\Phi(r)$ is a complex function, the real and imaginary parts of it are also useful, in some case they are more reliable than the modulus. The adjacent peaks can interfere with each other. The modulus of $\Phi(r)$ sometimes brings the false peaks and sometimes cause the overlap of two adjacent peaks. Some representative instances are shown in Figure 2.5.4 and Figure 2.5.5. [55]

First one is the simulation results of $GeSe_2$ $|\Phi(r)|$ at difference Ge-Se distance. All of the $|\Phi(r)|$ are phase-uncorrected, and the periodic oscillation curves are imaginary parts $\mathrm{Im}(\Phi(r))$. Figure 2.5.4(a) is a simulation result from $GeSe_2$ with 2 equivalent Ge-Se bonds (distance = 2.59 Å), both $|\Phi(r)|$ and $\mathrm{Im}(\Phi(r))$ reveal that only one peak exists at 2.32 Å. Thus the phase shift is about 0.27 Å. Then, one of Ge-Se is fixed to 2.59 Å, while the other is changed to various values. Figure 2.5.4(b) shows the situation of $r_{Ge\text{-}Se}$ = 2.69 Å, only one peak can be observed, however, the position shift to 2.36 Å (corrected value: 2.63 Å), which is the average value of two distances. However, when the $r_{Ge\text{-}Se}$ is changed to 2.74 Å. Two peaks appear at 2.19 Å (2.46 Å) and 2.65 Å (2.93 Å) in the $\Phi(r)$, while in the $\mathrm{Im}(\Phi(r))$, a main peak appears at 2.32 Å (2.59 Å) with a shoulder at 2.47 Å (2.74 Å) which are corresponding to the model. Thus, the two peaks appeared in the $\Phi(r)$ are false peaks. Moreover, when the $r_{Ge\text{-}Se}$ is changed to 2.89 Å, only a broad single peak with average distance of 2.42 Å (2.69 Å) is observed in the $\Phi(r)$, while two separated peaks at 2.32 Å(2.59 Å) and 2.62 Å (2.89 Å) have been already distinguished in the $\mathrm{Im}(\Phi(r))$ (Figure 2.5.4(e)). Unit one Ge-Se bond is extended to 3.09 Å (about 0.5 Å larger than original one), two distinguished peaks appeared at 2.32 Å(2.59 Å) and 2.82 Å(3.09 Å) in the $\Phi(r)$ become to be in agreement with the model.

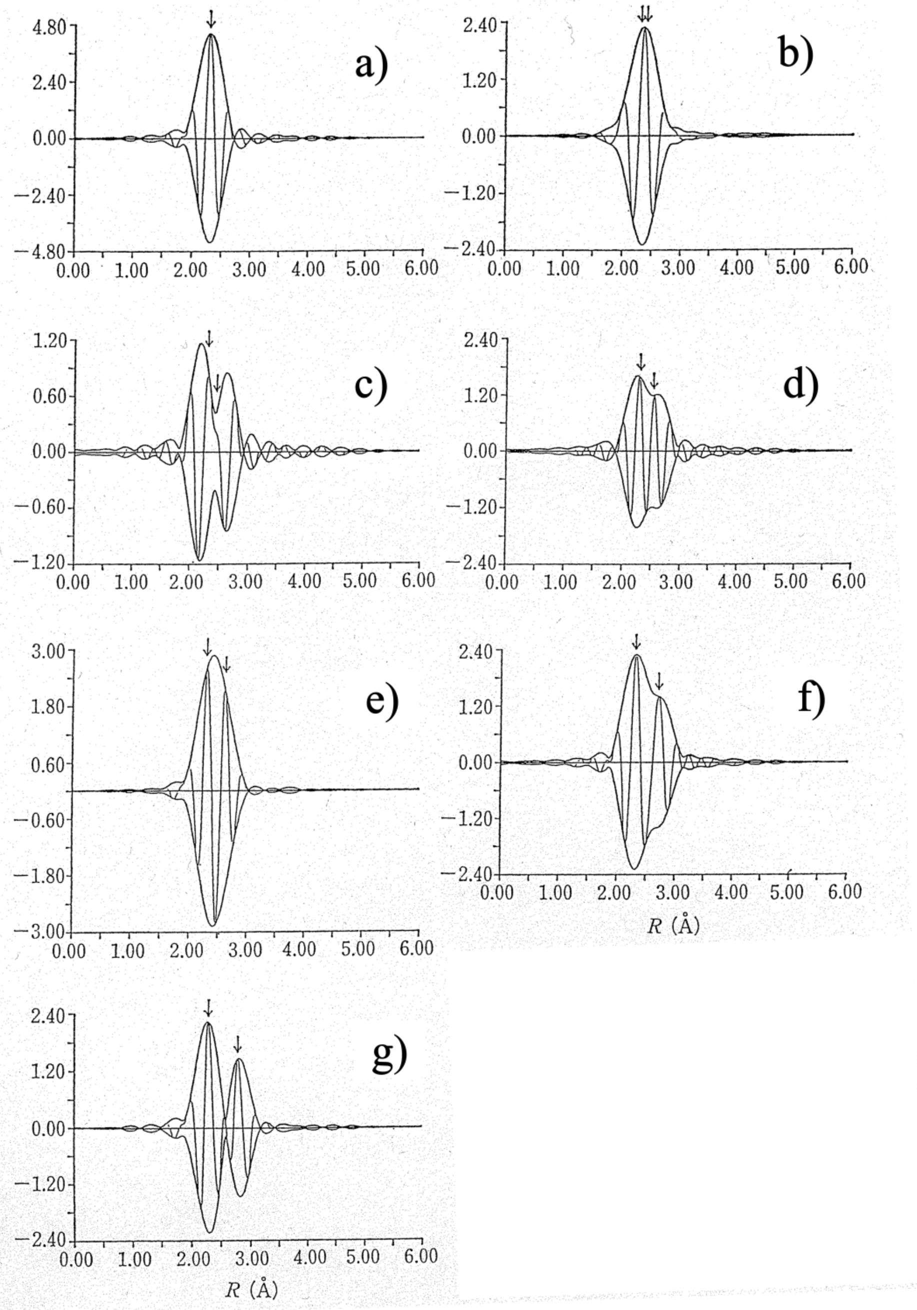

Figure 2.5.4 The simulation of $|\Phi(r)|$ of $GeSe_2$ with various Ge-Se bond length. One Ge-Se bond is fixed at 2.59 Å, and the other one is changed to following values a) 2.59 Å (two equivalent bonds), b) 2.69 Å, c) 2.74 Å, d) 2.79 Å, e) 2.89 Å, f) 2.99 Å, g) 3.09 Å. All of the $\Phi(r)$ are phase-uncorrected. The periodic oscillation curves are imaginary parts $\mathrm{Im}(\Phi(r))$. The corresponding Ge-Se distances (real distance – phase shift) are marked by arrows. [55]

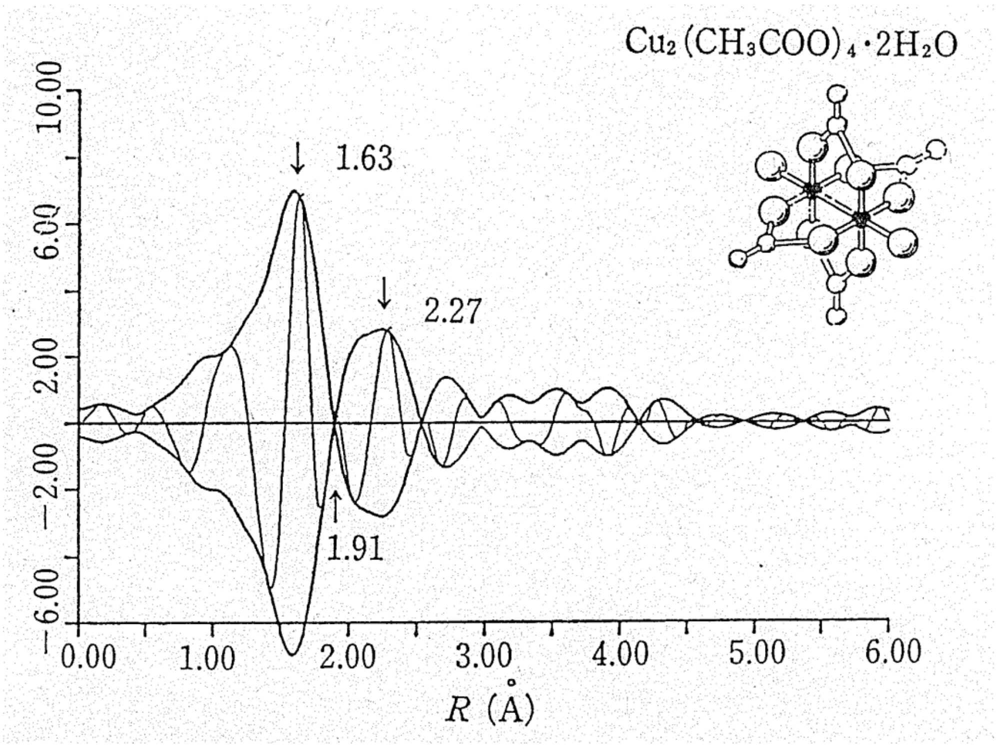

Figure 2.5.5 The phase-uncorrected $|\Phi(r)|$ and imaginary parts $\mathrm{Im}(\Phi(r))$ of $Cu_2(OAc)_4 \cdot 2H_2O$. The peaks at 1.63 Å, 1.91 Å, 2.27 Å marked by arrows in the $\mathrm{Im}(\Phi(r))$ correspond to the Cu-O_{ac} (1.97 Å), Cu-O_{OH} (2.20 Å) Cu-Cu (2.64 Å), respectively. Molecular model is shown in the inset. [55, 56]

Figure 2.5.5 shows experimental results of $Cu_2(OAc)_4.2\ H_2O$. Two kinds of Cu-O bonds exist in this molecule. Cu-O of acetate ligand is about 1.97 Å and the ones of H_2O ligand is about 2.20 Å, the Cu-Cu bond is around 2.64 Å. As shown in the $\Phi(r)$, only two peaks can be observed, the first one with distance of 1.63 Å belongs to Cu-O bond. However, in the $\Phi(r)$, besides the large peaks attributed to Cu-O_{ac} of acetate ligand, a small one at 1.91 Å can also be distinguished, which is attributed to Cu-O_{OH} of water ligand.

All of these instances mean the $\mathrm{Im}(\Phi(r))$ always can give the correct information of coordination condition of absorbing atoms, while the $\Phi(r)$ sometimes brings the false information, in spite of its intuitive view about the local structure. It should be paid more attention during the analyses on $\Phi(r)$.

2.5.3 Curve fitting

The key step in curve fitting is how to determine the phase shift and backscattering amplitude. McKale table is very useful for rough fitting, but is not suitable for accurate analysis. There is two methods to determine the phase shift and backscattering: 1) Extract these parameters from an appropriate reference sample; 2) Calculate by FEFF code basing on structure model. The former method will be introduced in this section.

This method is to extract phase shift and backscattering from EXAFS data of some standard samples. REX2000 offers a program called "Reference Sample" to achieve this process. Figure 2.5.6(a)-(c) show phase shift and backscattering amplitude of Rh foil firs three shell. Once these parameters for the appropriate shells are determined, EXAFS oscillation will be calculated by following formula: [53]

$$\chi(k)_{fit} = \sum_i \frac{N_i|f(k,\pi)|\, exp\left(-2\sigma^2 k^2 + \frac{2}{3}C_4 k^4\right) exp\left(-\frac{2R_i}{\lambda_i}\right) sin\,(2kR_i + \phi_i(k) - \frac{4}{3}C_3 k^3)}{kR_i^2} \tag{2.5.5}$$

where the definition of most symbols are same as before, the $\phi_i(k)$ is phase shift consisted of absorber and scatter parts. C_n are the cumulant coefficients of k^n which are usually used to correct the EXAFS oscillations of disorder systems (with non Gaussian distributions) such as liquid metals, but in ordered systems, the C_n (n≧3) are generally zero. Thus, C_n cannot be considered in this study. To find best fitting curve $\chi(k)_{fit}$, a program evaluates values of various parameters: N_i, σ^2, R_i, $\phi_i(k)$ in Eq. (4.3.5), to find minimum misfit between experimental data $\chi(k)_{data}$ and calculation results $\chi(k)_{fit}$. The misfit factor called R_{rex} factor can be calculated as follows: [24]

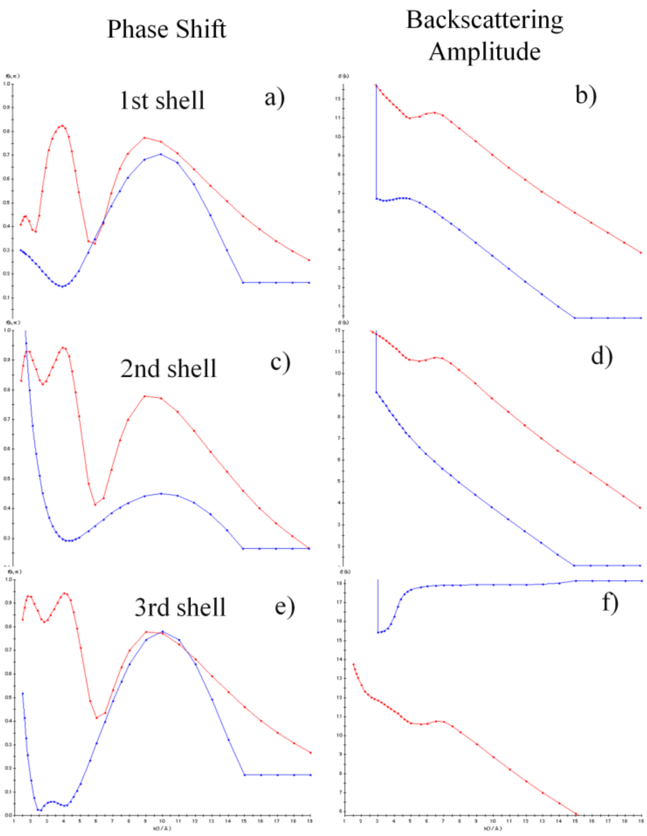

Figure 2.5.6 The phase shifts **a), c)**, **e)** and backscattering amplitudes **b)**, d), **f)** for 1st, 2nd, 3rd shell of Rhodium fcc crystal structure, respectively. The red lines are Mckale calculation data, and the blue lines are experimental data from the reference sample Rh foil.

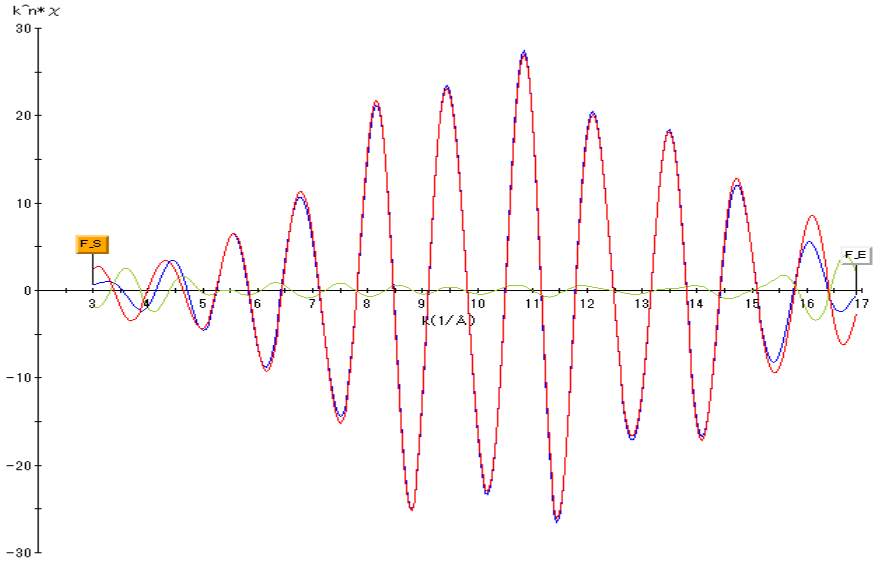

Figure 2.5.7 The curve fitting result of Rh foil $|\Phi(r)|$. A Red line is a fitting curve calculated by Eq. (2.5.5) and a blue line is an experimental results. The difference between them is shown by a green line. The R factor is about 0.6 %.

$$R_{rex} = \frac{\Sigma_1^N [Im(\chi(k)_{data} - \chi(k)_{fit})]^2 + [Re(\chi(k)_{data} - \chi(k)_{fit})]^2}{\Sigma_1^N \left[Im((\chi(k)_{data})]^2 + [Re(\chi(k)_{fit})] \right]^2} \qquad (2.5.6)$$

where N is the number of points in the fitting range of the data. In general, the value of R factor should be less than 1 for a reliable fitting.

Figure 2.5.7 shows the fitting result of first two shells in Rh foil, the R factor is about 0.83%, and the CN and distance values are listed in Table 2.5.1.

Table 2.5.1 Curve-fitting results of first two shells in Rh foil

Rh foil	**Bond**	**CN**	**Distance (Å)**	R_{rex} **%**
1st shell	Rh-Rh	11.3 ±1.8 (12)*	2.68 ±0.01 (2.69)	0.83
2nd shell	Rh-Rh	4.1 ±2.0 (6)	3.81 ±0.01 (3.80)	

* The values in parentheses are the reference values based on the Rh fcc crystal model.

The distance of individual shell is very close to the Rh fcc crystal model, however the coordination numbers have wide errors. Especially, for the second shell, the calculation value is quite smaller than the reference value. In REX 2000 program, four parameters ***N, R, ΔE,*** $\boldsymbol{\sigma^2}$ are used to find best fitting curve. However, these parameters correlate with each others, such as coordination number and Debye-Waller factor which affect the amplitude. These correlations sometimes cause large uncertainties of fitting results Thus, in order to determine the local structure of absorber correctly, some additional constraints need be imposed, such as fixing some parameters (Detailed discussion will be given in the following section)..

4.3.4 FEFF calculation

FEFF code calculates the theoretical EXAFS oscillation χ(k) for a given structure. The first step is to construct an appropriate model structure basing on rough curve fitting for unknown sample, or to search structural information from crystal database (e.g. ICSD, CCDC). Next the "muffin-tin" potential for each atom type is calculated as a scattering potential by program. Then, the scattering amplitude of the photoelectron can be determined. Similar to discussion in Section 2.3, not only single scattering but also multiple scatterings are calculated. And the energy loss due to the phonon vibrations and other interaction are also considered in FEFF code. The results of the FEFF calculation are containing terms of the effective scattering amplitude, phase shift and mean free path of the photoelectron as a function of wave number for every possible scattering path of the photoelectrons.

$$\chi(k)_{FEFF} = \sum_{\Gamma} Im\,(\chi_{\Gamma}(k)) \tag{2.5.7a}$$

$$\chi_{\Gamma}(k) = \frac{\boldsymbol{N_{\Gamma}} \boldsymbol{S_0^2} F_{\Gamma}(k)}{k \boldsymbol{R_{\Gamma}^2}} exp\left(-2\boldsymbol{\sigma_{\Gamma}^2} k^2 - \frac{2\boldsymbol{R_{\Gamma}}}{\lambda} + \frac{2}{3}\boldsymbol{C_4} k^4\right) exp\,(2k\boldsymbol{R_{\Gamma}} + \phi_{\Gamma}(k) - \frac{4}{3}\boldsymbol{C_3} k^3) \tag{2.5.7b}$$

$$\boldsymbol{R_{\Gamma}} = R_0 + \boldsymbol{\Delta R_{\Gamma}} \tag{2.5.7c}$$

$$k = \sqrt{k_0^2 - \boldsymbol{\Delta E_{\Gamma}} \frac{2\mathrm{m}}{\hbar^2}} \tag{2.5.7d}$$

where Γ is the scattering paths. $F_{\Gamma}(k)$ and $\phi_{\Gamma}(k)$ are backscattering amplitude and total phase shift calculated by a given structure. The symbols in **bold** type $\boldsymbol{N_{\Gamma}}$, $\boldsymbol{S_0^2}$, $\boldsymbol{\sigma_{\Gamma}^2}$, $\boldsymbol{C_3}$, $\boldsymbol{C_4}$, $\boldsymbol{\Delta R_{\Gamma}}$, and $\boldsymbol{\Delta E_{\Gamma}}$ are seven fitting parameters, which are usually called **path parameters**. The structural information is contained in these parameters.

< Path parameters >

Eqs. (2.5.7a~d) are very similar to the XAFS oscillation equation, but a few difference from it. Number of atoms in each path $\boldsymbol{N_{\Gamma}}$, amplitude of oscillation $\boldsymbol{S_0^2}$, Debye-Waller factor $\boldsymbol{\sigma_{\Gamma}^2}$, and cumulant coefficients $\boldsymbol{C_3}$, $\boldsymbol{C_4}$ have been already discussed previously. Only new parameters $\boldsymbol{\Delta R_{\Gamma}}$, and $\boldsymbol{\Delta E_{\Gamma}}$ are interpreted here. In (2.5.7c), R_0 is the half path length calculated from structural information given as input to FEFF. The $\boldsymbol{\Delta R_{\Gamma}}$ represents a change in the half path length, meaning change of the radial distance (scatter and absorber) in Γ path. And $\boldsymbol{\Delta E_{\Gamma}}$ refers to an energy shift. In (2.5.7d), k_0 corresponds to the E_0 chosen to be the energy of edge step. Thus, $\boldsymbol{\Delta E_{\Gamma}}$ is a difference between experimentally determined photoelectron kinetic energy zero and that used for the theoretical calculation for phase shift and backscattering amplitude functions of the Γ scattering path.

Generally, these seven parameters are used to fitting the experimental results. As mentioned above, in this study, cumulant coefficients $\boldsymbol{C_3}$, $\boldsymbol{C_4}$ for disorder systems are not needed. Thus, $\boldsymbol{N_{\Gamma}}$, $\boldsymbol{S_0^2}$, $\boldsymbol{\sigma_{\Gamma}^2}$, $\boldsymbol{\Delta R_{\Gamma}}$, and $\boldsymbol{\Delta E_{\Gamma}}$ will be discussed in the following section. It is worthy to note that $\boldsymbol{N_{\Gamma}}$ and $\boldsymbol{S_0^2}$ are proportionalities for the amplitude of $\chi_{\Gamma}(k)$ in whole k range, while $\boldsymbol{\sigma_{\Gamma}^2}$ is coefficient for exponential function. It means $\boldsymbol{\sigma_{\Gamma}^2}$ mainly effect amplitude at high k region.

< Parameter correlations >

Some path parameters have similar effects to other ones. As mentioned above, both coordination number and amplitude can alter the EXAFS oscillation magnitude uniformly as a function of *k*. Changing the $\boldsymbol{\sigma_{\Gamma}^2}$ also affects the amplitude, but it has a greater effect at high *k* than low *k*. The similar effect of these parameters implies that they are correlated. A similar correlation is also observed between $\boldsymbol{\Delta R_\Gamma}$ and $\boldsymbol{\Delta E_\Gamma}$. Both of them affect the slope of the phase, but in different ways. The shorter the range of data in k space, the more significantly they will be correlated.

These correlations cause large uncertainties in the parameter errors. You do not know how to select accurate balance of these correlated parameters which are corresponding to the real structures. As shown above, general fitting method is to adjust all of these parameters to find best fitting curve $\chi(k)_{fit}$ which has minimal mismatch with the experimental data. However, due to the correlations, a good fitting is not equivalent to a correct result, sometimes the fitting is ill-determined.

In order to obtain accurate information by curve-fitting, some parameters should be pre-determined at first, and fixed as constant during the FEFF calculation.

< Real space model method >

The real space model method was developed by Chun and coworkers, [57] and has been successfully applied in a lot of XAFS data analysis. The process can be described as:

1) ***Model building*****:** first step is to speculate some probable model structures according to the roughly fitting results, XANES, and other information (e.g. XPS, STM, IR etc.).

2) ***Calibration*****:** this step is to determine $\boldsymbol{S_0^2}$, $\boldsymbol{\sigma_\Gamma^2}$ by FEFF fitting of some reference materials which are similar to expected models structures. Because the structures of reference materials are known, the coordination number and bond length are fixed as constants. An example of Rh foil calibration will be shown below.

3) ***Comparison*****:** Calculate theoretical EXAFS oscillation $\chi(k)_{cal}$ of every model structure when $\boldsymbol{S_0^2}$, $\boldsymbol{\sigma_\Gamma^2}$ are fixed as constant and compare them with experimental data. Adjust the interatomic distances in a reasonable range to find best-fitting structure. The evaluation factor of mismatch between theoretical and experimental curve is calculated according to next equation:

$$R = \sqrt{\frac{\Sigma(\chi(k)_{data} - \chi(k)_{cal})^2}{\Sigma(\chi(k)_{data})^2}} \qquad (2.5.8)$$

where N is data number. The distribution of measurement errors is a normal distribution with variance errors, the error function consists of a sum of N random normal deviates of zero mean and unit variance, which follows a χ-square distribution.

4) *Optimization*: final step is the fine adjustments of $\boldsymbol{S_0^2}$, $\boldsymbol{\sigma_r^2}$ in permitted ranges in order to obtain the best fitting result.

< Example: Rh foil calibration >

The bulk Rhodium has fcc crystal structure with the nearest shell at 2.69 Å with 12 Rh atoms, second shell (6 atoms, 3.80 Å), third shell (12 atoms, 4.65 Å)…… All of Rh atoms positions can be estimated by *Atom program*. Then, the FEFF input file (feff.inp) can be created. The calculation result and experimental data are shown in Figure 2.5.8(a), where the default value of each parameter is used: $\boldsymbol{S_0^2} = 1.00$, $\boldsymbol{\sigma^2}$ (SIG2) $= 0.0060$. And other parameter RPATH is set to 6 Å and EXCHANGE (Vr) has been optimized to -4. The shape of calculation result is very similar to the experimental data, especially in the low k range, the amplitude is almost same. However in the high k range, the amplitude of calculation damps quickly. It suggests that $\boldsymbol{\sigma^2}$ (SIG2) is too large. Thus, we just need to reduce the $\boldsymbol{\sigma^2}$ (SIG2) and adjust $\boldsymbol{S_0^2}$ slightly so as to keep the amplitude in the low k range unchanged. The best fitting result is shown in Figure 2.5.8(b), the $\boldsymbol{S_0^2} = 0.78$, $\boldsymbol{\sigma^2}$ (SIG2) $= 0.0038$.

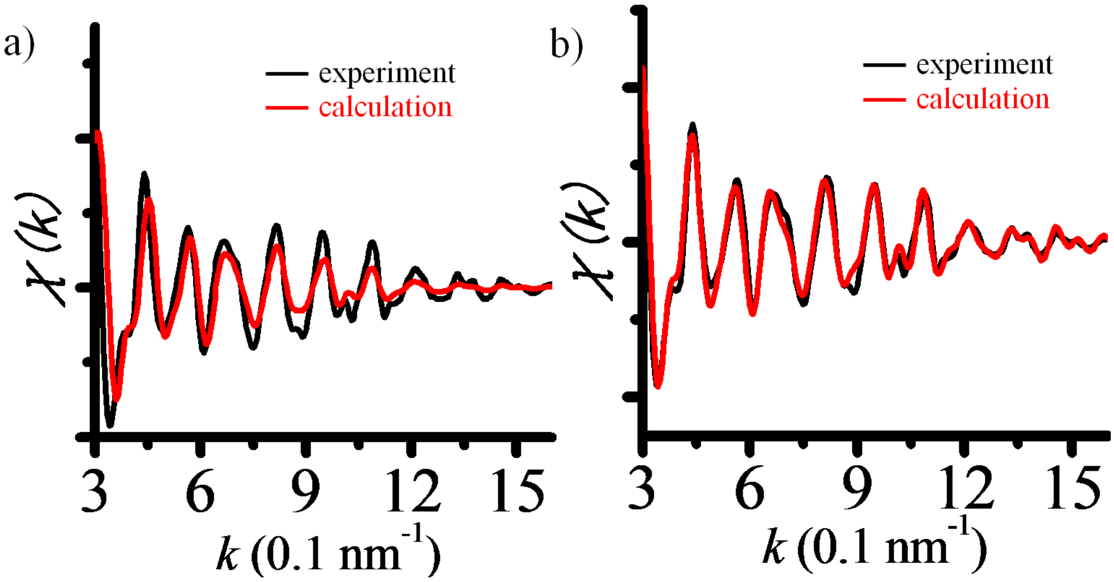

Figure 2.5.8 FEFF calculation results of bulk Rh (red) and experimental data of Rh foil (black). **a)** before and **b)** after optimization of the path parameter. The best fitting result is obtained, when $S_0^2 = 0.78$, σ^2 (SIG2) = 0.0038.

2.6 Pulse Valve method

In order to deposit precursor molecules onto well-ordered oxide thin film surface under UHV condition, pulse valve method was adopted in this study. As mentioned briefly in Chapter 1, this method was developed by Kawai and coworkers.[58] They injected a small amount of solution containing DNA molecules onto Cu(111) surface in vacuum through a pulse valve and successfully image DNA by STM (Figure 2.6.1).

The concept of this method is very simple, volatile solvent such as H_2O, C_2H_5OH, CH_2Cl_2, $C_6H_5CH_3$……) just act as carriers to take the target compounds onto the substrate surface, then solvent will be evacuated. Due to the injection of solution, this method can be applicable to different kinds of precursors. This method has been successfully applied to deposition of various compounds and such as DNA/RNA,[59] conducting polymers,[60] CdSe nanodevices,[61] Ag nanotube[62] and so on.

As shown in Figure 2.6.2, a pulse valve has a valve body with a valve nozzle and a coil assembly. Inside the coil assembly, a movable valve operating part called “armature” with a poppet is disposed in axial alignment with the valve body for opening and closing the valve. The position of armature is controlled by two springs (main spring and buffer spring) and electromagnetic force F_{EM} arising from applied pulse voltage. Thus, the state of valve can be described by

$$Valve = \begin{cases} Open & F_{EM}(t) + f_b(x_b) > f_m(x_m) + mg \\ Closing & f_b(x_b) < f_m(x_m) + mg \end{cases} \qquad (2.6.1)$$

where $f_b(x_b)$, $f_m(x_m)$ are elastic forces of main spring and buffer spring, respectively. Therefore, valve opening period depends upon the duration time of pulse voltage.

In this study, the orifice diameter of pulse valve (Parker Hannifin) is about 1.6 mm and the minimum duration time is 160 μs. The experimental setup is shown in Figure 2.6.3.

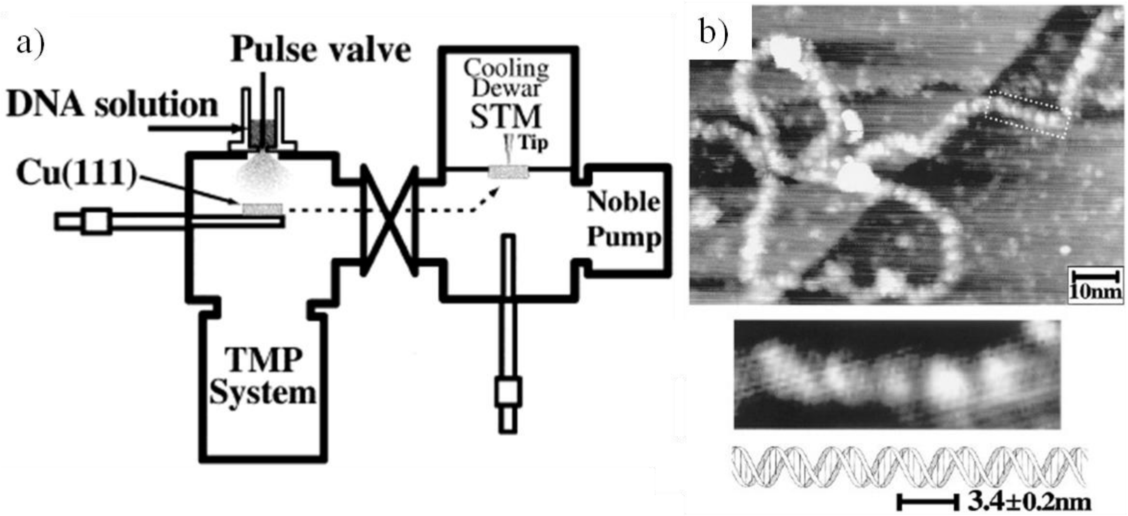

Figure 2.6.1 **a)** Pulse valve setup in Prof. Kawai's experiments. **b)** High resolution STM images of DNA molecule deposited on Cu(111) surface by pulse valve method and its structural model.[59]

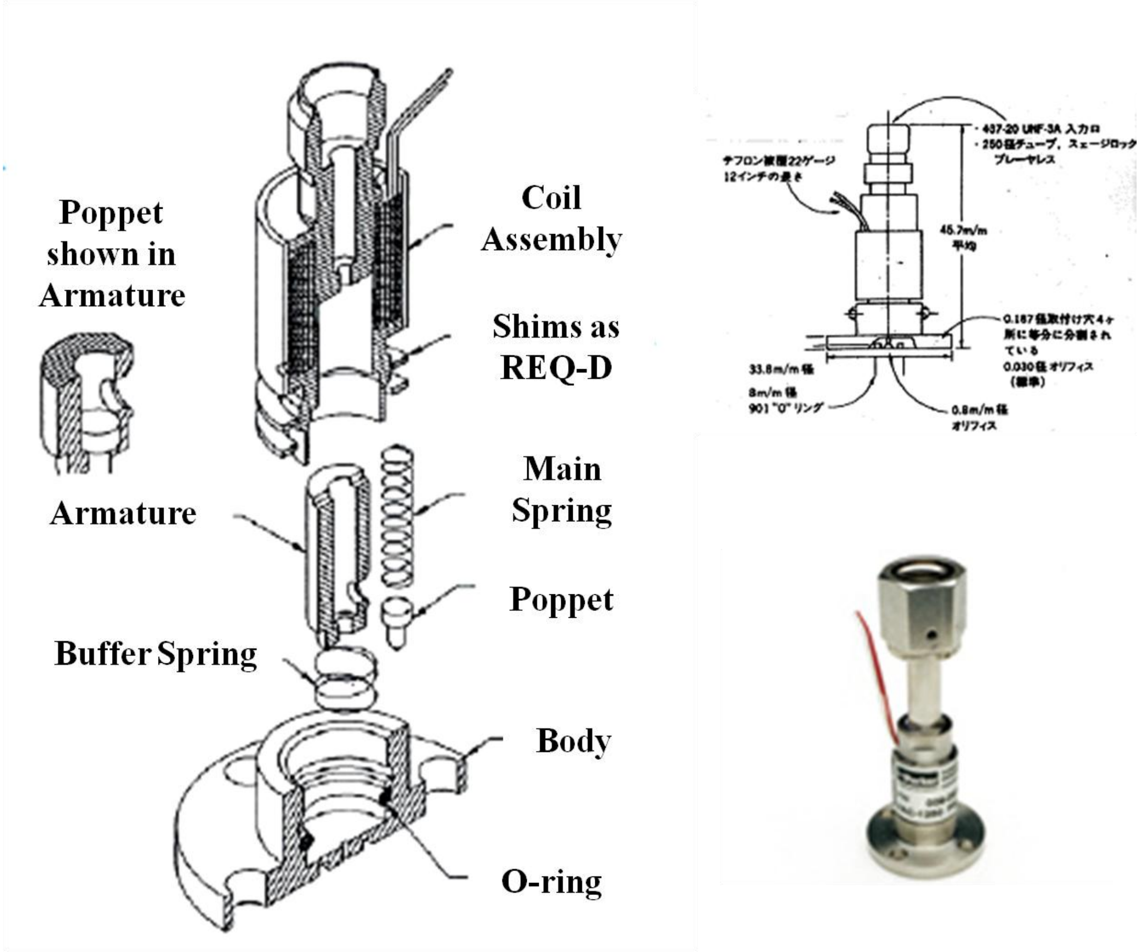

Figure 2.6.2 Illustration of pulse valve inside structure.

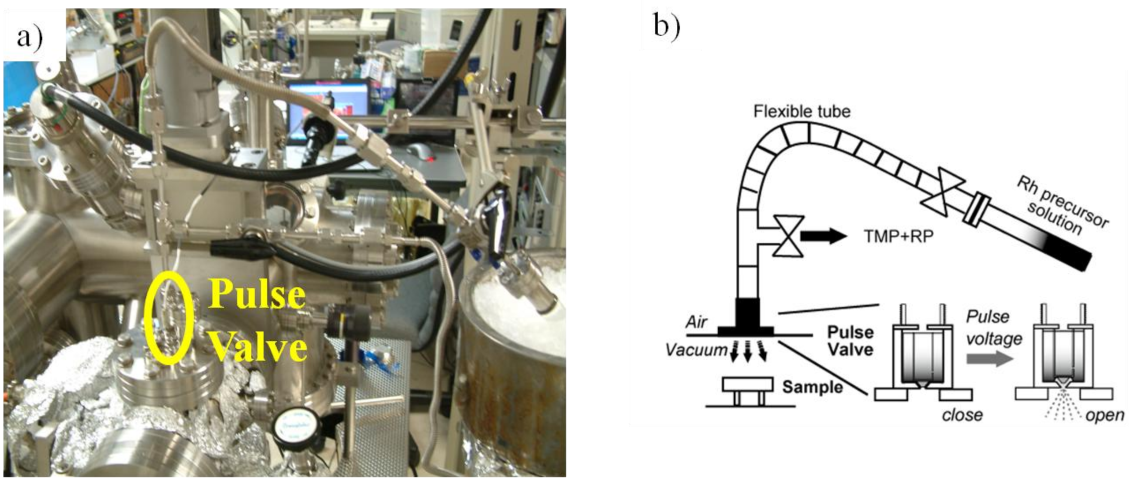

Figure 2.6.3 Pulse valve setup in this study. **a)** Photo and **b)** schematic of the pulse-deposition method. After degassing a solution containing a precursor, it is introduced to the pulse valve through a flexible tube. The pulse valve opens for a short time by applying voltage pulse of controlled duration and repetition and the solution is sprayed through the vacuum to the substrate surface.

Dilute precursor solution was prepared under N_2 atmosphere in a globe box and then sealed into Pyrex-glass ampoule with a bellows sealed valve. Then, the Pyrex-glass ampoule was connected to pulse valve set as shown in Figure 2.6.3. The solution was degassed by freeze-pump-thaw cycles. After degassing, a fraction of precursor solution was transferred to the pulse valve through the flexible tube. Then, the pulse valve was opened several times to deposit the precursor onto substrate.

The deposition amount is dependent on the opening duration time, pulse number, orifice diameter, solution concentration, solvent viscosity, distance between the substrate and pressure difference between the chamber and atmosphere and other inherent factors from the pulse valve. For simplicity, we only consider main factors such as pulse number N, duration time t, nozzle size S_{nozzle}, solution concentration C, pressure difference (P_{atm} and $P_{chamber}$), and assume that all of injected precursor molecules are deposited onto the substrate surface. Then, the

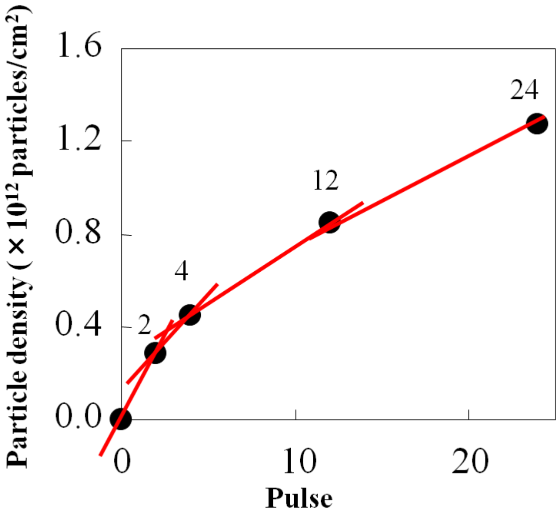

Figure 2.6.4 Plot of deposition $Rh_2(OAc)_4$ particle density versus pulse number. The $Rh_2(OAc)_4$ aqueous solution (2×10^{-5} mol/l) was injected on to Al_2O_3/NiAl(110) surface by pulse valve with 2, 4, 12, 24 pulses (duration time = 170 μs). The particle number was counted from STM images [63]

deposition amount can be described as

$$\rho S_{\text{sample}} = \frac{N}{2\text{m}}(P_{atm}S_{atm} - P_{chamber}S_{nozzle} + mg) \times t^2 \times S_{nozzle} \times C \qquad (2.6.2)$$

Fujita [63] has checked the correlation between the deposition $Rh_2(OAc)_4$ particle density and pulse number by a series of experiments and found the particle density is nearly in proportion to the pulse number under condition of duration time = 170 μs and concentration = 2×10^{-5} mol/l.

References

1 Operating Manual of Oxford-UHV-STM

2 C. L. H. Devlin, D. N. Futaba, A. Loui, J. D. Shine, S. Chiang. *Mater. Sci. Eng. B,* 2002 **96**, 215.

3 S. Behler, M. K. Rose, J. C. Dunphy, D. F. Ogeltree, M. Salmeron, C. Chapelier *Rev.Sci. Instrum,* 1997, **68**, 2479.

4 G. Binnig, H. Rohrer, Ch. Gerber, E. Weibel, *Appl. Phys. Lett.* 1982, **40**, 178.

5 G. Binnig, H. Rohrer, Ch. Gerber, E. Weibel, *Phys. Rev. Lett.* 1982, **49**, 57.

6 J. C. Chen, "*Introduction to Scanning Tunneling Microscopy"*, Oxford University Press, New York, 1993.

7 C. Bai, "*Scanning Tunneling Microscopy and Its Application (Springer Series in Surface Sciences)"*, 2nd edition, Springer; Shanghai, 2000.

8 M. Bowker and P. R. Davies, "*Scanning Tunneling Microscopy in Surface Science, Nanoscience and Catalysis"*, Wiley-VCH Verlag GmbH, 2010.

9 http://nobelprize.org/nobel_prizes/physics/laureates/1986/

10 J. Tersoff and D. R. Hamann, *Phys. Rev. B,* 1985 **31**, 805.

11 J. W. Niemantsverdiet, "S*pectroscopy in Catalysis- An introduction 3rd, Completely Revised and Enlarged Edition"*, Wiley-VCH Verlag GmbH, 2007.

12 日本表面科学会 編, X 線光電子分光法, 表面分析技術選書, 丸善株式会社. 1998

13 H.J. Borg, L. C. A. Oetelaar, J. W. Niemantsverdriet, *Catal. Lett.* 1993, **17**, 81.

14 W. Kossel, *Z. Phys.,* 1920, **1**, 119.

15 R. Kronig, *Z. Phys.,* 1931, **70**, 317.

16 R. Kronig, *Z. Phys.,* 1932, **75**, 468.

17 R. Kronig, *Z. Phys.*, 1932, **80**, 203.

18 T. Shiraiwa, T. Ishimura, M. Sawada, *J. Phys. Soc. Jpn*, 1958,**13**, 847.

19 L. V. Azaroff, *Rev. Mod. Phys.* 1963, **35**, 1012.

20 D. E. Sayers and E. A. Stern, *Phys. Rev. Lett.* 1971, **27**, 1204.

21 W. L. Schaich, *Phys. Rev. B.* 1976, **14**, 4420.

22 P. H. Citrin, P. Eisenberger, B. M. Kincaid, *Phys. Rev. Lett.* 1976, **36**, 1346.

23 B. K. Teo, and P. A. Lee, *J. Am. Soc. Chem.*, 1979, **101**, 2815.

24 A. G. McKale, B. W. Veal, A. P. Paulikas, S. K. Chan, G. S. Knapp, *J. Am. Soc. Chem.*, 1988, **110**, 376.

25 K. O. Hodgson, B. Hedman, J. E. Penner-Hahn . "*EXAFS and Near Edge Structure (III): proceedings of an international conference, Stanford, CA, July 16-20, 1984"* Springer-Verlag, Berlin 1984.

26 B. K. Teo, "*EXAFS: Basic Principles and Data Analysis", *Springer-Verlag, Berlin, 1986

27 M. Newville, P. Livins, Y. Yacoby, J. J. Rehr, E. A. Stern, *Phys. Rev. B.* 1993, **47**, 14126.

28 B. Ravel and M. Newville, *J. Synchrotron Rad.*, 2005, **12**, 537.

29 V. Prochazaka, PhD Thesis. " *Study of cobaltites and maganites by NMR and EXAFS*" Charles University in Prague & AGH University of Science and Technology 2009

30 S. D. Kelly, PhD Thesis. " *XAFS Study of the pressure induced B1→B2 phase transition*" University of Washington, 1999

31 FEFF8 Manual.

32 野村昌治, 「XAFS 実験ステーション利用の手引」.2001

33 M. Nomura, Y. Koike, M. Sato, A. Koyama, Y. Inada, K. Asakura, *X-RAY ABSORPTION FINE STRUCTURE - XAFS13: 13th International Conference. AIP Conference*

Proceedings, 2007, **882**, 896.

34 M. Nomura, *KEK Prog. Rep.*, 2006, **3**, 82.

35 T. Ohta, P. M. Stefan, M. Nomura, H. Sekiyama, *ibid. A.*, 1986, **246**, 373.

36 T. Matsushita, T. Ishikawa, H. Oyanagi, *Nul. Instrum. Methods A*, 1986, **246**, 377.

37 M. Nomura and A. Koyama. *Nul. Instrum. Methods A*, 2001, **467**, 733.

38 http://pfwww.kek.jp/inada/xafsbl/nw10a/nw10a.html

39 X. Liu, PhD Thesis, "*Photoluminescence and Extended X-ray Absorption Fine Structure Studies on CdTe Material*", The University of Toledo, 2006.

40 P. A. Lee, et.al., *Rev. Mod. Phys.*, **53**, (1981), 769.

41 S. S. Hasnain, P. D.Quinn, G. P. Diakun, E. M. Wardell, C. D. Garner, *J. Phys. E: Sci. Instrum*, 1984, **17**, 40.

42 J. Jaklevic, et.al. *Solid State Comm.*, **23**, (1977), 679.

43 V. G. Harris and W. T. Elam, *Rev. Sci. Instrum*, 1997, **68**, 1972.

44 野村 昌治, 「電離箱、多素子SSDのXAFSへの応用」1999 http://pfwww.kek.jp/nomura/pfxafs/detector/pfktext.pdf

45 Glenn F. Knoll, *Radiation Detection and measurement*, J. Wiley, New York, 3rd Ed., Table 11.1, 2000.

46 K. Zhang, G. Rosenbaum , G. Bunker. *Jpn. J. Appl. Phys.Suppl.* 1993, **32**, 147.

47 M. Nomura, *J. Synchrotron Rad.* 1998, **5**, 851.

48 B. K. Teo and P. A. Lee, *J. Am. Soc. Chem.* 1979, **101** 2815.

49 A. L. Ankudinov, B. Ravel, J. J. Rehr, S. D. Conradson, *Phys. Rev. B* 1998, **58**, 7565.

50 B. Ravel, "*Introduction to EXAFS Experiments and Theory*" Text for EXAFS analysis workshop, 2000. http://cars9.uchicago.edu/~ravel/talks/course/Welcome.html

51 J.J. Rehr, A. L. Ankudinov, and B. Ravel, *FEFF manual*, 2006

http://leonardo.phys.washington.edu/feff/Docs/feff8/feff84/feff84.pdf

52 T. Taguchi, T. Ozawa and H. Yashiro, *Physica Scripta*, 2005, **T115**, 205.

53 Rigaku Corporation 編 「XAFS 解析ソフトウェア REX2000 取扱説明書」 Manual No. MJ13242B02, 2006.

54 J. M. D. Coey, *Acta. Cryst. B*, 1970, **26**, 1876.

55 宇田川康夫 編著 日本分光学会測定法シリーズ26 「X線吸収微細構造—XAFS 測定と解析」（1993）学会出版センター

56 J. N. Van Niekerk and F. R. L. Schoening, *Acta. Cryst.* 1953, **6**, 227.

57 W.-J. Chun, K. Asakuara and Y. Iwasawa, *Chem. Phys. Lett.* 1998, **288**, 868.

58 T. Kanno, H. Tanaka, T. Nakamura, H. Tabata, T. Kawai, *Jpn. J. Appl. Phys., Part2*, 1999, **38**, L606

59 Y. Terada, B. Choi, S. Heike, M. Fujimori, T. Hashizume, *Nano Lett.* 2003, **3**, 527.

60 Y. Shirai, *Chem. Soc. Rev.* 2006, **35**, 1043.

61 R. Bernard, G. Comtet, G. Dujardin, V. Huc, A. J. Mayne *Appl. Phys. Lett.* 2005, **87**, 053114.

62 Y Lai, H. Zhuang, K. Xie, D. Gong, Y. Tang, L. Sun, C. Lin, Z. Chen, *New J. Chem.* 2010, **34**, 1335.

63 S. Fujita, Master Thesis at Dept. Chem., Tokyo Institute of Technology 2006.

Chapter 3 STM Studies on the Formation of Precursor Dependent Rh Clusters on Al_2O_3/NiAl(110) Surface

3.1 Introduction

Supported metal catalysts comprising small metal particles dispersed on the high-surface-area support material (ex. Al_2O_3, SiO_2, MCM-41) have a wide range of oil field, industrial and environmental application. [1-3] The activity, selectivity and stability of supported catalysts are determined by the properties of active metal species such as size, [4, 5] distribution, [6, 7] local structure,[8] interaction with the support surface [9-11] and so on. Generally, these parameters are significantly dependent upon the preparation methods,[12-14] the nature of supports[9, 10, 15, 16] and the variety of metal precursors. [17-20] Thus, the fundamental understanding of the correlation between these preparation conditions and properties of the active metal species is crucial issue in the field of catalyst, which can provide the probability to optimize the performance of supported catalysts with respect to target reaction.

During the last two decades, combination of scanning probe microscopy (SPM) and oxide thin films or oxide single crystals has been proved to be a promising methodology to provide molecule-level insight into the fundamental issues of catalytic processes such as adsorption, diffusion, surface reaction and catalytic process (some examples are shown in Chapter 1). For examples, Freund and co-workers studied formation process, adsorption behaviors of different metal clusters (e.g. Pt, Pd, Rh, Co, Au, etc.) deposited on various oxide thin film (MgO/Mo(001), FeO/Pt(111), Al_2O_3/NiAl(110), etc.) by STM and conductance spectroscopy. [21,

[22]Goodman and co-workers monitored the growth kinetics and deactivation process (sintering) of Au clusters on TiO_2 by in-situ STM measurements. [23] Libuda et al. has investigated the growth of Pd and BaO on Al_2O_3/NiAl(110) prepared by sequential co-deposition of Pd, Ba and subsequent oxidation, which is promising catalyst for elimination NO_X from exhaust gas of lean-burn engine vehicles. [14] They found the structure and growth of active species can be strongly influenced via the deposition sequence.

Such studies provided important view on the properties of metal particles on the support surface, however, the preparation conditions have not been considered there since the metal clusters were directly deposited onto oxide surface by physical vapor deposition in all of these cases. The vastly different treatments and precursor types in the preparation of catalyst will probably lead to significant structural difference, thus limiting the comparability of these results. Some basic problems about formation process and adsorption sites of active metal species included

a) How about the initial placement of the precursors on the support surface?
b) Where and how the precursors convert to final products?
c) How the surface defect sites and ligands in precursors affect the formation process?
d) How about the final structures of active species?

need be clarified in molecule-level at first.

To answer these questions, it is required to conduct model surface by using analogous method to wet chemical techniques which are used to prepare practical catalysts, such as starting from metal precursors instead of physical vapor deposition of metal cluster. In this way, one can study adsorption behavior of precursors, their decomposition mechanism and formation process of active species.

Early researches in this direction can be traced back to AFM observations on the

$RhCl_3/SiO_2/Si(100)$ surface by group of Niemantsverdriet.[24, 25] They have deposited the $RhCl_3$ onto $SiO_2/Si(100)$ surface (2×10^{12} particles/cm^2) by spin-coating and observed the decrease of particle height after reduction. Goodman and co-workers have succeeded to investigated the atomic structure of $Ru_3Sn_3/SiO_2/Mo(112)$ prepared via wet impregnation.[26] By taking advantage of good stability of $SiO_2/Mo(112)$, they dropped the diluted $Ru_3(CO)_9(SnPh_2)_3$ toluene solution onto the fresh $SiO_2/Mo(112)$ surface, then transferred the sample to UHV chamber. The STM measurements were carried out after annealing up to 450 K to remove the organic ligands. The benefit of this work is to provide structural information directly related to real catalysts. However, they did not report the surface morphology of $Ru_3(CO)_9(SnPh_2)_3/SiO_2/Mo(112)$. In order to estimate both initial state of precursor and final products after decomposition, chemical vapor deposition method is a good choice for preparation model surface. There are quite a few reports on the behavior of organometallic complexes on different support surface.[27-29] Recently, Lei have established morphological changing of the $Rh(acac)(CO)_2/Al_2O_3/Ni_3Al(111)$ surface after annealing up to different temperature. [30] Alexander have also studies the formation of Ru-Sn nanoparticles from precursor $Ru_3(CO)_9(\mu\text{-}SnPh_2)_3$ on a partially oxidized $Ni_3Al(111)$ and found the different formation mechanism on the alloy and oxidized surface patches. [31] However, vapor deposition methods are just applicable to the precursor which can be converted to vapor state before decomposition. It is not suitable for low vapor-pressure precursors (ex. inorganic precursors as $RhCl_3$, $Rh(NO_3)_3$ etc.), or some precursors with low decomposition temperatures.

Recently, a new deposition technique: pulse deposition method (PDM) has been developed by Kawai et al. [32] and applied to deposition of various compounds for biology, electronic device and material researches (See Chapter 2). The concept of this method is very simple, solvents (such as H_2O, C_2H_5OH, CH_2Cl_2, $C_6H_5CH_3$…) just act as carriers to take the target compounds onto the substrate surface, the solvent molecules will vanish by vacuum expansion or after heat treatment. Because of the injection of solution, this method can be applicable to various compounds.

In our studies, we have firstly applied pulse deposition method to catalyst studies, in order to understand how precursors disperse, decompose and form to active species on oxide surface. Moreover, we hope to obtain molecule-level understanding on the precursor effect by using this new methodology. The precursor effect has been discussed several ten years, only a little knowledge based on experience has been recognized, however, these mechanisms are still not clear.

We have prepared $[Rh^{II}(OAc)_2]_2/Al_2O_3/NiAl(110)$ surface and $RhCl_3/Al_2O_3/NiAl(110)$ surface by pulse deposition method, where remarkable difference in catalytic activity has been reported in practical catalyst researches.[32,33] We estimated the properties and precursor adsorption behavior of these two surfaces before and after decomposition by using STM measurements. By comparison, we would demonstrate the formation process of Rh particles and discuss the influence of ligands of precursors.

3.2 Experimental

The experiments were performed in an ultrahigh vacuum (UHV) variable temperature (VT) STM (Oxford Instru.), a detailed description can be found in Chapter 2. Briefly, this instrument consisted of a main chamber (base pressure < 2×10^{-8} Pa) and a fast entry load-lock chamber (base pressure < 2×10^{-6} Pa). The main chamber was equipped with a low-energy electron diffraction (LEED) optics, an ion sputtering gun, a quadrupole mass spectrometer, and VT-STM head. A NiAl(110) single crystal disc (4 mm in diameter and 0.5 mm thick) (Surface Preparation Laboratory) was mounted in a Mo holder and could be heated up to 1500 K by radiation from a heating W filament from the back side and the temperature was measured with K-type thermocouple mounted on the side face of the NiAl(110) disc. STM images were recorded in constant current mode (topography image) using electrochemically etched W tips at room temperature unless otherwise noted.

The NiAl(110) surface was cleaned by repeated cycles of Ar^+ ions sputtering and subsequent annealing at 1350 K for 3 min. Chemical composition, flatness, and periodicity of the cleaned surface was checked by Auger electron spectroscopy (AES), STM, and LEED, respectively. The ultra-thin Al_2O_3 films were prepared by exposing the clean NiAl(110) surface to oxygen gas (2×10^{-4} Pa for 1600 s) while keeping the sample temperature at 600 K followed by annealing the sample at 1100 K for 10 minutes as described in previous litrure. [21] The quality of the films was confirmed by AES , LEED, and STM.

Dilute $[Rh^{II}(OAC)_2]_2$ (Alfa. 99.99%) aqueous (Milli-Q water) solution (or $RhCl_3$ anhydrous (Alfa. 99.9%) ethanol (0Aldric, 99.9%) solution) (10^{-4}-10^{-5} mol l^{-1}) was prepared under N_2 atmosphere in a globe box and then sealed into a Pyrex-glass ampoule with a bellows sealed valve. The solutions were degassed by freeze-pump-thaw cycles.

The pulse-deposition method was adopted to deposit Rh precursors from their solutions on a clean Al_2O_3/NiAl(110) surface under vacuum in the fast entry chamber. The pulse valve opens for a short time by applying voltage pulse with a controlled duration and repetition and the solution is sprayed through the vacuum to the substrate surface where most of solvent molecules are evacuated and non-volatile precursor can be deposited on the substrate surface. Schematic of the system is shown in Figure 3.2.1. A pulse valve with the orifice size of 1.6 mm (Parker Hannifin) was used. The distance between the sample and the valve was about 12 cm. Firstly, small amount of solution of a precursor is transferred to the pulse valve through the flexible tube just before deposition. Then, the pulse valve opens several times while monitoring the pressure of the fast entry chamber. Finally the pressure rise becomes constant by each pulse and the system gets ready for the solution injection. Pulse duration was set close to the minimum value (170 μs) that achieved constant pressure rise for each pulse.

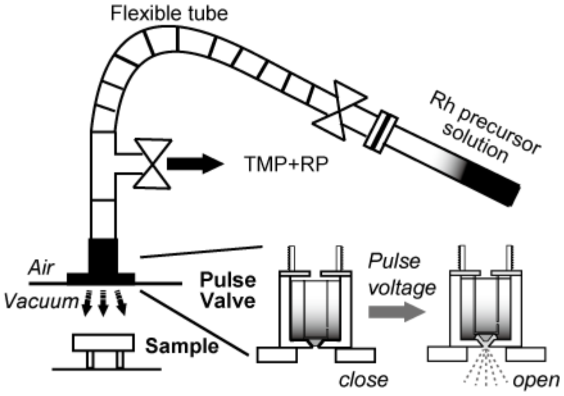

Figure 3.2.1 Schematic of the pulse-deposition method. After degassing a solution containing a precursor, it is introduced to the pulse valve through a flexible tube. The pulse valve opens for a short time by applying voltage pulse of controlled duration and repetition and the solution is sprayed through the vacuum to the substrate surface where most of solvent molecules are evacuated and non-volatile precursor can be deposited on the substrate surface.

3.3 Results and Discussion

3.3.1 NiAl(110) surface

NiAl is a binary intermetallic alloy that has been subject to numerous studies due to its superior oxidation resistance and mechanical properties (ex. ductility).[34, 35] NiAl is also an important compound in the fields of surface science. The NiAl(110) was the first metal alloy where a rippled relaxation in the topmost surface layer was observed by LEED.[36] Furthermore, the NiAl single crystal surface serves as a good substrate for preparation of well ordered ultra-thin Al_2O_3 film, and the various Al_2O_3 phase can be obtained by changing the surface composition of NiAl substrate such as NiAl(110),[21] NiAl(001),[37] $Ni_3Al(111)$[38] and so on.

Figure 3.3.1(a) shows the unit cell of NiAl single crystal consists of 50% Ni and 50% Al, where the blue balls are Al atoms and red balls Ni atoms. The unit cell has the cesium chloride (CsCl) structure, two simple cubic lattices of Ni and Al atoms interpenetrate with each other to form a body-centered cubic lattice with a lattice parameter of 2. 88 Å.[39] The melting point of NiAl is quiet high, about 1638℃, which is higher than the melting point of Ni (1455℃) and Al (660℃), therefore annealing can be carried out at a high enough temperature to prepare the well-ordered Al_2O_3 thin film.

The ideal NiAl(110) surface consists of Ni and Al arrays on the same plane, the unit cell parameters are 2. 88 Å and 4. 02 Å ($\fallingdotseq \sqrt{2} \times 2.88$ Å) as shown the top view of NiAl (110) in Figure 3.3.1(b). However, the relaxation of the topmost atomic layer causes that the Al atoms are displaced toward the vacuum and the Ni atoms are displaced inward the bulk producing a ripple of 0. 22 Å[36] (see the side view of NiAl(110) surface in Figure 3.3.1(c).)

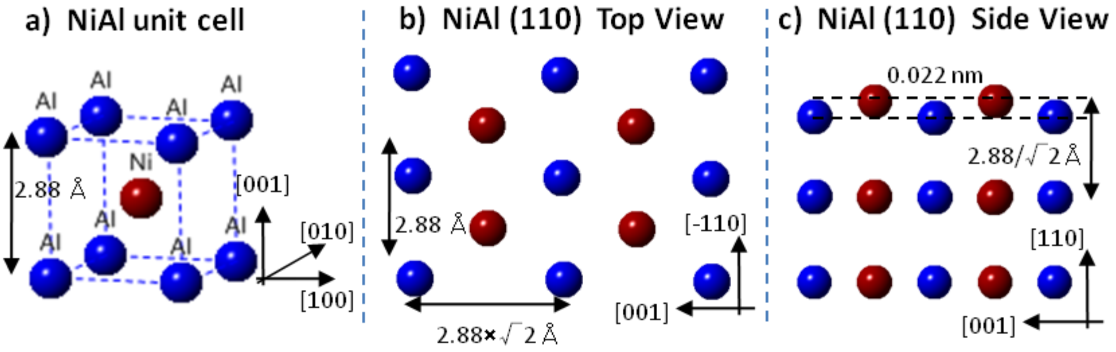

Figure 3.3.1 Structure of NiAl crystal. **a)** 3D unit cell of NiAl and atomistic model of NiAl(110) surface **b)** Top view and **c)** Side view showing the relaxiation.

The clean NiAl(110) was prepared by the cycles of sputtering and annealing (see Chapter 3.2). Auger and LEED measurements were carried out to confirm the contamination had been completely removed, which was key factor for preparation of a good Al_2O_3 thin film at next step. The Figure 3.3.2 shows the Auger spectra before and after the cleaning process. Before cleaning, the main peaks in the Auger spectra around 270 eV and 503 eV belong to carbon and oxygen, respectively, while three Ni peaks at 700-850 eV were very weak. The surface carbon could be removed easily by sputtering, but bulk ones would diffuse onto the surface after heat treatment since increase of carbon peak was observed after annealing. The oxygen from surface oxides was only reduced after annealing. The sputtering-annealing processes were repeated until the peaks of impurities had disappeared completely and Ni peaks increased to the maximum. In the LEED pattern (Figure 3.3.3) of clean NiAl(110), a rectangle structure (1: $\sqrt{2}$) corresponding to NiAl(110) unite cell can be clearly observed, means that well-ordered surface is completed.

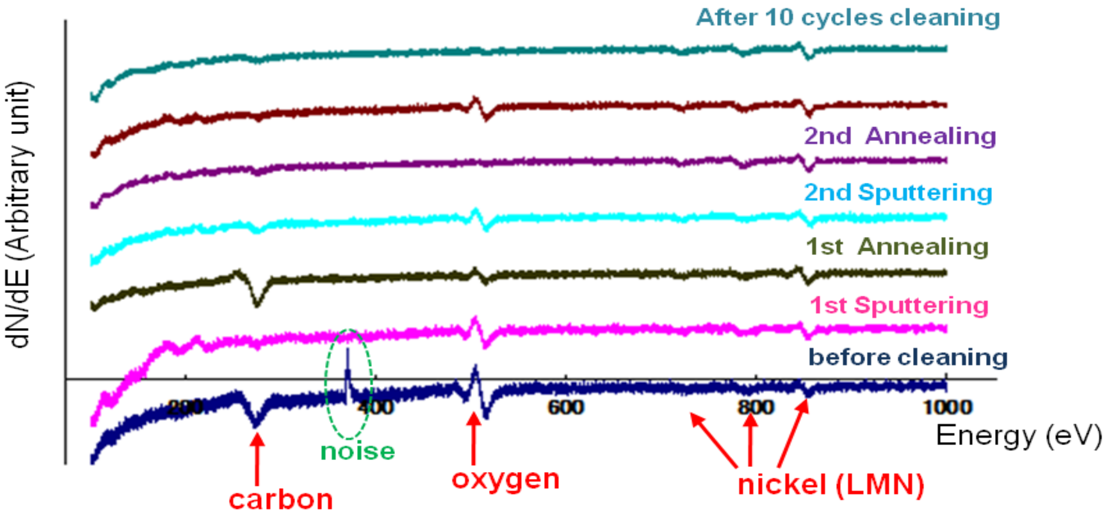

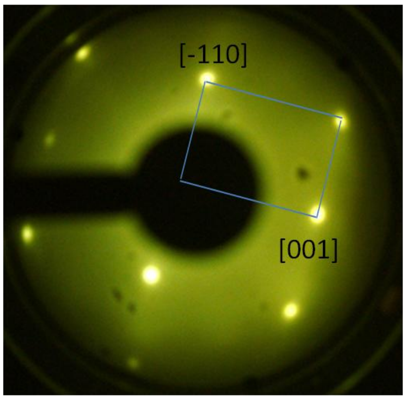

Figure 3.3.2 (upper) A series of Auger spectra measured before and after different cleaning steps. After 10 cycles sputtering and annealing, peaks of impurities disappear and ones belong to Ni increase to max.

Figure 3.3.3 (left) LEED pattern of clean NiAl(110) surface, the rectangle structure (1:√2) corresponding to NiAl (110) surface unite cell

The STM images of clean of NiAl(110) surface (Figure 3.3.4) were obtained at the condition: positive sample bias (V_S) = 1.5 V, tunneling current (I_t) = 0.7 nA. The distinct terrace and step structures could be observed, where large terrace width was about 80 nm ~ 100 nm and mean step height was measured at ~ 2 Å corresponding to monoatomic layer height (2.88/√2 Å) of NiAl(110) surface structure (Figure 3.3.1(c)). At some locations, we also found some vicinal surfaces with a lot of oriented step edges and narrow terraces of ~ 10 nm width, probably resulting from too much sputtering. The steps edges appeared with ragged shape, which were clearly distinguishable in the close up of the vicinal surface (insert Figure 3.3.5(a)). It has been reported that the growth of Al_2O_3 films on a vicinal NiAl surface is

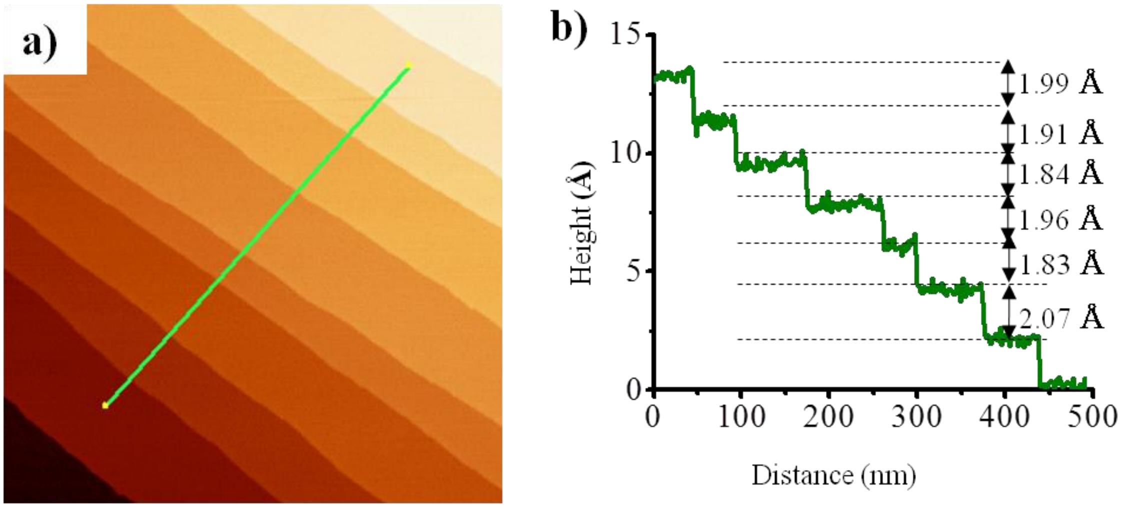

Figure 3.3.4 STM results of clean NiAl(110) surface **a)** Topographic image (500 nm × 500 nm, V_S = 1. 5 V, I_t = 0. 7 nA) of large terraces and monoatomic steps and **b)** A cross section along the white line in **a)**. **c)** Topographic image (300 nm × 300 nm, V_S = 1. 5 V, I_t = 0. 7 nA) of vicinal surface with oriented steps and narrow terrace, insert figure shows a close up of step structures. d) A cross section along the white line in **c)**

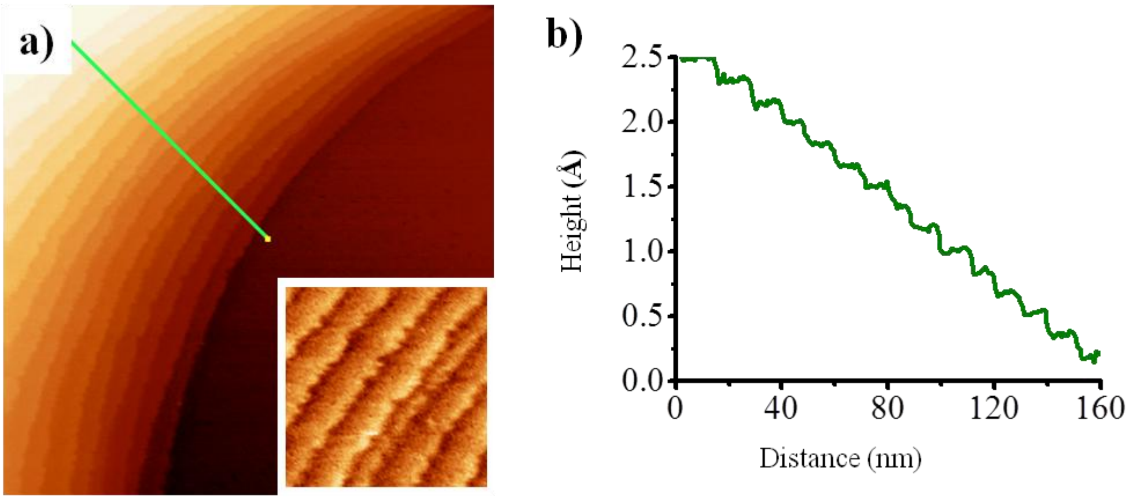

Figure 3.3.5 STM results of c vicinal NiAl surface **a)** Topographic image (300 nm × 300 nm, V_S = 1. 5 V, I_t = 0. 7 nA) of vicinal surface with oriented steps and narrow terrace, insert figure shows a close up of step structures. **b)** A cross section along the white line in **a)**

quietly different from the case of flat NiAl (110) surface, since the narrow terrace width of ~ 10 nm is similar to the characteristic domain size of the alumina film on flat NiAl(110), the periodic steps can release of interfacial strain instead of domain boundaries which are main line defects on Al_2O_3/NiAl(110) surface.[40] However, the vicinal surface was negligible in this study, due to their low existence probability.

3. 3. 2 Al_2O_3/NiAl(110) surface

The Al_2O_3 films, generated on the NiAl(110) surface after oxidation and annealing, have two-layer Al_S-O_S-Al_i-O_i structure with thickness of 0.5 nm. The nature of Al_2O_3 film will be mentioned here briefly. The oxide film has a parallelogram unit cell with b_1 = 10.55 Å, b_2 = 17.88 Å, β= 88. 6° , and grows two orientationally related domains rotated ±24.1 ° relative to the [1-10] direction of the underling NiAl(110) surface. The dominating defect structures are two types of line defects, i. e. antiphase domain boundaries (APDB) between domains of equal orientation and rotational domain boundaries (RDB) between different domains. The oxide film is commensurate with substrate along the [1-10] direction and incommensurate along [001].[21, 41-46]

Figure 3.3.6 shows the LEED pattern after oxidation (2400L O_2 at 610 K) and subsequent annealing at 1380 K. Due to the thickness of oxide, diffraction spots of both oxide and substrate were observed together. The oxide pattern was much more complicated than that of NiAl(110), because the oxide unite cell is about 16 times larger than that of NiAl(110) and two domains grow along the different directions. In the LEED pattern, several tens oxide diffraction spots emerged in each NiAl reciprocal lattice. Figure 3.3.6(b) shows the real-space and reciprocal-space schematics of the oxide diffraction spots based on calculation, red spots correspond to the NiAl reciprocal lattice. In Figure 3.36(a), NiAl reciprocal unit cell is marked by red rectangle, while oxide spots are identified by white mesh. By using these schematics, all of the spots in LEED pattern can be explained, which indicates well-ordered Al_2O_3 thin films have been prepared. From our experience, the LEED pattern like Figure 3.3.6(a) means that quality of Al_2O_3 thin films was pretty good. Nevertheless, 1) brighter the NiAl spots compared with oxide spots, or 2) partial emergence of oxide spots, or 3) quasi hexagonal pattern would be observed in the case of imperfect oxide thin films.

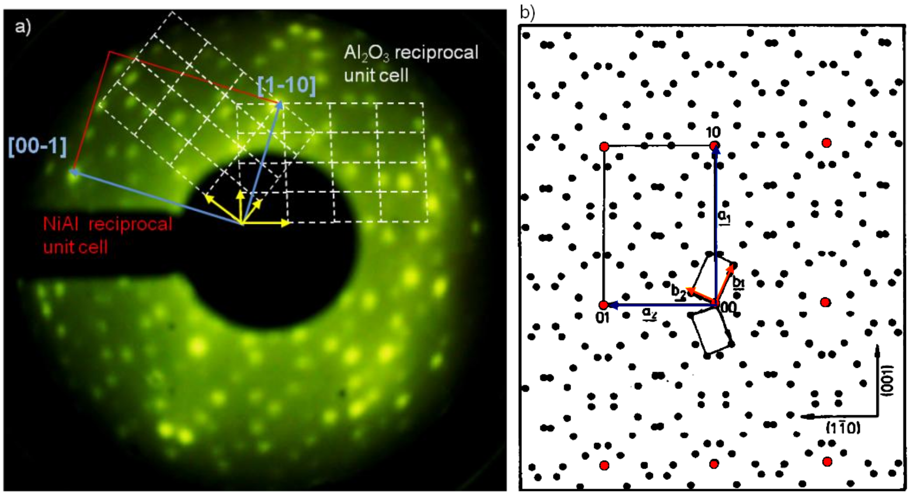

Figure 3.3.6 **a)** LEED pattern of well-ordered Al_2O_3/ NiAl(110) surface, reciprocal unit cell of NiAl and Al_2O_3 are marked by red rectangle and white parallelogram , respectively. **b)** Real-space and reciprocal-space schematics of the oxide unit mesh based on calculation, the diffraction spots of NiAl are marked by red circles. [21]

Al_2O_3 film has a band gap of ~ 6. 7 eV, but because of the limited thickness of the film, it is possible to obtain stable tunneling current at the bias voltage range from a few mV up to around 10 eV at both positive and negative bias voltage.[43] Moreover, the presence of unoccupied gap states induced by the domain boundaries lead the domain boundaries appear much more brightly than the others location at high positive bias. So the most predominate feature of the Al_2O_3 film on NiAl(110) when imaged with the STM is the appearance of domain boundaries. Figure 3.3.7 shows the topographic image of perfect well-ordered Al_2O_3/NiAl(110) at V_S = 2. 8

eV . Besides large terrace with width of 100 nm, steps and all of the domain boundaries were clearly distinguished. The domain boundaries were observed as white lines with various shape spread over the whole surface. The separation of adjacent domain boundaries was measured about 8 nm ~ 10 nm (Figure 3.3.8), which is consistent with previous studies.[44] The structure information of the surface is also shown in the Figure 3.3.7. The orientation of substrate was determined by the direction of the oxide domain boundaries.

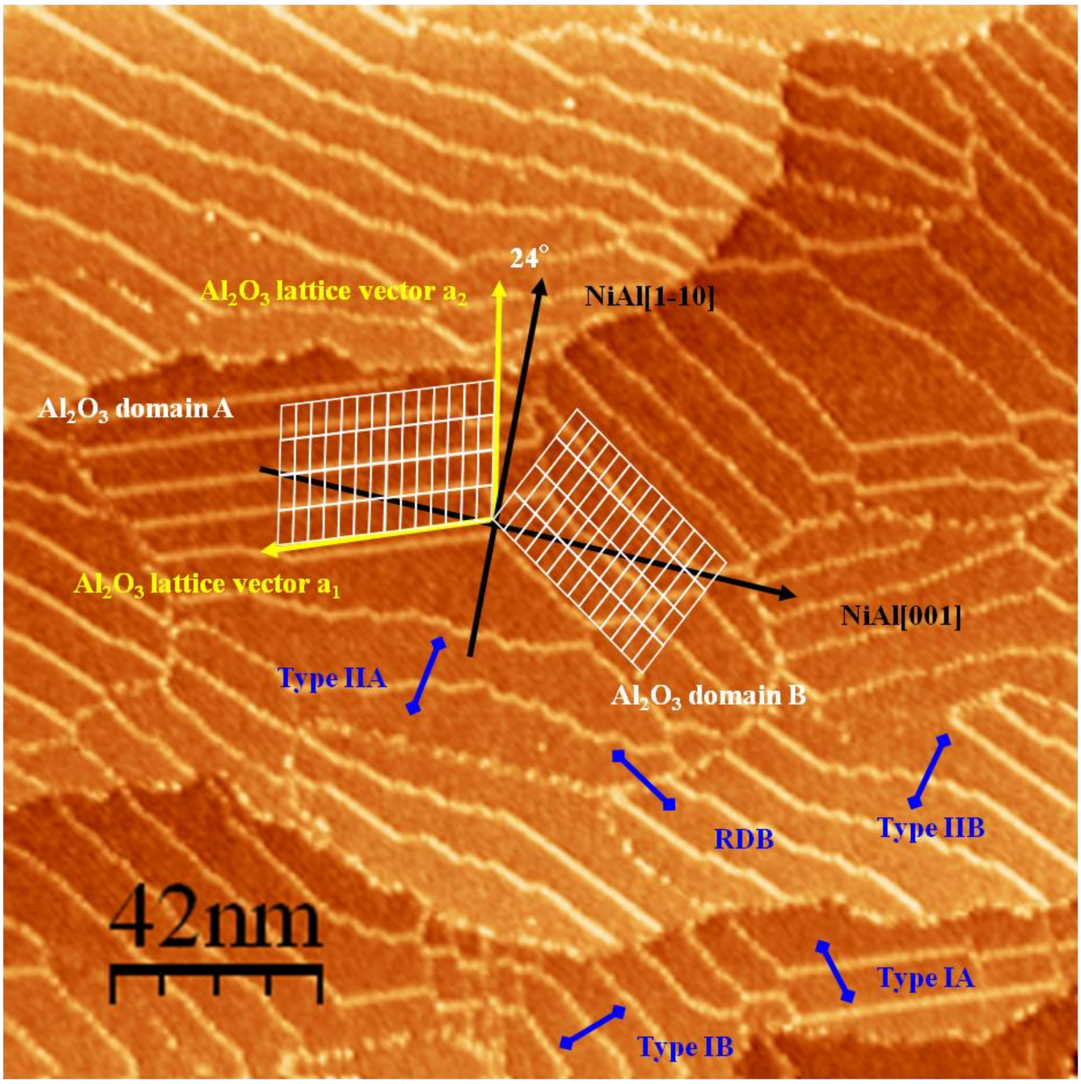

Figure 3.3.7 STM image of well-ordered Al_2O_3/NiAl(110) (210 nm × 210 nm, V_S = 2. 8 V, I_t = 0. 8 nA). All of the domain boundaries APDB (Type IA, IIA, IB, IIB) and RDB are marked by blue lines. The Al_2O_3 unit cells are also shown by white parallelogram mesh.

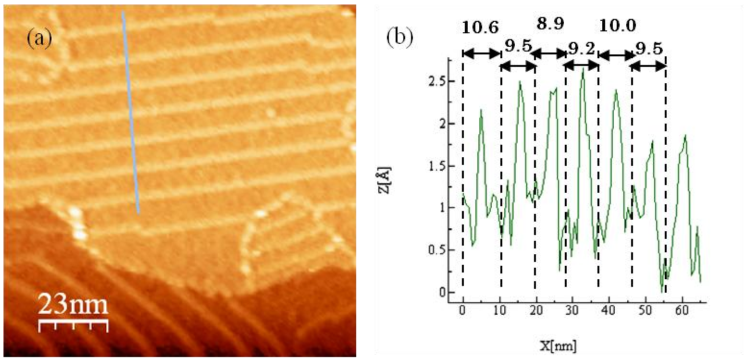

Figure 3.3.8 Measurements of distance between two APDBs **a)** STM image （114 nm×114 nm、V_S = 2. 8 V, I_t = 0. 8 nA） and **b)** A cross section along the white line in **a)** The distance is around 9 nm ~ 10 nm

The antiphase domains boundaries (APDB), which separate two domains of the same type were identified as IA and IB for straight shape, and IIA ,IIB for zigzag shape. The boundaries separate two different domain (A and B) were marked. RDB (Reflection Domains Boundaries). The APDB have been well studied by Prof. Freund group, [43-45] a remarkable bias dependence of domain boundaries has been confirmed by tuning the bias voltage over the range from a few mV to 4.0 V or higher. As shown in Figure 3.3.9, there was no domain boundary structure on the surface below the 1.0 V. When the bias voltage was increased over 1.0 V, domain boundary structures emerged but blurrily. The strong contrast of the domain boundaries appeared in the range of 2.5 eV ~ 3.0 eV, the maximum was observed at 3.0 eV. Above the 3.0 eV, the brightness of boundaries decreased again. This observed bias-dependent corrugation of domain boundaries was consistent with the previous studies, and could be explained by defect-induced states in the oxide band gap.

Figure 3.3.10 shows close up of APDBs (type I) taken under constant height mode. The images had a little noise, but exhibited more detailed information about the surface structure. First, a lot of stripe structures were visible inside of domain. The distance between two neighboring stripes was measured to about 8.9 Å, which was extremely similar to half of b_2 (17. 88 Å) lattice vector of the oxide. Previous STM and AFM studies revealed some surface oxygen atoms (O_S) give strong contrast due to higher tunneling probability or short-range

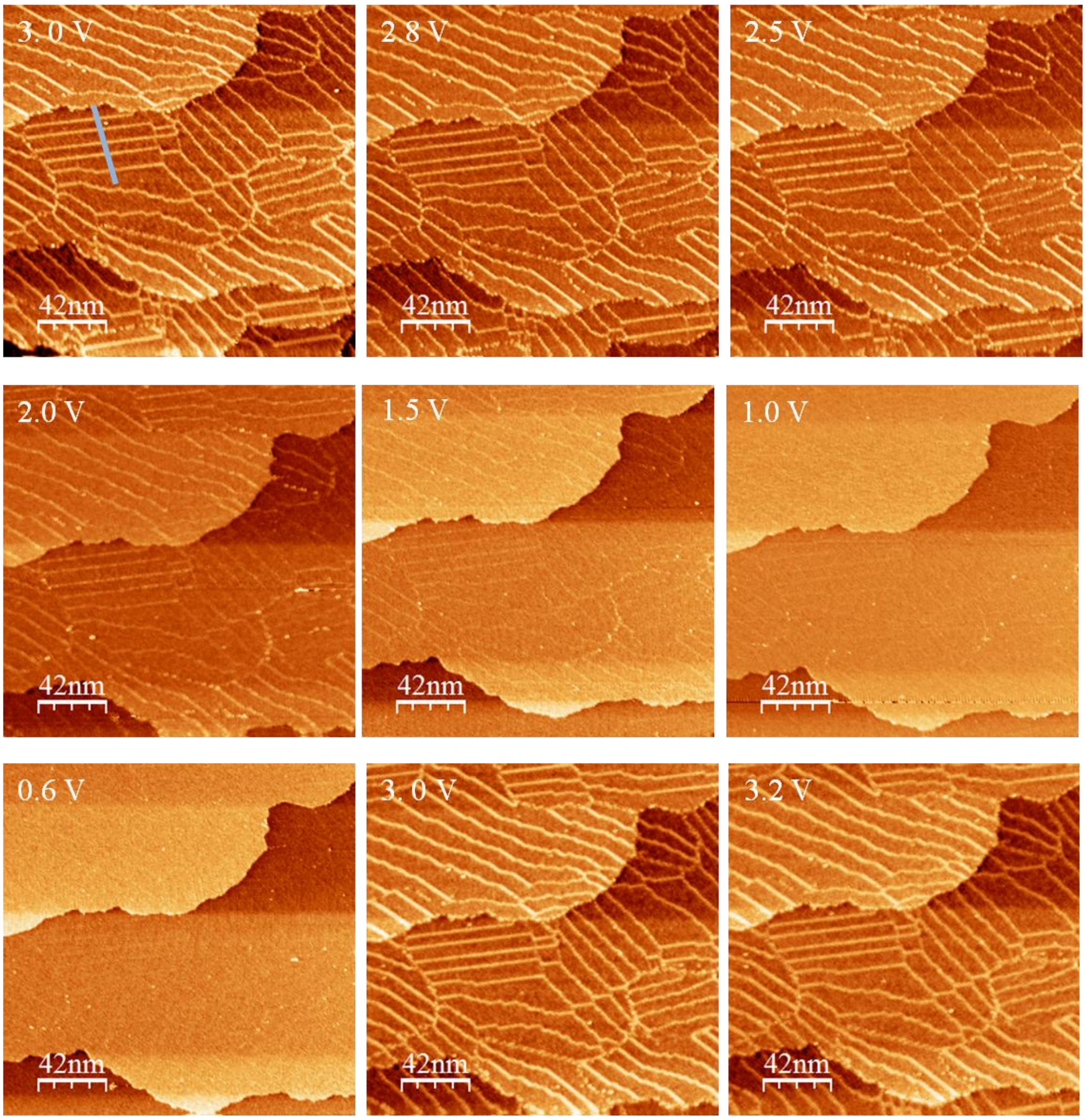

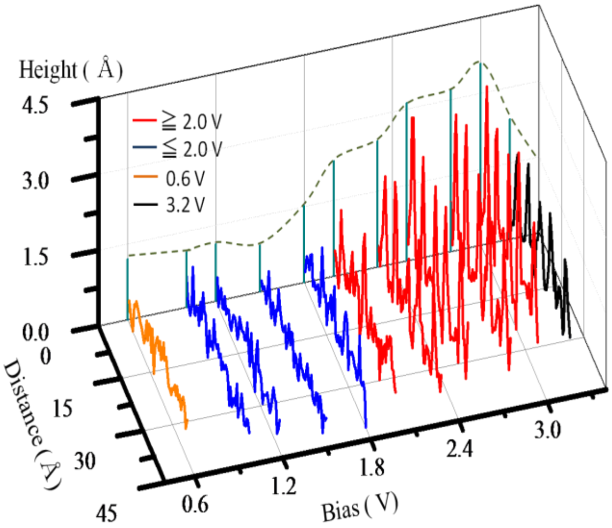

Figure 3.3.9 **(upper)** STM topographic images (210 nm × 210 nm, I_t = 0. 7 nA) of Al_2O_3/NiAl(110) taken at the different sample bias voltage from 3. 0 V to 0. 6 V, then back to 3.0 V, 3.2 V **(left)** Series of line profiles of APDB (type IA) shown in first STM image (3.0 V) taken at different bias voltage. At this bias range, the height of APDB increases along with bias below 3.0 V. Above 3.0 V, the height decreases again.

chemical interaction with tip. Usually these brighter O_S atoms formed rows along the b_1 lattice direction, furthermore they changed orientation on adjacent rows as shown in Figure 3.3.10(c). Therefore, we suppose that these stripes are composed with b_1 lattice direction -orientated O_S rows. In fact, these stripes can be well fitted by unit cell of the oxide as shown in Figure 3.3.10(b).

On the domain boundaries, the situation was more interesting. The orientation change of O_S rows was clearly distinguished. The domain boundaries were also fitting perfectly by a set of extended oxide unit cell with extension of 3.0 Å along the b_2 lattice direction. This is in agreement with previous AFM/STM and SPA-LEED results. Besides, a lateral displacement of straight APDB was also observed in this STM image. The domain boundaries shifted to next to O_S rows at the displacement.

Besides the domain boundaries which were main line defects on the Al_2O_3/NiAl(110), others unordered structures such as bare NiAl areas, vacancy islands, amorphous areas, dot structures will be discussed below :

1) Bare NiAl areas: Bertrams *et. al*[47] pointed out that bare NiAl surface would be exposed at some place when the dosing amount of oxygen was not sufficient. A systematic study of NiAl “holes” has been performed by K. H. Hanson,[48] the apparent height (or deepness) of edge between NiAl substrate and Al_2O_3 strongly depends upon the bias voltage.

2) Vacancy islands: vacancy islands appear on both perfect and incomplete Al_2O_3 film as hole-like structures shown in Figure 3.3.11(a). Usually domain boundaries are visible inside the holes at high positive bias voltage, suggesting that vacancy islands are composed with Al_2O_3 films. Since the presence of hole-like structures are not observed on clean NiAl(110) surface, the vacancy islands seem to be induced in the oxidation process. The detail is unknown. Vacancy islands can be distinguished from bare NiAl surface by existence of domain boundaries, or on the basis of bias dependent imaging. The height profile of this structure is not affected by bias voltage due to the same composition with surrounding surface (Figure 3.3.11(c)).

3) Amorphous areas: Generally, the amorphous areas appear as rough, random structures on the incomplete film or complete film after reduction. The amorphous areas have the same bias dependence as well-ordered Al_2O_3 surface shown in Figure 3.3.11(b).

The random structures were visible at high bias voltage, but disappeared below 1.0 V. It indicates amorphous areas possess properties of Al_2O_3 thin films. The appearance of this unordered areas are explained as insufficient oxidation of NiAl. Lozovoi *et. al*[49] reported that a precursor–like Al_2O_3 interface layer consisting of pure Al formed at first, thus Ni was excluded from topmost layer, while bulk Al diffused onto the surface. The unordered areas could be due to a lack of oxygen in the interface area.

4) dot array on APDBs: Occasionally, arrays of close packed dots were observed on some APDBs of clean Al_2O_3/NiAl(110) surface as shown in the Figure 3.3.12. However, not all of APDBs exhibited these structures even at the same image. These structures were hardly explained by adsorption of impurities or residual metal atoms deposited at former experiments, since the dots structures appear even on a new sample surface. The mean diameter of dots was about 1.7 nm, which was different from the lattice parameter of extended oxide unit cell on APDBs. Similar dot-array structure was found in STM images in literature.[43,50] These structures cannot be explained now, but it seems not to influence the properties of oxide surface.

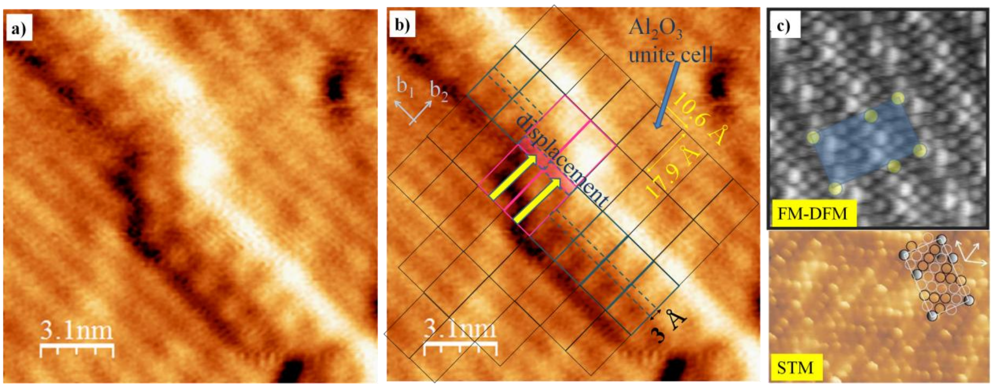

Figure 3.3.10 a) STM constant height images of straight APDB (type I) of Al_2O_3/NiAl(110) (15.5 nm × 15.5 nm, V_S = 3.0 V). The image is reproduced in (b) covered with oxide unit cell (10. 6 Å×17.9 Å) inside domain and extended unit cell (10.6 Å×20.9 Å) on the domain boundaries. The lateral displacement of straight APDB is denoted by yellow arrows. c) Atomic resolution STM and FM-DFM images of Al_2O_3/NiAl(110) reported by Freund's group.

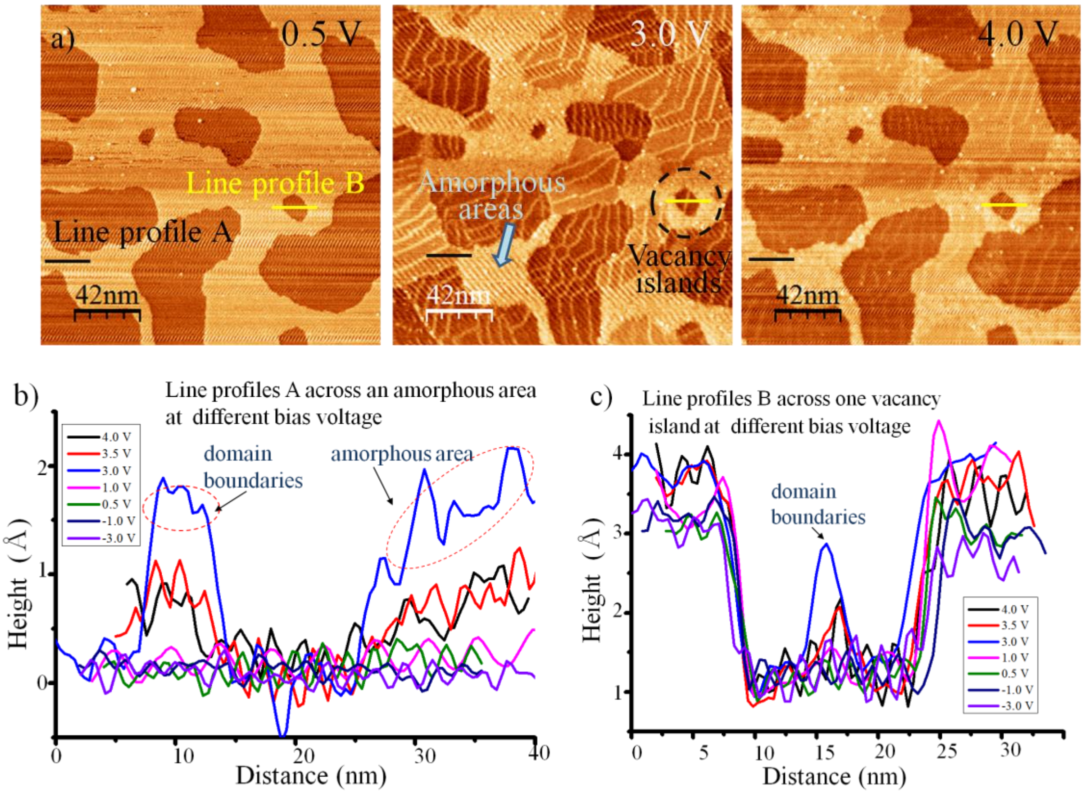

Figure 3.3.11 **a)** STM images (at V_S = 0. 5 V, 3. 0 V, 4. 0 V) of incomplete Al_2O_3/NiAl(110) (210 nm × 210 nm) where vacancy islands and amorphous areas are visible. **b)** Line profiles A at different bias voltages across the domain boundaries and amorphous areas. **c)** Line profiles B at different bias voltages across the vacancy islands. All of images are acquired with I_t = 0.7 n A.

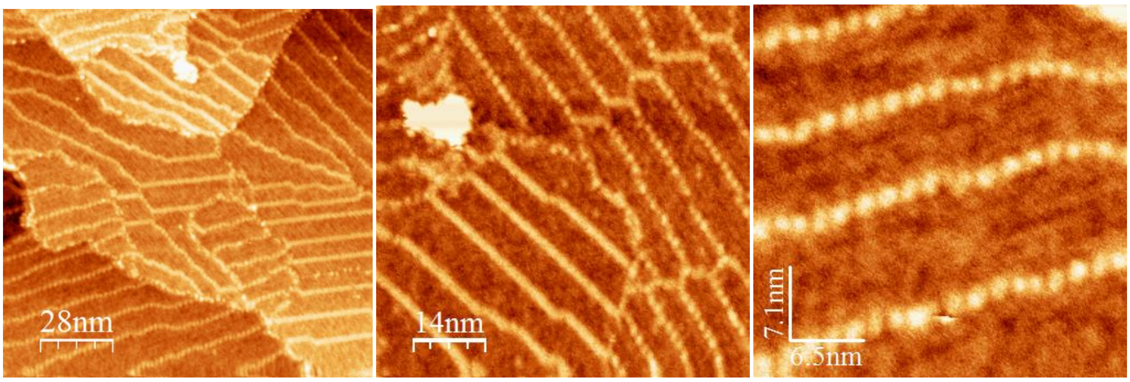

Figure 3.3.12 STM images of clean Al_2O_3/NiAl(110) surface (140 nm×140 nm, 70 nm×70 nm, 35.5 nm×32.5 nm, V_S = 3.0 V, I_t = 0.6 nA). Arrays of dot structures are visible on some APDBs, whereas others APDBs are just white lines.

3.3.3 Adsorption and Thermal Decomposition of the $[Rh^{II}(OAc)_2]_2$ $/Al_2O_3/NiAl(110)$

The $[Rh^{II}(OAC)_2]_2$ precursor consists of four acetate ligands bridging a Rh dimer with a short Rh-Rh distance. The size of the precursor molecule can be estimated as shown in Figure 3.3.13(a) by assuming van der Waals radius for each atom for the structure determined by X-ray diffraction analyses of the single crystal of $[Rh^{II}(OAC)_2H_2O]_2$.[51] It is known that some adducts can be coordinated to the both sides of the wheel-like molecule: H_2O, CH_3CN, tetrahydrofuran, etc. by coordinate bonding to Rh atoms.[51,52] Thus, $[Rh^{II}(OAC)_2H_2O]_2$ may be a stable form in aqueous solution, but it was reported that the coordinated water molecule was readily replaced by some adducts noted above.[52]

Figure 3.3.13(b) shows a representative STM image after injection of 2×10^{-5} mol l^{-1} aqueous solution of the $[Rh(OAC)_2]_2$ precursor through the pulse valve by 20 pulses. A wider range image (200×200 nm^2) including this region is also shown in Figure 3.3.13(c). Compared with the clean surface, particles with bright contrast were observed inside domains and on domain boundaries. A typical particle marked by a white circle is enlarged in the inset of Figure 3.3.13(b). Dot arrays with vague contrast on domain boundary lines, which were also observed on the clean surface as in the Figure 3.3.12, were distinguishable from the newly added particles from the different contrast. These newly added particles were not observed after injection of pure water, so they originated from the $[Rh(OAc)_2]_2$ molecules. The apparent diameter and height of each particle was measured by line-profile analyses of STM images at different areas of the surface and the data for about 600 particles were summarized as histograms in Figure 3.3.13(f) and (h). The average diameter and height for the particle was 2.1 ± 0.2 nm and 0.28 ± 0.10 nm, respectively. The apparent diameter and height of the

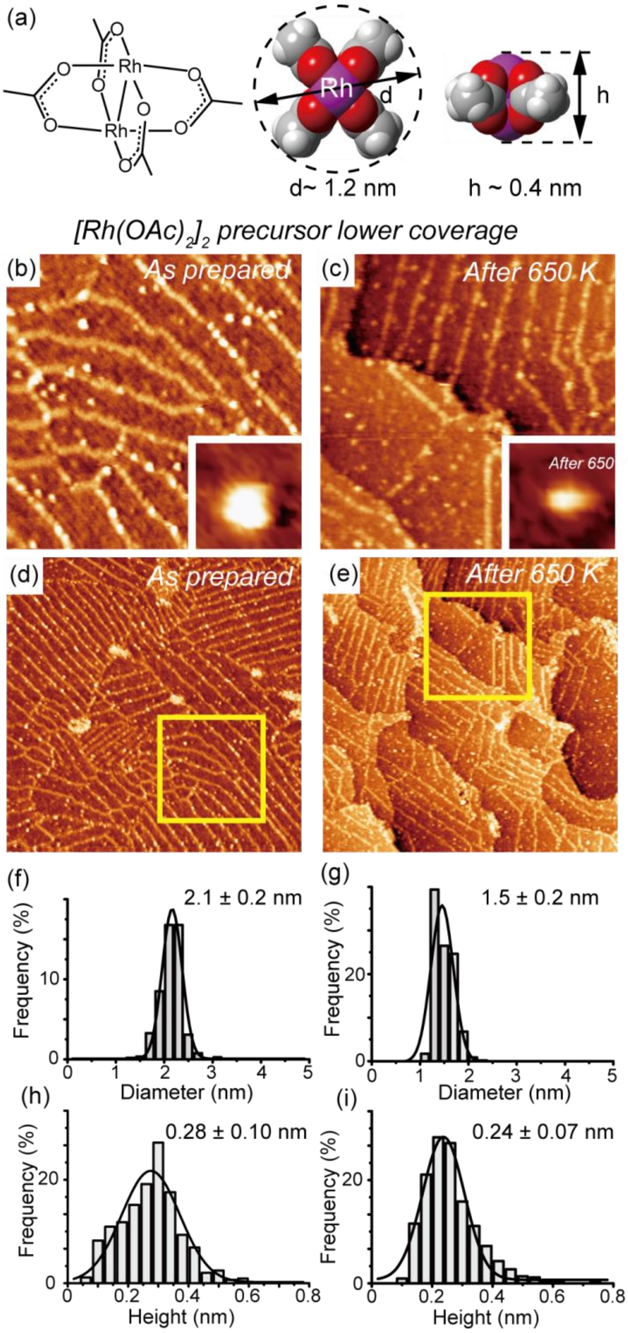

Figure 3.3.13 Adsorption and thermal decomposition of the $[Rh(OAc)_2]_2$ precursor on $Al_2O_3/NiAl(110)$ at lower coverage. **(a)** Structure of the $[Rh^{II}(OAc)_2]_2$ precursor. Four acetate ligands are bridge-bounded to two Rh atoms. Diameter and height are estimated by bond lengths and van der Waals spheres for each atom. STM images (70 × 70 nm^2, $V_S = 3.0$ V, $I_t = 0.06$ nA) obtained **(b)** after deposition of the precursor at RT and **(c)** subsequent heating at 650 K. An inset for each figure is a close-up image of a particle (5 × 5 nm^2) indicated by a white circle. Wide range STM images (200 × 200 nm2, $V_S = 3.0$ V, I_t = 0.06 nA) obtained **(d)** after deposition of the $[Rh(OAc)_2]_2$ precursor on $Al_2O_3/NiAl$ (110) at lower coverage and **(e)** subsequent heating at 650 K. Yellow squares in **(d)** and **(e)** correspond to the region of **(b)** and **(c)**, respectively Apparent diameter and height of about 600 particles obtained from line-profile analyses of several STM images at different areas are summarized in histograms: **(f)** and **(h)** for as-prepared surface, **(g)** and **(i)** for the surface after heat treatment at 650 K, respectively.

particles as well as the image of the substrate structure had some dependency on the bias voltage, of course, but it was confirmed that the difference was not serious to compare the results in the range of bias voltages we adopted in this work (detailed discussion will be shown in Appendix I). Generally, STM does not directly trace the real structure from its principle: different density of states extends or shrinks the height, and finite size of the tip enlarges the diameter of a protruding object.[14, 53, 54] A simple model for the latter case is discussed in detail in the Appendix II. Thus the diameter of a protrusion in the STM image is always overestimated. By estimation of the effective radius of the tip apex for imaging by a procedure described in the Appendix II, the diameter of the particle can be estimated as small as 1.3 ± 0.2 nm. We have to note that the value depends on the model, so it is just for reference, however, the size roughly corresponds to that of the $[Rh(OAc)_2]_2$ molecule in Figure 3.3.13(a). Therefore, we consider that each bright particle in Figure 3.3.13(b) probably corresponds to a single $[Rh(OAc)_2]_2$ molecule with their four acetate ligands parallel to the surface as will be discussed below. Average density of the $[Rh(OAc)_2]_2$ molecules was 1.4×10^{12} molecules cm^{-2}.

The $[Rh(OAc)_2]_2$ molecule preferred to be adsorbed on line defects such as domain boundaries and steps. Such preference is apparent in distribution value defined in the footnote of Table 3.1. Even after such normalization, the $[Rh(OAc)_2]_2$ prefered the line defect sites by 22 times of the domain sites. Previous STM results clearly indicated that metal nano-particles were preferentially formed at the line defects when metal atoms were evaporated on the surface.[14, 55] As noted above, oxygen-deficient composition of the line defects, not the surface oxygen vacancies, was suggested to be an origin for the preferential adsorption of the species with high electron affinity.[35, 36] Electron donation at the line defect sites to coordinate with a Rh atom of the flat-lying $[Rh(OAc)_2]_2$ molecule seems to be favorable for adsorption. It is difficult to judge whether H_2O molecules were still attached on adsorbed $[Rh(OAc)_2]_2$ by STM results.

Coordinated H_2O molecule perhaps reduces the density of states of the lowest unoccupied orbital of the molecule, which results in reduction of tunneling current in spite of increase in molecular height. Preferential adsorption at the line defect sites indicates that at least one H_2O molecule is replaced by an oxygen atom of the Al_2O_3 substrate at the line defect sites.

Table 3.1: Summary of diameter, height, density, and distribution of Rh-containing particles for $[Rh(OAc)_2]_2$ or $RhCl_3$ precursors on Al_2O_3/NiAl(110) before and after decomposition

Sample	**Diameter (nm)**	**Height (nm)**	**Density ****	**Distribution***
$[Rh(OAc)_2]_2$ (Lower coverage)				
As-prepared	2.1 ±0.2	0.28 ±0.10	1.4	1 : 22
After 650 K	1.5 ±0.2	0.24 ±0.07	1.5	3 : 5
$[Rh(OAc)_2]_2$ (Higher coverage)				
As-prepared	2.6 ±0.5	0.28 ±0.07	2.1	1 : 12
		0.46 ±0.09		
After 650 K	1.4 ±0.2	0.20 ±0.08	5.9	3 : 2
$RhCl_3$				
As-prepared	2.2 ±0.4	0.24 ±0.08	1.0	1 : 11
After 650 K	2.1 ±0.3	0.20 ±0.06	0.7	1 : 6
After 850 K	2.7 ±0.5	0.29 ±0.11	0.3	1 : 9

* Distribution: $Distribution = \frac{N(\text{domain})}{S_{\text{area}} - \sum_{\text{defects}} L \times d} : \frac{N(\text{defects})}{\sum_{\text{defects}} L \times d}$,

where N(domain), N(defects) are the numbers of particles inside domains and on the line defects, i.e. steps and domain boundaries in the image area S_{area}, respectively. L and d are the length and width of the line defects, respectively.

** Unit: 10^{12} particles cm^{-2}

It was reported that $[Rh^{II}(OAc)_2]_2$ in solid phase decomposed at 523 K to form neutral Rh atoms, $CH_3COOH(g)$, and CO(g). [56] The as-prepared $[Rh(OAc)_2]_2/Al_2O_3$ surface was slowly heated up to 650 K to completely decompose the $[Rh(OAc)_2]_2$ precursor (Figure 3.3.13(c)). A wider range image (200 × 200 nm^2) including this region is shown in Figure 3.3.13(e). Compared with the as-prepared surface in Figure 3.3.13(b), the diameter of each bright spot decreased as was evident from the histograms in Figure 3.3.13(g) and (i) as well as the magnified images in the insets. The average apparent diameter was reduced to 1.5 ± 0.2 nm. By estimation of the effective radius of the tip apex for imaging in the same procedure noted above, the diameter of the particle was as small as 0.7 ± 0.2 nm. In situ STM measurements during heating the sample showed that the apparent diameter decreased at temperature as low as 450 K and maintained the value during further heating (Figure 3.3.14). The result suggests that the decomposition of the $[Rh(OAc)_2]_2$ precursor on Al_2O_3 occurred below 500 K. IR measurements of $[Rh(OAc)_2]_2$ on a high surface-area Al_2O_3 support (100 m^2 g^{-1}) partially support the conclusion: the IR bands from the precursor partially changed after reduction in H_2 at 423 K, and completely disappeared after 673 K reduction. [4]

Note that the decomposed products had homogeneous size as was evident from the narrow size distribution in the histograms. Besides, the particle density was 1.5×10^{12} particles cm^{-2}, which is almost the same as that before heating (Table 3.1). These results strongly indicate that the $[Rh(OAc)_2]_2$ precursor decomposes while keeping the Rh contents in an product particle; i.e. two Rh atoms for each particle. A preliminary x-ray photoelectron spectroscopy (XPS) measurement of the $[Rh(OAc)_2]_2$ precursor on α-$Al_2O_3(0001)$ after decomposition by heating at 650 K under N_2 flow indicated that Rh was oxidized (Rh $3d_{5/2}$ at 309 eV) as shown in Figure 3.3.15(b) and Table 3.2. The binding energy of 309.8 eV is slightly higher than that for

Rh_2O_3 reported in the literature (308.1 – 308.9 eV) and rather close to the value for RhO_2 (309.3 – 309.4 eV).[57, 58]

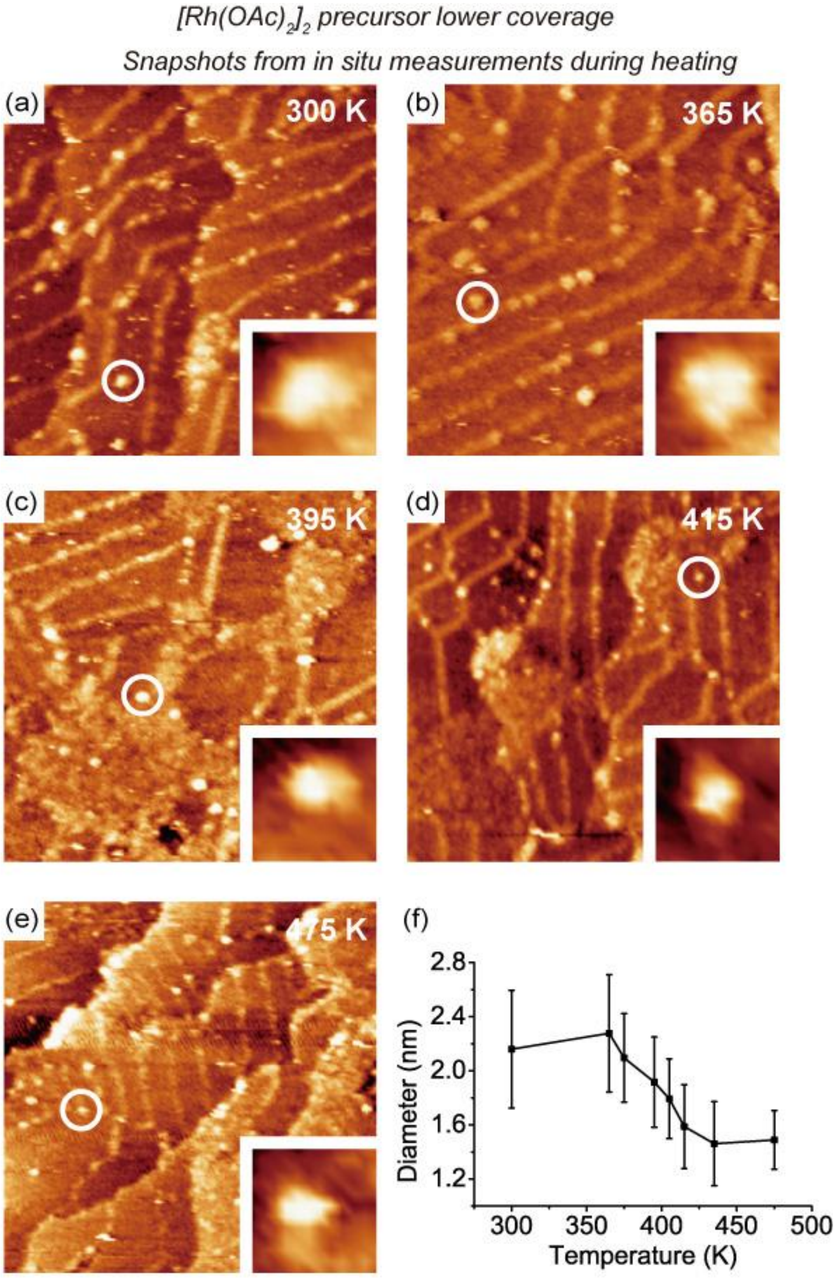

Figure 3.3.14 STM snapshots (70 × 70 nm_2, V_S = 3.0 V, I_t = 0.06 nA) from in situ measurements during heating the Al_2O_3/NiAl(110) surface after deposition of the $[Rh(OAc)_2]_2$ precursor at lower coverage at RT at following temperatures: **(a)** 300 K (before heating), **(b)** 365 K, **(c)** 395 K, **(d)** 415 K, **(e)** 475 K. **(f)** The apparent diameter of the Rh-containing particle during heat treatment.

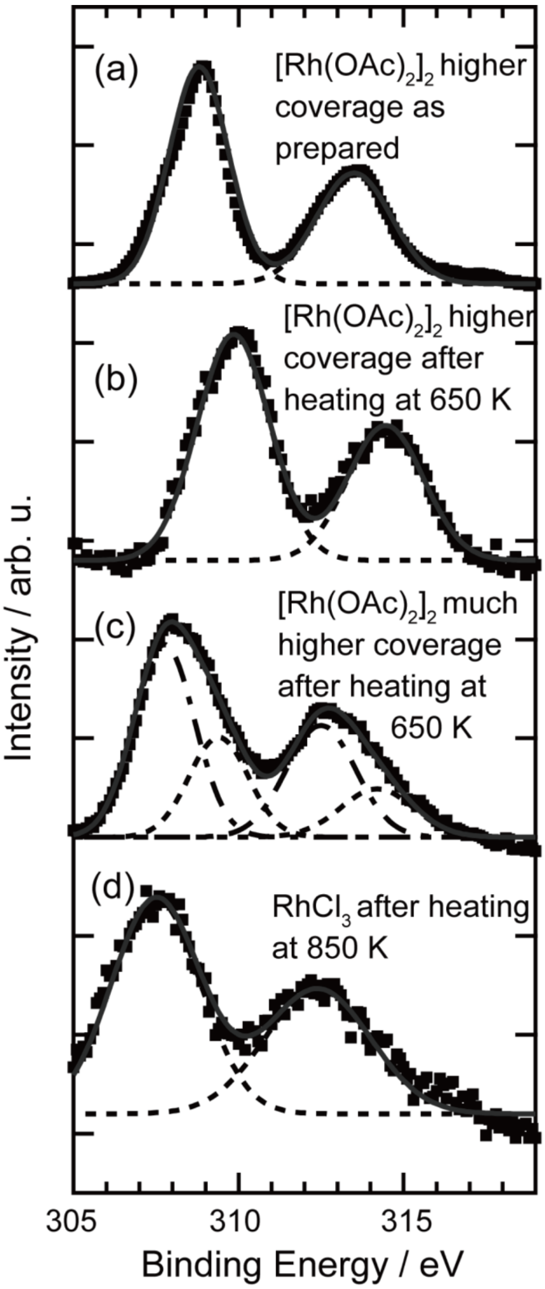

Figure 3.3.15 XPS spectra for the Rh precursors on α-Al_2O_3(0001) by using a monochromatized Al Kα source (Shimadzu KRATOS AXIS Ultra HSA). Solution of a Rh precursor was deposited on Al_2O_3(0001) under N_2 atmosphere and heated under N_2 gas flow. Samples were introduced to the XPS apparatus through air ambient. **(a)** As prepared [Rh(OAc)$_2$]$_2$/Al_2O_3(0001) whose coverage roughly corresponded to the higher coverage sample in STM measurements. **(b)** After heating **(a)** at 650 K. **(c)** After heating [Rh(OAc)$_2$]$_2$/Al_2O_3(0001) with much higher coverage (approximately 5 times larger than **(a)**) at 650 K. **(d)** After heating $RhCl_3$/Al_2O_3(0001) with similar coverage to **(a)** at 850 K.

Table 3.2: Summary of peak position of Rh $3d_{5/2}$ for Figure 3.3.15 by curve fitting

Sample		**Rh $3d_{5/2}$ peak (eV)**
[Rh(OAc)2]2 precursor		
	As-prepared (a)	308.8
	After 650 K (b)	309.8
[Rh(OAc)2]2 precursor (higher coverage)		
	After 650 K (c)	309.4*
		307.8*
RhCl3 precursor		307.8
	After 850 K (d)	307.5

* Deconvoluted to two sets of peaks (dotted line and fragmented line)

Another feature of the decomposed Rh-containing clusters was that their spatial distribution analyzed by STM images was random on the surface as indicated in Table 3.1. It is in contrast to the case of the precursor before decomposition, where preferential adsorption on the line defects such as domain boundaries or steps were observed. Change in the distribution indicates that the $[Rh(OAc)_2]_2$ precursor was not strongly bound even on the line defects and migrated during heating. Besides, the fact that decomposed Rh-containing clusters were observed during heating the surface at 475 K indicated that they were not mobile anymore at this temperature (Figure 3.3.14). If the cluster was mobile in the time scale for scanning several lines, the cluster would show a highly distorted or a fragmented shape. Rh-containing particles with intermediate size were also observed during heating between 365 K and 415 K (Figure 3.3.14). So it is also supposed that the partially decomposed Rh-containing species were much less mobile than the precursor molecule. It was difficult to estimate the mobility of the precursor by in-situ measurements during heating at temperature lower than 365 K because the observation became difficult during heating at low temperatures. Migrating precursor molecules might disturb the observations.

The Rh-containing clusters were not aggregated even after further heating at 850 K as is evident from STM images and histograms in Figure 3.3.16. The apparent diameter of each particle (1.6 ± 0.3 nm) was almost the same as that after heating at 650 K (Figure 3.3.13(g)). Notable difference after this high temperature treatment was the decrease of the cluster density to 0.8×10^{12} clusters cm^{-2}. It corresponds to 43 % reduction.

It is probably due to migration of Rh into the Al_2O_3 film. Freund and co-workers have examined thermal stability of metal particles of Co, Rh, and Pd on Al_2O_3/NiAl(110) prepared by evaporation of metal atoms and the STM images after heating at about 900 K showed considerable decrease in the number of metal particles.[14, 59] Some metal particles disappeared from the surface at much below their desorbing temperature. Therefore they concluded that it was due to migration of metal atoms into the Al_2O_3 film. Agglomeration of metal atoms were also observed as the size of the metal particles left on the surface became larger.

It was confirmed that neither noticeable decrease in density nor the increase in size were observed after heating at 730 K for our Rh-containing clusters. Thus, the Rh-containing clusters obtained in this work showed high thermal stability against aggregation. The clusters began to migrate into the Al_2O_3 film between 730 K and 850 K without coalescence with the other clusters. The decrease in the height of the cluster (Figure 3.3.16(d)) may suggest the change of the cluster structure, however, other supporting data are necessary to conclude that.

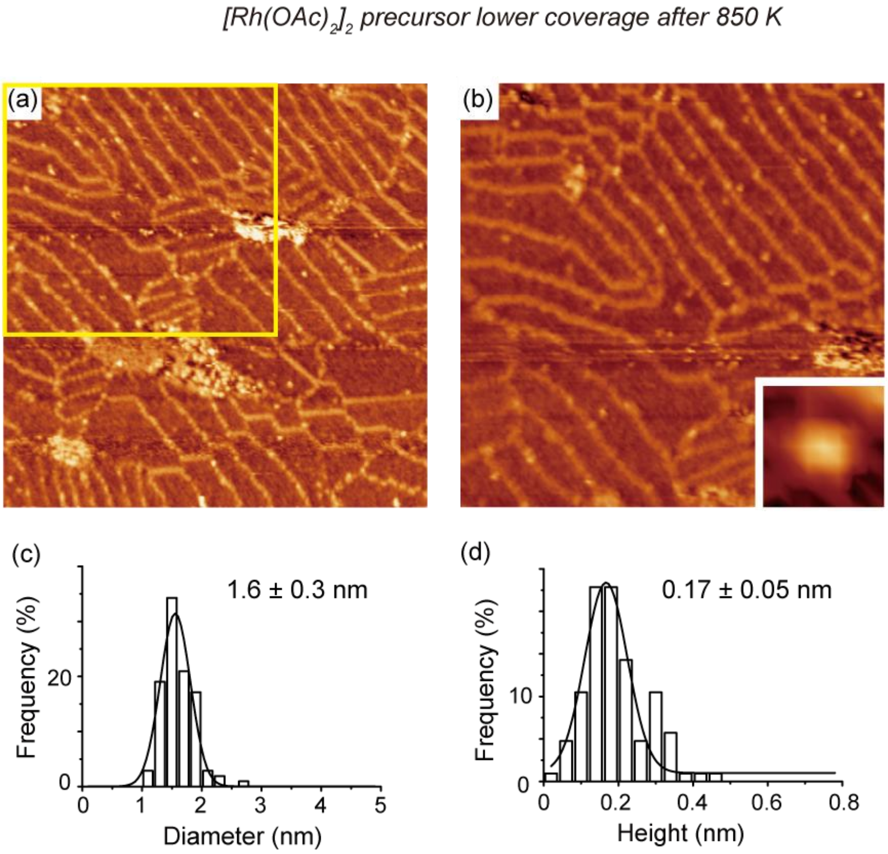

Figure 3.3.16 STM images (V_S = 3.0 V, I_t = 0.06 nA) after the $[Rh(OAc)_2]_2$/ Al_2O_3/NiAl(110) surface at lower coverage (1.4 × 10^{12} molecules cm^{-2}) in Figure 3.3.13 was further heated at 850 K: **(a)** 140 × 140 nm^2, (b) 100 × 100 nm^2. The area in (b) corresponds to a white square in **(a)**. Noticeable decrease in the particle density to 0.8 × 10^{12} clusters cm^{-2} was observed. Inset is a close-up image of a Rh containing particle (5 × 5 nm^2) indicated by a white circle in **(b)**. The apparent diameter and height of about 100 particles obtained from line-profile analyses of several STM images at different areas are summarized in histograms of **(c)** and **(d)**. The histograms indicate the size of each particle did not increase from the values in Figure 3.3.13, thus the decrease in the particle density was not due to the agglomeration of the Rh-containing particles.

3.3.4 Coverage dependency for the distribution of Rh clusters from the $[Rh(OAc)_2]_2$ precursor

Homogeneity is generally hard to be achieved at higher coverage. Five times concentrated $[Rh(OAc)_2]_2$ aqueous solution (1×10^{-4} mol l^{-1}) was injected on a clean Al_2O_3 /NiAl(110) surface with the same condition as the previous deposition other than the concentration. Thus about five times of molecules (7×10^{12} molecules cm^{-2}) were deposited on the surface. An STM image of the surface after the deposition (Figure 3.3.17(a)) shows variation in height and diameter for the deposited particles. Particularly the height shows at least two maxima in a histogram in Figure 3.3.17(g), suggesting that agglomeration of deposited precursor molecules in contrast to the lower coverage case in Figure 3.3.13(b). The average density of the deposited particles was 2.1×10^{12} particles cm^{-2}, thus each aggregation consists of about three molecules in average. In the single crystal of $[Rh^{II}(OAc)_2H_2O]_2$, the wheel-like $[Rh^{II}(OAc)_2]_2$ parts are stacked with displacement along the diagonal axis forming hydrogen bonding through the H_2O adducts. Two maxima in the height may reflect this type of stacking.

When the surface was heated at 650 K to decompose the deposited precursor, however, the situation changed. The produced particles had homogeneous size (Figure 3.3.17(b)), whose average diameter and height (Figures 3.3.17(f) and (h)) were almost the same as those obtained at lower coverage surface (Figures 3.3.13(g) and (i)). Besides, the particle density increased to 5.9×10^{12} particles cm^{-2} and the spatial distribution is close to random one (Table 3.1). Homogeneity and random distribution of the Rh-containing clusters can be confirmed by a wider range STM image (200×200 nm^2) in Figure 3.3.17(d). Thus, the agglomerates of the $[Rh(OAc)_2]_2$ precursor molecules were re-dispersed on the surface before the decomposition process and formed the same Rh-containing clusters in homogeneous size as those observed in the lower coverage case.

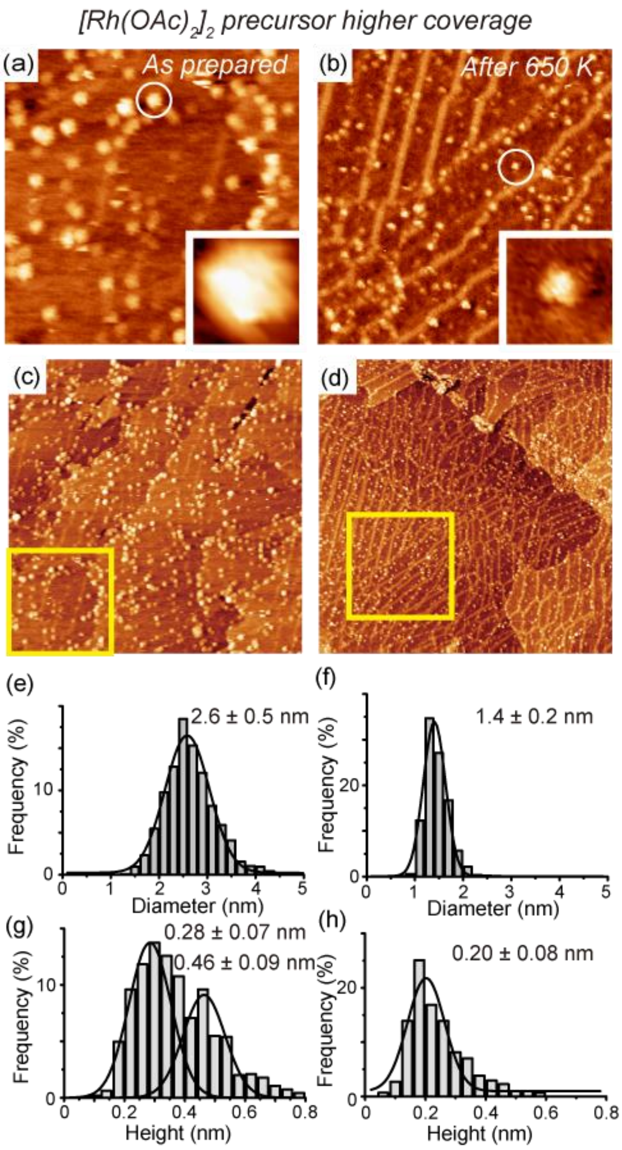

Figure 3.3.17 Adsorption and thermal decomposition of the [Rh(OAc)$_2$]$_2$ precursor on Al$_2$O$_3$/NiAl(110) at higher coverage (five times of Figure 3.3.13). STM images (70 × 70 nm^2, V_S = 3.0 V, I_t = 0.06 nA) obtained **(a)** after deposition of the precursor at RT and **(b)** subsequent heating at 650 K. An inset for each figure is a close-up image of a particle (5 × 5 nm^2) indicated by a white circle. Wide range STM images (200 × 200 nm^2, V_S = 3.0 V, I_t = 0.06 nA) obtained **(c)** after deposition of the [Rh(OAc)$_2$]$_2$ precursor on Al$_2$O$_3$/NiAl(110) at higher coverage and **(d)** subsequent heating at 650 K. Yellow squares in **(c)** and **(d)** correspond to the region of **(a)** and **(b)**, respectively

Apparent diameter and height of about 600 particles obtained from line-profile analyses of several STM images at different areas are summarized in histograms: **(c)** and **(d)** for as-prepared surface, **(e)** and **(f)** for the surface after heat treatment at 650 K, respectively.

The agglomerates of the $[Rh(OAc)_2]_2$ precursor molecules are not necessarily favored on the surface, because only isolated precursor molecules were observed at lower coverage (Figure 3.3.13(b)). Thus they can probably become isolated by thermal energy or by losing a coordinated H_2O molecule that may act as a binder of the molecules as noted above. Once the molecules are isolated, the decomposition process should be the same as that for the lower coverage case.

3. 3. 5 Adsorption and thermal decomposition of the $RhCl_3$ precursor on Al_2O_3/NiAl(110) to examine the precursor dependency

Precursor dependence was examined using a typical inorganic Rh precursor of rhodium chloride ($Rh^{III}Cl_3$). $RhCl_3$ was deposited on a clean Al_2O_3/NiAl(110) surface by injection of 4×10^{-5} mol l^{-1} ethanol solution of the $RhCl_3$ precursor with the same pulse condition as previous experiments. The expected density was 2.8×10^{12} molecules cm^{-2}. A typical STM image after the deposition is shown in Figure 3.3.18(a). The particle size has wider distribution as is obvious from the histograms (Figures 3.3.18(c) and (d)) as well as the STM image. The average particle density was 1.8×10^{12} particles cm^{-2}. Although some large aggregates were found in wider range STM images (see Figure 3.3.19(a)), but their portion was not high.

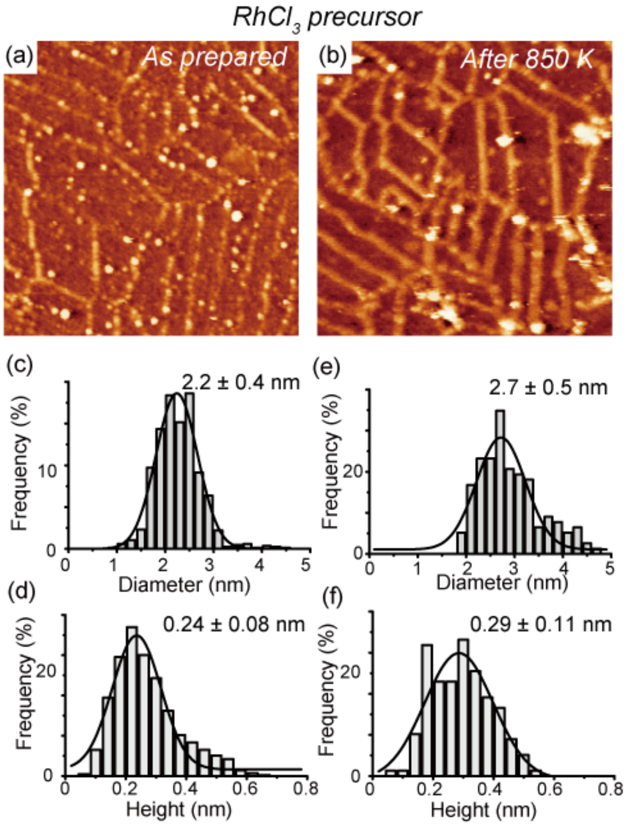

Figure 3.3.18 Adsorption and thermal decomposition of the RhCl$_3$ precursor on Al$_2$O$_3$/NiAl(110). **(a)**, **(b)** STM images (100 × 100 nm^2) obtained **(a)** after deposition of the precursor at RT (V_S = 2.5 V, I_t = 0.07 nA) and **(b)** subsequent heating at 850 K (V_S = 3.0 V, I_t = 0.08 nA). Apparent diameter and height of about 600 particles obtained from line-profile analyses of several STM images at different areas are summarized in histograms: **(c)** and **(d)** for the as-prepared surface, **(e)** and **(f)** for the surface after heat treatment at 850 K, respectively.

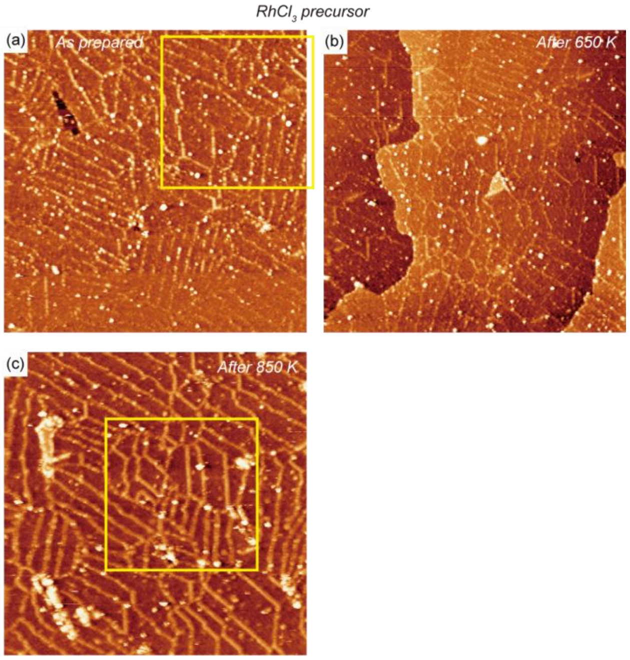

Figure 3.3.19 Wide range STM images (200 × 200 nm^2) obtained **(a)** after deposition of the RhCl3 precursor on Al$_2$O$_3$/NiAl(110) and subsequent heating (V_S = 2.5 V, I_t = 0.07 nA), **(b)** at 650 K (V_S = 2.5 V, I_t = 0.07 nA), and **(c)** at 850 K (V_S = 3.0 V, I_t = 0.08 nA), respectively. Yellow squares in (a) and **(c)** correspond to the region of **Figures 3.3.18(a)** and **(b)**, respectively.

Thermal decomposition of the $RhCl_3$ precursor was examined. One obvious change after heating the $RhCl_3/Al_2O_3$/NiAl(110) surface at 650 K was the decrease in particle density (Table 3.1). But the size of the particles were similar (Table 3.1) as can be confirmed in an STM image in Figure 3.3.19(b). Previous studies indicated that annealing at 773 K was not sufficient to completely decompose $RhCl_3$ precursor on oxide substrates in absence of H_2 as a reductant. [60] Thus, the decrease in particle density probably indicates the beginning of aggregation of partially decomposed species from $RhCl_3$. The size decrease by elimination of Cl atoms may counterbalance the size increase by aggregation. Further decomposition of the precursor can be expected by heating at 850 K. Increase in the particle size was observed as shown in Figure 3.3.18(b) (and wider area image in Figure 3.3.19(c)). Histograms in Figures 3.3.18(e) and (f) reveal that portion of large particles (> 3.5 nm) distinctly increased, which was probably due to sintering of the Rh particles in contrast to the case of the Rh-containing cluster from the $[Rh(OAc)_2]_2$ precursor, where the cluster size was constant even some of them began to migrate into the Al_2O_3 film. Decrease in the particle density to 0.3×10^{12} particles cm^{-2} for $RhCl_3$ after heating at 850 K (Table 3.1) can be attributed to the sintering as well as the migration of Rh atoms into the Al_2O_3 film that generally occurs for metals on Al_2O_3/NiAl(110). [14, 54]

Our preliminary XPS results for $RhCl_3$ precursor on α-Al_2O_3(0001) showed no Cl 2p peak after heating at 850 K under N_2 flow. It indicates that the $RhCl_3$ completely decompose by heating at 850 K and gave a Rh 3d5/2 peak at 307.5 eV (Figure 3.3.15(d) and Table 3.2). This binding energy is slightly higher than that for Rh metal (307.0 eV),[61] and the peak width is broader than the signal from a single component. The XPS measurements were performed after exposing to air for transfer into the XPS chamber, so the surface of metallic Rh may be partially oxidized. [62] Distinct difference in the binding energy of Rh 3d was found between the

$Rh/Al_2O_3$from different precursors. Thus, the different chemical natures of the precursors provided the differences in the size and state of the Rh particles formed by thermal decomposition.

Spatial distribution of the Rh-containing particles did not obviously change by heat treatment in contrast to the case of the $[Rh(OAc)_2]_2$ precursor (Table 3.1). The Rh containing particles from the $RhCl_3$ precursor always favored the line defect sites. Aggregation of partially decomposed species seemed to occur by heating at 650 K as noted above, and finally the Rh particles grew at 850 K probably by Ostwald ripening. Metal nano-particles prepared by physical vapor deposition on Al_2O_3/NiAl(110) also favored the line defect sites. [14, 52] So it seems to be a thermodynamically favored structure for metallic Rh particles regardless of the preparation methods.

3. 3. 6 Possible origins for the precursor dependence of the local structure of Rh/Al_2O_3

The results of the size and the spatial distribution of the two precursors of $[Rh(OAc)_2]_2$ and $RhCl_3$ before and after decomposition on Al_2O_3/NiAl(110), which have been discussed, are summarized in Figure 3.3.20. The $[Rh(OAc)_2]_2$ precursor formed homogeneous Rh clusters which contained two Rh atoms each independent of the initial coverage in the range of less than 10^{13} molecules cm^{-2}, while the $RhCl_3$ formed larger particles containing about a little less than ten Rh atoms. Preliminary XPS results showed that the former one has oxidized Rh, while the latter has metallic Rh after decomposition. Therefore, the final size and states of Rh are quite different depending on the precursor for the same elemental combination of Rh and Al_2O_3. Lei et al. examined a formation of Rh/Al_2O_3/NiAl(111) from a $Rh(CO)_2$(acac) vapor precursor. [33] On this different Al_2O_3 structure, they observed preferential adsorption of the $Rh(CO)_2$(acac) precursor at specific sites but aggregation of Rh metal was found by heating at 673 K. Therefore, the situation is similar to the $RhCl_3$ precursor in our study.

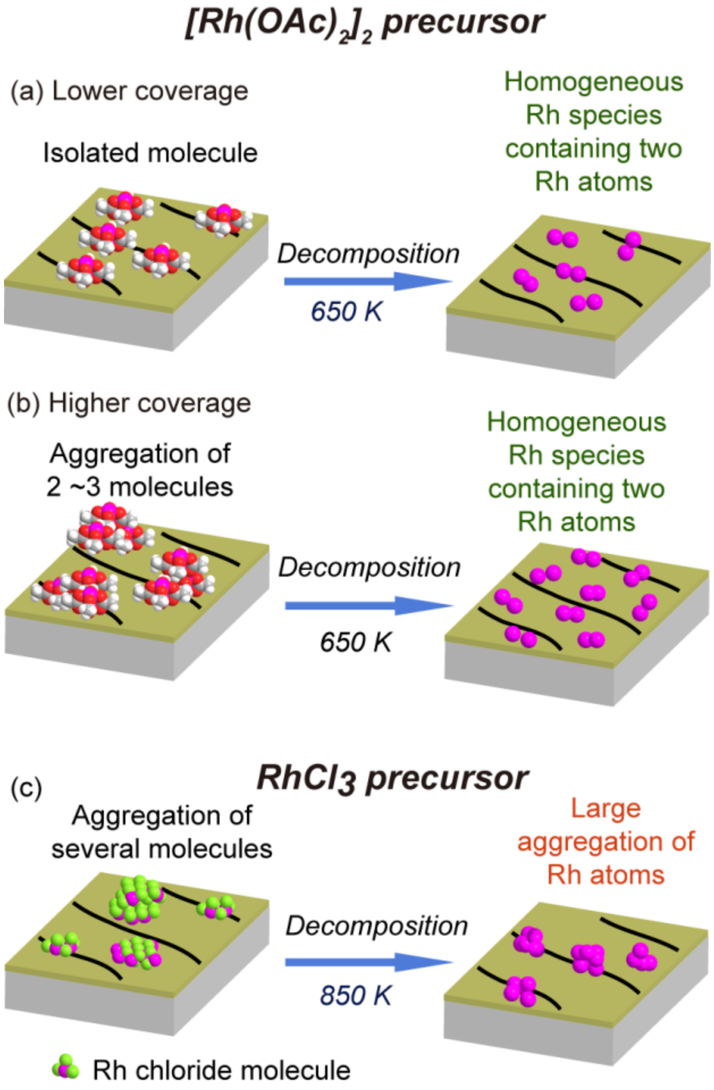

Figure 3.3.20 Schematic summary of the states of precursors before and after thermal decomposition on Al_2O_3/NiAl(110): **(a),(b)** for the $[Rh(OAc)_2]_2$ precursor at lower and higher coverages, respectively, **(c)** for the $RhCl_3$ precursor.

Formation of homogeneous metal clusters on oxide surfaces was reported in literature. Small clusters of Cu [63] and Ni [64] on $TiO_2(110)$ prepared by evaporation of metal atoms showed narrow size distributions, whose major contribution was considered to be the strain originating from the lattice mismatch between the metal particle and the substrate. This mechanism is not applicable to our results on $[Rh(OAc)_2]_2/Al_2O_3/NiAl(110)$ because each particle contains only two Rh atoms, therefore, too small to assume the lattice mismatch. Takakusagi et al reported the self-limiting growth of Pt nanoparticles from a metal-organic precursor on $TiO_2(110)$. [65] Their model assumed the incorporation of the substrate material (TiO_x) into the Pt particle particular at its edge to block further decomposition of the precursor at the particle, thus it was the kinetics limited growth. For the decomposition of the $[Rh(OAc)_2]_2$ precursor in the present study, the decomposed Rh-containing cluster did not serve the active site for decomposition of another precursor molecule as is evident from the higher coverage case in Figure 3.3.17, because the particle size was the same as the lower coverage case in Figure 3.3.13. Interaction between the precursor and the Al_2O_3 is perhaps a key issue, but mixing of the substrate material does not seem to be a case because the spatial distribution of the Rh containing clusters was at random: at inside of domains and line defects (Table 3.1). The line defects have different electronic states as noted above, [44, 45, 47] but the cluster formation was not affected by that. High thermal stability of the cluster suggests that formation of chemical bond between the cluster and substrate oxygen. The result of Rh 3d XPS partially supports this assignment. Therefore, the strong affinity of Rh of partially decomposed precursor against surface oxygen seems to be the origin of the nonspecific formation of the cluster.

Degree of agglomeration of the precursor may relate with the particle size after the decomposition of the precursor. $RhCl_3$ tends to be agglomerated because each $RhCl_3$ component in the $RhCl_3$ crystal connects to surroundings by Rh-Cl bonds with the same strength as intramolecular bonds.[65] Actually the particle size of the as-prepared $RhCl_3/Al_2O_3$/NiAl(110) was not homogeneous (Figures 3.3.18(a) and Figure 3.3.19(a)). Anyway, the size of particles after heating at 850 K became larger (Figures 3.3.18(b) and Figure 3.3.19(c)), so further aggregation during heating was evident. In contrast, the $[Rh(OAc)_2]_2$ precursor at higher coverage redispersed as particles containing two Rh atoms each during thermal decomposition (Figures 3.3.17(b) and (d)). It is noted, however, that at much higher coverage of the $[Rh(OAc)_2]_2$ precursor on α-Al_2O_3(0001), XPS showed a dominant peak of metallic Rh (Rh $3d_{5/2}$ peak at 307 eV) after thermal decomposition of the precursor in contrast to oxidized Rh for the coverage used for the present study. Therefore, the agglomeration of Rh atoms, which is thermodynamically favorable, cannot be avoided completely, but the preference was greatly reduced by using the $[Rh(OAc)_2]_2$ precursor.

3.4. Conclusions

By adopting the pulse-deposition method to deposit Rh precursors of $[Rh^{II}(OAc)_2]_2$ and $RhCl_3$ on a clean Al_2O_3/NiAl(110) surface, precursor dependence of the final forms of Rh/Al_2O_3 was examined with high spatial resolution by using STM. By analyses of STM images on the size and spatial distribution of Rh-containing species, it was found that homogeneous and thermally stable Rh species containing two Rh atoms each were formed by decomposition of the $[Rh(OAc)_2]_2$ precursor in the range less than 10^{13} molecules cm^{-2}, while large metallic Rh particles were formed from the $RhCl_3$ precursor. The decomposition process of the acetate ligands was suggested to be a key for the different states of the decomposed Rh containing products.

3.5 Appendix

Procedure for estimation of the tip-size effect

A simple model for the latter case is summarized in the Figure 3.5.1. It is based on an assumption that the minimum distance between the tip and the nanoparticle (major tunneling path length) is constant, similar to the method firstly proposed by Keller.[66] The problem is reduced to a simple geometry. As shown in Figure 3.5.1(a), the shapes of the tip apex and nanoparticle are assumed to be a hemisphere and a disc, respectively. The true diameter of the naoparticle is $d + 2r$. The apparent diameter of the nanoparticle D is described by a following equation.

$$D = d + 2\sqrt{(R+r)^2 - (R-r)^2} = d + 2\sqrt{4Rr} \qquad (3.\ 1)$$

Therefore, if one knows the effective diameter of the tip apex R, the true diameter of the nanoparticle can be calculated from the apparent diameter and height from the STM image. A typical radius of an electrochemically etched tungsten tip apex is about 10 nm, but effective radius R must be smaller than this value, from several Å to a few nm. The effective radius of the tip apex R was estimated by using the width of anti-phase domain boundaries (APDB) (ca. 2.09 nm) of the Al_2O_3/NiAl(110) substrate as a standard by adapting eq. (3.1). Typical line profiles of APDB from an STM image are shown in Figure 3.5.1(b). Based on the histograms of the apparent height and apparent width of APDB measured from such line profiles, the average height and width were 0.21 nm and 2.9 nm respectively. The effective tip radius was calculated to be about 0.63 nm for this image. With the estimated effective tip radius R, the intrinsic diameter of the particle can be estimated from model in Figure 3.5.1(a) and eq. (3.1).

Based on this model, the relation between the size of a protruding object and the range of an effective tip radius can be simulated. Figure 3.5.1(c) shows such an example. The observed particle diameter and height for the $[Rh(OAc)_2]_2$ precursor adsorbed on

Al_2O_3/NiAl(110) in Figure 3.3.13 was 2.1 ± 0.2 nm and 0.28 ± 0.10 nm, respectively. When the model in Figure 3.5.1(a) and eq. (3.1) were adopted for a $[Rh(OAc)_2]_2$ monomer, a dimer, and a trimer, the effective tip radii that can reproduce the experimental result are gray, red, and blue region, respectively. The effective tip radius of less than 0.3 nm is not realistic, thus a monomer is the most probable for the observed particle (Note: the estimation depends on the model, e.g. shapes of the tip and the particle. Besides, one may have to consider variation of local density of states on the particle. Therefore, the estimation does not intend to reproduce the real structure or real diameter, but makes the particle sizes in different STM images with different effective tip radii more comparable with each other.).

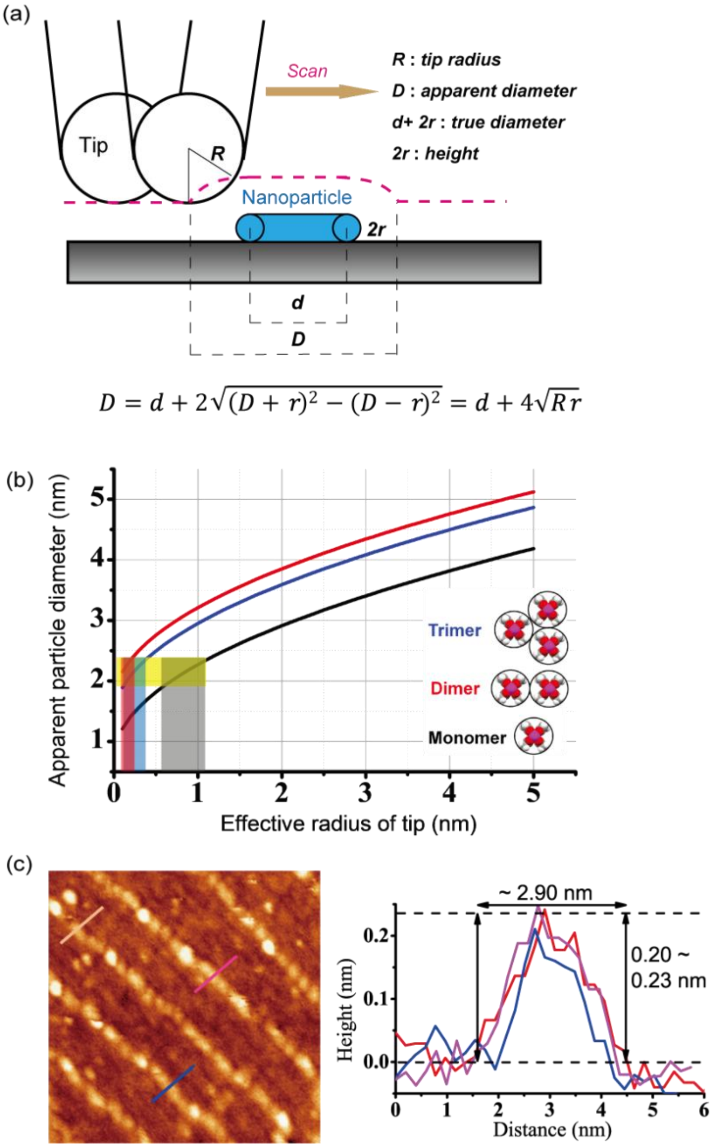

$$D = d + 2\sqrt{(D + r)^2 - (D - r)^2} = d + 4\sqrt{Rr}$$

Figure 3.5.1 Schematic of estimation of the tip-effect in the STM image. **(a)** Illustration of how the STM measurement with a finite size tip overestimates the size of a protruding object on a flat surface. The shapes of the tip apex and the nanoparticle are assumed to be a hemisphere and a disc, respectively and it is assumed that the minimum distance between the tip and the nanoparticle (major tunneling path length) is constant. The tip traces the dotted line. **(b)** The apparent width and height of anti-phase domain boundaries of the Al_2O_3/NiAl(110) substrate for estimation of the effective tip radius *R*. **(c)** Relationship between the effective tip radius *R* and the apparent particle diameter. Three kinds of particles are calculated here: black, red, blue lines correspond to a $[Rh(OAc)_2]_2$ monomer, a dimer, and a trimer, respectively. The three colored blocks show the corresponding effective tip radius range that can reproduce the observed apparent diameter (2.1 ±0.2 nm, yellow block) for the $[Rh(OAc)_2]_2$ precursor adsorbed on Al_2O_3/NiAl(110) (**Figure 3.3.13(b)**)

References

1 G. Ertl, H. Knözinger, F. Schüth, J. Weitkamp, "*Handbook of Heterogeneous Catalysis*": Wiley-VCH Verlagsgesellschaft mbH: Weinheim, 2nd edn. , 2007.

2 D. C. Sherrington, A. P. Kybett, "*Supported Catalysts and Their Applications*": The Royal Society of Chemistry: Cambridge, 2001

3 E. G. Derouane, *Cattech,* 2001, **5**, 214.

4 M. Valden, X. Lai, D. W. Goodman, *Science* 1998, **281**, 1647.

5 W. E. Kaden, W. A. Kunel, M. D. Kane, F. S. Roberts, S. L. Anderson, *J. Am. Chem. Soc.* 2010, **132**, 13097.

6 K. Yuzaki, T. Yarimizu, K. Aoyagi, S. Ito, K. Kunimori, *Catal. Today* 1998, **45**, 129.

7 H. Sakagami, S. Ogata, N. Takahashi, T. Matsuda, *Phys. Chem. Chem. Phys.* 2001, **3**, 1930.

8 S. Mostafa, F. Behafarid, J. R. Croy, L. K. Ono, L. Li, J. C. Yang, A. I. Frenkel, B. R. Cuenya; *J. Am. Chem. Soc.* 2010; **132**; 15714.

9 B. C. Gates, *Chem. Rev.* 1995, **95**, 511

10 K. K. Bando, K. Asakura, H. Arakawa, K. Isobe, Y. Iwasawa, *J. Phys. Chem.* 1996, **100**, 13636.

11 M. Tada, R. Bal, Y. Iwasawa, *Catal. Today* 2006, **117**, 141.

12 N. H. H. Abu Bakar, M. M. Bettahar, M. Abu Bakar, S. Monteverdi, J. Ismail, Catal. Lett. 2009, **130**, 440.

13 S. –H. Kang, J. W. Bae, P. S. S. Prasad, S. –J. Park, K. –J. Woo, K. –W. Jun, *Catal. Lett.* 2009, **130**, 630.

14 A. Desikusumastuti Z. Qin, T. Staudt, M. Happel, Y. Lykhach, M. Laurin, Sh.Shaikutdinov, J. Libuda, *Surf. Sci.* 2008, **603**, L9.

15 M. Heemeier, S. Stempel, Sh. K. Shaikhutdinov, J. Libuda, M. Bäumer, R. J. Oldman, S. D. Jackson, H. –J. Freund, *Surf. Sci.* 2003, **523**, 103.

16 W. T. Wallace, B. K. Min, D. W. Goodman, *J. Mol. Catal. A* 2005, **228**, 3.

17 H. Kusana, K. K. Bando, K. Okabe, H. Arakawa, *Appl. Catal. A* 2001, **205**, 285.

18 P. Kim, H. Kim, J. B. Joo, W. Kim, I. K. Song, J. Yi, *J. Mol. Catal. A* 2006, **256**, 178.

19 E. Ronzón, G. D. Angel, *J. Mol. Catal. A* 1999, **148**, 105.

20 M. C. Roman-Martinez, D. Cazorla-Amoros, A. Linares-Solano, C. S. De Lecea, H. Yamashita, M. Anpo, *Carbon*, 1995, **33**, 3.

21 Z. Xu, F. –S. Xiao, S. K. Purnell, O. Alexeev, S. Kawi, S. E. Deutsch, B. C. Gates, *Nature* 1994, **372**, 346.

22 Q. Fu, T. Wagner, *Surf. Sci. Rep.* 2007, **62**, 431.

23 J. H. Kwak, J. Hu, D. Mei, C. –W. Yi, D. H. Kim, C. H. F. Peden, L. F. Allard, J. Szanyi, *Science* 2009, **325**, 1670.

24 N. Nilius, *Surf. Sci. Rep.* 2009, **64**, 595.

25 S. Ro, A. Baiker, *Chem. Rev.* 2009, **109**, 4054.

26 G. A. Somorjai, R. M. Rioux, *Catal. Today* 2005, **100**, 201.

27 J. W. Niemantsverdriet, A. F. P. Engelen, A. M. de Jong, W. Wieldraaijer, G. J. Kramer, *Appl. Surf. Sci.* 1999, **144-145**, 366.

28 C. M. Leewis, W. M. M. Kessels, M. C. M. van de Sanden, J. W. Niemantsverdriet, *J. Vac. Sci. Technol. A* 2006, **24**, 296.

29 F. Yang, E. Trufan, R. D. Adams, D. W. Goodman, *J. Phys. Chem. C* 2008, **112**, 14233.

30 Y. Maeda, M. Okumura, Daté S. Tsubota, M. Haruta, *Surf. Sci.* 2002, **514**, 267.

31 J. Evans, B. Hayden, F. Mosselmans, A. Murray, *Surf. Sci.* 1994, **301**, 61.

32 J. H. Horton, J. G. Shapter, T. Cheng, W. N. Lennard, P. R. Norton, *Surf. Sci.* 1997, **375**, 171.

33 Y. Lei, A. Uhl, C. Becker, K. Wandelt, B. C. Gates, R. Meyer, M. Trenary, *Phys, Chem. Chem. Phys.* 2010, **12**, 1264.

34 A. Uhl, Y. Lei. H. Khosravian, C. Becker, K. Wandelt, R. D. Adams, M. Trenary, R. Meyer, R. *J. Phys. Chem. C* 2010, **114,** 17062.

35 T. Kanno, H. Tanaka, T. Nakamura, H. Tabata, T. Kawai, *Jpn. J. Appl. Phys , Part2* 1999, **38**, L606-L607.

36 Y. Terada, B. K. Choi, S. Heike, M. Fujimori, T. Hashizume, *Nano Lett.* 2003, **3**, 527.

37 Y. Shirai, J. F. Morin, T. Sasaki, J. M. Guerrero, J. M. Tour, *Chem. Soc. Rev.* 2006, **35**, 1043.

38 R. Bernard, G. Comtet, G. Dujardin, V. Huc, J. Mayne, *Appl. Phys. Lett.* 2005, **87**, 053114.

39 Y. Lai, H. Zhuang, K. Xie, D. Gong, Y. Tang, L. Sun, C. Lin, Z. Chen *New J. Chem.* 2010, **34**, 1335,

40 S. Guo, A. Kandel, *J. Phys. Chem. Lett.* 2010, **1**, 420.

41 M. Baumer, H. –J. Freund, *Prog. Surf. Sci.* 1999, **61**, 127.

42 R. M. Jaeger, H. Kuhelenbck, H. –J. Freund, M. Wuttig, W. Hoffmann, R. Franchy, H. Ibach, *Surf. Sci.* 1991, **259**, 235.

43 G. Kresse, M. Schmid, E. Napetschnig, M. Shishkin. L. Kohler, P. Varge, *Science*, 2005, **308**, 1440.

44 N. Nilius, M. Kulawik, H. –P. Rust, H. –J. Freund, *Phys. Rev. B* 2004, **69**, 121401.

45 M. Schmid, M. Shishkin, G. Kresse, E. Napetschnig, P. Varga, M. Kulawik, N. Nilius, H. –P. Rust, H. –J. Freund, *Phys. Rev. Lett*. 2006, **97**, 046101.

46 G. H. Simon, T. Konig, H. –P. Rust, M. Heyde, H. -J. Freund, *New. J. Phys.* 2009, **11**, 093009.

47 L. Heinke, L. Lichtenstein, G. H. Simon, T. Konig, M. Heyde, H. –J. Freund, *Phys. Rev. B* 2010, **82**, 075430.

48 Libuda, J. ; Freund, H. -J. *Surf. Sci. Rep.* **2005**, *57*, 157.

49 A. Deikusumastuti, T. Staudt, Z. Qin, M. Happel, M. Laurin, Y. Lykhach, S. Shaikutdinov, F. Rohr, J. Libuda, *ChemPhysChem.* 2008, **9**, 2191.

50 M. Sobota, M. Schmid, M. Happel, M.. Amende, F. Maier, H. –P. Steinruck, N. Paape, P. Wasserscheid, M. Laurin, M. J. Gottfried, J. Libuda, *Phys. Chem. Chem. Phys.* 2010, **12**, 10610.

51 F. A. Cotton, B. G. Deboer, M. D. Laprade, J. R. Pipal, D. A. Ucko, *Acta Crystallogr.* 1971, **B27**, 1664.

52 S. A. Johnson, H. R. Hunt, H. M. Neumann, *Inorg. Chem.* 1963, **2**, 960

53 D. Keller, *Surf. Sci.* 1991, **253**, 353.

54 J. S. Villarrubia, *Surf. Sci.* 1994, **321**, 287.

55 M. Bäumer, M.Frank, J. Libuda, S. Stempel, H. –J. Freund, *Surf. Sci.* 1997, **391**, 204.

56 J. Kitchens, J. L. Bear, *J. Inorg. Nucl. Chem.* 1970, **32**, 49.

57 Z. Weng-Sieh, R. Gronsky, A. T. Bell, *J. Catal.* 1997, **170**, 62.

58 S. Suhonen, M. Valden, M. Hietikko, R. Laitinen, A. Savimäki, M. Härkönen, *Appl. Catal., A* 2001, **218**, 151.

59 M. Heemeier, S. Stempel, SH. K. Shaikhutdinov, J. Libuda, M. Bumäer, R. J. Oldman, S. D. Jackson, H. -J. Freund, *Surf. Sci.* 2003, **523**, 103.

60 G. Munuera, A. R. Gozalez-Elipe, J. P. Epsinos, A. Munoz, J. C. Conesa, J. Soria, J.Sanz, *Catal. Today* 1988, **2**, 663.

61 D. R. Lide, "*Handbook of Chemistry and Physics*", 88th ed.; CRC Press: Boca Raton, FL, 2007.

62 H. J. Borg, L. C. A.van den Oetelaar, J. W. Niemantsverdriet, *Catal. Lett.* 1993, 17, 81.

63 D. A. Chen, M. C. Bartelt, R. Q. Hwang, K. F. McCarty, *Surf. Sci.* 2000, **50**, 78.

64 K. Fujikawa, S. Suzuki, Y. Koike, W. –J. Chun, K. Asakura, *Surf. Sci.* 2006, **600**, L117.

65 H. Bärnighausen, B.K. Handa, *J. Less Common Met.* 1964, **6**, 226.

66 D. Keller, *Surf. Sci.* 1991, **253**, 353.

Chapter 4 XAFS Analyses on Precursor-Dependent Local Structures of Supported Rh Cluster Catalysts

4.1 Introduction

X-ray absorption fine structure (XAFS) spectroscopy provides a means of deriving the chemical state (by XANES), interatomic distance and coordination number (by EXAFS) about a chosen atom in either ordered surface (e.g. single crystal oxide thin film) or totally amorphous media (e.g. supported catalyst powder). In this respect, it has very considerable applicability to the fields of catalysts, nanoscience, semiconductor industry, etc. Many industrial catalysts are heterogeneous solids, thus their structural information is difficult to be obtained. Without any clear structural models for the active sites, the correlation of the local structures and the catalytic activity or the reaction mechanism cannot be elucidated. A promising solution called model surface study (detailed discussion in Chapter 1) is to use some well-ordered model surface to reduce the structural complexity of the material and allow the use of diffraction techniques (e.g. X-ray or neutron for bulk solids, low energy electron for solid surfaces). However, lots of problems still remain. Especially, a “material gap” problem refers to the structural difference between a real catalyst and a model system. Therefore, the XAFS techniques which are applicable to all of these types of materials can act as a bridge-building technique correlating information between the model and the real catalyst.

Successful applications of the XAFS technique on active metal sites of supported catalysts were found in a pioneering work of Lytle and coworkers.[1, 2] Koningsberger has analyzed metal-interface structures of supported metal catalysts, by using a different file method to distinguish weak contribution of metal-interface interaction from much stronger metal-metal interaction.[3] On the other hand, the bond orientation and the location of active metal sites on a support surface are also critical issues in understanding the supported catalysts.[4] However, in regard to real catalysts (powder), the structural information of active sites is derived as one dimensional value averaged over all directions. Recently, Asakura and coworkers developed a technique called polarization-dependent total-reflection fluorescence XAFS (PTRF-XAFS) to obtain detailed structural information selectively along the direction of an X-ray electric vector.[5] When one measures EXAFS of metal species on a flat substrate (e.g. α-Al_2O_3, TiO_2(110)) with different polarizations, the pseudo-three dimensional structural information can be obtained. During the past ten years, they used this technique and a real space model/FEFF calculation to clarify various structures of metals highly dispersed on single crystal oxide surfaces such as Co_3O_4/Al_2O_3(0001),[6] Pt/Al_2O_3(0001),[7] Ni/Al_2O_3(0001),[8] Mo/TiO_2(110),[9] Cu/TiO_2(110)[10] and so on. Thus, XAFS techniques have been proved to be a powerful tool to study nano-structures of active sites of catalysts.

In previous STM study, in order to clarify the precursor-dependent structures of Rh/Al_2O_3 catalysts, we have adopted the pulse-deposition method to deposit two Rh precursors of rhodium acetate dimer ($[Rh^{II}(OAc)_2]_2$) and rhodium trichloride anhydrous ($RhCl_3$) from their solution to a clean Al_2O_3/NiAl(110) surface under vacuum. By STM observation before and after thermal decomposition of the precursor, it was found that the $[Rh^{II}(OAc)_2]_2$ precursor formed homogeneous and oxidized Rh clusters containing two Rh atoms each (Rh dimer species), in contrast to agglomeration to metallic Rh particles from the $RhCl_3$ precursor. Furthermore, the distribution of Rh dimer species was random, regardless of different local structures of Al_2O_3. It indicates that this process can be adapted not only on the Al_2O_3 thin film but also on the Al_2O_3 single crystal surface, the Al_2O_3 polycrystal surface or even a Al_2O_3 powder with large surface area. The homogeneity and stability of active species are the important issues in the field of catalyst, moreover, the homogenous Rh dimer species may be used as nucleation sites for various Rh-containing compounds (e.g. Pt-Rh particles). Thus it is worthy to clarify the local structure and the formation process of the Rh species on an Al_2O_3 powder and XAFS is the best characterization method for this purpose.

4.2 Experimental Details

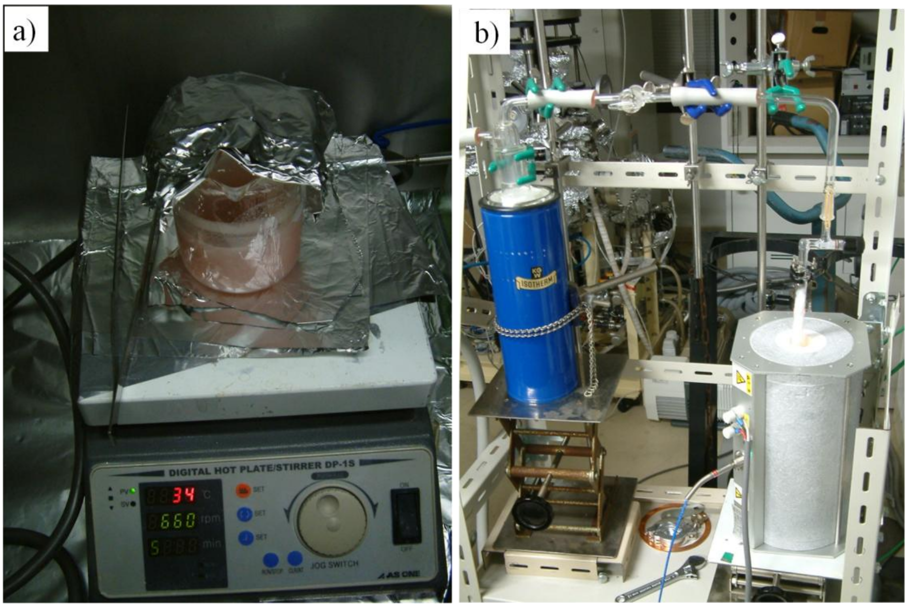

Figure 4.2.1 Preparation of Rh/Al_2O_3 samples **a)** Impregnation process of Rh precursor/Al_2O_3. **b)** Heat treatment set up.

The Rh/Al_2O_3 catalysts were prepared from three kinds of Rh precursors, $[Rh^{II}(OAc)_2]_2$ (Alfa Aesar), $Rh^{III}(OAc)_3$ (Soekawa Chemical), and $RhCl_3$ anhydrous (Wako) on γ-Al_2O_3 (JRC-ALO-6) . The precursor $Rh^{III}(OAc)_3$ was selected because of its local structure and valence state similar to $RhCl_3$. The Rh loading of all the samples were set at 0.2 wt %. We prepared the Rh/γ-Al_2O_3 catalysts by incipient wetness impregnation method. Before the impregnation, the γ-Al_2O_3 support was evacuated at 1100 K for 1 h and then transferred to a N_2 globe box without exposing to air. The impregnation processes were performed in N_2 globe box as shown in the left panel of Figure 4.2.1. The γ-Al_2O_3 powder was immerged into an ethanol solution (2.4×10^{-4} mol l^{-1}) containing the precursor and stirred for 8 h before the ethanol solvent was removed by evacuation. The as-prepared samples are then heated in vacuum to 500 K, 650 K, 850 K, respectively as shown in the right panel of Figure 4.2.1.

The setup of XAFS measurements has been described in Chapter 2.

4.3 Results and Discussion

4.3.1 XANES Spectra

Figures 4.3.1(a)-(c) show Rh K-edge XANES spectra of Rh/γ-Al_2O_3 samples prepared from three precursor of $[Rh^{II}(OAc)_2]_2$, $Rh^{III}(OAc)_3$, and $RhCl_3$. In each figure, a blue curve is a spectrum of the as-prepared sample and black curves are spectra after heat treatments (each sample will be denoted as S-T hereafter; S = Ac-d ($[Rh^{II}(OAc)_2]_2$), Ac-m ($Rh^{III}(OAc)_3$), CL ($RhCl_3$), T = 650 or 850. For example, Ac-d-850 denotes the sample which was prepared from the $[Rh^{II}(OAc)_2]_2$ precursor and heated at 850 K). Red curves in Figures 4.3.1(d) were spectra of the reference materials.

As for the $[Rh^{II}(OAc)_2]_2$ precursor (Figure 4.3.1(a)), the XANES spectrum of the as-prepared sample has features similar to the bulk $[Rh^{II}(OAc)_2]_2$ reference without any obvious peak shift or change in relative amplitude of absorption bands. It suggests that the precursor was fixed on the γ-Al_2O_3 surface with negligible structure change and charge transfer between the precursor and support. Heat treatments of the sample changed the shape of XANES spectra. Two major changes can be found in the spectra after heating at 650 K; downward shift of the peak at 23237 eV to 23230 eV and disappearance of the peak at 23298 eV. These changes already began to be observed after heating at 500 K (not shown) and did not change further by heating the sample to 850 K. As XANES region usually gives information about the unoccupied states related to the coordination environment of the X-ray-absorbed atom, we suppose that the Rh-O and Rh-Rh bonds have changed by thermal decomposition of the precursor. XANES spectra of Ac-d-650 and Ac-d-850 do not have a peak at 23255 eV, which is typical for metallic Rh, and they are rather analogous with that of the Rh_2O_3 reference shown in Figure 4.3.1(d). It suggests that the decomposed product from the $[Rh^{II}(OAc)_2]_2$ precursor possesses a local structure around a Rh atom similar to Rh_2O_3. Similar results to the Rh dimer precursor were obtained for the $Rh^{III}(OAc)_3$ precursor (Figure 4.3.1(b)). The XANES spectrum of as prepared sample was different from that of the $[Rh^{II}(OAc)_2]_2$ precursor, but the spectra after thermal decomposition seem to be very similar to those from the $[Rh^{II}(OAc)_2]_2$ precursor.

On the contrary, quite different spectra were obtained after thermal decomposition of the $RhCl_3$ precursor on γ-Al_2O_3 (Figure 4.3.1(c)). Peak shape with two maxima at 23230 eV and 23255 eV of CL-650 and CL-850 was similar to that of Rh foil shown in Figure 4.3.1(d). It strongly suggests formation of metallic Rh species. Besides, these two maxima became shaper and stronger by higher temperature heating at 850 K. Thus, we suppose that the most of the $RhCl_3$ precursors have already decomposed at 650 K to form metallic Rh particles. Aggregation of Rh particles probably occurred at higher temperature. It will become clear by EXAFS analyses in the next section.

As a brief summary of XANES analyses, thermally decomposed Rh species on γ-Al_2O_3 were quite different depending on the Rh precursor: Rh oxide-like compounds from the Rh acetate precursors, $[Rh^{II}(OAc)_2]_2$ and $Rh^{III}(OAc)_3$, and metallic Rh species from the $RhCl_3$ precursor.

4.3.2 EXAFS Spectra

Each EXAFS oscillation curve was extracted from the X-ray absorption spectrum by removing the background, which was calculated as X-ray absorbance of isolated atoms. I used Victoreen1 function ($C\lambda^3 - D\lambda^4$+Const.) to calculate the background. Then, the oscillation curve $\chi(E)$ was converted to $\chi(k)$ and multiplied by three power of k to give $k^3\chi(k)$ to compensate for the attenuation of the EXAFS amplitude at high *k* vales. Figures 4.3.2(a)-(c) show the $k^3\chi(k)$ curves from the $[Rh^{II}(OAc)_2]_2$, $Rh^{III}(OAc)_3$, and $RhCl_3$ on γ-Al_2O_3, respectively. The $k^3\chi(k)$ curves can provide the most accurate information about the local structure of absorbing atom because there is no loss of original data (if the removed background is correct).

Considerable differences were found by heat treatments of the sample from the $RhCl_3$ precursor (Figure 4.3.2(c)). The $k^3\chi(k)$ curves of CL-650 and CL-850 show larger amplitude at high *k* region, which is typical for metallic species as is evident from the curve of Rh foil in Figure 4.3.2(d). This result is consistent with the XANES results.

In the case of the $[Rh^{II}(OAc)_2]_2$ precursor (Figure 4.3.2(a)), the $k^3\chi(k)$ oscillation of the Ac-d-650 was different from that of the as prepared sample in the oscillation periodicity and amplitude. The curve finds some similarity with that of the Rh_2O_3 reference but also has some differences. As I supposed by XANES spectra, the local structure of Ac-d-650 and that of Rh_2O_3 somewhat resemble with each other but curve fitting analyses are necessary for further comparisons. Although the S/N ratio was poor for the $k^3\chi(k)$ curve of Ac-d-850, no obvious change from the Ac-d-650 curve was observed. The result suggests high thermal stability of the Rh species formed from the $[Rh^{II}(OAc)_2]_2$ precursor.

After thermal decomposition of the $Rh^{III}(OAc)_3$ precursor, the periodicity of the $k^3\chi(k)$ oscillation in Figure 4.3.2(b) looked similar to that of the $[Rh^{II}(OAc)_2]_2$ precursor after thermal decomposition (Figure 4.3.2(a)). However, careful comparison reveals that the curves are apparently different in the range from 9 $Å^{-1}$ to 11 $Å^{-1}$. Ac-d-650 exhibits a double-peak feature in this range which rather corresponds to the Rh_2O_3 reference. In contrast to that, Ac-m-650 shows a single peak in this range. As the Rh-O bonds (lighter element of oxygen) contribute to smaller *k* range, contribution of the Rh-Rh bond becomes clearer at larger *k* range. We can suppose that the coordination conditions of the first shell (Rh-O bonds) of Ac-d-650 and

Ac-m-650 are similar with each other, however, the second shell (Rh-Rh bonds) is different. This hypothesis can be confirmed by the Fourier transforms of $k^3\chi(k)$ and their curve-fittings.

Figure 4.3.3(a) - (c) show the Fourier transforms of the $k^3\chi(k)$ curves in Figure 4.3.2. Each curve corresponds to the radial distribution function from the Rh atom contained in each sample and can offer instinctive insights into the structure of the Rh species. In the case of the $RhCl_3$ precursor, only one peak appeared around 0.27 nm after heat treatments (CL-650 and CL-850). It can be assigned to the Rh-Rh bond of Rh metal by comparing with the corresponding peak of the Rh foil. Increase of the peak intensity at higher temperature indicates the increase of coordination number (growth to larger Rh particles). In contrast, in the case of Rh acetate precursors, both of $[Rh^{II}(OAc)_2]_2$ and $Rh^{III}(OAc)_3$, the first peak around 0.20 nm assignable to the Rh-O bond was predominant after thermal decomposition. A smaller peak attributable to the Rh-Rh bond was also observed around 0.27 nm for Ac-d-650, but did not appear for Ac-m-650. A small peak appeared around 0.27 nm for Ac-m-850 suggests the formation of the Rh-Rh bond at higher temperatures.

Curve-fitting results are summarized in Table 4.1 ~ 4.3. The fitting results for the samples from the $RhCl_3$ precursor (Table 4.3) are consistent with previous qualitative discussion. After thermal decomposition at 650 K, metallic Rh particles with average coordination number (CN) of 8.0 ± 1.5 formed on γ-Al_2O_3. Heat treatment at 850 K increased average CN to 9.8 ± 1.9, which was close to the value of the Rh foil (CN is 12). In the case of Rh acetate precursors, each Rh atom possesses Rh-O bonds with CN of 3 ~ 6 after thermal decomposition. The CN of Rh-Rh for the thermally decomposed $[Rh^{II}(OAc)_2]_2$ precursor was around 1 ~ 3, suggesting each Rh species roughly contains 2 ~ 8 Rh atoms. This result is in a good agreement with the STM results discussed in Chapter 3. Although STM results suggest that Rh dimers species (Rh-Rh: CN=1) formed on γ-Al_2O_3 after decomposition, the deviation of

STM observation and fitting results may result from the inappropriate path parameters used in these preliminary analyses. More accurate fitting by FEFF calculations will be discussed in the next section.

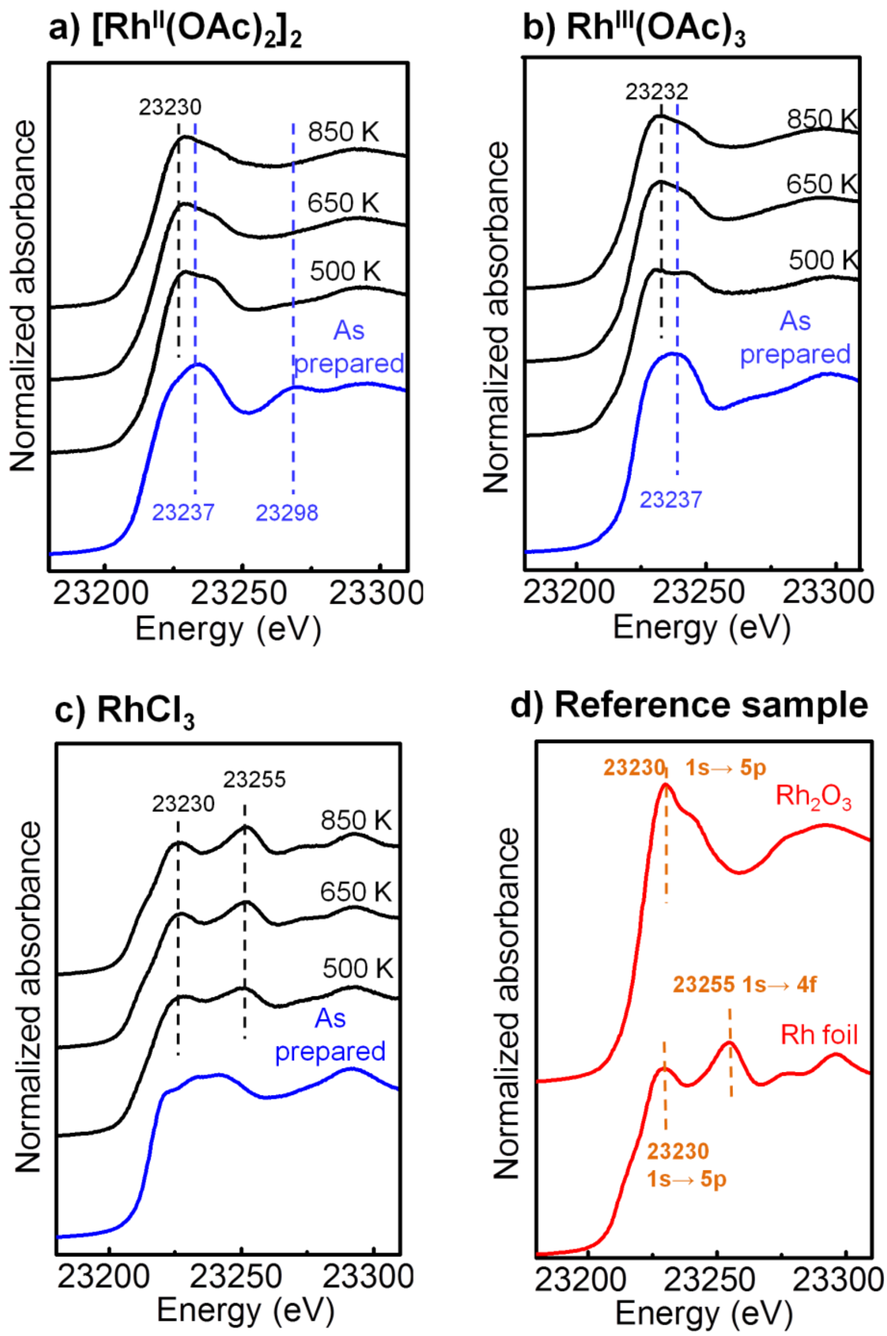

Figure 4.3.1 Rh K-edge XANES spectra of Rh/Al_2O_3 samples prepared from $[Rh^{II}(OAc)_2]_2$, $Rh^{III}(OAc)_3$, and $RhCl_3$ precursors on the course of heat treatments. Red lines: reference samples; Blue lines: as prepared samples.

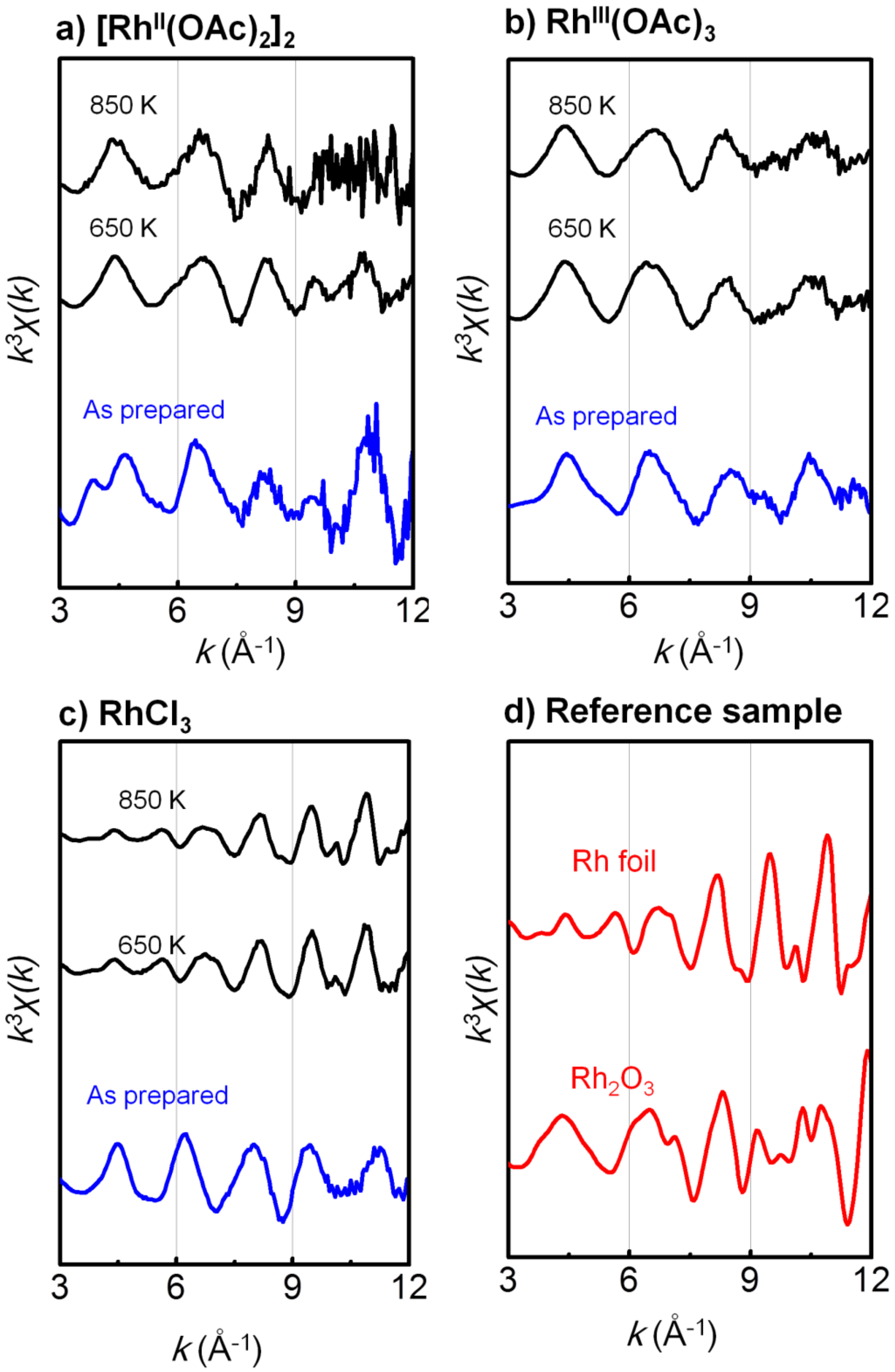

Figure 4.3.2 k^3 weighted Rh K-edge EXAFS oscillation curves $k^3\chi(k)$ of Rh/Al_2O_3 samples prepared from $[Rh^{II}(OAc)_2]_2$, $Rh^{III}(OAc)_3$, and $RhCl_3$ precursors on the course of heat treatments. Red lines: reference samples; Blue lines: as prepared samples.

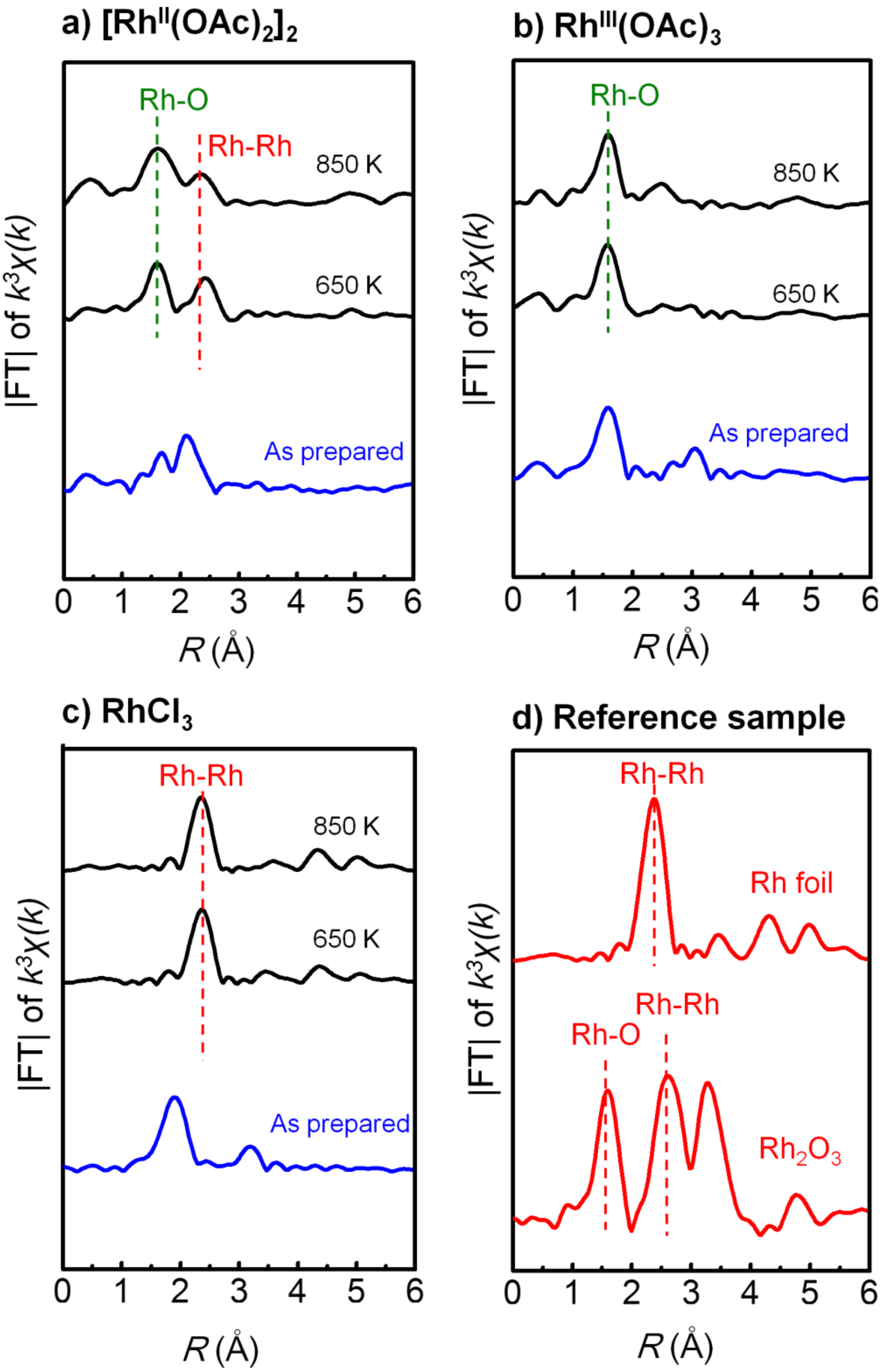

Figure 4.3.3 Fourier transform of k^3 weighted Rh K-edge EXAFS oscillation curves $k^3\chi(k)$ of Rh/Al_2O_3 catalysts prepared from $[Rh^{II}(OAc)_2]_2$, $Rh^{III}(OAc)_3$, and $RhCl_3$ precursors on the course of heat treatments. Red lines: reference samples; Blue lines: as prepared samples.

Table 4.1 Curve fitting results of the Rh/γ-Al_2O_3 catalyst prepared from the $[Rh^{II}(OAc)_2]_2$ precursor

$[Rh^{II}(OAc)_2]_2$	**Bond**	***N***	***R* (Å)**	**ΔE_0 (eV)**	**$\Delta\sigma^2$ (10^3 Å^2)**	**R factor**
As prepared	Rh-O	4.8 ± 1.2	2.02 ± 0.02	-2.46 ± 5.19	5.18 ± 0.40	1.60%
	Rh-Rh	1.0 ± 0.3	2.78 ± 0.01	1.86 ± 4.27	2.92 ± 0.28	
After 650 K	Rh-O	4.1±0.9	2.04±0.02	-0.058±3.51	0.083±0.022	3.06%
	Rh-Rh	2.3±1.0	2.70±0.02	3.93±4.67	0.086±0.030	
After 850 K	Rh-O	6.1±1.5	2.06±0.02	4.24±3.27	0.104±0.025	5.15%
	Rh-Rh	1.9±1.1	2.62±0.02	-7.85±5.89	0.092±0.039	

Notation: *N*: coordination number, *R*: bond distance between absorber and backscatter atoms; $\Delta\sigma^2$: Debye-Waller factor relative to that of the reference compound; ΔE_0: Inner potential correction that accounts for the difference in the inner potential between the sample and the reference compounds; *R* factor is a goodness of the curve fit.

Table 4.2 Curve fitting results of the Rh/γ-Al_2O_3 catalyst prepared from the $Rh^{III}(OAc)_3$ precursor

$Rh^{III}(OAc)_3$	**Bond**	***N***	***R* (Å)**	**ΔE_0 (eV)**	**$\Delta\sigma^2$ (10^3 Å^2)**	**R factor**
As prepared	Rh-O	3.2 ± 0.4	2.04 ± 0.01	-0.10 ± 2.46	0.06 ± 0.02	0.10%
After 650 K	Rh-O	5.3±0.9	2.04±0.01	-0.15±2.62	0.084±0.017	3.68%
After 850 K	Rh-O	4.4±0.8	2.02±0.01	-3.41±3.03	0.077±0.020	3.10%
	Rh-Rh	2.5±1.7	2.70±0.04	5.20±6.80	0.107±0.043	

Table 4.3 Curve fitting results of the Rh/γ-Al_2O_3 catalyst prepared from the $RhCl_3$ precursor

$RhCl_3$	**Bond**	***N***	***R* (Å)**	**ΔE_0 (eV)**	**$\Delta\sigma^2$ (10^3 Å^2)**	**R factor**
As prepared	Rh-Cl	2.5 ± 0.4	2.31 ± 0.01	0.83 ± 2.17	3.14 ± 0.19	1.50%
	Rh-Rh	2.4 ± 1.5	3.44 ± 0.03	0.88 ± 5.86	3.48 ± 2.02	
After 650 K	Rh-Rh	8.0 ± 1.5	2.68 ± 0.01	-0.42 ± 2.55	0.06 ±0.01	0.30%
After 850 K	Rh-Rh	9.8 ± 1.9	2.68 ± 0.01	-0.88 ± 2.65	0.06 ± 0.01	0.10%

4.4 FEFF Calculation Based on Real Space Model Method

The FEFF calculations based on real space models were performed to determine the structures of Rh species on Al_2O_3 prepared from $RhCl_3$, $Rh^{III}(OAc)_3$ and $[Rh^{II}(OAc)_2]_2$ precursors. As our STM results and previous literatures showed, the Rh particles prepared from $RhCl_3$ have various morphologies, only average structural information can be obtained from XAFS analyses. Thus, $RhCl_3$ will be discussed very simply just by geometrical considerations. On the other hand, FEFF calculations for real space models will be performed to clarify the detailed structures for the products from the Rh acetate precursors.

4.4.1 $RhCl_3$

Since both XAFS spectra and curve-fitting results of $RhCl_3$ show that the thermally decomposed products possess only Rh-Rh bonds and have metallic property, we assume that the decomposition products are metallic Rh particles with fcc crystal structure. The averaged coordination number and particle size (number of Rh atom) correlate with each other and can be estimated by a geometric model. For simplicity, we only consider the cubic structure with n^3 unit cells as shown Figure 4.4.1. Then, coordination number of every Rh atom can be estimated: all of atoms inside have 12 nearest neighbors, while those at the surface are less:

・Rh cluster with n^3 unit cells: number of Rh atoms is $(n+1)^3 + 3n^2(n+1)$

・Surface Rh atoms and their coordination numbers (CN)

a) Atoms at corner: 8 atoms, CN = 3, shared with 8 unit cells

b) Atoms at edge: $12 \times (n-1)$ atoms, CN = 5, shared with 4 unit cells

c) Atoms at surface: $6 \times n^2 + 6 \times (n-1)^2$ atoms, CN = 8, shared with 2 unit cells

・Bulk Rh atoms ant their CN

$(n+1)^3 + 3n^2(\mathrm{n}+1) - 8 - 12(\mathrm{n}-1) - 6n^2 + 6(n-1)^2$ atoms, CN = 12

Then, the average coordination number and particles size can be given as:

$$\overline{CN} = 12 - \frac{9\times 8}{(n+1)^3+3n^2(n+1)} - \frac{7\times 12(n-1)}{(n+1)^3+3n^2(n+1)} - 4\times\frac{6n^2+6(n-1)^2}{(n+1)^3+3n^2(n+1)} \tag{4.1}$$

$$Size = 3.80\times\sqrt{3}\times n + 2.68 \tag{4.2}$$

The curve fitting results show, after 650 K, the coordination number of Rh-Rh is about 8.0. According to Table 4.4, the average total number of Rh atoms should be several tens, and the average size is larger than 1 nm. At higher temperature, small Rh clusters aggregate to form large one, the size of which is around 3 nm with several hundred Rh atoms. These results are in good agreements with our previous STM studies.

Table 4.4 Total number of atoms, ratio of N_{surf}/N_{bulk}, size and average coordination number in the n^3 $(\mathrm{n}=1\sim6)$ cubic Rh cells.

$\boldsymbol{n}$	Total number of atoms (N)	N_{surf}/N_{bulk}	Size (Å)	$\overline{\boldsymbol{CN}}$
1	4	4/0	9.26	5.14
2	32	19/13	15.9	7.62
3	108	46/62	22.4	8.79
4	256	85/171	29.0	9.47
5	500	136/364	35.6	9.91
6	864	199/665	42.2	10.2

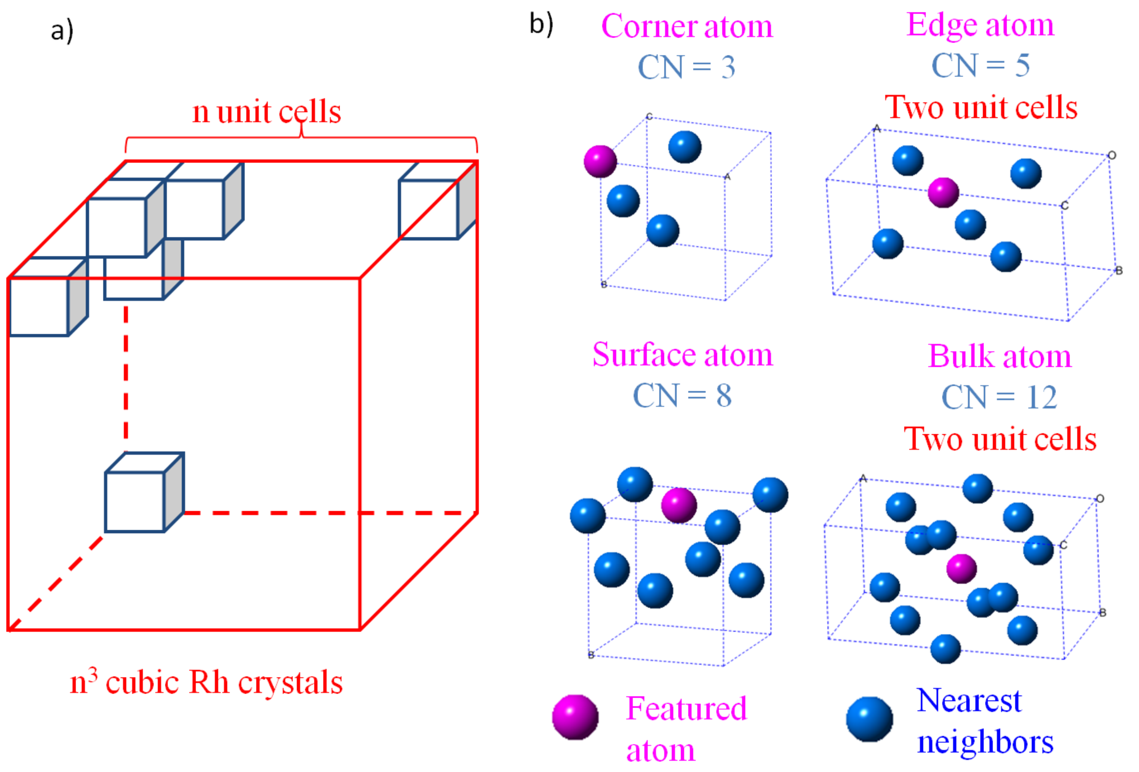

Figure 4.4.1 **a)** Cubic model of Rh fcc crystal structure: containing n^3 unit cells. **b)** Types of Rh atoms and their coordination number; corner atom: CN = 3; edge atom: CN = 5; surface atom: CN = 8 and bulk atom: CN = 12.

4.4.2 Rh acetate dimer and monomer

All of the following discussion is focused on Rh acetate decomposition products. XANES and EXAFS spectra of the Rh/Al_2O_3 samples from the Rh acetate precursors (both dimer and monomer) suggested that the decomposition products have local structures somewhat similar to Rh_2O_3. Possibility of direct interaction between Rh and Al seems to be low due to absence of Rh-Al bonding features in EXAFS spectra. Therefore, we assume that Rh atoms are mainly adsorbed on surface oxygen sites. To reduce the complexity of discussion on the local structures of Rh species on Al_2O_3 surface, it is helpful to extract ideal rhodium oxide structures and determine appropriate coordination number and distance of Rh-O, Rh-Rh by using the FEFF code and the real space model method.

To evaluate the validity of the FEFF calculation, some path parameters were determined for a standard sample. As the decomposition products are speculated to be rhodium oxide-like compounds, Rh_2O_3 (ICSD No. 10894)[11] was selected as a standard sample to calibrate the path parameters such as amplitude S_0^2, Debye-Waller factor σ^2, and exchange term. The calibration result was S_0^2 = 0.78, σ^2 = 0.00220, exchange term = 4. These parameters will be used in fitting $\chi(k)$ of the thermally decomposed products.

1) Rh acetate monomer ($Rh^{III}(OAc)_3$)

According to the curve fitting results (Table 4.2) of Ac-m-650, only one peak attributed to the Rh-O bond with the coordination number of 2.5 ± 0.3 was observed. Thus, we supposed the structure of Ac-m-650 was RhOx (x = 1 ~ 4). Four possible RhOx structures (RhO, RhO_2, RhO_3, and RhO_4) are shown in the right part of Figure 4.4.2. Rh_2O_5 was also calculated in order to check the possibility of a multi-core structure. The bond distances of Rh-O, Rh-Rh, O-O were set at 2.04 Å, 3.00 Å and 2.80 Å, respectively, which are extracted from the Rh_2O_3 crystal[27] but rather common for realistic rhodium oxides. The calculated $\chi(k)$ curves of the model structures are shown in Figure 4.4.2 together with the experimental curve (black) of Ac-m-650. Double peaks (9 ~ 12 $Å^{-1}$) appeared for Rh_2O_5 but not for the experimental curve. It suggests that Rh species in Ac-m-650 does not have a multi-core structure. The evaluation factor R' of mismatch between theoretical result $\chi(k)_{cal}$ and experimental data $\chi(k)_{data}$ was calculated by the following formula.

$$R' = \sqrt{\frac{\sum(\chi(k)_{data} - \chi(k)_{cal})^2}{\sum(\chi(k)_{data})^2}} \tag{4.3}$$

The best fitting result was obtained when a Rh atom coordinates to four oxygen atoms, the evaluation factor *R'* was calculated to be 0.20, while the values for RhO$_3$, RhO$_2$ and RhO were 0.31, 0.50 and 0.75, respectively. This result may suggest that Rh atoms prefer to be adsorbed on the four-fold surface oxygen sites. However, the three-fold sites cannot be excluded because the degree of deviation from the experimental curve was not so large, and the arrangements of surface oxygen atoms of γ-Al$_2$O$_3$ are a little different from the ideal model. The on-top or bridge sides seem to be unfavorable for fixing the single Rh atom. Smaller amplitude at first two peaks of $\chi(k)$ for RhO and RhO$_2$ suggests that the number of coordinated oxygen atoms is not enough.

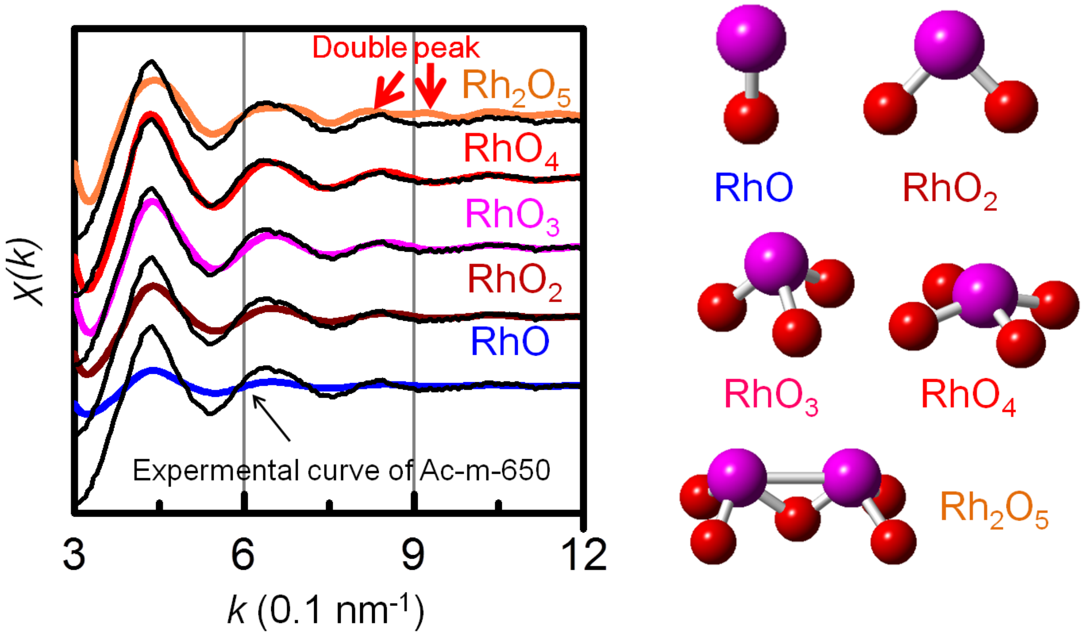

Figure 4.4.2 Comparison of an experimental curve (Ac-m-650) (black lines) and curves from FEFF calculations of RhOx (x=1, 2, 3, 4) and Rh$_2$O$_5$ models (colored lines). The Rh-O and Rh-Rh, O-O distances were fixed at 2.04 Å, 3.00 Å and 2.80 Å, respectively, based on the Rh$_2$O$_3$ crystal structure. Characteristic double peaks for Rh$_2$O$_5$ are indicated by red arrows. The best fitting is found in the case of RhO$_4$.

2) Rh acetate dimer ($[Rh^{II}(OAc)_2]_2$)

The situation of the Rh acetate dimer is more complicated than the monomer. For simplicity and according to the results of $Rh^{III}(OAc)_3$, all Rh atoms are located on the three or four fold sites and only symmetrical structures are considered.

Figure 4.4.3 illustrates possible structures of Rh_2O_5, Rh_2O_6, Rh_3O_6, Rh_4O_6, and Rh_4O_9. All of oxygen atoms are located at the same plane at first, then we put the Rh atoms on the three or four fold sites to keep symmetry and Rh-O and O-O bond lengths to be 2.04 Å and 2.80 Å (3.00 Å for Rh_2O_5), respectively. Preliminary curve fitting results revealed that the Rh-Rh is around 2.70 Å (Table 4.4), which is close to the value of bulk Rh. Thus, we alter the Rh-Rh distances to 2.70 Å in all of the model structures. In order to keep the Rh-O distance around 2.04 Å, the oxygen atoms cannot stay at the same plane. The position of center oxygen atoms have been adjusted down and up, respectively. The final model structures and calculation results (color lines) are given in Figures 4.4.3. Both of Rh_2O_5 model 1 and model 2 well reproduced the experimental curve (black lines) with the evaluation factors *R'* of 0.22 and 0.23, respectively. The curve of Rh_2O_6 also showed a good agreement with the experimental data in high *k* range, but the amplitude of the first peak was a little larger, suggesting the number of coordinated oxygen was larger than the real structure. The *R'* factor was 0.27. This structure cannot be excluded because *R'* factor is still small, and the degree of deviation from the experimental curve is not so large. In the case of trimer and teteramer, the amplitudes of calculated $\chi(k)$ was larger at the high *k* range, and the number of peaks was more than the experimental curve. Especially in the case of Rh_4O_6 (CN of Rh-Rh is 3), an additional peak appeared at k=4~5 $Å^{-1}$ which was not found in the experimental curve. All of these results suggest that the trimer and teteramer structures are different from the real structure.

As a consequence, the most probable structure of the thermally decomposed product from the $[Rh^{II}(OAc)_2]_2$ precursor are Rh dimer species adsorbed on two threefold oxygen or fourfold oxygen sites of the γ-Al_2O_3 surface with Rh-Rh bond of 2.70 Å and Rh-O bond of 2.04 Å. Two arrangements of the two threefold sits are possible: one is *cross type* as Rh_2O_5 model 1, and the other is *neighbor type* as Rh_2O_5 model 2. This conclusion agree with our previous STM results, the Rh dimer species are main products by using $[Rh^{II}(OAc)_2]_2$ as the precursor.

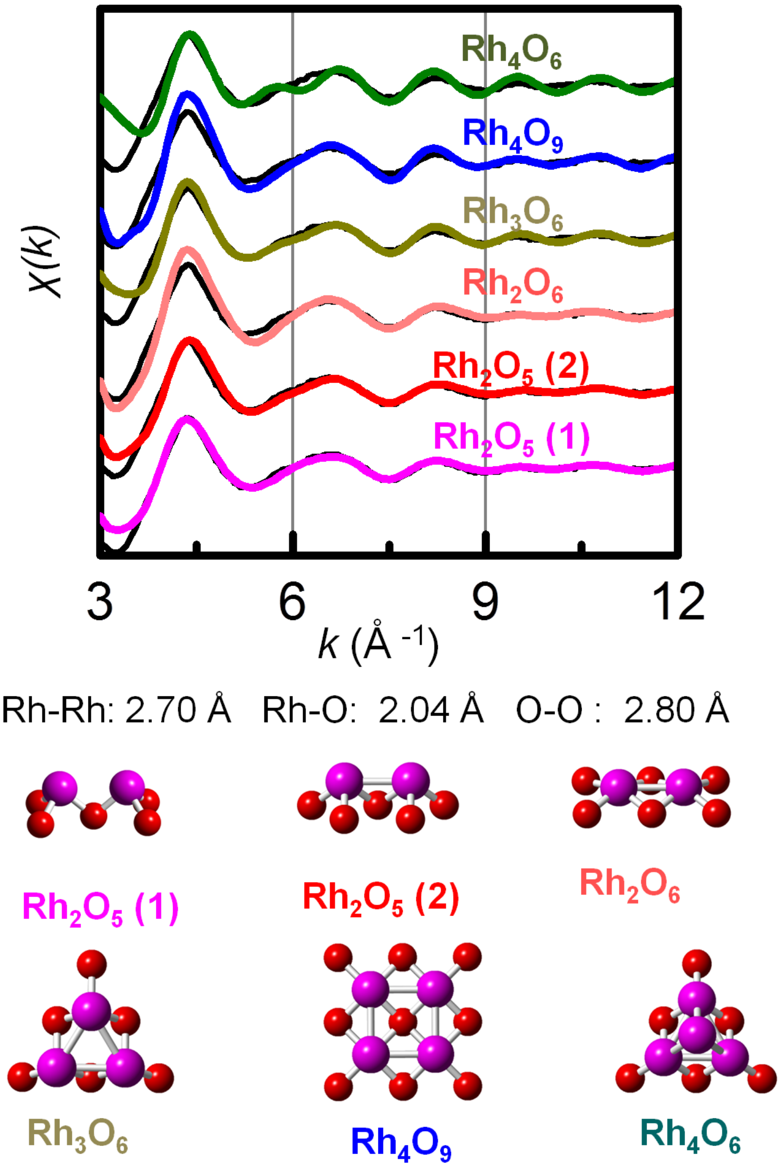

Figure 4.4.3 Comparison of an experimental curve (Ac-d-650) (black lines) and curves from FEFF calculations (colored lines) of various Rh oxide models shown at the bottom. Bond lengths were fixed at the following values; Rh-O: 2.04 Å; Rh-Rh: 2.70 Å or 2.80 Å; O-O: 2.80 Å.

4.4.3 Structures of Rh species on γ-Al_2O_3

In order to determine the realistic structures of Rh species on γ-Al_2O_3 prepared by Rh acetate precursors, it is necessary at first to distinguish the probable adsorption sites of the support. γ-Al_2O_3 is a metastable transition alumina obtained by calcination of a boehmite γ-AlOOH powder at 700 K.[27] During the calcination process, the transformation is topotactic, the particle morphology remains unchanged. The predominant surfaces of γ-Al_2O_3 are (100), (110) and (111). Bulk γ-Al_2O_3 possesses the cubic spinel structure (space group P21/m) and Al atoms occupy the tetrahedral (T_d) and octahedral (O_h) sites of fcc oxygen sublattice.[12]

Figure 4.4.4 shows ideal structures of (100), (110) and (111) surfaces of γ-Al_2O_3. The stable (100) surface is terminated by fivefold coordinated aluminum (Al_V) and threefold coordinated oxygen (O_{III}) atoms. The surface density of missing Al-O bonds is about 17.1 bonds/nm^2. On the (110) surface, the density of missing Al-O bonds is higher, about 20.7 bonds/nm^2. Various kinds of atoms, fourfold Al_{IV}, threefold coordinated Al_{III}, twofold O_{II} and threefold O_{III}, are exposed. The (111) surface exhibits alternating stacking oxygen atoms and aluminum atoms. As a result, this surface is polar and has two types: O-terminated surface and Al-terminated surface. This situation is very similar to the (0001) surface of α-Al_2O_3, thus, we suppose that the O-terminated surface is more stable than Al-terminated one. The surface density of missing Al-O bonds is the highest, about 27.0 bonds/nm^2.[13] Practically, unsaturated Al sites cannot be stabilized under realistic air atmosphere and in aqueous or ethanol solution, thus they are fully terminated by oxygen atoms or hydroxyl group. For simplicity, in this study we just discuss the O-saturated alumina surface. And according to the previous discussion, only three or four fold sites will be considered.

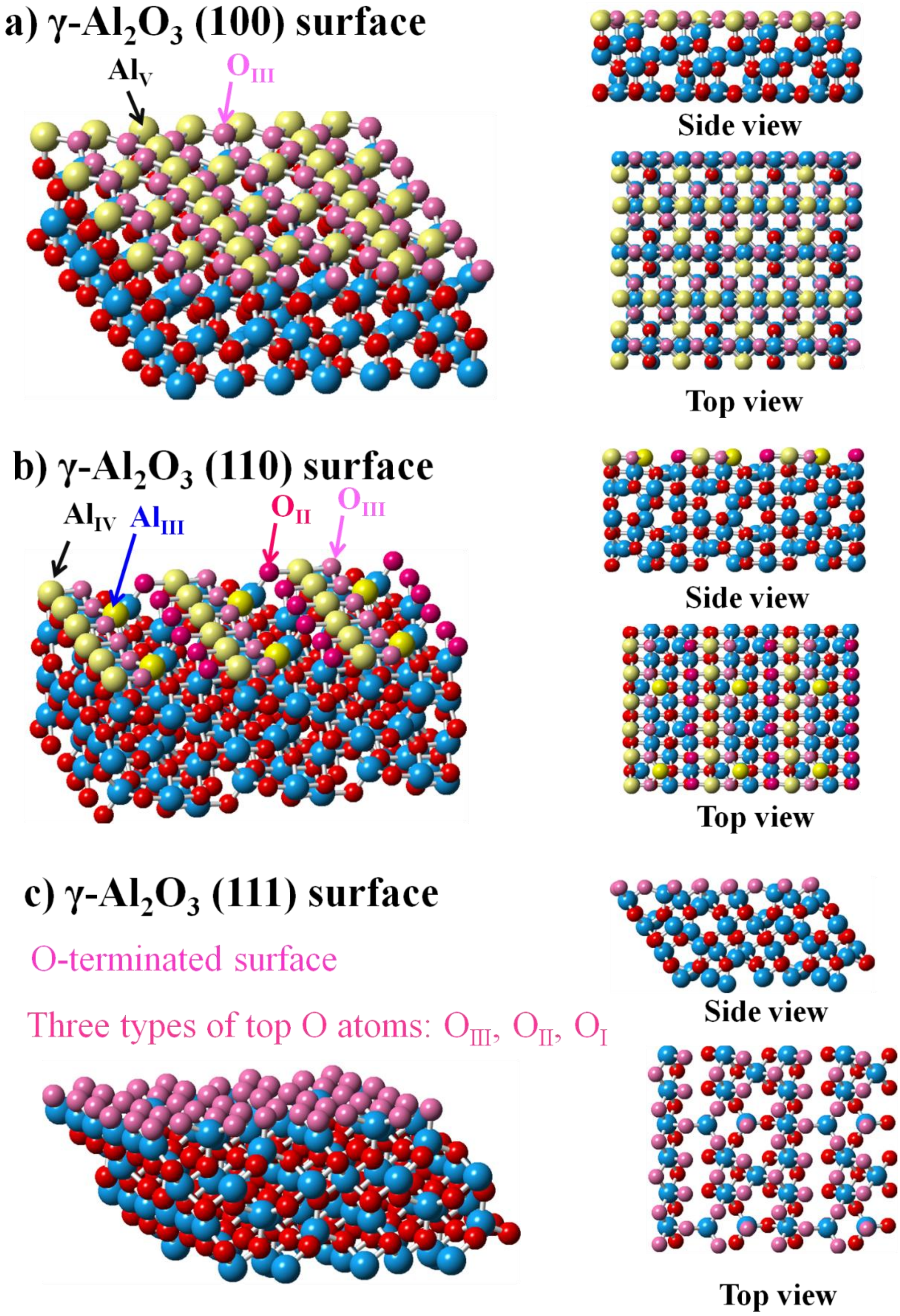

Figure 4.4.4 Structures of a) (100), b) (110), c) (111) faces of γ-Al_2O_3. Oxygen and Al atoms in bulk are displayed by blue and red balls, respectively. The surface atoms are displayed by other color balls (Al is larger than O), which are dependent on the type and coordination number of atoms.

1) Rh acetate monomer ($Rh^{III}(OAc)_3$)

The most plausible sites for Rh single atoms are discussed at first. In order to build reasonable structural models and reduce the complexity of FEFF calculations, some additional constraints are assumed:

a) The top oxygen atoms are located at the same positions as bulk oxygen at first.

b) Rejection by bond lengths: According to previous discussion, all of the nearest Rh-O distances should be set to around 2.04 Å. And the coordination number is about 3 ~ 4.

c) The positions of Al and O atoms (2nd layer Al and O) in Al_2O_3 lattice are fixed, while the top O is allowed to be slightly adjusted in reasonable range to get the best-matching calculation curve. The position adjustment of the top O atom should be less than 0.1 Å and bond angle change should be smaller than 1.4 degree.

The structures of adsorption sites satisfying these constraints are shown in Figure 4.4.5. Most of the sites are threefold sites, expect site 3 (rectangle) on (100) surface and site 4 (tetrahedral) on (110) surface are fourfold sites.

(100) surface

A good agreement is found for site 3 on this surface. Although the first peak position slightly shifts to low *k* range, the oscillation shape and amplitude are similar to the experimental data. Thus we suppose that site 3 is a plausible site to stabilize the Rh single atom. The slight red-shift of the first peak can be explained by longer Rh-O distance (2.12 Å), resulting from larger separation the O-O (2.90 ~ 3.00 Å) in this site.

Site 2 also gives a good agreement with the experimental data, if the top oxygen is slightly moved towards to Rh atoms with shift of 0.1 Å from the original position. The matching of the first peak is particularly good. However, a small peak appears in the middle of the second and the third peak. This additional peak originates from the nearest Al atom with Rh-Al distance of 2.50 Å which is similar to the value in RhAl alloy crystal.

For site 1, however, data matching is not good. Smaller amplitude at first two peaks indicates that the number of coordinated oxygen is not enough. The insufficiency of coordinated atoms probably reduces the stability of Rh single atoms on these sites, thus, Rh single atoms cannot be fixed.

(110) surface

Except for site 6, all of the calculation results essentially agree with the experimental data. The site 6 is similar to the previous case of site 2 at the (100) surface. Besides, in this case, for satisfying the Rh-O bond length range, the distance between Rh and Al under three-fold O site have to be reduced to a too short Rh-Al distance (2.15 Å). This distance causes large Rh↔Al electrostatic repulsion, which makes this configuration unstable. Thus, site 6 is not appropriate for fixing Rh single atom.

(111) surface

All of the calculation results are analogous to the experimental data. However, there remained two considerable differences in some calculation results. Firstly, the amplitudes of the first two peaks are a little smaller than those of experimental data. Secondly, a small shoulder appears at 6 ~ 7 (0.1 nm^{-1}) near the second peak. Actually, the same differences are also observed in the case of the (110) surface. We propose that these differences are originated from not only the arrangement of top oxygen atoms but also the positions of Al and O atoms in the 2nd layer with longer distances from Rh.

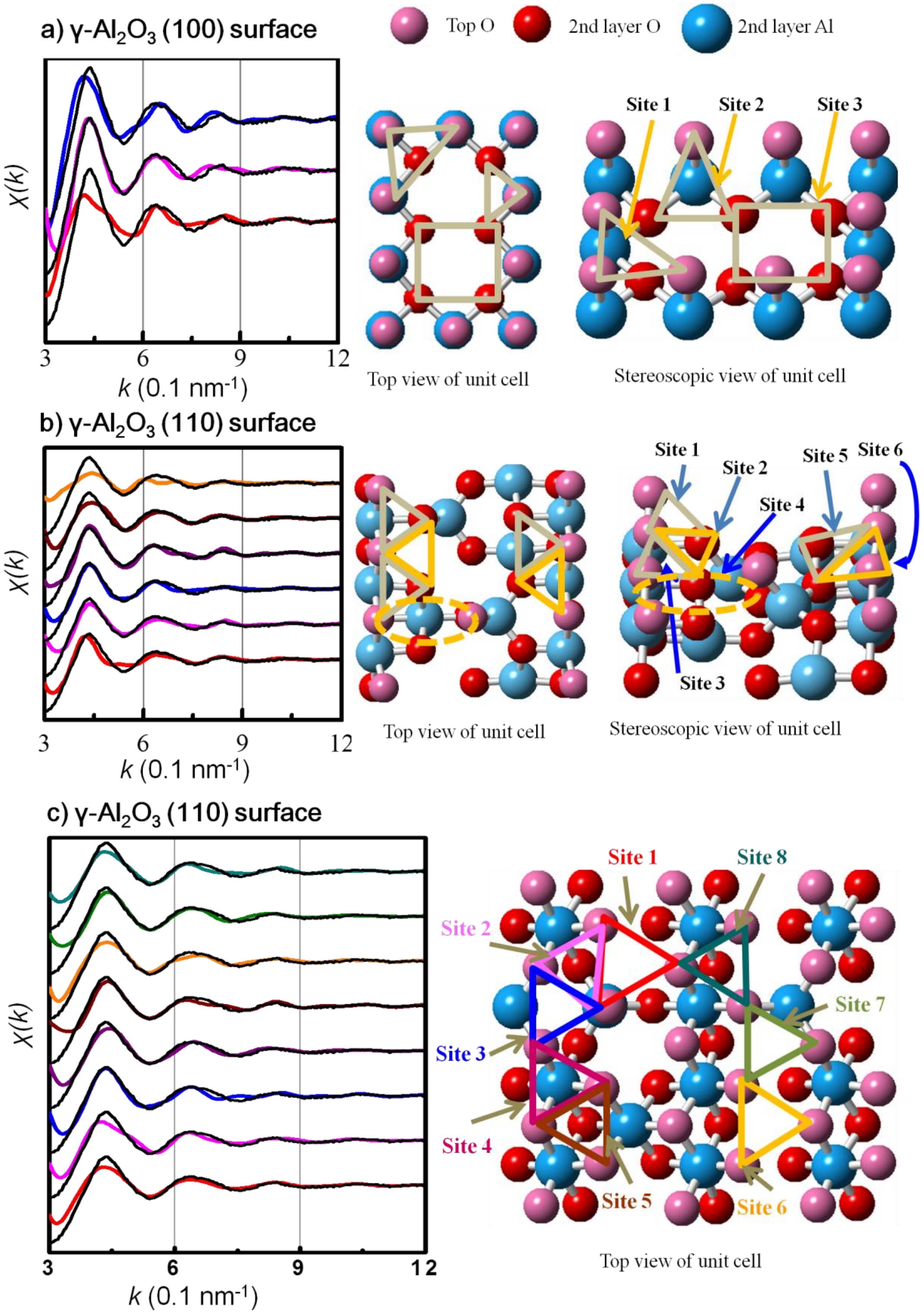

Figure 4.4.5 Comparison of experimental data Ac-m-650 (black lines) and FEFF calculation results (colorful lines starting from site 1 at the bottom) of single Rh atom on various sites of γ-Al_2O_3 faces; **a)** (100) , **b)** (110) , **c)** (111).

Coordination condition, calculation results and reliability factor *R'* of each probable structure are listed in Table 4.5 to clarify the correlation between the EXAFS oscillation and local structure of adsorption sites. There are three kinds of top O on the γ-Al_2O_3 surface. We denote them as O_{III}, O_{II}, and O_I, where the Roman number indicates the number of Al-O bonds between top O and 2nd layer Al. We find that type of top O somewhat influences the *R'* factor. The *R'* factor tends to be lower for the structure that contains lower coordinated O. In other words, Rh single atoms seem to be adsorbed on low coordinated O sites.

The nearest Rh-Al distance and Al number seem to affect the second peak of EXAFS oscillation. A short Rh-Al distance and large Al number result in the appearance of shoulder or a small peak in the range of 6 ~ 7 (0.1 nm^{-1}). However, if the Rh-Al distance is as long as 3.00 Å, this effect become very weak, and it is negligible when the distance is larger than 3.50 Å.

Compared to the threefold sites, the fourfold sites are more favorable for stabilizing the Rh single atoms. We find the calculated EXAFS oscillation $\chi(k)$ of site 2 and site 3 of (100) surface, site 4 of (110) surface, site 6 of (111) surfaces exhibit the best agreement with the experimental data. The first three are fourfold sites or semi-fourfold sites, and the last one is threefold site but possesses two single coordinated oxygen atoms and large distance (3.60 Å) away from the nearest Al atoms. The R' factors for these sites are about 0.29 ~ 0.32, which are close to the values of ideal structures discussed in the previous section: threefold sites ~ 0.31 and fourfold sites ~ 0.20. Thus, it is reasonable to believe that these sites are most probable sites for Rh single atom.

Table 4.5 Calculation results and local structure for possible adsorption site

Site	**Coordinated O**	**Nearest Al atoms**		**Difference**	***R'***
		Distance (Å)	Number		**factors**
(100) surface					
Site 2	$2\times O_{II}$ and O_{I}	2.50	1	Small peak at 2nd peak	0.32
Site 3	$2\times O_{II}$ and $2\times O_{II}$	2.80	3	Red shift: 1st peak	0.29
(110) surface					
Site 1	$3\times O_{II}$	2.67	1	Red shift: 1st peak	0.36
Site 2	$3\times O_{II}$	3.05	2	Small amplitude: 1st peak Shoulder of 2nd peak	0.48
Site 3	$3\times O_{II}$	2.50	1	Small amplitude: 2nd peak	0.37
Site 4	$3\times O_{II}$ and O_{I}	3.00	3	Small shoulder at 2nd peak	0.32
Site 5	$3\times O_{II}$	2.40	1	Small amplitude: 1st peak	0.46
(111) surface					
Site 1	$2\times O_{II}$ and O_{I}	3.50	2	Small amplitude: 1st peak	0.35
Site 2	$2\times O_{II}$ and O_{I}	3.00	1	Small amplitude: 1st peak	0.37
Site 3	$2\times O_{II}$ and O_{I}	2.50	1	Shoulder of 2nd peak	0.37
Site 4	O_{III}, O_{II} and O_{I}	3.60	1	Small amplitude: 1st peak	0.42
Site 5	$3\times O_{II}$	3.00	3	Small amplitude: 1st peak Shoulder of 2nd peak	0.50
Site 6	$2\times O_{I}$ and O_{II}	3.60	4	Small amplitude: 1st peak	0.32
Site 7	$2\times O_{II}$ and O_{I}	2.40	1	Small amplitude: 1st peak	0.42
Site 8	$2\times O_{II}$ and O_{I}	3.00	2	Small amplitude: 1st peak	0.41

In the above discussion, we postulated Al and O atoms in the 2nd layer were fixed in their original position all along. However, in the realistic materials, the situation is more complicated. Ijima and coworkers reported a surface reconstruction of Ni/α-Al_2O_3 (0001).[8] They suggested when Ni atoms are deposited on the α-Al_2O_3 (0001) surface, the surface oxygen would be lifted close to Ni by 0.36 Å and the 2nd layer aluminum located beneath Ni would be thrust by 0.33 Å to relax the stress and repulsion. By analogy, the reconstruction of γ-Al_2O_3 surface may also happen for Rh/Al_2O_3. For example, if the nearest Rh-Al distance of 3.00 Å for site 4 on the (110) surface was expanded to 3.10 Å, the shoulder in the range of 6 ~ 7 (0.1 nm^{-1}) would become very weak.

As a summary, by using FEFF calculation and real Rh/γ-Al_2O_3 structure models, we found the number of low-coordinated O atom, the separation of the nearest Al and their number play important roles in adsorption of the single Rh atom on γ-Al_2O_3. Low-coordinated O atom (especially O_I) possesses excess dangling bonds and high spatial freedom (flexible). The former term can provide good stabilization for the Rh atom and the flexiblility is helpful to optimize the configuration of adsorption structure to minimize the structural stress and electrostatic repulsion. On the other hand, the long separation of Rh-Al and low number of the nearest Al atoms are also required to reduce the electrostatic repulsion between Rh and Al.

In conclusion, the most probable sites for adsorption of Rh single atoms are suggested to be site 2 and site 3 of (100) surface, site 4 of (110) surface, site 6 of (111) surfaces.

< Rh acetate dimer ($[Rh^{II}(OAc)_2]_2$) >

Previous discussion revealed that Rh species prefer to adsorb on two three-fold oxygen sites with Rh-Rh bond of 2.70 Å and Rh-O bonds of 2.04 Å. Both of two arrangements: *cross type* and *neighbor type* give good agreements with the experimental data. However, on the realistic γ-Al_2O_3 surface, it seems that the *cross type* is hardly achieved. The *cross type* requires larger upward shift of side O atoms and downward shift of center O atoms. These position changes will cause huge lattice stresses on the γ-Al_2O_3 surface, thus, *cross type* is not favorable arrangement. In this section, we will only discuss *neighbor type*.

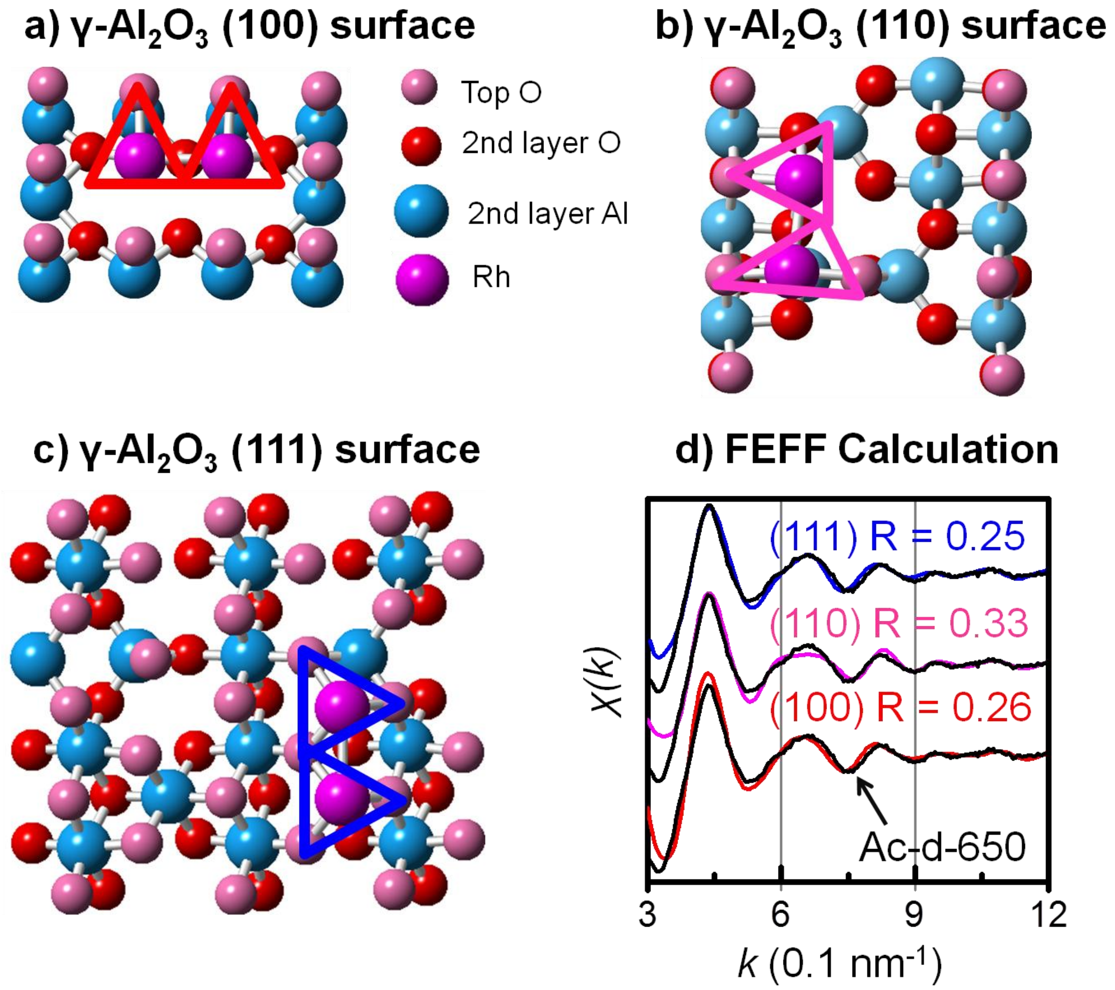

Figure 4.4.6 Probable Rh dimer structures on different faces of γ-Al_2O_3; **a)** (100) , **b)** (110), **c)** (111). **d)** Comparison of experimental data Ac-d-650 (black lines) and FEFF calculation results (color lines) of Rh dimer on various sites of γ-Al_2O_3

Similar to the discussion on the Rh acetate monomer, every probable adsorption site has been evaluated by FEFF calculation. In the end, we found three structures could reproduce the experimental data (Ac-d-650) very well. Figure 4.4.6 shows the structures of probable adsorption sites and calculation results. The *R'* factors are calculated to be 0.26, 0.33 and 0.25, respectively. Except for the (110) surface site, these values are almost same as those of ideal *neighbor type* structure. Thus, it is reasonable to believe (111) site and (100) site are most plausible sites for stabilization of two Rh atoms. The distortion of the second peak in the curve of (110) surface site are possibly attributed to the four nearest Al cations facing to the Rh dimer.

It is worthy to note that these three sites contain at least one O_I atom. Especially, in the case of (111) surface, we have tested all of possible *neighbor type* structures, only the site with two O_I atoms as shown in Figure 4.4.6(c) can give a satisfiable result. Therefore, we conclude that the low coordinated oxygen and the separation between Rh and nearest Al also act as critical factors for stabilization of Rh dimer on γ-Al_2O_3.

4.5 Conclusion

The local structures of Rh/γ-Al_2O_3 prepared from three different precursors, $[Rh^{II}(OAc)_2]_2$, $Rh^{III(}OAc)_3$, $RhCl_3$ have been studied by XAFS. Metallic Rh cluster with size of 1-3 nm were generated from $RhCl_3$, while rhodium-oxide-like compounds formed in the case of Rh acetate dimer and monomer precursors.

By using FEFF calculation and real space model method, we have successfully determined the local structures of these rhodium-oxide-like compounds: one or two Rh atoms from the Rh precursors are selectively fixed on three or four-fold sites on the γ-Al_2O_3 surface. These results give a good agreement with previous STM study.

Furthermore, we found the single Rh atoms or Rh dimers prefer to adsorb on some specific surface sites which possess low coordinated oxygen and large separation between Rh and the nearest Al, because these sites can provide high stabilization and flexible adsorption configuration to minimize surrounding stress.

In the end, we speculate on the reason why metallic Rh cluster formed from $RhCl_3$ precursor is that these specific surface sites are masked by Cl^- anions. The Rh atom cannot be stabilized by other surface sites and have to be aggregated together.

References

1 F. W. Lytle, G. H. Via and J. H. Sinfelt, *J. Chem. Phys.* 1997, **67**, 3831.

2 Y. Iwasawa, in: “*X-ray Absorption Fine Structure for Catalysis and Surfaces”*, ed. World Scientific, Singapore, 1996 p. 1.

3 D. C. Koningsberger and B. C. Gates, *Catal. Lett.* 1992, **14**, 271.

4 Y. Iwasawa, *Adv. Catal.* 1987, **35**, 187.

5 K. Asakura, W.-J. Chun and Y. Iwasawa, *Top. Catal.* 2000, **10**, 209. W.-J. Chun, M. Shirai, K. Tomishige, K. Asakua, and Y. Iwasawa, *J. Mol. Catal. A,* 1996, **107**, 55.

6 M. Shirai, T. Inoue, H. Onishi, K. Asakura and Y. Iwasawa, *J. Catal.* 1994, **145**, 159.

7 K. Asakura, W.-J. Chun, M. Shirai, K. Tomishige and Y. Iwasawa, *J. Phys. Chem.* 1997, **101**, 5549.

8 K. Ijima, Y. Koike, W.-J. Chun, Y. Saito, Y. Tanizawa, T. Shido, Y. Iwasawa, M. Nomura and K. Asakura, *Chem. Phys. Lett.* 2004, **384**, 134.

9 A. Yamaguchi, A. Suzuki, T. Shido, Y. Inada, K. Asakura, M. Nomura, *J. Phys. Chem. B* 2002, **106**, 2415.

10 Y. Tanizawa, T. Shido, W.-J Chun, K. Asakura, M.Nomura and Y. Iwasawa, *J. Phys. Chem. B* 2003, **107**, 12917.

11 S. J. Wilson, *J. Solid State Chem.* 1979, **30**, 247.

12 C. Wolverton and K. C. Hass, *Phys. Rev. B* 2000, **63**, 024102.

13 M. Digne, P. Sautet, P. Raybaud, P. Euzen and H. Toulhoat, *J. Catal.* 2004, **226**, 54.

Chapter 5 Conclusion and Outlook

5.1 Conclusion

Precursor-dependence is a key issue for catalyst design. Choice of a catalyst precursor sometimes affects the properties of the catalyst due to its local structure is apart from the thermodynamically favored one. However, there is still lack of fundamental knowledge about this effect. In order to gain the molecular level insight into this effect by a surface science approach, a new preparation method of metal precursor supported model surfaces has been developed by using a pulse valve. This method can be applicable to almost catalysts, thus it provides a new way to discover the behavior of precursor on the support surface. In this thesis, we have discussed the precursor-dependence of Rh/Al_2O_3.

In Chapter 3, we studied on precursors dependent structures of Rh/Al_2O_3 catalysts by high-resolution STM measurements and found that homogeneous Rh dimer species could be randomly dispersed on Al_2O_3 thin film/NiAl(110) by using $[Rh^{II}(OAc)_2]_2$ precursor. Moreover, the Rh dimer species were quiet stable up to 800 K. However, when a common precursor $RhCl_3$ was used for the precursor instead, larger Rh particles were formed. This phenomenon is very interesting because the homogeneity and high stability of active species are very important issues in the field of the catalyst. Moreover, the homogenous Rh dimer species can be used as the nucleation sites, on which various Rh relative compounds can be prepared.

In Chapter 4, we confirmed the same phenomena on the high surface-area Al_2O_3 support by XAFS measurements when the appropriate pre-treatment of Al_2O_3 and similar preparation procedures were adopted. Furthermore, we determined local structures of Rh species prepared from various precursors and found that Rh-O bond preferentially formed along with the decomposition of acetate ligand and it stabilized the Rh core on the Al_2O_3 surface.

According to these STM and XAFS results, two questions will be discussed here: First, why homogenous Rh dimer species can be formed on various Al_2O_3 surfaces, not only Al_2O_3/NiAl(110), α-Al_2O_3(0001) but also powder γ-Al_2O_3; Second, what is the origin of precursor-dependence, especially, in this case: $[Rh^{II}(OAc)_2]_2$ vs $RhCl_3$.

The first question relates to stable adsorption sites of the Rh dimer on Al_2O_3 surfaces. In Chapter 4, we found that the Rh dimers preferred to adsorb on three-fold oxygen or four-fold oxygen sites of Al_2O_3 surfaces (See Figure4.4.3). Especially, some sites with low coordinated oxygen atoms and large separation between Rh and the nearest Al can provide the highest stabilization because of the flexible adsorption configuration and low Rh-Al repulsion. The situation for powder γ-Al_2O_3 surfaces has been discussed in Chapter 4, several stable adsorption sites have been established by real space mode and FEFF calculation. In the case of α-Al_2O_3(0001), the surface structure showed in Figure 5.1.1(a) is quite similar to the γ-Al_2O_3(111) surface , thus the same stable adsorption sites for Rh dimers can be also found on the α-Al_2O_3(0001) surface. And in the case of Al_2O_3/NiAl(110), as shown in Figure 5.1.1(b), the surface is full of three-fold oxygen or four-fold oxygen sites, which are also stable adsorption sites for the Rh dimers. Therefore the Rh dimer species can be formed on these various Al_2O_3 surfaces.

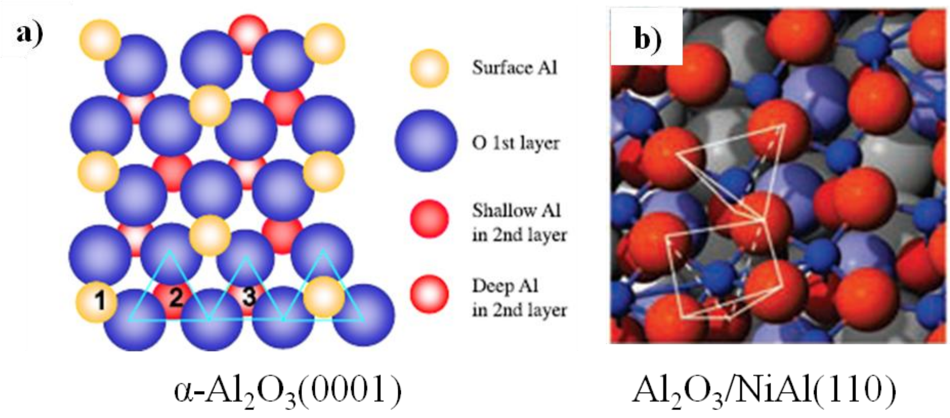

Figure 5.1.1 Surface structure of **a)** α-Al_2O_3(0001)[1] and **b)** Al_2O_3/NiAl(110)[2]

What about the second question: what is the origin of precursor-dependence, especially, in the case of $[Rh^{II}(OAc)_2]_2$ vs $RhCl_3$? We think the surface oxygen atom plays an important role in stabilizing the Rh atoms. The formation of Rh-O bond should occur before or during the precursor decomposition, which can prevent the Rh atoms diffusing and aggregating into large particles. The $[Rh^{II}(OAc)_2]_2$ seems to be attacked by surface oxygen more easily than $RhCl_3$, because formation of Rh-O occurred in the former case but not in the latter one. In other words, the Cl^- atoms perhaps block the attack from surface oxygen atoms or destroy the stable adsorption sites. We have checked the Cl^- effect by a simply experiment: two 0.2 wt% Rh/γ-Al_2O_3 samples were prepared from $[Rh^{II}(OAc)_2]_2$ only and $[Rh^{II}(OAc)_2]_2$ + NaCl (1:5). The . Fourier-transformed EXAFS spectra shown in Figure 5.1.2 indicates that the Rh/γ-Al_2O_3 prepared from NaCl doping showed the same behavior as $RhCl_3$: only metallic Rh particles formed after $[Rh^{II}(OAc)_2]_2$ decomposition. The existence of Cl^- seems to hinder the formation of Rh-O bonds. Therefore, the precursor-dependence may originate from the nature of ligands which determines Rh-O bond formation or not.

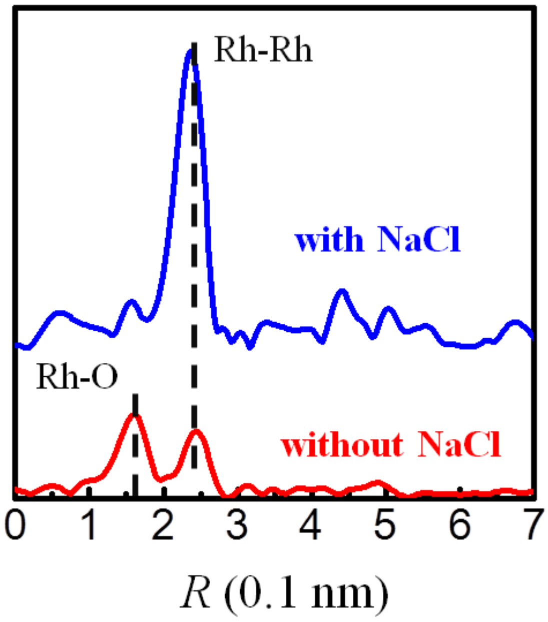

Figure 5.1.2 Fourier transform of k^3 weighted Rh K-edge EXAFS oscillation curves $k^3\chi(k)$ of Rh/Al_2O_3 catalysts prepared from $[Rh^{II}(OAc)_2]_2$, precursors with (blue curve) and without (red curve) NaCl doping.after heat treatments.

5.2 Outlook

The STM and XAFS studies provided us some new knowledge about precursor-dependence of Rh/Al_2O_3, and we found the formation of Rh-O bond was a key process which affected morphology and stability of Rh particles, however, in order to make precursor-effect more clearly, several questions must be answered:

1) How about the decomposition mechanism of Rh acetate precursors and formation mechanism of Rh-O bond? **2)** Why Rh atoms aggregate when doping some Cl^- ions into Rh acetate precursors? How do Cl^- ions work? **3)** How about the catalysis of the Rh/Al_2O_3 prepared from Rhodium acetate precursor?

For the first question, one can perform in-situ STM and RAIRS measurements to trace the decomposition process of Rh acetate precursor on Al_2O_3/NiAl(110) surface. Prior in-situ STM measurements (Chapter 3) suggested that almost all the $[Rh^{II}(OAc)_2]_2$ molecules decomposed around 420 K. Thus, a carful and accurate STM and RAIRS study should be carried out around this temperature. STM can give some morphological change while RAIRS will provide some information about bonds change during the decomposition. On the other hand, one can get some detailed structural information by using polarization-dependent total-reflection fluorescence X-ray absorption fine structure (PTRF-XAFS) spectroscopy as shown in Figure 5.2.1. This technique gives 3-dimensional information about the local structure around the X-ray absorbing atom. Thus the adsorption sites can be determined accurately, and detailed structure information is very important to clarify the mechanism of decomposition of precursor and formation process of Rh-O bond The second question is hard to be answered. I think the Cl^- ions maybe destroy the active oxygen sites to hinder formation of Rh-O bonds, thus the amount of Cl^- ions is a key parameter. And for the third question, methanol partial oxidation (MPO) is a good candidate reaction for testing the catalysis of the Rh dimer species on Al_2O_3.

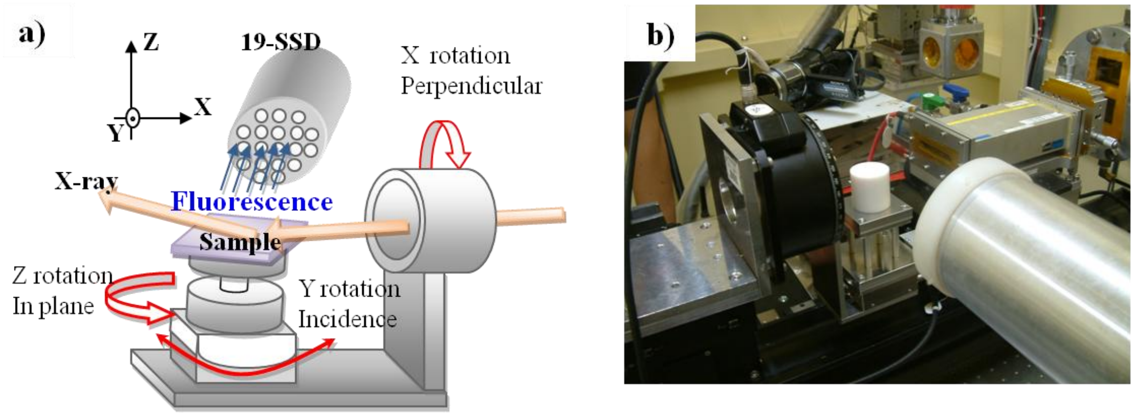

Figure 5.2.1 Experimental setting of PTRF-XAFS method

In the end of this Chapter, I want to refer the surface science study again. As mentioned in Chapter 1, **"Nowadays, surface science study is not just a tool to shed light on some element surface processes, the new concepts generated in the process of surface science studies sometimes can bring about evolution of catalysis."** Actually, in this work, we have performed combined STM and XAFS studies on the precursor dependent structures of Rh/Al_2O_3: first we got a clue from STM measurements on model surfaces: *by using acetate precursor, small, uniform, and stable Rh species with the same core atom number can be obtained*. And then we confirmed this concept could also be applicable to real catalysts by XAFS studies. Through this work, we find in spite of various gaps between the model surface and real catalysts, the concepts generated by surface science studies sometimes can also be applicable to real catalysts, if we adopt appropriate preparation procedure. In our STM studies, we just discussed surface morphology, however, in surface science, for examples: tunneling spectroscopy can provide the electron density of states of metal particles, RAIRS (Reflection Absorption Infrared Spectroscopy) can be used to trace the formation process of active site.

By using these powerful approaches, we hope more and more new concepts will be generated to develop the catalysis.

References

1 G. Kresse, M. Schmid, E. Napetschnig, M. Shishkin, L. Köhler, P. Varga, *Science* 2005, **308**, 1440.

2 K. Ijima, Y. Koike, W.-J. Chun, Y. Saito, Y. Tanizawa, T. Shido, Y. Iwasawa, M. Nomura and K. Asakura, *Chem. Phys. Lett.* 2004, **384**, 134.

List of Publication

1) “Scanning Tunneling Microscopy study on the Precursor-Dependent Formation of Homogeneous Rh Clusters on Al_2O_3 / NiAl(110)”,

Z. W. Chen, S. Fujita, K. Fukui, *J. Phys. Chem. C* **115**, 14270-14277 (2011).

Acknowledgement

First of all, it is a great pleasure to express my gratitude and appreciation to my advisor, Professor Ken-ichi Fukui for his continual guidance, helpful discussions and invaluable advice for 7 years from bachelor course until now. Thank you for helping me expand my thinking and research skills. I would like to express my sincere gratitude to Associate Professor Akihito Imanishi for his helpful advice about XAFS experiments and daily discussion. I would also like to express my sincere gratitude to Assistant Professor Yasuyuki Yokota for helpful discussion about all my work, friendly encouragement not only in Osaka University. but also in Tokyo Institute of Technology.

I would like to express my gratitude to Senior Associate Professor Wang Jae Chun in International Christian University, who has been collaborating with us on the XAFS work in the past four years. The XAFS work presented in this thesis would not have been completed without his collaboration. Thank you for helping me design and finish the XAFS experiments, and guiding me to complete the XAFS analysis and FEFF simulations.

I must also thank several doctors: Dr. Daikou Takamatsu, Dr. Xiang Shao, Dr. Xunwen Xiao. Much appreciation goes to them for daily helpful discussion and encouragement.

Many collective thanks go to Toshiaki Enoki for his guidance during my master course, to Kenji Hara for sharing XAFS machine-time, to Etsushi Tsuji for daily helpful discussion and advice, to Fumitake Matsuoka for daily helpful discussion and collaboration, to all the members of the laboratories of Professor Ken-ichi Fukui, Wang Jae Chun, Toshiaki Enoki for their helpful discussion and encouragement.

Finally, I want to thank my family for their continuous love, encouragement and support.

March 2012

Zhiwen Chen